The Pennsylvania State University

The Graduate School

Department of Chemical Engineering

HYDROCARBON CONVERSION CATALYSIS ON CERIA-BASED MIXED METAL OXIDES

A Dissertation in

Chemical Engineering

by

Adam D. Mayernick

© 2011 Adam D. Mayernick

Submitted in Partial Fulfillment
of the Requirements
for the Degree of

Doctor of Philosophy

May 2011

The dissertation of Adam D. Mayernick was reviewed and approved* by the following:

Michael J. Janik
Assistant Professor of Chemical Engineering
Dissertation Advisor
Chair of Committee

Robert M. Rioux
Friedrich G. Helfferich Assistant Professor of Chemical Engineering

Kristen A. Fichthorn
Merrell R. Fenske Professor of Chemical Engineering and Physics

Adri C.T. van Duin
Associate Professor of Mechanical and Nuclear Engineering

Andrew L. Zydney
Walter L. Robb Chair and Professor of Chemical Engineering
Head of the Department of Chemical Engineering

*Signatures are on file in the Graduate School

ABSTRACT

Ceria (CeO_2) is a rare-earth metal oxide with a wide variety of applications in hydrocarbon conversion catalysis due to its ability to exchange lattice oxygen with reactant species. Ceria in combination with other rare earth or transition metals exhibits unique activity for hydrocarbon oxidation and high-temperature desulfurization. The structure and functionality of the transition metal-ceria surface is a function of synthesis and pretreatment methods, as well as catalytic operating conditions. The development of novel ceria-based catalysts is thus largely limited by difficulties in identifying the specific nature of active sites and establishing structure-function relationships therein.

This dissertation utilizes computational chemistry methods to examine the catalytic stability and activity of transition metal-ceria surface structures at the atomistic level and motivate future efforts in catalyst design. Density functional theory and *ab initio* thermodynamics ares used to calculate activation barriers and free energies of elementary reaction steps. The activity and thermodynamic stability of supported Pd species on Pd-ceria oxidation catalysts are probed, with emphasis on quantifying the unique hydrocarbon oxidation activity of Pd-ceria mixed oxides. The C-H bond breaking activity of a series of transition metal-ceria mixed oxides is assessed, and a correlation is found between C-H activation energetics and oxide reducibility. The energetics of adsorption of H_2S over ceria-lanthanide mixtures are also calculated, to assess the requirements of an effective ceria-based high temperature desulfurization sorbent.

The use of DFT and reactive force field methods to probe multi-component heterogeneous catalyst surfaces is evaluated to direct future multi-scale studies of palladium-ceria oxidation catalysts and ceria-lanthanide desulfurization sorbents.

TABLE OF CONTENTS

LIST OF FIGURES vii

LIST OF TABLES xi

ACKNOWLEDGEMENTS xiii

Chapter 1 Introduction – Ceria Catalysis of Hydrocarbon Conversion 1

- 1.1 Background 1
- 1.2 Summary of Chapters 8
- 1.3 References 12

Chapter 2 Methane Activation and Oxygen Vacancy Formation over CeO_2 and Zr, Pd substituted CeO_2 surfaces 17

- 2.1 Introduction 18
- 2.2 Methods 22
- 2.3 Results and Discussion 27
    - 2.3.1 Oxygen Vacancy Formation 27
    - 2.3.2 Thermodynamics of Dissociative Methane Adsorption 35
    - 2.3.3 Methane Adsorption on Pre-reduced Surfaces 38
    - 2.3.4 Dependence of ΔE_{vac} and ΔE_{ads} on Value of Hubbard U-term 39
    - 2.3.5 Correlation between Vacancy Formation and Methane Adsorption 42
    - 2.3.6 Activation Barrier for Dissociative Methane Adsorption 42
- 2.4 Conclusions 45
- 2.5 References 46

Chapter 3 Ab initio thermodynamic evaluation of Pd atom interaction with CeO_2 surfaces ... 50

- 3.1 Introduction 51
- 3.2 Computational Methodology 55
    - 3.2.1 Electronic Structure Method 55
    - 3.2.2 Model Construction 56
    - 3.2.3 Adsorption and Insertion Energy Calculation 58
    - 3.2.4 Relative Stability of PdO_x-CeO_2 Systems 58
    - 3.2.5 Surface Formation Energy 61
- 3.3 Results and Discussion 62
    - 3.3.1 Pd, Pd_4, and PdO_x Adsorption on CeO_2 Surfaces 62
    - 3.3.2 Pd Insertion into CeO_2(111) and CeO_2(110) 66
    - 3.3.3 Incorporation of Pd atoms into the CeO_2 surface 67
    - 3.3.4 Relative Stability of Different States of Pd atoms on CeO_2 Surfaces 68
    - 3.3.5 Surface Formation Energies 77
    - 3.3.6 Relative Energy of Pd_4 clusters 78
- 3.4 Conclusions 80
- 3.5 References 80

3.6 Supporting Information 85

Chapter 4 Methane Oxidation on Pd-ceria: A DFT study of the mechanism over $Pd_xCe_{1-x}O_2$, Pd, and PdO 88

4.1 Introduction 89
4.2 Methods 92
    4.2.1 Electronic Structure Method 92
    4.2.2 Surface Models 94
    4.2.3 Reaction Free Energies 95
    4.2.4 Reaction Free Energies 99
4.3 Results and Discussion 100
    4.3.1 Reaction Free Energy Diagrams for Methane Oxidation 100
    4.3.2 Dependence of Rate Determining Steps on Operating Conditions 111
4.4 Conclusions 115
4.5 References 117
4.6 Supporting Information 121

Chapter 5 Correlating C-H bond Activity and Oxide Reducibility: Electronic Structure Analysis of the Catalytic Activity of Dopant Metals in Ceria 136

5.1 Introduction 137
5.2 Methods 139
    5.2.1 Electronic Structure Method 139
    5.2.2 Surface Models 139
    5.2.3 Adsorption, Oxygen Vacancy Formation, and Work Function 141
5.3 Results and Discussion 142
    5.3.1 Electronic Structure of the $Pd_xCe_{1-x}O_2(111)$ Surface 142
    5.3.2 Correlations between C-H Bond Activity and Surface Reducibility 145
5.4 Conclusions 148
5.5 References 149
5.6 Supporting Information 151

Chapter 6 Energetics and Mechanism for H_2S Adsorption by Ceria-Lanthanide Mixed Oxides: Implications for the Desulfurization of Biomass Gasifier Effluents 154

6.1 Introduction 155
6.2 Methods 158
    6.2.1 Synthesis of Ceria-Lanthana and Ceria-Terbia 158
    6.2.2 Sulfur Adsorption Capacity Measurements 158
    6.2.3 Electronic Structure Method 159
    6.2.4 Surface Models 160
    6.2.5 Free Energies of H_2S Adsorption and Dissociation 161
6.3 Results and Discussion 163
    6.3.1 Experimental Sulfur Adsorption Capacities 163
    6.3.2 H_2S Adsorption and Dissociation 164
    6.3.3 Thermodynamic Limit for Sulfidation of Oxide Surfaces 171
    6.3.4 Thermodynamic Cycle for H_2S adsorption by Ceria-Based Mixed Oxides ... 177
6.4 Conclusions 178

6.5 References 179
6.6 Supporting Information 182

Chapter 7 A ReaxFF Reactive Monte Carlo Study of Surface Enrichment and Step Structure on Yttria-Stabilized Zirconia 188

7.1 Introduction 189
7.2 Methods 193
  7.2.1 Electronic Structure Method 193
  7.2.2 Model Construction 193
  7.2.3 Calculation of Surface Formation Free Energies 195
  7.2.4 ReaxFF Methodology 196
7.3 Results and Discussion 199
  7.3.1 DFT Surface Energies of YSZ(111) 199
  7.3.2 DFT Surface Energies of YSZ(111) 200
7.4 Conclusions 207
7.5 References 209
7.6 Supporting Information 212

Chapter 8 Summary, Conclusions, and Recommendations for Future Study 214

8.1 Hydrocarbon Oxidation on Ceria-Based Mixed Oxides 214
8.2 Ceria-Based Mixed Oxides for Syngas Cleanup 218
8.3 Perspective and Suggestions for Future Study 219
8.4 References 222

Appendix A Standard INCAR file for CeO_2 223

LIST OF FIGURES

Figure 1-1. Schematic of heterogeneous distribution of surface sites, particle sizes, and Pd oxidation states on palladium-ceria catalyst. Ce atoms are tan (light), Pd atoms are blue (gray), oxygen atoms are red (dark). 6

Figure 2-1. (a) Bulk CeO_2 fluorite unit cell. (b) 111, (c) 110, (d) 100 surface slabs of CeO_2. 24

Figure 2-2. Top views of CeO_2 (a) 111, (b) 110, (c) 100. Side views of (d) 111, (e) 110, (f) 100 with $^*CH_3$ and *H. 27

Figure 2-3. Total DOS plotted vs. energy (referenced to vacuum potential) for (a) CeO_2 (111), (b) vacant CeO_2 (111), (c) CeO_2 (111) + $^*CH_3$ + *H, and (d) Pd-substituted vacant CeO_2 (111). Spin-down states are plotted on the negative y-axis, all states below the Fermi level are highlighted, and ΔE_{gap} is labeled for reference. 31

Figure 2-4. Intact CeO_2 (a) 111, (c) 110, (e) 100 and vacant (b) 111, (d) 110, (f) 100 surfaces with the substitution of Pd for Ce into the surface metal layer. Oxygen atoms removed to form the first vacancy (α) and second vacancy (β) are labeled..........33

Figure 2-5. Dependence of the methane adsorption energy (ΔE_{ads}) and surface vacancy formation energy (ΔE_{vac}) on the choice of U value. (•) Pd-substituted CeO_2 surfaces, (■) Zr-substituted CeO_2 surfaces, and (▲) pure CeO_2. Closed circles represent E_{vac} data and open circles represent ΔE_{ads} data. 40

Figure 2-6. Plot of the methane adsorption energy (ΔE_{ads}) vs. the surface vacancy formation energy (ΔE_{vac}). (•) Pd-substituted CeO_2 surfaces, (■) Zr-substituted CeO_2 surfaces, and (▲) pure CeO_2. Pre-reduced surfaces are noted by open symbols. 43

Figure 2-7. Plot of the methane adsorption energy (ΔE_{ads}) vs. the surface vacancy formation energy (ΔE_{vac}). (•) Pd-substituted CeO_2 surfaces, (■) Zr-substituted CeO_2 surfaces, and (▲) pure CeO_2. Pre-reduced surfaces are noted by open symbols. 44

Figure 3-1. Adsorption sites for Pd on CeO_2(111) surface (a), (110) surface (b), and (100) surface (c). Tan (light) spheres represent cerium atoms and red (dark) spheres represent oxygen atoms. 57

Figure 3-2. Optimized structure of Pd_4* on the CeO_2(111) surface (a) and (110) surface (b). Palladium atoms are represented in large space-filling format for emphasis, and Ce(tan, light) and O(red, dark) atoms are shown in ball and stick format. 64

Figure 3-3. Optimal conformation of PdO* on the CeO_2(111) surface (a), (110) surface (b), (100) surface (c). PdO_2* on the CeO_2(111) surface (d), (110) surface (e), (100) surface (f). Ce atoms are tan (light), Pd atoms are blue (gray), and O atoms are red (dark). 65

Figure 3-4. Insertion for Pd (blue, gray) in the CeO_2(111) surface (a), (110) surface (b). 66

Figure 3-5. The Pd/inc/2V_O surface for the CeO_2(111) termination(a), and (110) termination (b). Ce atoms are tan (light), Pd atoms are blue (gray), and O atoms are red (dark)....................68

Figure 3-6. The relative stability of Pd-ceria(111) surface configurations (a) and phase diagram for most stable single Pd atom states on the (111) surface (b). Data in (a) is labeled as follows: (◊) Pd/ins, (▼) Pd/inc, (■) Pd/inc/V_O, (●) Pd/inc2V_O, (□) PdO*, (▽) PdO_2*, (○) Pd*....................69

Figure 3-7. Relative stability of Pd-ceria (110) surface configurations (a) and phase diagram for most stable single Pd atom states on the (110) surface (b). Data in (a) is labeled as follows: (◊) Pd/ins, (▼) Pd/inc, (■) Pd/inc/V_O, (●) Pd/inc2V_O, (□) PdO*, (▽) PdO_2*, (○) Pd*)....................72

Figure 3-8. Relative stability of Pd-ceria (100) surface configurations (a) and phase diagram for most stable single Pd atom states on the (100) surface (b). Data in (a) is labeled as follows: (◊) Pd/ins, (▼) Pd/inc, (■) Pd/inc/V_O, (●) Pd/inc2V_O, (□) PdO*, (▽) PdO_2*, (○) Pd*)....................72

Figure 4-1. Top and side views of slab models for CeO_2(111), $Pd_xCe_{1-x}O_2$(111), Pd*/CeO_2(111), PdO(100), and Pd(111) surfaces. Ce is displayed as tan (light), Pd as light blue (gray), and O as red (dark)....................95

Figure 4-2. Reaction free energy diagram for CH_4(g) + $2O_2$(g) → CO_2(g) + $2H_2O$(g) over CeO_2(111). Inset: HCO* ($HCOO^-$), the most stable intermediate in methane oxidation over CeO_2(111). Ce is displayed as tan (light), O as red (dark), C as gray, and H as white. Oxygen (O_2) is not explicitly included in the oxidation mechanism, as addition of O_2 to the surface occurs in oxygen vacancy filling steps. 104

Figure 4-3. Initial (a, d, g), transition (b, e), and final (c, f, h) states for methane activation on CeO_2(111) (a, b, c), Pd(111) (d, e, f) and $Pd_xCe_{1-x}O_2$(111) (g, h). Ce is displayed as tan (light), Pd as light blue (gray), O as red (dark), C as grey, and H as white....................104

Figure 4-4. Reaction free energy diagram for CH_4(g) + $2O_2$(g) → CO_2(g) + $2H_2O$(g) over $Pd_xCe_{1-x}O_2$(111). Inset: H* (-OH), the most stable intermediate in methane oxidation over $Pd_xCe_{1-x}O_2$ (111). Ce is displayed as tan (light), O as red (dark), Pd as light blue (gray), and H as white....................106

Figure 4-5. Reaction free energy diagram for CH_4(g) + $2O_2$(g) → CO_2(g) + $2H_2O$(g) over PdO(100). Inset: HCO* ($HCOO^-$), the most stable intermediate in methane oxidation over PdO(100). Pd is displayed as light blue (grey), O as red (dark), C as grey and H as white....................108

Figure 4-6. Reaction free energy diagram for CH_4(g) + $2O_2$(g) → CO_2(g) + $2H_2O$(g) over Pd(111). Inset: CO*, the most stable intermediate in methane oxidation over Pd(111). Pd is displayed as light blue (gray), O as red (dark), and C as gray....................111

Figure 4-7. Phase regions of rate determining steps of methane oxidation over $CeO_2(111)$ at 298K/catalytic combustion operating conditions (a) and 973K/SOFC conditions (b). Filled circles (•) represent conditions at the labeled conversions for (a) 298K/catalytic combustion and (b) 973K/SOFC. 113

Figure 4-8. Phase regions of rate determining steps of methane oxidation over $Pd_xCe_{1-x}O_2(111)$ at 298K/catalytic combustion operating conditions (a) and 973K/SOFC conditions (b). Filled circles (•) represent conditions at the labeled conversions for (a) 298K/catalytic combustion and (b) 973K/SOFC. 114

Figure 5-1. Side (a),(c) and top (b), (d) views of the $Pd_xCe_{1-x}O_2(111)$ (a), (b) and the oxygen vacant $Pd_xCe_{1-x}O_y(111)$ (c), (d) surfaces. Ce atoms are colored tan, Pd are colored blue, and oxygen are colored red. Oxygen atoms not coordinated to the Pd atom in (b) and (d) are colored brown. 140

Figure 5-2. Crystal field splitting diagram for d orbitals in octahedral and square-planar fields. 143

Figure 5-3. Side (a),(c) and top (b), (d) views of the $Pd_xCe_{1-x}O_2(111)$ (a), (b) and the oxygen vacant $Pd_xCe_{1-x}O_y(111)$ (c), (d) surfaces. Ce atoms are colored tan, Pd are colored blue, and oxygen are colored red. Oxygen atoms not coordinated to the Pd atom in (b) and (d) are colored brown. 144

Figure 5-4. (a) Methane dissociative adsorption energy (E_{ads}) vs. oxygen vacancy formation energy (E_{vac}) and (b) E_{ads} (•), E_{vac}(■) vs. work function (φ) for single metal atoms substituted for Ce atoms into the $CeO_2(111)$ surface. 146

Figure 6-1. Top (a), (c), (e), and side (b), (d), (f) views of surface unit cell for (a), (b), $CeO_2(111)$, (c), (d) $La_2O_3/CeO_2(111)$, and (e), (f) $Tb_2O_3/CeO_2(111)$. Ce atoms are colored tan (light), O atoms red (dark), La atoms blue (gray), and Tb atoms teal (dark gray). 161

Figure 6-2. Top (a), (c), (e), and side (b), (d), (f) views of surface unit cell for (a), (b), $CeO_2(111)$, (c), (d) $La_2O_3/CeO_2(111)$, and (e), (f) $Tb_2O_3/CeO_2(111)$. Ce atoms are colored tan (light), O atoms red (dark), La atoms blue (gray), and Tb atoms teal (dark gray). 164

Figure 6-3. Top (a), (c), (e), and side (b), (d), (f) views of surface unit cell for H_2S^* (a), (b), SH* (c), (d) and S* (e), (f) on $CeO_2(111)$. Ce atoms are colored tan (light), O atoms red (dark), S atoms green (gray), and H atoms white. Surface metal atoms are denoted Ce_1, Ce_2, and M as referenced in The Supporting Information for bond lengths between surface atoms and adsorbed sulfur species. 166

Figure 6-4. (a) Free energy diagram for H_2S adsorption dissociation over $CeO_2(111)$ at 1100K, and PH2 = 0.35 atm, PH2S = 10^{-2} atm, and PH2O = 0.03 atm and (b) phase diagram for $CeO_2(111)$ surface at 1100K as a function of $H_2S(g)$ and $O_2(g)$ pressure. Oxygen vacancies are denoted VO··. 166

Figure 6-5. (a) Free energy diagram for H_2S adsorption dissociation over $La_2O_3/CeO_2(111)$ at 1100K, and PH2 = 0.35 atm, PH2S = 10^{-2} atm, and PH2O = 0.03 atm and (b) phase diagram for $La_2O_3/CeO_2(111)$ surface at 1100K as a function of $H_2S(g)$ and $O_2(g)$ pressure. Oxygen vacancies are denoted VO··. 169

Figure 6-6. (a) Free energy diagram for H_2S adsorption dissociation over $Tb_2O_3/CeO_2(111)$ at 1100K, and PH2 = 0.35 atm, PH2S = 10^{-2} atm, and PH2O = 0.03 atm and (b) phase diagram for $Tb_2O_3/CeO_2(111)$ surface at 1100K as a function of $H_2S(g)$ and $O_2(g)$ pressure. Oxygen vacancies are denoted VO··. 172

Figure 6-7. Thermodynamic cycle for H_2S adsorption and dissociation on ceria-based mixed metal oxide. 177

Figure 7-1. DFT slab models of (a) ZrO_2 (111) surface (top view), (b) ZrO_2 (111) surface (side view), and (c), (d) stepped ZrO_2 (111) surface. Cell length and cell width are defined in (a) and (b), step width in (c), and oxygen vacancy sites (V_x) and yttrium doping sites (Y_x) in (d). 194

Figure 7-2. (a) Thinnest ReaxFF slab model of the (10 10 8) YSZ surface with blue atoms corresponding to surface metal atoms, green atoms as 2nd layer metal atoms, purple atoms as third layer metal atoms and red atoms as oxygen. (b) ReaxFF slab model of the (10 10 12) YSZ surface with blue atoms corresponding to surface metal atoms. 198

Figure 7-3. Y% at the step edge (●) and surface (▲) on the YSZ surface as a function of bulk yttrium concentration. 201

Figure 7-4. Y% at the step edge (●), surface (▲), 2nd surface layer (■), and 3rd surface layer (▼) on the YSZ surface as a function of slab thickness. 203

Figure 7-5. Relative surface formation energies for flat and stepped pure zirconia (ZrO_2) and YSZ surfaces. 208

LIST OF TABLES

Table 1-1. Methane combustion rates over several samples palladium-ceria synthesized by incipient wetness impregnation (IWI) and solution combustion synthesis (SCS). Data taken from Colussi et al.[6] 4

Table 2-1. Vacancy formation energies (ΔE_{vac}) for each surface, the resulting change in Bader charge for each related metal atom (M_{1-4}). and vacancy formation energies for each pre-reduced surface ($\Delta E'_{ads}$). 29

Table 2-2. Adsorption energies (ΔE_{ads}) for each surface, the resulting change in Bader charge for each related metal atom (M_{1-4}), and adsorption energies for each pre-reduced surface ($\Delta E'_{ads}$). 37

Table 2-3. Energy differences ΔE_{gap} between the valence band and gap state for the vacant CeO_2, Zr-substituted CeO_2, and Pd-substituted CeO_2(111) surfaces. 41

Table 2-4. Relative energy of the methyl radical state (E_{rad}) over each surface and the resulting change in Bader charge for each related metal atom (M_{1-4}). 44

Table 3-1. Adsorption energies and insertion energies for Pd atoms on CeO_2(111), (110) and (100) surfaces. 63

Table 3-2. DFT+U energy calculated for reference species used in calculating relative free energies (Eq. 3) and surface formation energies (Eq. 17). 70

Table 3-3. DFT calculated energies for each surface system, used with data in Table 2, oxygen chemical potentials (tabulated in Supporting Information), and equations 3 and 17 to determine relative free energies and surface formation energies. 71

Table 3-4. Surface formation energies for single Pd atom species on ceria, calculated at 973K and 1 atm. Italicized values are relative within each Pd oxidation state to species on the (111) surface. The non-italicized values are given in J m^{-2}. 78

Table 4-1. Activation barriers at 0K, free energies of activation at catalytic combustion conditions, relative combustion rate (normalized to the rate over CeO_2(111)) and stable intermediates for methane oxidation over CeO_2(111), $Pd_xCe_{1-x}O_2$(111), PdO(100), Pd(111), and Pd*/CeO_2(111). [a]-calculated at 273K, PCH4= 1 atm; [b]-Δ‡S0 approximated at 0.33 eV 101

Table 4-2. Reaction energies at 0K for each elementary step in methane oxidation over CeO_2(111), $Pd_xCe_{1-x}O_2$(111), PdO(100), Pd*/CeO_2(111), and Pd(111). 102

Table 6-1. Surface areas for ceria-lanthana and ceria-terbia mixtures after calcination in flowing air at 773K. 164

Table 6-2. Energies for thermodynamic cycle (Figure 6-7) over CeO_2, $LaCeO_x$, and $TbCeO_x$ 178

Table 7-1. Energy differences for yttrium and oxygen vacancy location at the YSZ(111) surface calculated by ReaxFF and DFT. 192

Table 7-2. Surface Formation Energies for the cubic fluorite ZrO_2 and YSZ (111) surfaces calculated by DFT. Yttrium and oxygen vacancy positions within the step model are noted as labeled in Figure 7-1(d)..200

Table 7-3. Coordination numbers of oxygen and oxygen vacancies ($V_O^{\bullet\bullet}$) for Zr and Y atoms in the overall YSZ slab and for Zr and Y atoms in the surface layer. 206

Table 7-4. Oxygen vacancy concentration in different regions of the YSZ surface slab. 206

ACKNOWLEDGEMENTS

I want to thank my advisor Michael Janik for providing technical direction, inspiration, and a contagious work ethic throughout my studies. The standard of excellence which permeates the efforts of our lab group begins and ends with Dr. Janik. Gholamreza Rostamikia is an unbelievable friend and colleague, and has been a positive influence for the entirety of my study. I'd also like to thank the other members of the Janik lab and specifically Kuan-yu Yeh, Greg Mullen, and Kyungtae Lee with whom I've been able to develop technically, professionally, and personally. I wish the best to Tom Senftle and Matt Krcha, who have the task of continuing the work that I've initiated. I owe a great deal of thanks to Austin Antolik, whom I had the pleasure of mentoring and also learning from, and has directly facilitated my career path. Joe McDermott has been my best friend, roommate, and colleague for numerous years, and is a constant source of passion for science and research. It has been my privilege to work with some of the brightest and kindest individuals in the world during my time at Penn State, and the experience was invaluable.

Finally, I'd like to thank my mother, father, brother and sister for continuous support and encouragement. I'm eternally grateful for the opportunities I've been blessed with, and offer thanks to all those who have been there along the way.

Chapter 1

Introduction – Ceria Catalysis of Hydrocarbon Conversion

1.1 Background

Utilization of hydrocarbons is performed by either direct energy production (oxidation) from raw feedstock or chemical conversion of feedstock to fuel molecules. The efficiency of hydrocarbon utilization processes is reliant on the performance of hydrocarbon oxidation and conversion catalysts. Ceria (CeO_2) is a rare earth metal oxide widely used in automotive catalysis due to its ability to exchange oxygen with reactant species for either oxidation or reduction reaction steps, or more generally to transition between Ce^{4+} and Ce^{3+} oxidation states. This ability to provide facile oxygen exchange within catalytic environments motivates the use of ceria in numerous catalytic applications such as three-way automotive catalysis,[1-3] steam reforming,[4,5] and catalytic combustion.[6,7] The development of novel ceria-based catalysts is spurred by previous studies which have demonstrated that addition of other transition metals to ceria alters the redox properties[8-11] and catalytic activity[6-8,12-17] of ceria-based materials. The prospect of tailoring composition to optimize catalytic performance is essential to the implementation of ceria-based catalysts in energy conversion or energy production processes. Heterogeneous catalysts based on transition metal-ceria combinations are difficult to characterize experimentally, however, and may undergo chemical and structural changes during catalytic operation. The development of novel ceria-based catalysts is thus largely limited by difficulties in identifying the specific nature of active sites and establishing structure-function relationships therein. This dissertation utilizes computational methods based on density functional theory to examine the catalytic stability and activity of transition metal-ceria surface structures at the atomistic level and motivate future efforts in catalyst design.

In contrast to non-reducible metal oxide catalyst supports such as silica and alumina, ceria does not simply provide a physical support to maximize active metal surface area; strong interactions between the transition metal and the ceria support facilitate unique catalytic activity. Ceria may serve as an “oxygen reservoir” to increase the concentration of adsorbed oxygen species on supported metal particles, thereby increasing the rate of oxidation steps and reducing the rate of formation of carbon deposits. Strong interactions with the ceria surface can also stabilize surface sites with unique activity to that of the pure metal surface including oxidized metal species,[6,9,12,15,18] small metal particles,[3,19] and metal-ceria interface sites.[20,21] Transition metal-ceria combinations thus offer potential in the development of novel hydrocarbon oxidation catalysts as ceria can serve both as a conventional physical support to disperse metal atoms and as a catalytically active component. Palladium-ceria is particularly attractive for hydrocarbon oxidation applications such as catalytic combustors and solid oxide fuel cells (SOFCs), as catalysts containing Pd-O-Ce linkages display particularly high oxidation activity.[6]

Palladium is active for hydrocarbon oxidation,[22,23] however the oxidation state and chemical functionality of active sites on the palladium surface have not been characterized *in situ*. The oxidation state and the morphology of the palladium surface are strongly a function of catalytic operating conditions,[15,23] which complicates characterization efforts to elucidate the nature of active sites. *Ex-situ* characterization can be used to determine the Pd oxidation state before and after reaction, however these efforts illustrate further the complexity in determining the structure and functionality of the active phase. Hoflund et al. report ELS and XPS spectroscopy results which show that PdO forms during methane combustion on palladium powder.[22] Ribeiro et al. show that PdO decomposes to Pd at 907K in 1.5 torr O_2, and that this transition results in an order of magnitude drop in the methane combustion turnover rate.[23] Thus depending upon the temperature and oxygen pressure, Pd or PdO species may be stable, with dramatic effects on catalytic activity. For palladium-ceria the dependence of the stable surface structure and oxidation state on reaction conditions is even more complex, as Pd, PdO, or $Pd_xCe_{1-x}O_y$ may be stable during reaction.

The morphology and oxidation state of Pd on ceria are both strong functions of synthesis and pretreatment methods, and strong interactions between Pd and ceria stabilize oxidized Pd species. X-ray Photoelectron Spectroscopy (XPS) showed that Pd-ceria prepared by deposition-precipitation had a higher concentration of cationic $Pd^{\delta+}$ sites than Pd-ceria prepared by wet impregnation.[7] Preparation of Pd-ceria by solution-combustion synthesis methods can facilitate mixing of Pd atoms into the CeO_2 lattice framework.[6,24] A combination of XPS, X-ray Diffraction (XRD) and Extended X-ray Absorption Fine Structure (EXAFS) results were used to determine that Pd/ceria prepared by solution-combustion synthesis contains Pd^{2+} cations incorporated into cubic fluorite CeO_2 as a solid solution whereas wet impregnation result in samples containing primarily metallic Pd.[24] Colussi et al. also recently reported that surface solid solutions of

Pd^{2+}/CeO_x with distinct short and long range order can be prepared by solution-combustion synthesis.[6] High-resolution Transmission Electron Microscopy (HRTEM) and DFT calculations confirm that their Pd^{2+}/CeO_x samples consist of a reconstructed $CeO_2(110)$ surface with Pd^{2+} ions substituted for Ce^{4+}.[6] The rate of methane oxidation on this Pd^{2+}/CeO_x mixed oxide surface at both 1 and 1.71 wt.% was nearly twice that of palladium-ceria samples of equivalent composition prepared by incipient wetness (Table 1-1).[6]

Table 1-1. Methane combustion rates over several samples palladium-ceria synthesized by incipient wetness impregnation (IWI) and solution combustion synthesis (SCS). Data taken from Colussi et al.[6]

Sample	Pd	Surface Area	Methane Combustion Rate	
	[wt%]	[$m^2\ g^{-1}$]	[$\mu mol\ g_{Pd}^{-1}\ s^{-1}$]	[$10^2\ \mu mol\ m^{-2}s^{-1}$]
IWIa	1.00	3.4	9.5	2.8
IWIb	0.98	11.8	9.7	0.8
SCS1	1.09	5.4	25.1	5.1
IWI2a	1.72	3.3	5.5	2.9
IWI2b	1.74	12.2	7.0	1.1
SCS2	1.71	5.9	27.6	8.0

Previous experimental studies of palladium-ceria catalysts illustrate the complexity in characterizing the transition metal-ceria surface during reaction and identifying active surface species. An actual palladium-ceria catalyst will contain a heterogeneous distribution of surface sites, particle sizes, and Pd oxidation states (Figure

1-1), the relative distribution of which is a function of synthesis and pretreatment methods as well as catalytic operating conditions. Particle sizes and oxidation states determined before or after reaction thus may not accurately represent active species during operation, and stable surface intermediates may not correspond to those on active sites. Increased methane combustion rates on surfaces containing Pd-O-Ce linkages, however, illustrates that mixed oxides of palladium and ceria may provide increased catalytic activity with respect to supported palladium particles.[6] Mixed oxides also offer the potential for more efficient precious metal utilization, as the case of isolated metal atoms incorporated into the ceria lattice represents ideal particle dispersion.

Mixed oxides of ceria and numerous other transition and rare-earth metals including Pd,[6,24] Cu,[25] Zr,[26,27] Mn,[28] Gd,[29] La,[30,31] and Tb[11] are stable and have been prepared in previous studies. The addition of transition or rare-earth metals to ceria to form mixed oxides results in altered redox properties and catalytic activity. For example, oxidation enthalpies for ceria-zirconia solid solutions were between 200-300 kJ mol^{-1} less than those of pure ceria (for $Zr_xCe_{1-x}O_2$ where $0.08 < x < 0.86$).[27] Mixed oxides of ceria thus offer the possibility of catalyst tunability, whereby altering the concentration of other transition or rare-earth metals alters the catalytic activity. Experimental characterization of mixed oxide surfaces is challenging, however, as the distribution of metal and oxygen atoms may differ significantly from the overall bulk composition. For noble metals such as Pd, substitution of Pd atoms into Ce lattice positions has been demonstrated on the $CeO_2(110)$ surface,[6,24] however not in bulk CeO_2. Design and optimization of novel ceria-based catalysts requires identification of active species on the metal-ceria surface and synthesis targeted to form high yields of these surface species.

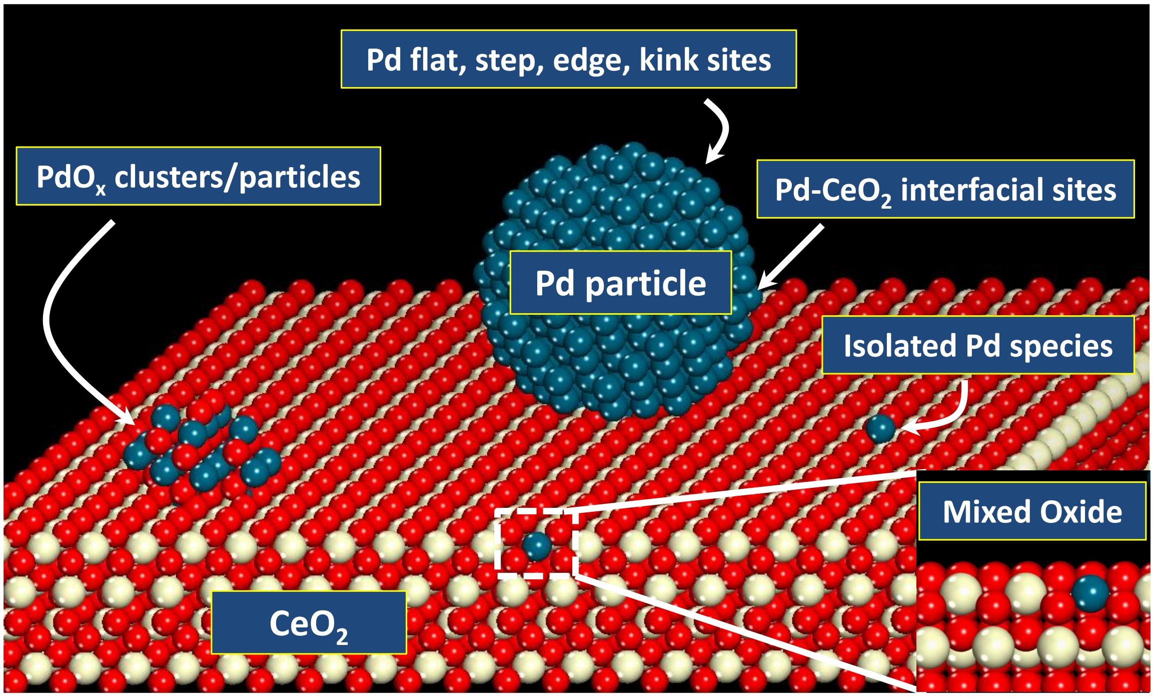
Pd flat, step, edge, kink sites
PdO$_x$ clusters/particles
Pd-CeO$_2$ interfacial sites
Pd particle
Isolated Pd species
Mixed Oxide
CeO$_2$

Figure 1-1. Schematic of heterogeneous distribution of surface sites, particle sizes, and Pd oxidation states on palladium-ceria catalyst. Ce atoms are tan (light), Pd atoms are blue (gray), oxygen atoms are red (dark).

Computational chemistry methods can probe structural details and elementary reaction energetics on catalyst surfaces at the atomistic level, and thus provide electronic level insight difficult to attain experimentally. Density functional theory (DFT) methods, coupled with *ab initio* thermodynamics, can evaluate the driving forces (free energies) for structural transformations and elementary reaction steps under catalytic operating conditions. The application of DFT methods to study catalytic reactions on metal-ceria surfaces therefore may be useful in quantifying the catalytic activity of various surface sites and oxidation states, and elucidating lowest energy reaction paths. Studies of ceria-transition metal systems using DFT methods, however, are restricted to small unit cells, and previous DFT investigations of ceria surfaces have focused on evaluating oxygen vacancy formation energies[32-36] and reaction energies[37-41] on the stoichiometric pure CeO_2 surface. Consideration of heterogeneous particle/surface structures is not possible within the constraints of the cell sizes (<200 atoms) computationally practical with DFT. Due to these limitations of model size in DFT, the impact of added transition metals to ceria on catalytic activity has been limited to the study of single transition metal atoms doped into the ceria lattice[17,25,42-44] or single supported transition metal atoms.[45,46] This dissertation utilizes DFT and *ab initio* thermodynamics methods to calculate relative free energies of varying surface structures and oxidation states, and elementary reaction steps on the transition metal-ceria surface. Limitations in cell size for modeling support particle structures do not permit direct consideration of supported metal clusters, however relative free energies of separated metal and metal oxide phases and free energies of reaction steps a number possible surface structures and oxidation states are calculated.

The DFT+U method is utilized herein, to address theoretical difficulties in representing the electronic structure of reduced ceria (CeO_{2-x}). Standard DFT representations fail to describe the partial occupation of Ce 4f states associated with the formation of oxygen vacancies and the reduction of Ce^{4+} to Ce^{3+}.[47-49] Due self-interaction error, DFT methods incorrectly predict delocalization of 4f electrons upon reduction of Ce^{4+} to Ce^{3+}. The DFT+U method introduces the Hubbard U-term as an on-site Coulombic interaction in the f states of ceria, which allows electrons to localize on Ce^{3+}. The localized 4f electrons appear as a gap state between the occupied valence band and the remaining unoccupied electronic states of ceria.[47-49] The energy between this gap state and the valence band is influenced by the value of the U parameter, and the dependence of the position of the gap state on U value is addressed in Chapter 2. A value of U = 5 eV is used for the majority of the calculations presented herein, which is consistent with values used in previous studies[32,35,46,50,51] and ensures proper localization of 4f electrons (see Chapter 2). As the band gap and relative reduction energies are dependent on choice of U value, hybrid functionals may alternatively be used (which incorporate a fixed amount of nonlocal Fock exchange into standard generalized gradient (GGA) or local density (LDA) functional), to address the self interaction error.[52] Hybrid functionals such as Heyd-Scuseria-Ernzerhof (HSE)[53] and Perdew-Burke Ernzerhof (PBE0)[54] accurately predict the lattice constants of both CeO_2 and Ce_2O_3 and correctly localize 4f electrons,[52] however still suffer inaccuracies in calculation of relative reduction energies and require large computational resources. The DFT+*U* method is thus utilized in the studies included in this dissertation, with consideration of the dependence of relative energetics on choice of U value.

1.2 Summary of Chapters

This dissertation examines the catalytic activity of pure ceria, and attempts to elucidate the structure and electronic properties active sites which provide for the unique catalytic activity of transition-metal ceria combinations. Chapter 2 reports oxygen vacancy formation energies and methane activation energies over pure ceria, and Zr and Pd-substituted ceria surfaces. Ceria-zirconia mixtures are stable and used in lieu of pure ceria in many catalytic applications due to increased reducibility of the oxide mixture with respect to the pure components.[1,2,26,27,55-61] Palladium-ceria is active for hydrocarbon oxidation,[6,7] however palladium-ceria mixed oxides of Pd^{4+} substituted into the CeO_2 lattice have not been prepared experimentally. Chapter 2 thus quantifies the relative changes in reduction and C-H activation energetics over ceria in the presence of Zr or Pd dopant metals, for Zr to compare with well established effects of Zr doping on ceria reducibility and for Pd to evaluate the influence of substituted Pd^{4+} on reduction energetics and catalytic activity. Chapter 2 also evaluates the sensitivity of relative energies and the position of the 4f gap state on U value. The results in this chapter demonstrate that ceria surfaces doped with Pd can provide highly active sites for C-H bond dissociation.

Though $Pd_xCe_{1-x}O_2$ surfaces are found to be active for C-H bond activation, their stability as a function of catalytic operating conditions must also be assessed. Chapter 3 addresses the thermodynamic stability of Pd species supported on the ceria surface in variety of configurations and oxidation states (Pd^{4+}, Pd^{2+}, Pd^0). The relative free energies of Pd in each of these three oxidation states both supported on the ceria surface and substituted into the ceria lattice for Ce are calculated. Phase diagrams are constructed to display regions of each lowest energy Pd surface species as a function of temperature and oxygen partial pressure. The data in Chapter 2 report low methane activation barriers over Pd-substituted ($Pd_xCe_{1-x}O_2$) surface terminations, and the data in Chapter 3 reports under what operating conditions these mixed palladium-ceria surfaces are stable with respect to other supported Pd species.

Chapters 2 and 3 establish that the $Pd_xCe_{1-x}O_2(111)$ surface is both thermodynamically stable and highly active for C-H bond dissociation, however catalytic activity must be established through examination of the entire oxidation catalytic cycle ($CH_4 + 2O_2 \rightarrow CO_2 + H_2O$). Chapter 4 reports the free energies of elementary steps in methane oxidation over CeO_2, Pd(111), PdO(100), and $Pd_xCe_{1-x}O_2$(111). The lowest energy path for CH_4 oxidation to CO_2 and H_2O is evaluated in Chapter 4, to quantify the barrier of the rate limiting step over each surface. The relative oxidation rate over each surface is reported, to compare the catalytic activity of the palladium-mixed oxide surface with that of palladium and palladium oxide. Chapter 5 addresses the electronic structure of the $Pd_xCe_{1-x}O_2$(111) surface, with respect to the unique thermodynamic stability and oxidation activity of Pd^{4+} in the CeO_2 surface established in Chapters 2-4. With the stability and activity of $Pd_xCe_{1-x}O_2$ established in Chapters 2-4, Chapter 5 also presents an examination of trends in C-H bond activation across a series of transition metal dopants in ceria.

Chapters 2-4 establish that $Pd_xCe_{1-x}O_2$ surface sites are active for C-H dissociation, and Chapter 5 considers the impact of transition metal dopants other than Pd on C-H bond activity. Thus Chapters 2-5 focus on evaluating the activity of transition metal-ceria mixed oxides for hydrocarbon oxidation, however mixed oxides of ceria also show activity for H_2S adsorption.[61-68] Sulfur adsorption activity, C-H bond activity and the ability to exchange oxygen with reactive environments offers potential for the application of ceria-based mixed oxides as a multi-functional hydrocarbon conversion catalyst in renewable energy production. The application of ceria-based metal oxides to the cleanup of syngas produced from biomass gasification may permit simultaneous reforming, tar cracking, and adsorptive removal of H_2S.[61-68] The free energies of H_2S adsorption and dissociation on ceria, ceria-lanthana, and ceria-terbia are reported in Chapter 6, with emphasis on identifying electronic and structural properties which contribute to the altered H_2S adsorption capacity of ceria-lanthana and ceria-terbia with respect to pure ceria. The results in Chapter 6 concerning desulfurization of syngas over ceria are further discussed in Chapter 8 with respect to recommendations for future study.

Chapters 2-6 discuss DFT studies of the catalytic activity of transition-metal ceria mixed oxides for hydrocarbon oxidation and H_2S removal, however DFT methods are restricted to the consideration of small unit cells and a finite number of surface configurations. The combined use of DFT and reactive force field (ReaxFF) methods to study complex heterogeneous metal/metal oxide surfaces is addressed in Chapter 7. The surface structure and composition of surface defects on yttria-stabilized zirconia (YSZ) is probed using DFT and ReaxFF, and is compared to STM images[69] of the YSZ(111) surface. Examination of the YSZ(111) surface as a model system for the combined ReaxFF and DFT approach is chosen due to collaboration expertise in STM imaging of the YSZ surface. The results in Chapters 2-7 motivate the use of DFT, ReaxFF and detailed experimental synthesis and characterization efforts to further investigate oxidation catalysis and structural characteristics on palladium-ceria and syngas cleanup chemistry on ceria-lanthanide mixtures. Chapter 8 summarizes the key results of Chapters 2-7 and discusses recommendations for future work.

1.3 References

(1) Graham, G. W.; Jen, H. W.; McCabe, R. W.; Straccia, A. M.; Haack, L. P. *Catalysis letters* **2000**, *67*, 99-105.

(2) Jen, H. W.; Graham, G. W.; Chun, W.; McCabe, R. W.; Cuif, J. P.; Deutsch, S. E.; Touret, O. *Catalysis Today* **1999**, *50*, 309-328.

(3) Nagai, Y.; Hirabayashi, T.; Dohmae, K.; Takagi, N.; Minami, T.; Shinjoh, H.; Matsumoto, S. i. *Journal of Catalysis* **2006**, *242*, 103-109.

(4) Jacobs, G.; Keogh, R. A.; Davis, B. H. *Journal of Catalysis* **2007**, *245*, 326-337.

(5) Wang, X.; Gorte, R. J. *Applied Catalysis A: General* **2002**, *224*, 209-218.

(6) Colussi, S.; Gayen, A.; Camellone, M. F.; Boaro, M.; Llorca, J.; Fabris, S.; Trovarelli, A. *Angewandte Chemie International* **2009**, *48*, 8481-8484.

(7) Xiao, L.; Sun, K.; Xu, X.; Li, X. *Catalysis Communications* **2005**, *6*, 796-801.

(8) Aneggi, E.; Boaro, M.; Leitenburg, C. d.; Dolcetti, G.; Trovarelli, A. *Journal of Alloys and Compounds* **2006**, *408-412*, 1096-1102.

(9) Bensalem, A.; Bozon-Verduraz, F.; Perrichon, V. *Journal of the Chemical Society, Faraday Transactions* **1995**, *91*, 2185-2189.

(10) Fornasiero, P.; Balducci, G.; Di Monte, R.; Kaspar, J.; Sergo, V.; Gubitosa, G.; Ferrero, A.; Graziani, M. *Journal of Catalysis* **1996**, *164*, 173-183.

(11) Zhou, G.; Gorte, R. J. *The Journal of Physical Chemistry B* **2008**, *112*, 9869-9875.

(12) Fu, Q.; Saltsburg, H.; Flytzani-Stephanopoulos, M. *Science* **2003**, *301*, 935-938.

(13) Jacobs, G.; Patterson, P. M.; Williams, L.; Chenu, E.; Sparks, D.; Thomas, G.; Davis, B. H. *Applied Catalysis A: General* **2004**, *262*, 177-187.

(14) Jacobs, G.; Ricote, S.; Graham, U. M.; Patterson, P. M.; Davis, B. H. *Catalysis Today* **2005**, *106*, 259-264.

(15) Oh, S. H.; Hoflund, G. B. *Journal of Physical Chemistry A* **2006**, *110*, 7609-7613.

(16) Pierre, D.; Deng, W.; Flytzani-Stephanopoulos, M. *Topics in Catalysis* **2007**, *46*, 363-373.

(17) Shapovalov, V.; Metiu, H. *Journal of Catalysis* **2007**, *245*, 205-214.

(18) Deng, W. *Applied Catalysis A: General* **2005**, *291*, 126-135.

(19) Si, R.; Flytzani-Stephanopoulos, M. *Angewandte Chemie* **2008**, *120*, 2926-2929.

(20) Hilaire, S.; Wang, X.; Luo, T.; Gorte, R. J.; Wagner, J. *Applied Catalysis A: General* **2004**, *258*, 271-276.

(21) Bunlesin, T.; Putna, E. S.; Gorte, R. J. *Catalysis Letters* **1996**, *41*, 1-5.

(22) Hoflund, G. B.; Hagelin, H.; Weaver, J. F.; Salaita, G. N. *Applied Surface Science* **2003**, *205*, 102-112.

(23) Guanghui Zhu, J. H., Dmitri Yu. Zemlyanov, Fabio H. Ribeiro *Journal of Physical Chemistry B* **2005**, *109*, 2331-2337.

(24) Priolkar, K. R.; Parthasarathi, B.; Sarode, P. R.; Hegde, M. S.; Emura, S.; Kumashiro, R.; Lalla, N. P. *Chemistry of Materials* **2002**, *14*, 2120-2128.

(25) Wang, X.; Rodriguez, J. A.; Hanson, J. C.; Gamarra, D.; Martinez-Arias, A.; Fernandez-Garcia, M. *Journal of Physical Chemistry B* **2005**, *109*, 19595-19603.

(26) Bozo, C.; Guilhaume, N.; Garbowski, E.; Primet, M. *Catalysis Today* **2000**, *59*, 33-45.

(27) Zhou, G.; Shah, P. R.; Kim, T.; Fornasiero, P.; Gorte, R. J. *Catalysis Today* **2007**, *123*, 86-93.

(28) Shi, L.; Chu, W.; Qu, F.; Luo, S. *Catalysis Letters* **2007**, *113*, 59-64.

(29) Borchert, H.; Borchert, Y.; Kaichev, V. V.; Prosvirin, I. P.; Alikina, G. M.; Lukashevich, A. I.; Zaikovskii, V. I.; Moroz, E. M.; Paukshtis, E. A.; Bukhtiyarov, V. I.; Sadykov, V. A. *Journal of Physical Chemistry B* **2005**, *109*, 20077-20086.

(30) Bernal, S.; Blanco, G.; Cifredo, G.; Pérez-Omil, J. A.; Pintado, J. M.; RodrIguez-Izquierdo, J. M. *Journal of Alloys and Compounds* **1997**, *250*, 449-454.

(31) Wilkes, M. F.; Hayden, P.; Bhattacharya, A. K. *Journal of Catalysis* **2003**, *219*, 305-309.

(32) Herschend, B.; Baudin, M.; Hermansson, K. *Surface Science* **2005**, *599*, 173-186.

(33) Jiang, Y.; Adams, J. B.; Schilfgaarde, M. v.; Sharma, R.; Crozier, P. A. *Applied Physics Letters* **2005**, *87*, 141917.

(34) Mayernick, A. D.; Janik, M. J. *The Journal of Physical Chemistry C* **2008**, *112*, 14955-14964.

(35) Nolan, M.; Parker, S. C.; Watson, G. W. *Surface Science* **2005**, *595*, 223-232.

(36) Teng, B.-T.; Jiang, S.-Y.; Yang, Z.-X.; Luo, M.-F.; Lan, Y.-Z. *Surface Science* **2010**, *604*, 68-78.

(37) Knapp, D.; Ziegler, T. *The Journal of Physical Chemistry C* **2008**, *112*, 17311-17318.

(38) Huang, M.; Fabris, S. *Journal of Physical Chemistry C* **2008**, *112*, 8643-8648.

(39) Muller, C.; Freysoldt, C.; Baudin, M.; Hermansson, K. *Chemical Physics* **2005**, *318*, 180-190.

(40) Nolan, M.; Parker, S. C.; Watson, G. W. *Journal of Physical Chemistry B* **2006**, *110*, 2256-2262.

(41) Nolan, M.; Parker, S. C.; Watson, G. W. *Surface Science* **2006**, *600*, 175-178.

(42) Chen, H.L.; Liu, S.H.; Ho, J.-J. *Journal of Physical Chemistry B* **2006**, *110*, 14816-14823.

(43) Rodriguez, J. A.; Wang, X.; Hanson, J. C.; Liu, G.; Iglesias-Juez, A.; Fernandez-Garcia, M. *Journal of Chemical Physics* **2003**, *119*, 5659-5669.

(44) Yang, Z.; Luo, G.; Lu, Z.; Woo, T. K.; Hermansson, K. *Journal of Physics: Condensed Matter* **2008**, *20*, 035210.

(45) Chafi, Z.; Keghouche, N.; Minot, C. *Surface Science* **2007**, *601*, 2323-2329.

(46) Yang, Z.; Lu, Z.; Luo, G.; Hermansson, K. *Physics Letters A* **2007**, *369*, 132-139.

(47) Fabris, S.; Gironcoli, S. d.; Baroni, S.; Vicario, G.; Balducci, G. *Physical Review B* **2005**, *71*, 041102.

(48) Fabris, S.; Gironcoli, S. d.; Baroni, S.; Vicario, G.; Balducci, G. *Physical Review B* **2005**, *72*, 237102.

(49) Kresse, G.; Blaha, P.; Silva, J. L. F. D.; Ganduglia-Pirovano, M. V. *Physical Review B* **2005**, *72*, 237101.

(50) Nolan, M.; Grigoleit, S.; Sayle, D. C.; Parker, S. C.; Watson, G. W. *Surface Science* **2005**, *576*, 217-229.

(51) Yang, Z.; Luo, G.; Lu, Z.; Hermansson, K. *The Journal of Chemical Physics* **2007**, *127*, 074704-5.

(52) Da Silva, J.; Ganduglia-Pirovano, M. V.; Sauer, J.; Bayer, V.; Kresse, G. *Physical Review B (Condensed Matter and Materials Physics)* **2007**, *75*, 045121-10.

(53) J. Heyd, G. S., M. Ernzerhof *Journal of Chemical Physics* **2003**, *118*.

(54) J. Perdew, M. E., K. Burke *Journal of Chemical Physics* **1996**.

(55) Aneggi, E.; de Leitenburg, C.; Dolcetti, G.; Trovarelli, A. *Catalysis Today*
Catalytic Control of Diesel Exhaust Emissions **2006**, *114*, 40-47.

(56) Boaro, M.; de Leitenburg, C.; Dolcetti, G.; Trovarelli, A. *Journal of Catalysis* **2000**, *193*, 338-347.

(57) Bozo, C.; Guilhaume, N.; Herrmann, J.-M. *Journal of Catalysis* **2001**, *203*, 393-406.

(58) Kuznetsova, T.; Sadykov, V.; Batuev, L.; Moroz, E.; Burgina, E.; Rogov, V.; Kriventsov, V.; Kochubey, D. *Journal of Natural Gas Chemistry* **2006**, *15*, 149-163.

(59) Mamontov, E.; Egami, T.; Brezny, R.; Koranne, M.; Tyagi, S. *J. Phys. Chem. B* **2000**, *104*, 11110-11116.

(60) Yao, M. H.; Baird, R. J.; Kunz, F. W.; Hoost, T. E. *Journal of Catalysis* **1997**, *166*, 67-74.

(61) Yi, K. B.; Podlaha, E. J.; Harrison, D. P. *Industrial & Engineering Chemistry Research* **2005**, *44*, 7086-7091.

(62) Chen, H.T.; Choi, Y.; Liu, M.; Lin, M. C. *The Journal of Physical Chemistry C* **2007**, *111*, 11117-11122.

(63) Flytzani-Stephanopoulos, M.; Sakbodin, M.; Wang, Z. *Science* **2006**, *312*, 1508-1510.

(64) Gong, M.; Liu, X.; Trembly, J.; Johnson, C. *Journal of Power Sources* **2007**, *168*, 289-298.

(65) Kempegowda, R.; Laosiripojana, N.; Assabumrungrat, S. *Korean Journal of Chemical Engineering* **2008**, *25*, 223-230.

(66) Meng, X. M.; De Jong, W.; Verkooijen, A. H. M. *Environmental Progress & Sustainable Energy* **2009**, *28*, 360-371.

(67) Wang, Z.; Flytzani-Stephanopoulos, M. *Energy & Fuels* **2005**, *19*, 2089-2097.

(68) Zeng, Y.; Kaytakoglu, S.; Harrison, D. P. *Chemical Engineering Science* **2000**, *55*, 4893-4900.

(69) Morrow, S. L.; Luttrell, T.; Carter, A.; Batzill, M. *Surface Science* **2009**, *603*, L78-L81.

Chapter 2

Methane Activation and Oxygen Vacancy Formation over CeO_2 and Zr, Pd substituted CeO_2 surfaces

This chapter is published as: A. D. Mayernick, M. J. Janik. *Journal of Physical Chemistry C* 2008, 112(38), 14955-14964.

ABSTRACT: The catalytic properties of CeO_2 for hydrocarbon oxidation reactions have implications for a variety of applications. Surface reduction and methane activation are key processes in the overall oxidation reaction, and are examined herein for pure CeO_2 (111), (110) and (100) surfaces and surfaces with Zr or Pd substituted in Ce lattice positions. Density functional theory, with the inclusion of an on-site Coulombic interaction (DFT+U), was used to calculate the energetics of oxygen vacancy formation and methane activation. Oxygen vacancy formation is more exothermic for Zr and Pd substituted ceria surfaces than for pure ceria, with Pd-substituted surfaces being significantly more reducible. Methane adsorbs dissociatively as *H and $*CH_3$, and the thermodynamics of dissociative methane adsorption correlate with those of oxygen vacancy formation over the pure and substituted surfaces. The lowest energy pathway for dissociative adsorption on the (111) surface proceeds through H abstraction and the formation of a methyl radical, and subsequent chemisorption of the radical species. Sensitivity of the reported results to the choice of U value within the DFT+U method is discussed.

2.1 Introduction

Ceria (CeO_2) offers unique properties as a heterogeneous catalyst or catalyst support for a number of applications, such as three-way automotive catalysts,[1] preferential CO oxidation,[2] and catalytic oxidation of hydrocarbons.[1-10] For each of these applications, the use of ceria is motivated by its ability to store and release oxygen, or more generally to readily transition between oxidation states. Ceria exhibits activity for the oxidation of hydrocarbons[3-10], making it suitable for catalytic combustion applications and as anode electrocatalysts for direct hydrocarbon solid oxide fuel cells (SOFCs). The addition of low levels of rare-earth or noble metals alters the redox properties[11-13] and hydrocarbon oxidation activity[5,7,9] of ceria-based materials. The redox properties of ceria-based materials have been probed using experimental[12-21] and theoretical[22-30] methods, however the correlation between redox properties and hydrocarbon oxidation activity with changes in composition is unclear. Herein, we use density functional theory, with the inclusion of an on-site Coulombic interaction (DFT+U), to examine the energetics of dissociative methane adsorption and oxygen vacancy formation over ceria surfaces with the addition of Zr or Pd. These results provide insight into the relationship between composition, surface reduction and catalytic activity of ceria-based materials.

The addition of Zr to CeO_2 alters structural and electronic properties of relevance for heterogeneous catalysis, however the impact of Zr addition on surface reducibility and activity is unclear. The substitution of Zr into the ceria lattice to form solid solutions of CeO_2-ZrO_2 results in greater reducibility and thermal stability as compared with pure CeO_2.[11,13,15,19,31,32] Structural doping of ceria with zirconia results in the substitution of Zr into Ce sites within the CeO_2 lattice.[11,13,19] Oxidation enthalpies for ceria-zirconia solid solutions[11] obtained by Coulometric and flow titrations were between 200-300 $kJ \cdot mol^{-1}$ less than those of pure ceria (for $Zr_xCe_{1-x}O_2$ where $0.08 < x < 0.86$). The presence of Zr increases the mobility of oxygen atoms within the lattice. Ionic conductivity measurements show that the bulk diffusion coefficient of O^{2-} ions is approximately two orders of magnitude higher for ceria-zirconia than for pure ceria.[15] Zr doping also increases the stability of ceria when used for the oxidation of hydrocarbons. For the oxidation of CH_4 to CO_2, microreactor experiments performed by Bozo et. al suggest that Zr doping may increase the thermal stability of ceria by preventing deactivation at high temperatures. While fresh samples of pure CeO_2 and $Ce_{0.67}Zr_{0.33}O_2$ resulted in similar fractional conversion of CH_4 to CO_2, the $Ce_{0.67}Zr_{0.33}O_2$ sample showed over 30% higher conversion than pure CeO_2 after ageing at 1000 K.[7] The effects of Zr on overall activity and reducibility are therefore well-defined experimentally, motivating the study of surface substitution effects on these properties. Additionally, the known substitution of Zr into Ce positions in the fluorite lattice provides a useful contrast with Pd-substituted systems studied herein.

Palladium supported on ceria has shown promise as an effective catalyst for hydrocarbon oxidation,[33-36] and also displays altered redox properties[37,38] as compared to pure ceria. Palladium deposited at 2 wt% on CeO_2 was observed to achieve 100% conversion for the catalytic combustion of methane at temperatures as low as 300 °C,[35] compared to temperatures in excess of 700 °C necessary for complete oxidation over pure CeO_2.[7] In experiments utilizing ceria-based anode materials for the direct oxidation of hydrocarbons in a solid oxide fuel cell,[9] the addition of 1 wt% Pd to ceria increased the maximum power density nearly two-fold for the oxidation of H_2 and *n*-butane, and by a factor of almost 10 for the oxidation of methane. For Pd supported on ceria, Fourier Transform Infrared Spectroscopy (FTIR) results indicate that surface reduction can occur at temperatures as low as 423 K, as compared to 623 K for pure ceria.[37,38] The mechanism by which Pd alters the catalytic activity and reducibility of ceria is not well understood. Although supported Pd particles may catalyze otherwise limiting bond activation steps, many studies have highlighted that the nature of the metal-support interaction is fundamental in dictating catalytic activity.[33-35,37-39] While the reduction properties of the Pd/CeO_2 system have been less extensively investigated than those of ZrO_2-CeO_2, unique interactions between Pd and CeO_2 at the metal-metal oxide interface have been observed.[34,36-39] High Resolution Electron Microscopy (HREM) images show evidence of alloying between Pd and Ce species at the Pd/CeO_2 interface after reduction at temperatures exceeding 1173K.[39] Based on X-ray Photoelectron Spectroscopy (XPS) data, Xiao et al. propose that palladium oxide (PdO_x) species may form at the Pd-CeO_2 interface.[35] Experimental studies have demonstrated the effects on catalytic performance and redox properties of the addition of Pd to ceria, however the mechanism responsible for these effects merits further theoretical investigation. Herein, we postulate that Pd atoms may occupy Ce lattice positions at the intact or reduced CeO_2 surface and probe the impact of this substitution on surface reducibility and methane activation energetics.

There are a number of DFT-based theoretical studies of ceria available in the literature which have informed the methodological choices made in this study, and provide analysis complementary to that presented.[22,25,26,28-30,40-46] The DFT+U methodology applied herein for substituted surfaces is similar to that implemented by Nolan et al. to study oxygen vacancy formation in bulk ceria as well as the (111), (110), and (100) surfaces of ceria.[25,44] The energy of oxygen vacancy formation was found to be more exothermic for ceria surfaces than for bulk ceria.[25,44] This result is in direct agreement with Coulometric and flow titration results obtained by Zhou et al., which show ceria surface oxidation enthalpies to be up to 200 $kJ\cdot mol^{-1}$ O_2 more exothermic than those of the bulk.[47] Nolan et al. also observe the appearance of a “gap state” between the valence band and unoccupied Ce 4f states upon formation of an oxygen vacancy, consistent with the reduction of Ce^{4+} to Ce^{3+}.[25,44] Yang et al. have published DFT+U results for oxygen vacancy formation for bulk ceria with the substitution of both Zr[27] and Pd[26] into Ce sites within the CeO_2 lattice. Using a 96-atom supercell to model the bulk fluorite lattice of ceria, one Zr or Pd atom was substituted into a Ce site corresponding to $Ce_{0.97}Zr_{0.03}O_2$ and $Ce_{0.97}Pd_{0.03}O_2$, respectively. For both $Ce_{0.97}Zr_{0.03}O_2$ and $Ce_{0.97}Pd_{0.03}O_2$, the most exothermic oxygen sites for vacancy formation are those coordinated to the substituted metal atom. They report that the oxygen vacancy formation energy (ΔE_{vac}) is lowered by 0.65 eV next to a Zr atom and by 2.4 eV next to a Pd atom as compared with values calculated for pure ceria. They also conclude based on spin-density, density of states (DOS), and atomic charge results, that oxygen vacancy formation results in the reduction of nearest Ce atoms for $Ce_{0.97}Zr_{0.03}O_2$ and the reduction of the Pd atom for $Ce_{0.97}Pd_{0.03}O_2$.[26,27] The current study extends a similar approach to the study of surface reducibility and activity for methane activation.

The addition of rare-earth or noble metals to ceria results in both altered redox properties as well as altered catalytic activity. The design of effective ceria-based catalysts motivates our application of electronic structure methods to investigate both reducibility and C-H activation energetics and their relationship to each other. The energetics of oxygen vacancy formation and methane adsorption over pure and Zr or Pd substituted ceria (111), (110) and (100) surfaces were determined using the DFT+U method. This theoretical approach allows us to determine key electronic, structural and chemical characteristics of ceria surfaces on the atomic scale, less accessible to experiment. We do not address the preference for Pd or Zr to occupy Ce surface sites, a topic which will be addressed in subsequent studies. Investigation of ceria containing Zr is chosen in large part due to the well established effects of Zr doping on ceria reducibility which allows for qualitative validation of our theoretical approach and results. Pd has been chosen for this study due to the substantial improvements in catalytic performance of Pd/CeO_2 materials. This study investigates the effects on redox properties and catalytic activity of Pd incorporation into the CeO_2 lattice, a phenomena which has been observed for $BaCe_{1-x}Pd_xO_{3-\delta}$.[48] Li et al. report neutron and X-ray diffraction data which confirm the substitution of Pd into the Ce sites in the perovskite structure of $BaCe_{1-x}Pd_xO_{3-\delta}$, and show that Pd substitution can be instigated by heating in an oxidizing (O_2) atmosphere or reversed by heating in a reducing atmosphere (H_2/N_2).[48] We report the energies of oxygen vacancy formation for each surface, the preferred adsorption mode and sites for methane adsorption, and the dissociative methane adsorption energy. The barrier for methane activation over the $CeO_2(111)$ surface is reported. Each result is discussed in the context of changes in electronic as well as structural features of each surface, and sensitivity of conclusions to the DFT+U method is discussed. These studies provide insight into properties of relevance to the catalytic performance of ceria-based materials, and ultimately will help facilitate future efforts in catalyst development.

2.2 Methods

Calculations were carried out using the Vienna Ab-initio Simulation Program (VASP), an ab-initio total-energy and molecular dynamics program developed at the Institute for Material Physics at the University of Vienna.[49-51] The strongly oscillating wave functions of core electrons are represented using the projector augmented wave (PAW) method.[52] Plane wave basis sets are used to expand the wavefunctions of valence electrons, with valence configurations for cerium being $5s^2 5p^6 6s^2 4f^1 5d^1$, for oxygen $2s^2 2p^4$, for Zr $3d^{10} 4s^2$, for Pd $4d^{10}$, for C $2s^2 2p^2$ and for H $1s^1$. A cutoff energy of 450 eV was used for the plane-wave basis set, and all calculations were spin-polarized. The Brillouin zone was sampled using a (2x2x2) Monkhorst Pack (MP) grid[53] for bulk ceria, and a (2x2x1) MP grid for surfaces, with the third vector perpendicular to the surface. The Perdew-Wang (PW91) version of the generalized gradient approximation (GGA) is used to incorporate exchange and correlation energies.[54] Structural optimizations were performed by minimizing the forces on all atoms to below $0.05\ eV \cdot Å^{-1}$.

Due to well-established difficulties within DFT to accurately represent the nature of 4f states in ceria,[22-24] we implement the DFT+U approach.[55,56] Standard DFT representations fail to describe the partial occupation of Ce 4f states associated with the formation of oxygen vacancies and the reduction of Ce^{4+} to Ce^{3+}. The DFT+U method introduces the Hubbard U-term as an on-site Coulombic interaction in the f states of ceria, which allows electrons to localize in these states. When electrons localize on cerium atoms, a gap state appears between the occupied valence band and the remaining unoccupied states representing the unpaired, localized Ce 4f occupation. The energy between this gap state and the valence band is influenced by the value of the U parameter. We use a value of U=5 eV for the majority of calculations presented herein, which is consistent with recommended values within this method used in previous DFT studies of ceria.[25-27,30,44,45,55-57] The reported energy differences for vacancy formation and methane adsorption differ based on the choice of U value, and therefore the sensitivity of reported values to the choice of the U parameter is discussed in Section 2.3.4.

Harmonic vibrational modes have been calculated to determine zero-point vibrational energy (ZPVE) corrections to adsorption energies and reaction barriers. Constrained vibrational calculations have been done for surface systems with adsorbates, where the Hessian matrix is populated solely with second derivatives of energy with respect to position of the adsorbate atoms. This approximation is sufficient to capture large energy differences associated with the breaking of C-H bonds and the forming of O-H and O-C bonds. The Climbing Image Nudged Elastic Band method (CI-NEB)[58-60] was used to isolate transition states, and thus determine reaction barriers for methane adsorption. Within the CI-NEB method, a sequence of images along the reaction path are optimized with the highest energy image required to climb up in energy along the elastic band to estimate the saddle point along the minimum energy path.[60] Four equally spaced images between reactant and product states were used in each search, and transition states were identified as the maximum energy image with an absolute tangential force of less than 0.04 $eV \cdot Å^{-1}$. Atomic charge data has been obtained by the Bader atoms-in-molecules method in which individual atoms are divided by “zero-flux surfaces” which are defined as 2-D planes in which the gradient of charge density is zero perpendicular to the plane.[61-63]

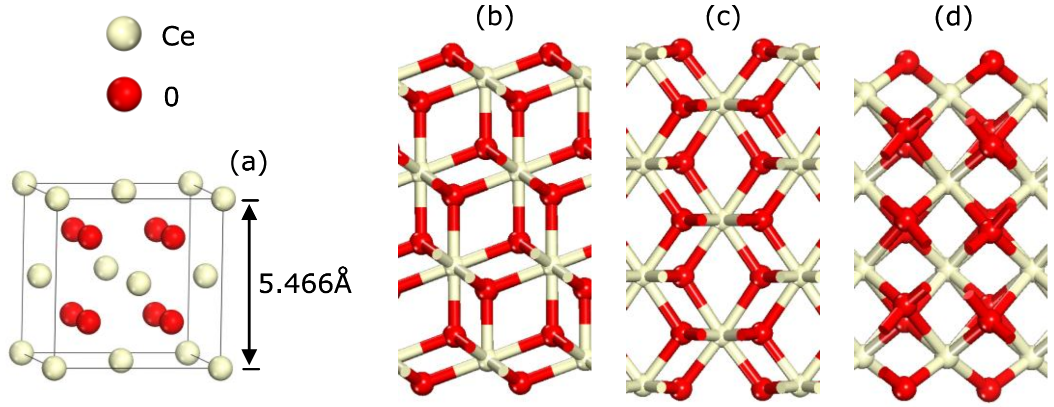

Figure 2-1. (a) Bulk CeO_2 fluorite unit cell. (b) 111, (c) 110, (d) 100 surface slabs of CeO_2.

Ceria has a cubic fluorite bulk structure, with four cerium and eight oxygen atoms per unit cell. Figure 2-1(a) shows the bulk fluorite unit cell of ceria. The optimized equilibrium lattice parameter is 5.466 Å, which is within 1% of the reported experimental value of 5.411 Å.[64] To examine the effects of Zr and Pd in bulk ceria, one cerium atom was substituted for either a Zr or Pd atom, creating a dopant concentration of 3.1%.

To model the ceria (111), (110) and (100) surfaces, slab models were constructed, with each slab separated by 15 Å of vacuum in the direction perpendicular to the surface. Mirrored slabs of 12 atomic layers ($Ce_{16}O_{32}$) for the (111), 7 atomic layers ($Ce_{14}O_{28}$) for the (110), and 9 atomic layers (Ce_8O_{16}) for the (100) were chosen to model the CeO_2 surface, with slab sizes chosen to converge surface energy and vacancy formation energy with respect to slab thickness. Figure 2-1 displays each mirrored surface slab of ceria used in our calculations. We use a p(2x2) expansion of the surface unit cell for (111) and (100), and a p(2x1) expansion for (110). For each surface, this expansion results in a termination of four surface oxygen atoms on each side of the slab per unit cell. To maintain the CeO_2 stoichiometry of the (100) unit cell, half of the oxygen atoms on each side (2 per side) of the slab were removed, as similarly addressed in previous DFT work done on ceria (100).[25,44] Mirrored slabs were used specifically to examine oxygen vacancy formation in order to minimize slab to slab interactions which result from a large net surface dipole moment upon formation of a surface oxygen vacancy. Energies of gas-phase molecules were obtained by optimizing free O_2, CH_4, $\bullet CH_3$ molecules within a 15 Å x 15 Å x 15 Å unit cell.

To calculate the energy of surface vacancy formation an oxygen atom was removed from both sides of each slab, and all slab layers were allowed to relax. We calculated the energy of oxygen vacancy formation from the following formula:

$$\Delta E_{vac} = \frac{\left(E_{Ce_nO_{2n-2}} + E_{O_2} - E_{nCeO_2}\right)}{2} \qquad (1)$$

where $E_{Ce_nO_{2n-2}}$ is the energy of the defective unit cell, E_{O_2} is the energy of a gas-phase O_2 molecule, E_{nCeO_2} is the energy of the intact unit cell, and division by two accounts for the mirrored surface. To calculate bulk vacancy formation energies, a 2x2x2 supercell ($Ce_{32}O_{64}$) was used and one oxygen atom was removed to create a vacancy concentration of 1.6%. The vacancy formation energies reported in this study are not direct analogs to experimental reduction enthalpies, with key differences, as highlighted by Wang et al.,[65] including DFT errors associated with overestimation of the O_2 binding energy and incorrect electronic representation of metal reduced states. The DFT+U method is employed herein as a correction to the electronic structure of reduced ceria, and thus the reported values of ΔE_{vac} can be expected to provide consistent qualitative results. Correction of the DFT calculated O_2 binding energy may be necessary for direct quantitative agreement with experiment, however will not affect relative values of ΔE_{vac}.

We calculated the energy of dissociative methane adsorption from the following formula:

$$\Delta E_{ads} = \frac{E_{2(*CH_3+*H)} - \left(E_{surf} + 2E_{CH_4}\right)}{2} \qquad (2)$$

where $E_{2(*CH_3+*H)}$ is the energy of a given surface slab with adsorbed H and CH_3 fragments, E_{surf} is the energy of the clean surface, and E_{CH4} is the energy of a gas-phase CH_4 molecule. Methane fragments were allowed to adsorb on both sides of the mirrored slab.

To evaluate the reaction energy barrier for $CH_4 \rightarrow *CH_3 + *H$, a non-mirrored slab of 6 atomic layers was used to model the (111) surface, due to difficulties in implementing the CI-NEB method for a mirrored reaction. Methane fragments were allowed to adsorb on the top of the slab, and the top half of ions in the surface slab were allowed to relax while the bottom half were fixed at their bulk positions. To validate that slab to slab dipole interactions do not alter the energetics, adsorption energies for H and CH_3 on the non-mirrored surface slab was compared with values obtained for the mirrored (111) slab. The dissociative adsorption energy (ΔE_{ads}) for methane differed between mirrored and non-mirrored slabs by no more than 0.03 eV for pure and substituted (111) surfaces.

The impact of Zr or Pd substitution on surface reducibility and methane dissociation was investigated by replacing a single Ce atom in the (111), (110) and (100) surfaces. Figure 2-2 shows top and side views of each surface, with the M_1 position corresponding to the dopant site. The surface cell dimensions were not allowed to relax, thus neglecting changes in lattice parameter due to the presence of Zr or Pd. Oxygen vacancy formation energies were calculated for these systems by removing surface oxygen atoms of closest proximity to the substituted metal atoms.

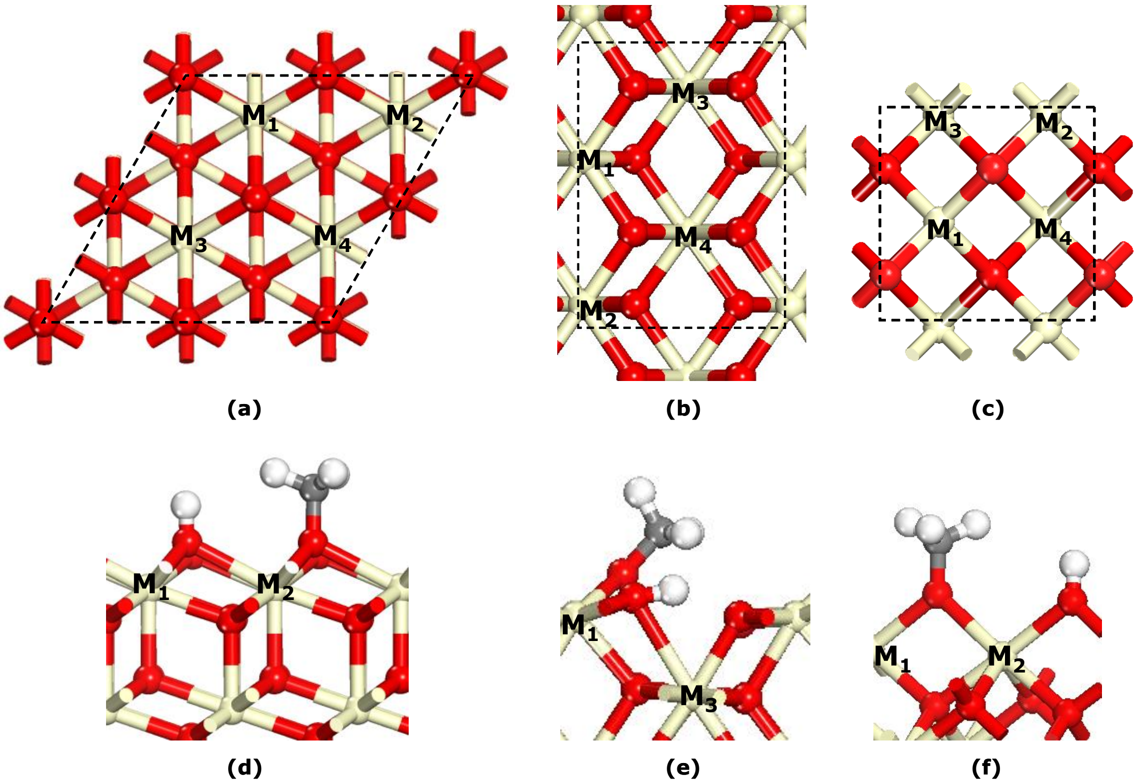

Figure 2-2. Top views of CeO_2 (a) 111, (b) 110, (c) 100. Side views of (d) 111, (e) 110, (f) 100 with $*CH_3$ and *H.

2.3 Results and Discussion

2.3.1 Oxygen Vacancy Formation

Oxygen vacancy formation was considered for both bulk and surface CeO_2, and Zr or Pd substituted CeO_2. Bulk results are summarized first to illustrate agreement with previous experimental and computational studies.

Substitution of Zr into the bulk ceria lattice results in a slight distortion of the local metal coordination environment, where Zr-O distances are 0.07 Å shorter than Ce-O distances for bulk pure ceria. The calculated bulk vacancy formation energy for $Ce_{0.97}Zr_{0.03}O_2$ is 2.96 eV, which is 0.9 eV lower than that for the same vacancy concentration in pure ceria (3.86 eV). This difference is qualitatively similar to that found by Yang et al.,[27] who reported the vacancy formation energy to be 0.6 eV lower for $Ce_{0.97}Zr_{0.03}O_2$ than for pure ceria, using a U value of 6 eV. The oxidation enthalpy of $Ce_{0.81}Zr_{0.19}O_2$ was experimentally determined to be 506 $kJ \cdot mol^{-1}O_2$,[11] which is in reasonable agreement with the calculated value of 2.96 eV per vacancy (570 $kJ \cdot mol^{-1}O_2$) for $Ce_{0.97}Zr_{0.03}O_2$, though as mentioned above, direct comparison with experimental enthalpies is challenged by methodological difficulties. The Bader charge of two Ce atoms next to the vacancy increases by 0.25-0.3 e^-, indicative of cerium reduction due to vacancy formation. An occupied electronic state emerges in the DOS data (not shown) between the top of the occupied valence band and the bottom of the unoccupied band following vacancy formation. Projected density of states (PDOS) data shows the presence of this gap state on both of the cerium atoms for which the Bader charge increased. These results are in agreement with previous DFT results,[25,44] as well as consistent with EELS[66] and XPS[67,68] data which attribute the presence of this gap state to the formation of Ce^{3+}. Yang et al. also conclude that Ce atoms are reduced rather than Zr atoms in $Ce_{0.97}Zr_{0.03}O_{2-x}$ based on DOS data and Bader analysis.[27]

Substitution of Pd into the bulk ceria lattice results in a slight distortion of the local coordination environment, where Pd-O distances are 0.06 Å shorter than Ce-O distances for bulk pure ceria. The bulk vacancy formation energy for $Ce_{0.97}Pd_{0.03}O_2$ is 0.67 eV, which is 3.19 eV lower than that for pure ceria (3.86 eV). This result is qualitatively similar to that found by Yang et al.,[27] who reported a similar vacancy formation energy change due to the addition of Pd to the bulk CeO_2 lattice. We determine a charge increase of 0.37 e^- for the Pd atom next to the vacancy, with no significant reduction of adjacent Ce atoms (<0.05 e^-). DOS analysis shows the presence of an occupied gap state between the valence and unoccupied bands, however this gap state has no net spin and PDOS data reveals that the gap state represents a newly occupied Pd state. Yang et al. also found evidence of Pd reduction rather than reduction of Ce, based on spin-density analysis and DOS data.[26]

Figure 2-2(a-c) shows the top view of each surface, and the surface metal atoms as well as specific near-surface atoms are labeled for reference. Surface oxygen atoms of the (111) surface are coordinated to three subsurface metal atoms and there are four total surface oxygen atoms in each p(2x2) unit cell. For the (110) surface, surface oxygen atoms are coordinated to two surface metal atoms in the same plane and one subsurface metal atom, with a total of four surface oxygen atoms in each p(2x1) unit cell. Each surface oxygen atom of the (100) surface is coordinated to two subsurface metal atoms, with two surface oxygen atoms in each cell.

Table 2-1. Vacancy formation energies (ΔE_{vac}) for each surface, the resulting change in Bader charge for each related metal atom (M_{1-4}). and vacancy formation energies for each pre-reduced surface ($\Delta E'_{ads}$).

Surface	**M_1**	**ΔE_{vac} (eV)**	**ΔQ_{M1} (e)**	**ΔQ_{M2} (e)**	**ΔQ_{M3} (e)**	**ΔQ_{M4} (e)**	**$\Delta E'_{vac}$ (eV)**
(111)	Ce	+2.76	+0.32	+0.32	0.00	+0.06	+3.01
	Zr	+1.63	+0.02	+0.32	+0.28	+0.06	+2.02
	Pd	+0.71	+0.43	+0.05	+0.05	+0.03	+2.78
(110)	Ce	+2.10	+0.32	+0.32	-0.01	-0.01	+3.91
	Zr	+1.24	+0.08	+0.31	+0.26	+0.06	+4.78
	Pd	-0.09	+0.38	+0.06	+0.04	+0.03	+0.82
(100)	Ce	+2.26	+0.35	+0.37	+0.02	+0.01	N/A
	Zr	+1.84	+0.07	+0.30	+0.26	+0.03	N/A
	Pd	-0.05	+0.51	+0.08	+0.01	+0.02	N/A

The oxygen vacancy formation energies for each surface and composition are shown in Table 2-1. For pure ceria, the values for vacancy formation energy are in agreement with similar calculations by Nolan et. al.[25,44] Bader charges (shown in Table 2-1) for each metal atom labeled in Figure 2-1 show a net charge increase in the range of 0.32-0.37 e^- for two of the cerium atoms next to each surface oxygen vacancy. The formation of a surface oxygen vacancy, therefore, results in the reduction of two adjacent cerium atoms. Figure 2-3 shows the density of states for the pure ceria (111) surface, with a plot for the intact surface, the surface with an oxygen vacancy, and the surface with CH_3 and H adsorbates. For the vacant (111) surface, a gap state similar to that for vacant bulk ceria is attributed to the reduced Ce^{3+} states. This gap state is observed in the DOS for each pure ceria surface termination (not shown).

Zr substitution into the (111), (110), and (100) surfaces of ceria results in similar distortion of the coordination environment as bulk substitution, including shorter metal-oxygen bonds around the Zr atom. Bader charges indicate that adjacent cerium atoms are reduced by 0.26-0.32 e^- during the formation of an oxygen vacancy, while Zr atoms show no significant reduction (<0.08 e^-). DOS analysis (not shown) yields a similar result for pure ceria, showing the presence of a gap state for each vacant surface tied to the formation of Ce^{3+}. The vacancy formation energy for Zr substituted ceria surfaces is 0.42-1.13 eV lower (dependent on surface termination) than for pure ceria, compared to a reduction of 0.9 eV in the vacancy formation energy for Zr substituted bulk CeO_2. The differences between bulk and surface vacancy formation energies for Zr substituted ceria indicate that the effects of Zr substitution on surface reducibility are dependent on surface structure. The thermodynamic preference of Zr to segregate to the surface versus bulk at these (low) dopant levels was not directly considered, however the range of vacancy formation energies spanning the bulk value suggests that segregation preferences for each surface termination are a function of atmospheric conditions. The substitution of Zr into the (111) surface decreases the energy of oxygen vacancy formation more

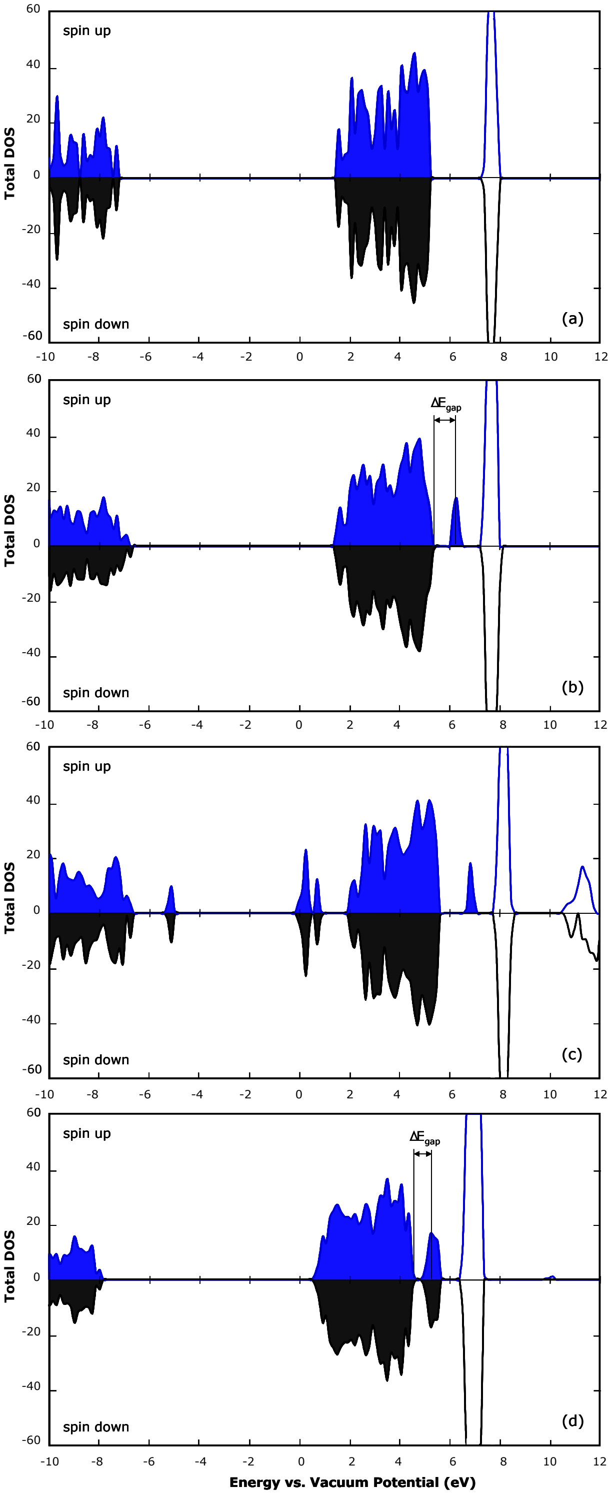

Figure 2-3. Total DOS plotted vs. energy (referenced to vacuum potential) for (a) CeO_2 (111), (b) vacant CeO_2 (111), (c) CeO_2 (111) + $*CH_3$ + *H, and (d) Pd-substituted vacant CeO_2 (111). Spin-down states are plotted on the negative y-axis, all states below the Fermi level are highlighted, and ΔE_{gap} is labeled for reference.

(1.13 eV) with respect to pure ceria than does Zr substitution into the bulk (0.9 eV). Thus in a reducing environment, Zr may prefer to segregate to the (111) surface, whereas in an oxidizing environment Zr may prefer to remain in the bulk.

Pd substitution into the (111) surface of ceria results in notable distortions of the surface structure as compared to pure ceria, especially when an oxygen vacancy is formed. Figure 2-4 shows the optimized structure for each fully oxidized and oxygen vacant structure containing a Pd atom, with each oxygen atom which was removed to form a vacancy labeled. For the (111) surface, Pd substitution results in contraction of the lattice around the Pd center to form Pd-O coordination lengths ~0.1-0.2 Å shorter than Ce-O lengths in the first three surface layers. Following vacancy formation, the distance between the Pd atom and subsurface O atom becomes 0.38 Å greater (2.74 Å) than the analogous Ce-O distance, allowing Pd to assume what resembles a square planar ligand coordination with four Pd-O distances of 2.10-2.20 Å (see Figure 2-4d) following vacancy formation. This type of configuration is consistent with the coordination environment for Pd^{2+} in PdO_2. The vacancy formation energy for the (111) surface containing a Pd atom is 2.05 eV lower (0.71 eV) than for pure ceria (111). Bader charges (Table 2-1), indicate that Pd is reduced by 0.43 e^- upon formation of a vacancy, and DOS data confirms the presence of newly occupied Pd gap states similar to oxygen vacant bulk $Ce_{0.97}Pd_{0.03}O_2$. As shown in Figure 2-3d, these newly occupied Pd states appear as a gap state with no net spin between the valence and unoccupied bands. This suggests that the formation of an oxygen vacancy in the presence of Pd on the (111) surface of ceria results in reduction of the Pd atom, and no change in the oxidation state of Ce atoms.

For the (110) and (100) surfaces, similar contraction around the Pd center is seen to that in the bulk however no surface specific distortions are observed for intact surfaces. The formation of an oxygen vacancy in the (110) surface results in significant lengthening of a

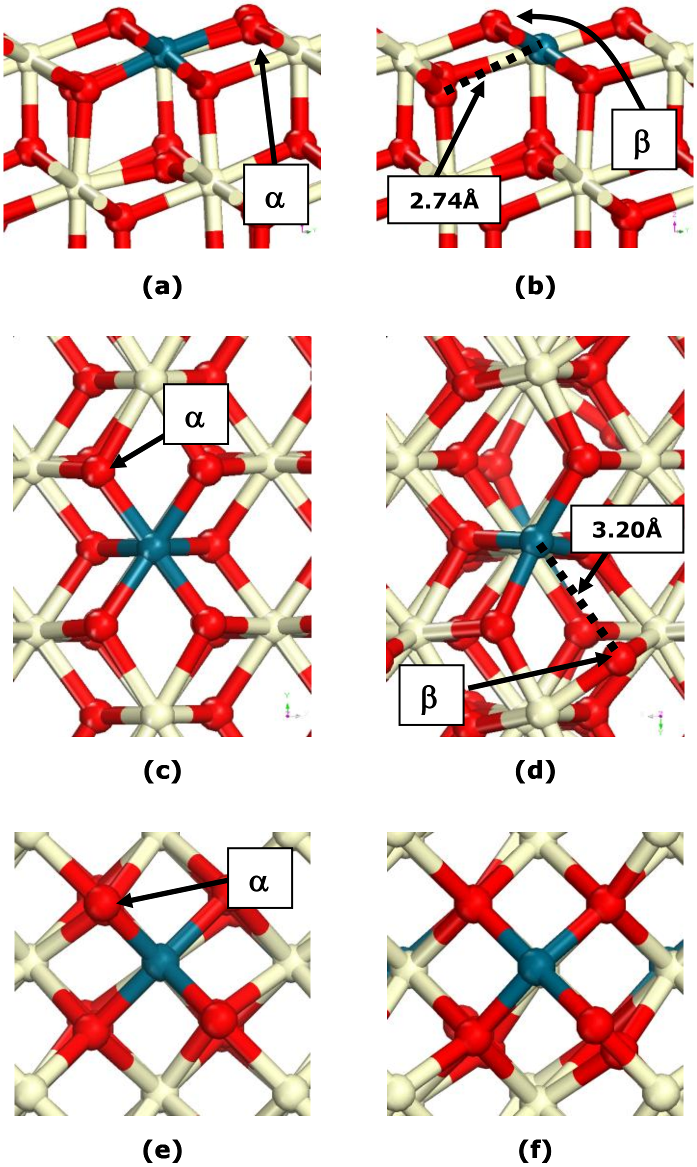

Figure 2-4. Intact CeO_2 (a) 111, (c) 110, (e) 100 and vacant (b) 111, (d) 110, (f) 100 surfaces with the substitution of Pd for Ce into the surface metal layer. Oxygen atoms removed to form the first vacancy (α) and second vacancy (β) are labeled.

remaining Pd-O interatomic distance from 2.17 Å previous to vacancy formation to 3.20 Å after vacancy formation. The Pd atom maintains the rest of its original coordination environment, resulting in four nearest neighbor oxygen at distances ≤2.16 Å. A vacancy in the (100) surface does not result in any significant distortions, yet similar to the (111) and (110) surfaces leaves the Pd atom in a four coordinate environment. The vacancy formation energies for the (110) and (100) Pd substituted surfaces are 2.19 eV and 2.29 eV lower than for pure ceria, respectively. For both of these surfaces, the vacancy formation energy is exothermic, indicating that reduction is favorable thermodynamically even without the inclusion of entropic terms. Bader charges and DOS data confirm that for both (110) and (100) surfaces of ceria, oxygen vacancy formation in the presence of Pd results in the reduction of the Pd atom.

A number of conclusions can be drawn from the analysis of surface vacancy formation. For pure ceria, oxygen vacancy formation is most exothermic for the (110) surface, followed by the (100) and then the (111) surface. Vacancy formation on these systems results in the reduction of two surface cerium atoms per vacancy. For Zr-doped surfaces, vacancy formation energies proceed in the following order: (100) > (111) > (110). The change in order can be attributed to the specific coordination environment of the (100) surface when Zr is substituted into the surface. The (100) surface becomes the most endothermic to reduce because the surface oxygen atoms are only coordinated with two metal atoms, one of which is Zr, which is not reduced upon formation of a vacancy. Thus, a subsurface Ce atom with a full oxygen coordination environment is reduced, which is less favorable than reducing a Ce atom adjacent to the vacancy. For Pd-doped surfaces, vacancy formation energies assume the same order as for pure ceria, with the (110) having the most exothermic ΔE_{vac}. In each case, Pd is reduced instead of Ce, as visible in Bader charge and DOS data.

The energetics of further reduction of each (111) and (110) surface was considered by calculating the energy of forming a second oxygen vacancy per surface cell. For the Pd-substituted (110) surface, the surface oxygen atom which extends away from the Pd atom (labeled in Figure 2-4d) as a result of the first vacancy was removed to form the second vacancy. For Pd-substituted (111) as well as Zr-substituted (111) and (110), one of the equivalent remaining nearest neighbor surface oxygen to the dopant metal was removed to form the second oxygen vacancy. For pure ceria (111) and (110), remaining surface oxygen in the vacant surface are equivalent and thus a surface oxygen was removed to form a second vacancy. For Pd-substituted surfaces, the removal of a second surface oxygen results in further reduction of the Pd atom. For pure CeO_2 and Zr-substituted CeO_2 (111) and (110), previously unreduced cerium atoms become reduced due to second vacancy formation. Second vacancy formation energies for each surface are listed in Table 2-1 as $\Delta E'_{vac}$. For each system, the formation of a second oxygen vacancy per surface is more endothermic than the formation of the first vacancy.

2.3.2 Thermodynamics of Dissociative Methane Adsorption

The dissociative adsorption of methane to the pure and Zr or Pd substituted CeO_2 surfaces was studied using the DFT+U method. We found no notable interaction (>0.05 eV) between the intact CH_4 molecule and the clean (111), (110) and (100) surfaces. The lack of an exothermic molecularly adsorbed state is consistent with the approach of a non-polar adsorbate to the ceria surface and with the difficulty of DFT to represent long-range dispersion interactions.[69] Methane dissociatively adsorbs exothermically as CH_3 and H fragments, with each fragment binding to different surface oxygen atoms as shown in Figure 2-2. Attempts to optimize adsorption configurations involving adsorbate interaction with surface cerium atoms were unsuccessful. For the (111) surface of pure ceria, O-H and O-C bonds align perpendicular to the surface giving each oxygen atom a tetrahedral coordination. Ce-O distances lengthen by 0.10 to 0.25 Å for those oxygen bound to H or CH_3 species. The (110) surface of pure ceria displays similar Ce-O lengthening, with the most dramatic change seen in the distance between surface oxygen and subsurface cerium atoms (0.60-1.20 Å). For the ceria (100) surface, CH_3 and H fragments also adsorb atop surface oxygen atoms, creating a trigonal coordination environment about O and lengthening the Ce-O distance by 0.30 Å.

Methane adsorption is a surface reduction process similar to that of vacancy formation, which suggests that surface reducibility and alkane adsorption thermodynamics are directly correlated. Bader charge analysis for each of the pure ceria surfaces reveals partial reduction of surface and subsurface ceria similar to that caused by oxygen vacancy formation. For two of the cerium atoms coordinated with oxygen atoms serving as adsorption sites, there is a 0.22-0.26 e^- increase in Bader charge following adsorption of CH_3 and H. The DOS for each surface with CH_3 and H adsorbed (shown for the (111) surface in Figure 2-3c), exhibits a similar “gap state” to that described earlier for vacancy formation. Thus, methane adsorption ($CH_4 \rightarrow *CH_3 + *H$) over CeO_2 (111), (110), and (100) surfaces results in the reduction of surface cerium atoms similar to that of vacancy formation.

The preferred adsorption configuration on Zr-substituted surfaces is consistent with pure ceria surfaces, with CH_3 and H both adsorbing on surface oxygen atoms. Adsorption is preferred with CH_3 and H adsorbed to surface oxygen atoms also coordinated with the Zr. Equilibrium structures could not be located with adsorbates bound to surface Ce or Zr atoms. Table 2-2 lists methane adsorption energies and the resulting changes in Bader charge for each surface. The adsorption energy was 0.15-0.38 eV more exothermic, depending on surface termination, for surfaces containing Zr versus those of pure ceria. Bader charge analysis illustrates that adsorption resulted in the reduction of surface and/or subsurface cerium atoms by 0.22-0.30 e^-, with minimal charge differences for Zr (<0.05 e^-). DOS data confirms the presence of newly occupied Ce states as a result of adsorption, consistent with the reduction of cerium atoms similarly to vacancy formation. This result is similar to that for vacancy formation in Zr containing surfaces, as in both cases the reduction process (whether it be vacancy formation or adsorption) results in the reduction of Ce atoms but not Zr atoms.

Table 2-2. Adsorption energies (ΔE_{ads}) for each surface, the resulting change in Bader charge for each related metal atom (M_{1-4}), and adsorption energies for each pre-reduced surface ($\Delta E'_{ads}$).

Surface	**M_1**	**ΔE_{ads} (eV)**	**ΔQ_{M1} (e)**	**ΔQ_{M2} (e)**	**ΔQ_{M3} (e)**	**ΔQ_{M4} (e)**	**$\Delta E'_{ads}$(eV)**
(111)	Ce	-0.76	+0.22	+0.22	+0.02	+0.02	-0.59
	Zr	-1.00	-0.01	+0.23	+0.22	+0.03	-0.82
	Pd	-1.93	+0.32	0.00	-0.03	-0.01	-1.52
(110)	Ce	-1.22	+0.21	+0.22	+0.03	+0.04	0.05
	Zr	-1.60	0.00	+0.30	+0.26	0.00	-0.28
	Pd	-2.50	+0.32	+0.08	+0.02	0.00	-1.82
(100)	Ce	-1.52	+0.25	+0.26	-0.01	-0.01	N/A
	Zr	-1.67	-0.04	+0.27	+0.03	+0.27	N/A
	Pd	-2.05	+0.43	-0.03	+0.04	0.00	N/A

Adsorption on surfaces containing Pd was most exothermic with CH_3 and H binding to surface oxygen coordinated with Pd. As with Zr incorporated and pure CeO_2 surfaces, equilibrium structures could not be located with CH_3 or H species bound to Ce or Pd atoms. Adsorption energies were more exothermic than those found for pure CeO_2 by 0.53-1.28 eV (Table 2). Bader charges indicate that Pd is reduced in these systems by 0.32-0.43 e^- with little change in Ce charge (<0.08 e^-), and DOS analysis confirms the reduction of Pd as a result of adsorption. Thus, the reduction caused by the dissociative adsorption of methane results in only reduction of the Pd atom, similar to that for vacancy formation. Adsorption is substantially more exothermic than over pure ceria due to the greater reducibility of the Pd-containing surfaces, despite no direct bonding of CH_3 or H species with Pd atoms.

2.3.3 Methane Adsorption on Pre-reduced Surfaces

Dissociative adsorption of methane was investigated on CeO_2 (111) and (110) surfaces with oxygen vacancies. Adsorption to vacant (100) surfaces was not studied due to the lack of two surface oxygen atoms in the vacant p(2x2) cell, and the excessive computational requirements of using larger supercells to model the (100) surface. For the vacant CeO_2 (111) and (110) surfaces, adsorption preferentially occurs for CH_3 and H on surface oxygen sites identical to those for intact surfaces. The adsorption energies for vacant surfaces (E'_{ads}) are given in Table 2-2. Adsorption is less exothermic on the vacant surfaces as compared to the fully oxidized surfaces by 0.17 eV (-0.59 eV) and 1.27 eV (0.05 eV) on the (111) and (110) surfaces, respectively, due to the pre-reduced nature of the vacant surface. Adsorption on both surfaces results in reduction of surface and/or subsurface Ce^{4+} ions which were previously unreduced by vacancy formation, confirmed by Bader charges and PDOS. The dramatic increase in adsorption energy for the vacant (110) surface is likely due to the required reduction of two subsurface Ce atoms, whereas adsorption on the defective (111) surface results in only reduction of Ce atoms in the surface layer.

The dissociative adsorption of methane was also considered on vacant, Zr or Pd substituted surfaces. In each case, adsorption was less exothermic than for intact surfaces due to the pre-reduced nature of surface metal atoms. For the vacant Zr-substituted CeO_2 (111) and (110) surfaces, the adsorption energy is 0.18 eV (-0.82 eV) and 1.32 eV (-0.28 eV) less exothermic, respectively. Adsorption on vacant Pd-substituted (111) and (110) is less exothermic by 0.41 eV (-1.52 eV) and 0.68eV (-1.82 eV), respectively. As vacancy formation opens coordination sites on Zr and Pd atoms, direct bonding of CH_3 and H species to metal atoms was considered for vacant surfaces. As with pure ceria surfaces, equilibrium structures could not be located with CH_3 or H fragments bound directly to Zr or Pd, and adsorption occurred preferentially on remaining oxygen atoms. Adsorption of CH_3 and H to surface oxygen atoms of vacant Zr-substituted CeO_2 surfaces results in the reduction of two additional Ce atoms. Adsorption to the vacant, Pd-substituted CeO_2 surface results in further reduction of the Pd atom. Thus, dissociative methane adsorption is a surface reduction process, and is less exothermic on surfaces which are pre-reduced due to the formation of oxygen vacancies.

2.3.4 Dependence of ΔE_{vac} and ΔE_{ads} on Value of Hubbard U-term

The proper choice of U value is not well defined, as the value of 5 eV used thus far is based on proper representation of the band gap in Ce_2O_3, and is not certain to represent vacancy formation energetics. Pacchioni et al.[70] highlighted that the differences between vacancy formation energies for CeO_2 determined by various computational methods may be as high as 3 eV, including methods which inaccurately describe the electronic structure of the reduced state. In this study, we have concentrated on implementing the DFT+U method to accurately describe the electronic structure of reduced ceria, and obtain consistent qualitative results. As discussed by Pacchioni et al., without a direct experimental benchmark, it is not possible to conclusively determine if the choice of U value reproduces the experimental vacancy formation energy. Therefore, the sensitivity of ΔE_{vac} and ΔE_{ads} to the U value was determined to provide context for the results presented within the DFT+U method herein and to further justify a U value of 5 eV. The energies of oxygen vacancy formation and dissociative methane adsorption on the (111) surface were calculated for values of U between 0 and 8. Figure 2-5 shows ΔE_{vac} and ΔE_{ads} plotted versus U value for pure ceria, Zr-substituted and Pd-substituted (111) surfaces. For pure and Zr-substituted ceria, the vacancy formation energy and adsorption energy increase in exothermicity linearly with increasing U value above 3 eV. For Pd-substituted ceria, the vacancy formation energy and adsorption energy linearly become less exothermic with increasing U value, however the values are considerably less dependent on the U value. Vacancy formation and adsorption on pure or Zr-substituted ceria reduces surface Ce atoms by Ce 4f occupation, leading to strong dependence of ΔE_{ads} and ΔE_{vac} on the value of U. For the Pd-substituted ceria, vacancy formation and adsorption reduce surface Pd atoms instead of Ce, and thus the lack of occupied Ce 4f states leads to little influence of U value on energetics.

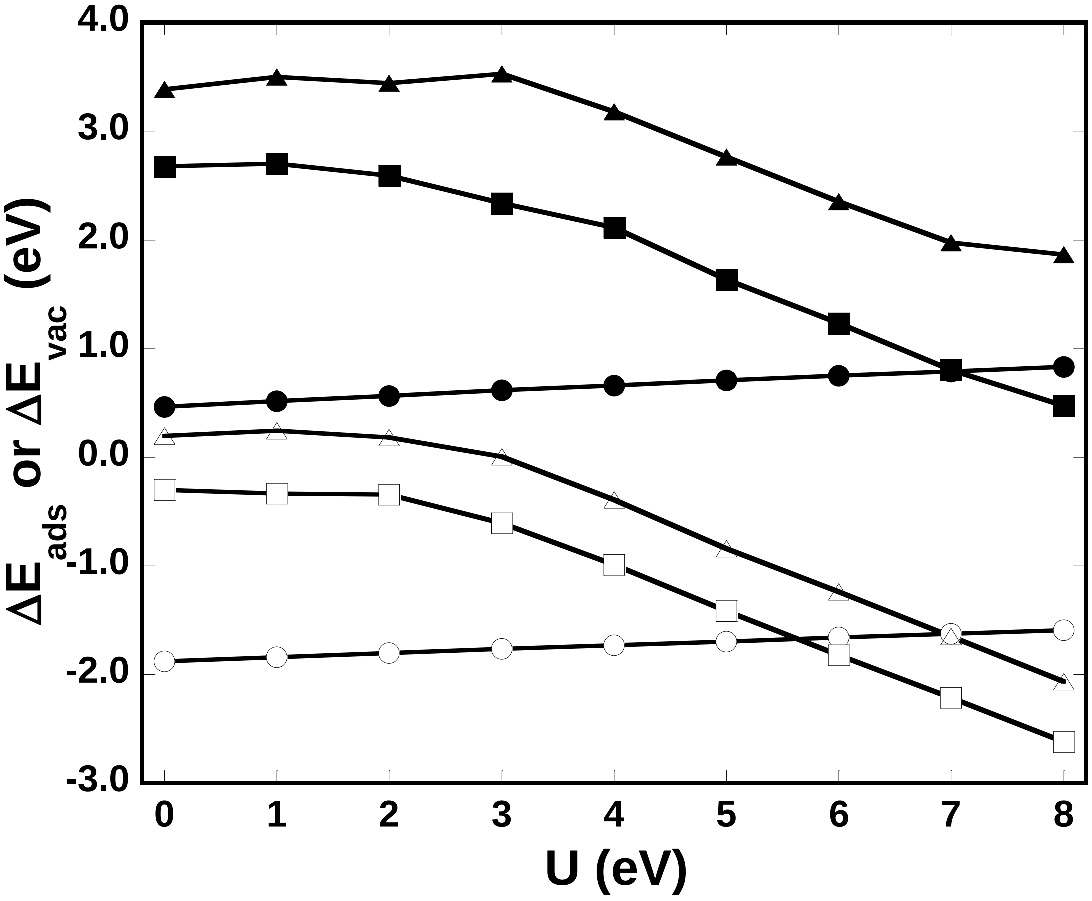

Figure 2-5. Dependence of the methane adsorption energy (ΔE_{ads}) and surface vacancy formation energy (ΔE_{vac}) on the choice of U value. (•) Pd-substituted CeO_2 surfaces, (■) Zr-substituted CeO_2 surfaces, and (▲) pure CeO_2. Closed circles represent E_{vac} data and open circles represent ΔE_{ads} data.

The influence of the U value on the energy of the Ce 4f states can be shown by considering the relative energy of the “gap state” (resulting from partial occupation of Ce 4f states due to reduction), with respect to the CeO_2 valence band (ΔE_{gap}). The energy difference between the CeO_2 valence band and the 4f gap state, ΔE_{gap}, is illustrated in Figure 2-3 and included for different U values in Table 2-3. The value of ΔE_{gap} is strongly dependent on the U value for pure and Zr-substituted ceria, but shows only slight dependence on the U value for Pd-substituted ceria. For pure ceria, ΔE_{gap} decreases with increasing U, and at U=7 eV no gap state peak is visible in the density of states, which can be attributed to an overlap in energy between the gap state and the CeO_2 valence band. At U=3 eV, the gap state peak also cannot be identified, due to delocalization of f electrons into the Ce 4f band. Similar to the pure ceria case, vanishing of a distinct gap state for Zr-substituted ceria is observed at U values of 4 eV and 7 eV. A U value of 5 eV results in a distinct gap state due to the localization of Ce 4f electrons, and lies between the 4 eV and 7 eV limits, thus further motivating its use in this study.

Table 2-3. Energy differences ΔE_{gap} between the valence band and gap state for the vacant CeO_2, Zr-substituted CeO_2, and Pd-substituted $CeO_2(111)$ surfaces.

	CeO_2	**Zr-substituted**	**Pd-substituted**
U	**ΔE_{gap}**	**ΔE_{gap}**	**ΔE_{gap}**
3	N/A	N/A	0.784
4	1.582	N/A	0.792
5	1.066	1.201	0.784
6	0.537	0.739	0.805
7	N/A	N/A	0.811

2.3.5 Correlation between Vacancy Formation and Methane Adsorption

Oxygen vacancy formation and methane adsorption are both reduction processes on ceria, specifically causing the reduction of surface metal atoms. Thus, since both processes result in similar changes in the electronic structure of the ceria surface, correlation between the vacancy formation energy and methane adsorption energy is expected. Figure 2-6 shows the dissociative adsorption energy of methane plotted versus vacancy formation energy for each surface investigated. Adsorption energies to intact surfaces are plotted versus first vacancy formation energies, whereas adsorption energies to prereduced, vacant surfaces are plotted versus second vacancy formation energies. This plot illustrates correlation between the vacancy formation energy and adsorption energy across surface composition, though scatter is introduced due to differences in surface termination. Surfaces containing Pd atoms exhibit the most exothermic vacancy formation energies as well as adsorption energies, followed by surfaces with Zr and finally those for pure ceria. Perfect linear correlation between vacancy formation and methane adsorption energies is complicated by variations in M-O bond energies in the intact and reduced states, and significant distortions of the surface structure for surfaces with two oxygen vacancies per unit cell. The general trend between the energetics of vacancy formation and methane adsorption, however, suggests that the energy of methane adsorption on ceria surfaces is dependent on surface reducibility.

2.3.6 Activation Barrier for Dissociative Methane Adsorption

The lowest energy reaction barrier for methane adsorption over CeO_2 surfaces, regardless of termination, occurs through the abstraction of H from CH_4. The highest energy state along this reaction path consists of an adsorbed (abstracted) H atom and a methyl radical. The initial, transition and final states for this process over CeO_2 (111) are shown in Figure 2-7. At the highest energy state along the reaction path, as located by the CI-NEB search method, the O-H bond is formed, the C-H bond elongated to >2.5 Å, and there is no indication of interaction between the methyl C atom and the O atom to which it is bound in the final $*CH_3$ state. Bader charge analysis is consistent with the highest energy state representing a $\bullet CH_3$ radical and a singly reduced, H* adsorbed surface. Comparison of the total energy of this highest energy state with the sum of H* adsorbed and isolated $\bullet CH_3$ fragments confirms the lack of interaction between the $\bullet CH_3$ fragment and the surface. This highest energy state does not have an imaginary vibrational frequency but instead is a local minimum along the potential energy surface. Attempts to use the CI-NEB method to locate a higher energy state between this minima and either the initial or final state indicated a monotonic increase in energy towards this state.

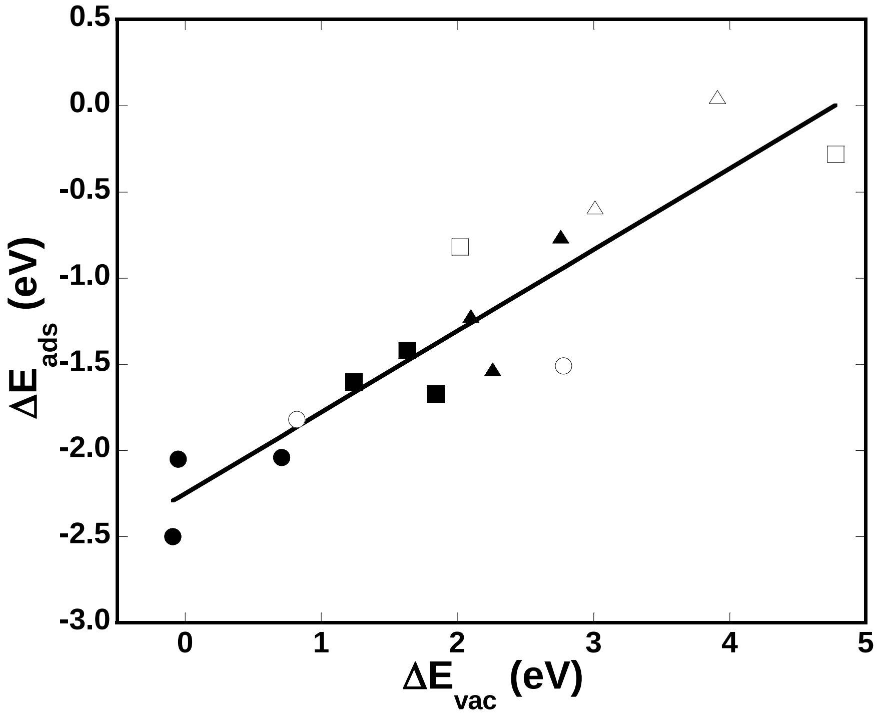

Figure 2-6. Plot of the methane adsorption energy (ΔE_{ads}) vs. the surface vacancy formation energy (ΔE_{vac}). (•) Pd-substituted CeO_2 surfaces, (■) Zr-substituted CeO_2 surfaces, and (▲) pure CeO_2. Pre-reduced surfaces are noted by open symbols.

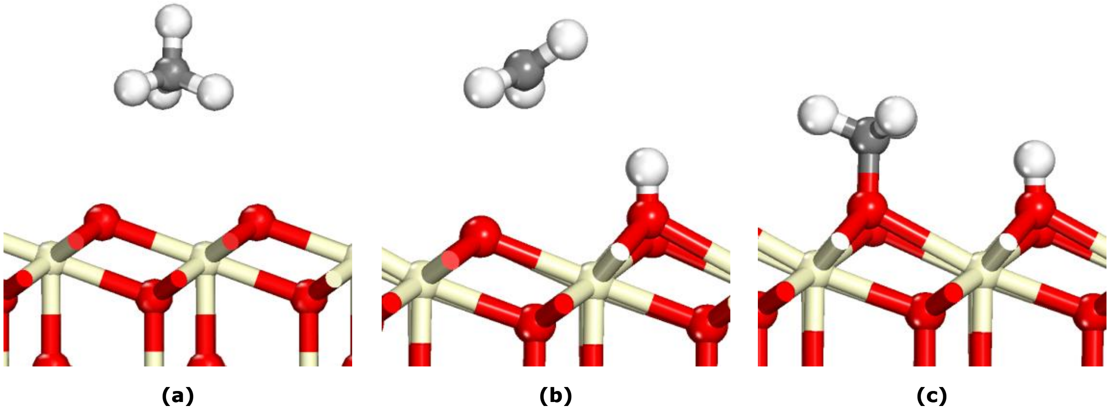

Figure 2-7. Plot of the methane adsorption energy (ΔE_{ads}) vs. the surface vacancy formation energy (ΔE_{vac}). (•) Pd-substituted CeO_2 surfaces, (■) Zr-substituted CeO_2 surfaces, and (▲) pure CeO_2. Pre-reduced surfaces are noted by open symbols.

The energy barrier for dissociative methane adsorption proceeding through a methyl radical state is listed for each (111) surface in Table 4, along with changes in surface metal Bader charge for the radical state with respect to the clean (111) surface. The methane activation barrier, given as the relative energy of the radical state (E_{rad}), decreases for Zr-substituted ceria with respect to pure ceria, and even further for Pd-substituted ceria. Pd incorporation thus leads to stronger adsorption and a lower energy barrier for dissociative adsorption, without direct involvement of Pd coordination sites. Based on the trends presented herein of the reduction energetics of pure, Zr-substituted and Pd-substituted ceria, the relationship between E_{rad} and composition is consistent with the expected trend for a one e^- reduction.

Table 2-4. Relative energy of the methyl radical state (E_{rad}) over each surface and the resulting change in Bader charge for each related metal atom (M_{1-4}).

Surface	M_1	E_{rad} (eV)	ΔQ_{M1} (e)	ΔQ_{M2} (e)	ΔQ_{M3} (e)	ΔQ_{M4} (e)
(111)	Ce	+1.40	+0.24	-0.02	-0.02	-0.02
	Zr	+1.06	-0.01	+0.23	-0.01	-0.02
	Pd	+0.22	+0.12	+0.01	+0.01	-0.03

In considering a number of possible methane activation paths over Mo_3O_9 clusters, Fu et al.[71] reported the H abstraction path to have the lowest barrier. Cheng et al. reported H abstraction with the formation of an iso-propyl radical as the lowest energy path for propane dehydrogenation over V_4O_{10} clusters.[72] The preference of this path over these flexible cluster structures, with the availability of bridging and terminal O atoms as well as a flexible coordination environment about the metal center, suggest that our findings over the more rigid CeO_2 surface are reasonable. Multiple attempts to identify a concerted reaction path involving C-O bond formation along with C-H dissociation were unsuccessful. Analysis of the potential energy surface for methane activation over CeO_2 and doped CeO_2 surfaces is a subject of continuing investigation. Due to the inability of the CI-NEB method to identify a true transition state, the activation barrier for methane adsorption will be investigated in more detail in future studies.

2.4 Conclusions

The DFT+U method was used to show that both oxygen vacancy formation and methane adsorption on ceria and doped ceria are surface reduction processes, and thus the reaction energy for methane oxidation correlates with surface reducibility. Dissociative methane adsorption proceeds through H abstraction and the formation of a methyl radical transition state in which a metal atom of the surface is reduced by a single electron. The activation barrier for this step, therefore, also correlates with the surface reducibility measured by the oxygen vacancy formation energy. The incorporation of metals such as Zr or Pd into the ceria lattice at the surface lowers the energy of oxygen vacancy formation, as well as the reaction energy and barrier for methane adsorption. Previous studies[13,19-21] have illustrated the incorporation of Zr into the fluorite lattice of ceria, however we have neglected to consider the thermodynamic preference of Pd surface substitution, which will be addressed in future studies.

This study illustrates the correlation between surface reducibility and catalytic activity for methane oxidation on CeO_2-based materials. Calculated reaction energies suggest that a fully-oxidized surface will provide enhanced activity for methane activation. The reducibility can be increased by the substitution of Zr or Pd into the CeO_2 surface, which also lowers the energy barrier for dissociative methane adsorption.

ACKNOWLEDGMENT: Acknowledgement is made to the Donors of the American Chemical Society Petroleum Research Fund #46724-G5 for support of this research.

2.5 References

(1) Trovarelli, A.; de Leitenburg, C.; Boaro, M.; Dolvetti, G. *Catalysis Today* **1999**, *50*, 353.

(2) Teschner, D.; Wootsch, A.; Pozdnyakova-Tellinger, O.; Krohnert, J.; Vass, E. M.; Havecker, M.; Zafeiratos, S.; Schnorch, P.; Jentoft, P. C.; Knop-Gericke, A.; Schlogl, R. *Journal of Catalysis* **2007**, *249*, 318.

(3) Picasso, G.; Gutierrez, M.; Pina, M. P.; Herguido, J. *Chemical Engineering Journal* **2007**, *126*, 119.

(4) Shi, L.; Chu, W.; Qu, F.; Luo, S. *Catalysis Letters* **2007**, *113*, 59.

(5) Kuznetsova, T.; Sadykov, V.; Batuev, L.; Moroz, E.; Burgina, E.; Rogov, V.; Kriventsov, V.; Kochubey, D. *Journal of Natural Gas Chemistry* **2006**, *15*, 149.

(6) Itome, M.; Nelson, A. E. *Catalysis Letters* **2006**, *106*, 21.

(7) Bozo, C.; Guilhaume, N.; Garbowski, E.; Primet, M. *Catalysis Today* **2000**, *59*, 33.

(8) McIntosh, S.; Gorte, R. J. *Chemical Reviews* **2004**, *104*, 4845.

(9) McIntosh, S.; Vohs, J. M.; Gorte, R. J. *Electrochemical and Solid-State Letters* **2003**, *6*, A240.

(10) Putna, E. S.; Stubenrauch, J.; Vohs, J. M.; Gorte, R. J. *Langmuir* **1995**, *11*, 4832.

(11) Zhou, G.; Shah, P. R.; Kim, T.; Fornasiero, P.; Gorte, R. J. *Catalysis Today* **2007**, *123*, 86.

(12) Borchert, H.; Borchert, Y.; Kaichev, V. V.; Prosvirin, I. P.; Alikina, G. M.; Lukashevich, A. I.; Zaikovskii, V. I.; Moroz, E. M.; Paukshtis, E. A.; Bukhtiyarov, V. I.; Sadykov, V. A. *Journal of Physical Chemistry B* **2005**, *109*, 20077.

(13) Fornasiero, P.; Dimonte, R.; Rao, G. R.; Kaspar, J.; Meriani, S.; Trovarelli, A.; Graziani, M. *Journal of Catalysis* **1995**, *151*, 168.

(14) Binet, C.; Daturi, M.; Lavalley, J.-C. *Catalysis Today* **1999**, *50*, 207.

(15) Boaro, M.; de Leitenburg, C.; Dolcetti, G.; Trovarelli, A. *Journal of Catalysis* **2000**, *193*, 338.

(16) Eguchi, K.; Setoguchi, T.; Inoue, T.; Arai, H. *Solid State Ionics* **1992**, *52*, 165.

(17) Mamontov, E.; Egami, T.; Brezny, R.; Koranne, M.; Tyagi, S. *J. Phys. Chem. B* **2000**, *104*, 11110.

(18) Rodriguez, J. A.; Wang, X.; Hanson, J. C.; Liu, G.; Iglesias-Juez, A.; Fernandez-Garcia, M. *Journal of Chemical Physics* **2003**, *119*, 5659.

(19) Balducci, G.; Fornasiero, P.; Monte, R.; Kaspar, J.; Meriani, S.; Graziani, M. *Catalysis Letters* **1995**, *33*, 193.

(20) Fornasiero, P.; Balducci, G.; Di Monte, R.; Kaspar, J.; Sergo, V.; Gubitosa, G.; Ferrero, A.; Graziani, M. *Journal of Catalysis* **1996**, *164*, 173.

(21) Martinez-Arias, A.; Fernandez-Garcia, M.; Ballesteros, V.; Salamanca, L. N.; Conesa, J. C.; Otero, C.; Soria, J. *Langmuir* **1999**, *15*, 4796.

(22) Fabris, S.; de Gironcoli, S.; Baroni, S.; Vicario, G.; Balducci, G. *Physical Review B* **2005**, *71*, 041102.

(23) Fabris, S.; de Gironcoli, S.; Baroni, S.; Vicario, G.; Balducci, G. *Physical Review B* **2005**, *72*, 237102.

(24) Kresse, G.; Blaha, P.; Silva, J.; Ganduglia-Pirovano, M. V. *Physical Review B* **2005**, *72*, 237101.

(25) Nolan, M.; Grigoleit, S.; Sayle, D. C.; Parker, S. C.; Watson, G. W. *Surface Science* **2005**, *576*, 217.

(26) Yang, Z.; Luo, G.; Lu, Z.; Hermansson, K. *The Journal of Chemical Physics* **2007**, *127*, 074704.

(27) Yang, Z.; Woo, T. K.; Hermansson, K. *The Journal of Chemical Physics* **2006**, *124*, 224704.

(28) Herschend, B.; Baudin, M.; Hermansson, K. *Surface Science* **2005**, *599*, 173.

(29) Jiang, Y.; Adams, J. B.; van Schilfgaarde, M.; Sharma, R.; Crozier, P. A. *Applied Physics Letters* **2005**, *87*, 141917.

(30) Yang, Z.; Lu, Z.; Luo, G.; Hermansson, K. *Physics Letters A* **2007**, *369*, 132.

(31) M. Daturi, C. B., J. C. Lavalley, G. Blanchard,. *Surface and Interface Analysis* **2000**, *30*, 273.

(32) Vidmar, P.; Fornasiero, P.; Kaspar, J.; Gubitosa, G.; Graziani, M. *Journal of Catalysis* **1997**, *171*, 160.

(33) Bozo, C.; Guilhaume, N.; Herrmann, J.-M. *Journal of Catalysis* **2001**, *203*, 393.

(34) Shen, W.; Matsumura, Y. *Journal of Molecular Catalysis A: Chemical* **2000**, *153*, 165.

(35) Xiao, L.; Sun, K.; Xu, X.; Li, X. *Catalysis Communications* **2005**, *6*, 796.

(36) Yee, A.; Morrison, S. J.; Idriss, H. *Journal of Catalysis* **1999**, *186*, 279.

(37) Badri, A.; Binet, C.; Lavalley, J. C. *Journal of the Chemical Society, Faraday Transactions* **1996**, *92*, 1603.

(38) Binet, C.; Jadi, A.; Lavalley, J. C.; Boutonnet-Kizling, M. *Journal of the Chemical Society, Faraday Transactions* **1992**, *88*, 2079.

(39) Bernal, S.; Calvino, J. J.; Cauqui, M. A.; Gatica, J. M.; Larese, C.; Perez Omil, J. A.; Pintado, J. M. *Catalysis Today* **1999**, *50*, 175.

(40) Chen, H.; Liu, S.; Ho, J. *Journal of Physical Chemistry B* **2006**, *110*, 14816.

(41) Esch, F.; Fabris, S.; Zhou, L.; Montini, T.; Africh, C.; Fornasiero, P.; Comelli, G.; Rosei, R. *Science* **2005**, *309*, 752.

(42) Ichikawa, N.; Sato, S.; Takahashi, R.; Sodesawa, T.; Fujita, H.; Atoguchi, T.; Shiga, A. *Journal of Catalysis* **2006**, *239*, 13.

(43) Muller, C.; Freysoldt, C.; Baudin, M.; Hermansson, K. *Chemical Physics* **2005**, *318*, 180.

(44) Nolan, M.; Parker, S. C.; Watson, G. W. *Surface Science* **2005**, *595*, 223.

(45) Nolan, M.; Parker, S. C.; Watson, G. W. *Physical Chemistry Chemical Physics* **2006**, *8*, 216.

(46) Wang, X.; Rodriguez, J. A.; Hanson, J. C.; Gamarra, D.; Martinez-Arias, A.; Fernandez-Garcia, M. *Journal of Physical Chemistry B* **2005**, *109*, 19595.

(47) Zhou, G.; Shah, P. R.; Montini, T.; Fornasiero, P.; Gorte, R. J. *Surface Science* **2007**, *601*, 2512.

(48) Li, J.; Singh, U. G.; Bennett, J. W.; Page, K.; Weaver, J. C.; Zhang, J. P.; Proffen, T.; Rappe, A. M.; Scott, S.; Seshadri, R. *Chem. Mater.* **2007**, *19*, 1418.

(49) Kresse, G.; Furthmuller, J. *Computational Materials Science* **1996**, *6*, 15.

(50) Kresse, G.; Furthmuller, J. *Physical Review B* **1996**, *54*, 11169.

(51) Kresse, G.; Hafner, J. *Physical Review B* **1993**, *47*, 558.

(52) Kresse, G.; Joubert, D. *Physical Review B* **1999**, *59*, 1758 LP

(53) Monkhorst, H. J.; Pack, J. D. *Physical Review B* **1976**, *13*, 5188 LP

(54) Perdew, J. P.; Chevary, J. A.; Vosko, S. H.; Jackson, K. A.; Pederson, M. R.; Singh, D. J.; Fiolhais, C. *Physical Review B* **1992**, *46*, 6671.

(55) Herbst, J.; Watson, R. ; Wilkins, J. W. *Physical Review B* **1978**, *17*, 3089 LP

(56) Anisimov, V. I.; Gunnarsson, O. *Physical Review B* **1991**, *43*, 7570 LP

(57) Nolan, M.; Parker, S. C.; Watson, G. W. *Journal of Physical Chemistry B* **2006**, *110*, 2256.

(58) Mills, G.; Jonsson, H.; Schenter, G. K. *Surface Science* **1995**, *324*, 305.

(59) Henkelman, G.; Jonsson, H. *Journal of Chemical Physics* **2000**, *113*, 9978.

(60) Henkelman, G.; Uberuaga, B. P.; Jonsson, H. *Journal of Chemical Physics* **2000**, *113*, 9901.

(61) Henkelman, G.; Arnaldsson, A.; Jonsson, H. *Computational Materials Science* **2006**, *36*, 354.

(62) Bader, R. *Accounts of Chemical Research* **1985**, *18*, 9.

(63) Sanville, E.; Kenny, S. D.; Smith, R.; Henkelman, G. H. *Journal of Computational Chemistry* **2007**, *28*, 899.

(64) Kummerle, E. A.; Heger, G. *Journal of Solid State Chemistry* **1999**, *147*, 485.

(65) Wang, L.; Maxisch, T.; Ceder, G. *Physical Review B (Condensed Matter and Materials Physics)* **2006**, *73*, 195107.

(66) Mullins, D. R.; Overbury, S. H.; Huntley, D. R. *Surface Science* **1998**, *409*, 307.

(67) Mullins, D. R.; Radulovic, P. V.; Overbury, S. H. *Surface Science* **1999**, *429*, 186.

(68) Henderson, M. A.; Perkins, C. L.; Engelhard, M. H.; Thevuthasan, S.; Peden, C. H. F. *Surface Science* **2003**, *526*, 1.

(69) Milas, I.; Nascimento, M. A. C. *Chemical Physics Letters* **2001**, *338*, 67.

(70) Pacchioni, G. *The Journal of Chemical Physics* **2008**, *128*, 182505.

(71) Fu, G.; Xu, X.; Lu, X.; Wan, H. *J. Am. Chem. Soc.* **2005**, *127*, 3989.

(72) Cheng, M. J.; Chenoweth, K.; Oxgaard, J.; vanDuin, A.; Goddard, W. A. *J. Phys. Chem. C* **2007**, *111*, 5115.

Chapter 3

Ab initio thermodynamic evaluation of Pd atom interaction with CeO_2 surfaces

This chapter is published as: A. D. Mayernick, M. J. Janik. *Journal of Chemical Physics* 2009, 131(8), 084701.

ABSTRACT: Palladium supported on ceria is an effective catalytic material for three-way automotive catalysis, catalytic combustion, and solid-oxide fuel cell (SOFC) anodes. The morphology, oxidation state, and particle size of Pd on ceria affects catalytic activity, and is a function of experimental conditions. This work utilizes *ab initio* thermodynamics using density functional theory (DFT+U) methods to evaluate the stability of Pd atoms, PdO_x species, and small Pd particles in varying configurations on CeO_2 (111), (110), and (100) single crystal surfaces. Over specific oxygen partial pressure and temperature ranges, palladium incorporation to form a mixed surface oxide is thermodynamically favorable versus other single Pd atom states, on each ceria surface. For example, Pd atoms may incorporate into Ce fluorite lattice positions in a Pd^{4+} oxidation state on the CeO_2 (111) surface. The ceria support shifts the transition between formal Pd oxidation states (Pd^0, Pd^{2+}, Pd^{4+}) relative to bulk palladium, and stabilizes certain oxidized palladium species on each surface. We show that temperature, oxygen pressure, and cell potential in an SOFC can influence the stable states of palladium supported on ceria surfaces, providing insight into structural stability during catalytic operation.

3.1 Introduction

Palladium supported on ceria is an effective catalytic material for three-way automotive catalysis,[1] catalytic combustion,[2] and solid-oxide fuel cell (SOFC) anodes.[3-7] Palladium can be supported on ceria as well-dispersed metal particles, however the morphology and oxidation state of Pd on ceria changes with variation in experimental conditions.[2, 8-14] Palladium deposition on CeO_2 can result in the formation of PdO_x species,[2, 11, 15, 16] and characterization of other noble metals (platinum and gold) deposited on ceria indicate that mixed oxides may form at the CeO_2 surface.[17-19] The mixed oxide formed at the surface may provide unique sites which supply altered catalytic activity relative to pure Pd^0 or CeO_2 sites. Herein, we present a computational investigation, utilizing the DFT+U method, of the thermodynamics of Pd atom interaction with single crystal CeO_2 surfaces. The *ab initio* thermodynamics approach is used to evaluate the stability of metal-ceria surface structures at varying oxygen pressure, temperature, and electrochemical potential. We find that at certain pressure, temperature and potential ranges, mixed palladium-ceria oxide formation at the CeO_2 surface is favorable relative to single adsorbed Pd atoms or PdO_x species.

Preparation and aging methods influence the particle size and oxidation state of Pd supported on the CeO_2 surface.[2, 8-14] Palladium particles can be dispersed on CeO_2 surfaces by methods such as deposition-precipitation[2, 15, 16] and impregnation techniques.[9, 11, 12] The size of Pd particles can be altered subsequent to deposition by aging in reducing or oxidizing atmospheres. However, *in situ* characterization of structural changes occurring during catalytic operation and identification of specific heterogeneous active sites are challenging. Extended X-ray Absorption Fine Structure (EXAFS) spectra along with Field Emission Transmission Electron Microscopy (FE-TEM) confirmed the growth of Pd particles supported on ceria after heat treatment in a reducing atmosphere (773 K, H_2/N_2).[13] The oxidation of Pd^0 to PdO_x or palladium hydroxide species can also occur subsequent to the deposition of Pd particles on CeO_2.[12] Temperature Programmed Reduction (TPR) measurements indicated that PdO is formed on Pd/CeO_2 catalysts after deposition by wet impregnation.[20] X-ray Photoelectron Spectroscopy (XPS) studies also showed that PdO species are present on Pd/CeO_2 before and after reduction in H_2.[2] X-ray Diffraction (XRD) data indicated that PdO is formed and that Pd particles became encapsulated in a CeO_2/ZrO_2 support after aging in automotive exhaust gases (oscillating feeds of $CO/H_2/N_2$ and $O_2/SO_2/H_2O/N_2$).[11] The coordination environment and oxidation of Pd species supported on ceria thus depends on both the thermodynamic stability and kinetic history of the particles, and can be tailored by changing experimental conditions.

Experimental studies of various transition metals supported on ceria have indicated that single metal sites, with single metal atoms incorporated into the ceria surface, may form under oxidizing conditions. Scott and co-workers[21] showed that $BaCe_{1-x}Pd_xO_{3-\delta}$ can be formed by grinding together BaO_2, CeO_2, and PdO, and heating in oxygen at 1000°C. The authors demonstrated that Pd egresses from the perovskite lattice to form metallic Pd and $BaCeO_3$ upon heating in reducing atmosphere (H_2/N_2) and also will re-incorporate to form $BaCe_{1-x}Pd_xO_{3-\delta}$ upon subsequent heating in oxygen. The characterization of palladium supported on other reducible supports, such as MgO,[22] demonstrates the importance of interactions between Pd and support oxygen vacancies on the stability of supported Pd clusters. Although the incorporation of Pd into the CeO_2 fluorite lattice has not been observed, other studies illustrated that ceria strongly interacts with supported metal particles[17, 18, 23] and that incorporation into the ceria support to form a mixed oxide is possible. Nagai et. al[17] showed that Pt particles supported on ceria grew in size when heating in reducing atmosphere (H_2/He), and disperse to form very small particles (~1nm) when heated in oxygen (O_2/He). These authors used *in-situ* X-ray Absorption Near Edge Structure (XANES) to show that highly dispersed Pt oxides are present after heating in oxygen at 600 °C, and that the same conditions applied to Pt supported on Al_2O_3 do not result in Pt oxide formation. Flytzani-Stephanopoulus and co-workers. also showed that ionic Pt[18] and Au[18, 23] species form when Au or Pt metals are supported on ceria, and that Pt can be dispersed in small clusters within bulk cerium oxide.[19] These results suggest that transition metals supported on ceria may incorporate into the ceria lattice, providing unique active sites for catalytic applications.

The specific morphology and composition of the ceria surface and the interactions of Pd with the support influence overall catalytic performance.[2, 9-14, 24] Wang et al. showed that the reaction rate of the water-gas shift reaction over Pd/CeO_2 is directly proportional to the total surface area of Pd, which decreases as a result of Pd particle sintering.[14] Field Emission Scanning Electron Microscopy (FE-SEM) and EXAFS data indicated Pd particle growth during methanol synthesis from H_2 and CO reactants, for which deactivation of the Pd/CeO_2 catalyst is attributed.[15] The turnover frequency (TOF) for the reaction $NO + CO \rightarrow N_2 + CO_2$ on Pd/CeO_2 catalysts had a maximum for approximately 2-nm diameter Pd particles, greater than that for Pd/CeO_2 catalysts with Pd particles of 4.5-nm and 1-nm.[10] This result suggests that the catalytic activity of Pd/CeO_2 for nitrogen reduction in CO is not directly dependent on metal surface area, but rather on a balance between metal surface area and metal-ceria contact area. Xiao et al. showed that Pd/CeO_2 catalysts prepared by different methods exhibit different minimum temperatures for total methane conversion to CO_2. These authors used X-ray Diffraction, Raman spectroscopy, and X-ray Photoelectron Spectroscopy analysis to conclude that the most active Pd/CeO_2 catalyst was a result of containing the highest concentration of PdO_x sites.[2] Our previous DFT study determined that both the reaction energy and barrier for the dissociation of methane into $*CH_3$ and *H on ceria surfaces are more favorable if a single Pd atom is substituted for a Ce atom at the surface.[25] The oxidation state and coordination environment of Pd on ceria influences the catalytic activity, motivating further study of Pd-ceria interactions.

Computational chemistry approaches to modeling heterogeneous supported catalysts can investigate support interactions and reactivity, providing electronic structure level insight difficult to attain experimentally where heterogeneity of supported particle structures complicates analysis. Density functional theory (DFT) methods, coupled with *ab initio* thermodynamics approaches, offer the capability to directly probe the relative stability and catalytic activity of different surface morphologies. Studies of ceria-noble metal systems using DFT methods, however, are restricted to small unit cells and are complicated by theoretical difficulties in representing the electronic structure of reduced ceria (CeO_{2-x}). Previous DFT studies of ceria and metal-doped ceria have focused on these methodological challenges[26-29] and evaluating bulk and surface reduction energetics.[30-33] Hermansson and co-workers previously used the DFT+U method to model reduction energetics for Pd substitution into bulk CeO_2[34] and the CeO_2 (111) single crystal surface.[33] Herein, we use the DFT+U method[35, 36] to evaluate the interaction of palladium with different surface terminations of ceria. We construct a series of surface models consisting of single crystal terminations of ceria, interacting with single Pd atoms, small Pd clusters, and PdO_x species. Previous DFT studies have modeled the incorporation of Au,[37] Pd,[33] Zr,[38] Pt,[39, 40] Rh,[40] Y,[41] La,[41] and Sm metals,[41] as well as Ni adsorption and insertion,[42] with emphasis on evaluating structural changes which result from doping and the effects of doping on ceria reducibility. However, to the best of our knowledge, no previous work has used DFT methods with *ab initio* thermodynamics to evaluate the relative stability of various Pd-CeO_2 surface structures as a function of temperature and partial pressure of oxygen. To further catalyst design and optimization, the relative stability of Pd and PdO_x phases supported on CeO_2 surfaces, as a function of environment, must be considered.

This work utilizes *ab initio* thermodynamics to evaluate the stability of Pd atoms, PdO_x species, and small Pd particles in varying configurations on CeO_2 (111), (110), and (100) single crystal surfaces. Though the size of the PdO_x species are limited, these models represent the limits of an ideally dispersed catalyst, an idealized M-support interface, and initial stages of particle formation/deposition. Within our ab initio thermodynamics approach, single Pd atoms are considered as adsorbed onto the surface, substituted into the surface at Ce sites and inserted into void spaces underneath the first CeO_2 layer. The free energy of each system is evaluated with respect to temperature, partial pressure of oxygen, and, for consideration as SOFC anodes, electrochemical cell potential. Specifically, we address the thermodynamic preference for Pd to incorporate into the CeO_2 surface to form a surface mixed PdO_x-CeO_x oxide versus adsorbing or forming large metallic Pd particles. The ceria support shifts the transition between formal Pd oxidation states (Pd^0, Pd^{2+}, Pd^{4+}) relative to bulk palladium, and under certain conditions it is favorable for Pd to incorporate into the ceria surface to form mixed PdO_x-CeO_x oxides.

3.2 Computational Methodology

3.2.1 Electronic Structure Method

Calculations were carried out using the Vienna Ab-initio Simulation Program (VASP), an ab-initio total-energy and molecular dynamics program developed at the Institute for Material Physics at the University of Vienna.[43-45] The methodology used herein is similar to that of our previous study examining the methane activation energetics and oxygen vacancy formation over CeO_2 with Zr and Pd substituted in the surface.[25] The projector augmented wave (PAW) method[46] was used to represent the core region, with valence electron wavefunctions expanded in a tractable plane wave basis set (with an energy cutoff of 450 eV, all calculations spin-polarized). Valence configurations were $5s^2 5p^6 6s^2 4f^1 5d^1$ for cerium, for oxygen $2s^2 2p^4$, and for Pd $4d^{10}$. The Brillouin zone was sampled using a (2x2x2) Monkhorst Pack (MP) grid[47] for bulk ceria, and a (2x2x1) MP grid for surfaces, with the third vector perpendicular to the surface. Structural optimizations were performed by minimizing the forces on all atoms to below 0.05 eV·Å^{-1}. The Perdew-Wang (PW91) version of the generalized gradient approximation (GGA) is used to incorporate exchange and correlation energies.[48] Due to well-established difficulties within DFT to accurately represent the nature of 4f states in ceria,[26-28] we implemented the DFT+U approach.[35, 36] The DFT+U method introduces the Hubbard U-term as an on-site Coulombic interaction in the f states of ceria, which properly localizes electrons in these states for reduced CeO_{2-x} structures. We used a value of U=5 eV, which is consistent with recommended values within this method used in previous DFT studies of ceria.[31-36, 38, 49, 50] As discussed by Pacchioni et al.,[51] without a direct experimental benchmark, it is not possible to conclusively determine if the choice of U value reproduces the experimental reduction energy. Though trends in relative reduction energetics are preserved with varying U,[25] this introduces an unknown error in the absolute values $(T,\ P_{O_2})$ at which transitions occur.

3.2.2 Model Construction

The ceria (111), (110) and (100) surfaces are modeled as slabs of cubic fluorite CeO_2 separated by 15 Å of vacuum in the direction perpendicular to the surface. We use a p(2x2) expansion of the surface unit cell for (111) and (100), and a p(2x1) expansion for (110). For each surface, this expansion results in a termination of four surface oxygen atoms on each side of the slab per unit cell and 4 Ce atoms in the layer below. Mirrored slabs of 12 atomic layers ($Ce_{16}O_{32}$) for the (111), 7 atomic layers ($Ce_{14}O_{28}$) for the (110), and 9 atomic layers (Ce_8O_{16}) for the (100) were chosen to model the CeO_2 surface, with slab sizes chosen to converge surface formation energy and vacancy formation energy with respect to slab thickness. A p(2x2) expansion of the (110) surface is used for consideration of an adsorbed Pd_4 cluster, as this larger unit cell is necessary to minimize interaction between adjacent clusters. To maintain the CeO_2 stoichiometry of the (100) unit cell, half of the oxygen atoms on each side of the slab were removed, as similarly addressed in previous DFT work done on ceria (100).[31, 32] Mirrored slabs were used specifically to minimize slab to slab interactions that may result from a large net surface dipole moment upon formation of surface oxygen vacancies.

The lattice parameters of bulk face-centered cubic Pd metal, bulk Palladium (II) oxide (PdO), and bulk Palladium (IV) oxide (PdO_2) were optimized and each was within 2% of its corresponding experimentally determined value.[52, 53] Adsorption of Pd atoms as well as single PdO and PdO_2 units was considered over all possible sites on each CeO_2 termination, and the energy of the most exothermic adsorption configuration on each surface is used in all relative stability evaluations. A cluster of 4 Pd atoms was optimized, and adsorption was considered over each surface termination. Figure 3-1 illustrates the sites for which Pd adsorption was considered and Figure 3-2 displays the optimized structures for Pd_4 adsorption. Figure 3-3 displays the optimized structures for PdO and PdO_2 adsorption on each CeO_2 surface. Figure 3-4 details the insertion sites for Pd atoms into void spaces in the CeO_2 (111) and (110) surfaces. Structures with Pd incorporated into Ce positions at the surface are illustrated in a previous publication.[25] Incorporated structures with one oxygen vacancy per Pd atom are illustrated in the same study, and structures with two oxygen vacancies per incorporated Pd atom are shown in Figure 3-5.

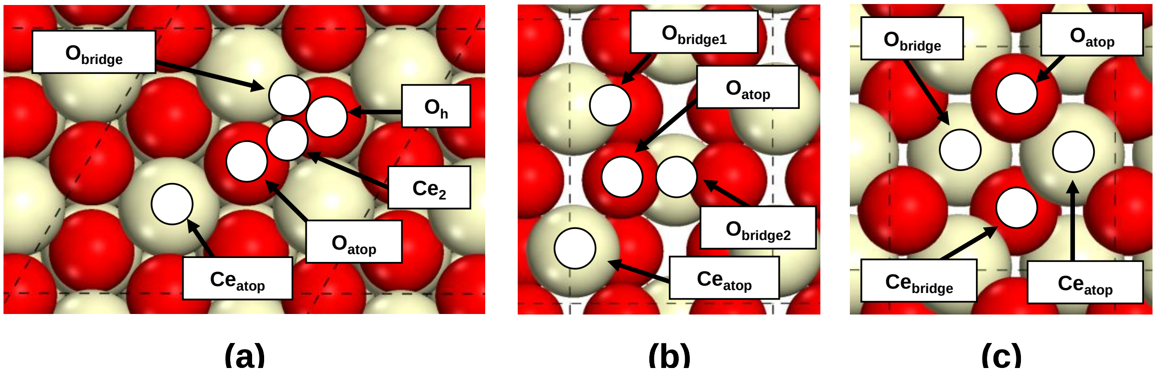

Figure 3-1. Adsorption sites for Pd on CeO_2(111) surface (a), (110) surface (b), and (100) surface (c). Tan (light) spheres represent cerium atoms and red (dark) spheres represent oxygen atoms.

3.2.3 Adsorption and Insertion Energy Calculation

We calculated the energy of palladium adsorption from the following formula:

$$\Delta E_{ads} = \frac{E_{Pd*} - \left(E_{CeO_2(\#\#\#)} + 2E_{Pd}\right)}{2} \qquad (1)$$

where E_{Pd*} is the energy of a given surface slab with an adsorbed Pd adatom on each side, $E_{CeO_2(\#\#\#)}$ is the energy of the clean slab, and E_{Pd} is the energy of a gas-phase Pd atom. A single gas-phase Pd atom was placed within a 15 Å x 15 Å x 15 Å unit cell to determine its DFT energy. The insertion energy for Pd into the CeO_2 lattice was calculated similarly by:

$$\Delta E_{ins} = \frac{E_{Pd/ins} - \left(E_{CeO_2(\#\#\#)} + 2E_{Pd}\right)}{2} \qquad (2)$$

where $\mathbf{E_{Pd/ins}}$ is the energy of a given surface slab with a Pd atom inserted into the void space beneath the surface atomic layer (see Figure 3-4a, b) of each side of the slab.

3.2.4 Relative Stability of PdO_x-CeO_2 Systems

When Pd is incorporated in the CeO_2 lattice, or PdO_x is supported, direct comparison with adsorbed and inserted configurations is complicated by the change in oxidation state and removal of a Ce atom. Comparison of the free energy among the adsorbed, inserted and incorporated structures, for a given CeO_2 termination, is done by expressing a system chemical potential $\mathbf{G_{system}}$ with a consistent reference:

$$G_{system} = \frac{\left\lfloor E_x + n_O\mu_O + n_{Pd}\mu_{Pd} + n_{PdO}\mu_{PdO} + n_{CeO_2}\mu_{CeO_2} \right\rfloor - \left\lfloor E_{CeO_2(\#\#\#)} + 2\mu_{PdO_2} \right\rfloor}{2} \quad (3)$$

where E_x is the VASP calculated energy of the Pd adsorbed/inserted/incorporated CeO_x surface and $E_{CeO_2(\#\#\#)}$ is the energy of the bare ceria surface (# = 1 or 0, depending upon surface termination). The μ_{Pd}, μ_{PdO}, μ_{PdO_2}, μ_{CeO_2} values represent the chemical potential of bulk Pd, PdO, PdO_2, or CeO_2 species, respectively, and μ_O is the free energy of oxygen which is described in detail later. Bulk solid chemical potentials are taken from optimized DFT structures, and therefore neglect entropic and enthalpic (T≠0) corrections, consistent with the treatment of surface structures.[54] The "n" values are set to balance the stoichiometry relative to a fully oxidized system, namely the CeO_2 surface slab and bulk PdO_2. The relative free energy is calculated for each system by subtracting the energy of this fully oxidized system, $\left\lfloor E_{CeO_2(\#\#\#)} + 2\mu_{PdO_2} \right\rfloor$. The free energy ($G_{system}$) is calculated, using equation 3, for each configuration from the following formulas:

Pd adsorbed:

$$G_{system} = \frac{E_{Pd*} + 4\mu_O - \left\lfloor E_{CeO_2(\#\#\#)} + 2\mu_{PdO_2} \right\rfloor}{2} \quad (4)$$

Pd inserted:

$$G_{system} = \frac{E_{Pd/ins} + 4\mu_O - \left\lfloor E_{CeO_2(\#\#\#)} + 2\mu_{PdO_2} \right\rfloor}{2} \quad (5)$$

Pd incorporated:

$$G_{system} = \frac{E_{Pd/inc} + 2\mu_{CeO_2} - \left\lfloor E_{CeO_2(\#\#\#)} + 2\mu_{PdO_2} \right\rfloor}{2} \quad (6)$$

Pd incorporated w/ vacancy:

$$G_{system} = \frac{E_{Pd/inc/V_O} + 2\mu_{CeO_2} + 2\mu_O - \left\lfloor E_{CeO_2(\#\#\#)} + 2\mu_{PdO_2} \right\rfloor}{2} \quad (7)$$

Pd incorporated w/ 2 vacancies:

$$G_{system} = \frac{E_{Pd/inc/2V_O} + 2\mu_{CeO_2} + 4\mu_O - \left\lfloor E_{CeO_2(\#\#\#)} + 2\mu_{PdO_2} \right\rfloor}{2} \quad (8)$$

PdO adsorbed:

$$G_{system} = \frac{E_{PdO*} + 2\mu_O - \left\lfloor E_{CeO_2(\#\#\#)} + 2\mu_{PdO_2} \right\rfloor}{2} \quad (9)$$

PdO_2 adsorbed:

$$G_{system} = \frac{E_{PdO_2*} - \left\lfloor E_{CeO_2(\#\#\#)} + 2\mu_{PdO_2} \right\rfloor}{2} \quad (10)$$

CeO$_2$ + bulk Pd: $$G_{system} = \frac{E_{CeO_2(\#\#\#)} + 2\mu_{Pd} + 4\mu_O - \lfloor E_{CeO_2(\#\#\#)} + 2\mu_{PdO_2} \rfloor}{2} \quad (11)$$

CeO$_2$ + bulk PdO: $$G_{system} = \frac{E_{CeO_2(\#\#\#)} + 2\mu_{PdO} + 2\mu_O - \lfloor E_{CeO_2(\#\#\#)} + 2\mu_{PdO_2} \rfloor}{2} \quad (12)$$

CeO$_2$ + bulk PdO$_2$: $$G_{system} = \frac{E_{CeO_2(\#\#\#)} + 2\mu_{PdO_2} - \lfloor E_{CeO_2(\#\#\#)} + 2\mu_{PdO_2} \rfloor}{2} = 0 \quad (13)$$

For surfaces with Pd incorporated at Ce sites in the surface CeO$_2$ lattice, the energy of the surface cell is summed with the energy of 2 bulk CeO$_2$ units (Eqs. 6-8), to compensate for the removal of 2 Ce atoms from the unit cell, and maintain a stoichiometry relative to PdO$_2$ and CeO$_2$.

The free energy of oxygen atoms, μ_O, is calculated as a function of temperature (T), oxygen partial pressure (P_{O_2}), and cell potential ($U_{cathode}$-U_{anode}) for comparison with SOFC operating conditions. For non-electrochemical systems, setting the cell potential equal to zero represents a direct O$_2$ atmosphere rather than that linked by an SOFC electrolyte. Oxygen anions are formed at the cathode of a SOFC from the reduction of molecular oxygen:

$$\frac{1}{2}O_2 + 2e^- \leftrightarrow O^{2-}_{electrolyte} \quad (14)$$

Assuming that the cathode reaction as well as O^{2-} ion conduction are operating with zero overpotential (cell deviation from equilibrium potential only due to anodic overpotential), the free energy of O^{2-} anions is calculated by:

$$G_{O^{2-}_{electrolyte}} = \frac{G_{O_2}}{2} - 2 \cdot |e| \cdot U_{cathode} \quad (15)$$

where $U_{cathode}$ is the cathode potential, e is the elementary electron charge and G_{O_2} is the free energy of a gas-phase oxygen molecule. The free energy of an O$_2$ molecule was calculated as the sum of the DFT energy (E_{O_2}), zero-point vibrational energy (ZPVE), entropy calculated by statistical mechanics multiplied by temperature (TS), and a pressure-volume term (PV). The difference between this calculated free energy of O_2 and experimentally determined values is minimal, therefore DFT values were used for consistency. The free energy of oxygen at the anode μ_O, however, is not simply $\mu_{O^{2-}_{electrolyte}}$ but rather the sum $\left(\mu_{O^{2-}_{electrolyte}} - 2 \cdot \mu_{e^-}\right)$ as movement of the ion from the electrolyte to the anode is a 2 electron reduction in the SOFC environment. The free energy of an electron at the anode is simply $\mu_{e^-} = 2eU_{anode}$, and thus the free energy of O^{2-} can be expressed as a function of the overall cell potential:

$$G_{O^{2-}_{electrolyte}} = \frac{G_{O_2}}{2} - 2e(U_{cathode} - U_{anode}) \qquad (16)$$

This approach is similar to that employed by Mukherjee and Linic to examine H_2 oxidation at SOFC anodes.[55]

3.2.5 Surface Formation Energy

To compare between terminations we calculate the surface formation energy:

$$\Delta G_{surf} = \frac{E_x - (n_{CeO_2} \cdot \mu_{CeO_2} + n_{Pd} \cdot \mu_{Pd} + n_O \cdot \mu_O)}{2 \cdot A_{slab}} \qquad (17)$$

where A_{slab} is the surface area of the mirrored surface slab and μ_{CeO_2} and μ_{Pd} are the bulk chemical potentials of palladium and ceria, respectively. For Pd incorporated into the ceria surface, $n_O = 4$ and for all surfaces $n_{CeO_2} = (\#CeO_2 \text{ units in slab})$ and $n_{Pd} = (\#Pd \text{ units in slab})$. Whereas equation 3 is convenient for comparison among systems with the same surface termination, this surface formation energy facilitates direct comparison of single Pd atoms and PdO_x clusters supported on different surface terminations. Specifically, we evaluate whether ceria-palladium interactions alter the relative surface formation energies of the CeO_2 (111), (110), and (100) surfaces.

3.3 Results and Discussion

3.3.1 Pd, Pd_4, and PdO_x Adsorption on CeO_2 Surfaces

Adsorption of a Pd atom on the CeO_2 surface was considered over surface sites detailed in Figure 3-1(a-c). In some cases, optimization resulted in movement of the Pd atom to another adsorption site. Adsorption energies of Pd atoms, calculated via equation 1, are tabulated in Table 3-1 for all located stable adsorption sites.

Palladium adsorption on the CeO_2 (111) surface was most favorable on the O_h site, residing overtop a subsurface oxygen atom. The Pd atom sits 2.99 Å above a subsurface oxygen atom, and is positioned 0.48 Å horizontally away from being centered above this oxygen, towards a neighboring Ce atom. The adsorption energy for Pd on the O_h site on CeO_2 (111) is -1.78 eV, similar to that found by Yang et. al for Pd adsorption on the (111) surface at the O_h site.[33] All optimization attempts for Pd adsorption on the (111) surface resulted in convergence to either the O_h or O_{atop} geometry. Adsorption on the O_{atop} site results in a Pd atom positioned 1.99 Å directly above a surface oxygen atom, and is less favorable than the O_h site with an adsorption energy of -1.49 eV.

The most favorable site of Pd adsorption on the CeO_2 (110) surface is on the $O_{bridge2}$ site, bridged equidistant between two surface oxygen atoms. The Pd atom is positioned 2.12 Å from the two nearest oxygen, and the adsorption energy is -1.78 eV. The adsorption energy on the O_{atop} site is -1.68 eV, and attempted optimization on the Ce_{atop} site resulted in convergence to

Table 3-1. Adsorption energies and insertion energies for Pd atoms on $\mathrm{CeO_2}$(111), (110) and (100) surfaces.

Adsorption Energies

Surface/Site	E_{ads}(eV)
(111)/$\mathrm{O_{atop}}$	-1.49
(111)/$\mathrm{O_h}$	-1.78
(110)/$\mathrm{O_{atop}}$	-1.68
(110)/$\mathrm{O_{bridge2}}$	-1.78
(100)/$\mathrm{O_{bridge}}$	-3.28
(100)/$\mathrm{O_{atop}}$	-1.48
(100)/$\mathrm{Ce_{atop}}$	-1.75

Insertion Energies

Surface	E_{ins}(eV)
(111)	0.79
(110)	0.03

$\mathrm{O_{atop}}$ site is -1.68 eV, and attempted optimization on the $\mathrm{Ce_{atop}}$ site resulted in convergence to adsorption on the $\mathrm{O_{atop}}$ site. No stable adsorption configuration of a Pd atom on the $\mathrm{O_{bridge1}}$ site was found.

Optimization attempts for Pd adsorption on the $\mathrm{CeO_2}$ (100) surface resulted in convergence to the $\mathrm{O_{bridge}}$, $\mathrm{O_{atop}}$, and the $\mathrm{Ce_{atop}}$ sites. The most favorable adsorption occurs on the $\mathrm{O_{bridge}}$ site with an adsorption energy of -3.28 eV and the Pd atom positioned between two surface oxygen atoms. The $\mathrm{Ce_{atop}}$ site is the next most favorable site for Pd on the (100) surface, followed by the $\mathrm{O_{atop}}$ site.

Overall, the adsorption of single Pd atoms on the $\mathrm{CeO_2}$ surface is most favorable on the (100) surface termination. The strong adsorption on $\mathrm{CeO_2}$ (100) is due to interaction with oxygen atoms with lower coordination than surface oxygen atoms on the (111) or (110) surface. The surface formation energy of CeO_2 (100), 1.48 J/m^2, is much more endothermic than the (111) or (110) surfaces, 0.69 J/m^2 and 1.10 J/m^2 respectively,[25] and thus the (100) termination is less likely to be present in a given sample of CeO_2. The impact of Pd adsorption on the relative surface energies of the various CeO_2 terminations is discussed in Section 3.3.5. The energetics of Pd adsorption on the (111) and (110) surfaces are very similar, with Pd adsorption on all three surfaces dictated by the specific geometry of available adsorption sites and surface oxygen coordination environments.

Adsorption of a Pd_4 cluster was considered over each CeO_2 surface; optimal structures are shown in Figure 3-2. The Pd_4 cluster was optimized within a 15 Å x 15 Å x 15 Å unit cell, and is a tetrahedron with Pd-Pd nearest neighbor distances of 2.61 Å, similar to the structure of a gas-phase Pd_4 cluster determined by Nava et al. using DFT.[56] Adsorption of Pd_4 is most exothermic at a site on each surface which maximizes interaction of tetrahedral Pd atoms in the cluster with surface oxygen atoms. Substantial variations in the structure of the supported Pd_4 cluster from its gas phase optimal tetrahedral form were not considered. The relative energy of this state is discussed in Section 3.3.5.

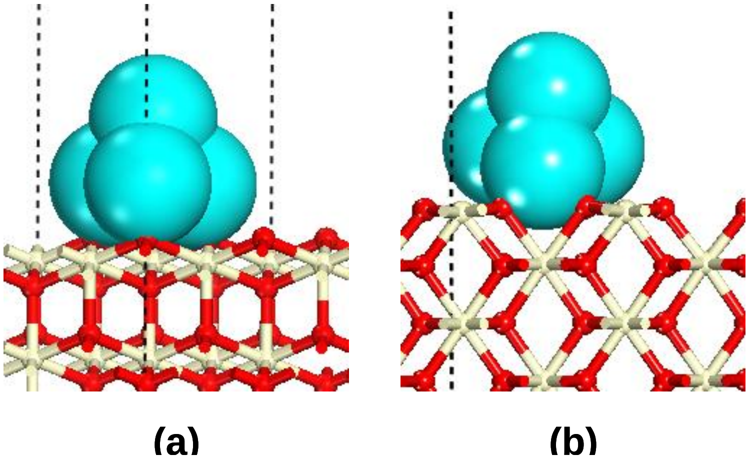

Figure 3-2. Optimized structure of Pd_4* on the CeO_2(111) surface (a) and (110) surface (b). Palladium atoms are represented in large space-filling format for emphasis, and Ce(tan, light) and O(red, dark) atoms are shown in ball and stick format.

Structures for PdO and PdO_2 adsorption on the CeO_2 surface were optimized by cutting PdO and PdO_2 units out of their respective bulk structures and considering various adsorption sites and configurations. The most exothermic adsorption for both PdO and PdO_2 on each surface occurs on sites where oxygen atoms interact with Ce atoms and Pd atoms interact with surface O atoms. Figure 3-3 displays the most favorable adsorption structures for PdO and PdO_2 on each CeO_2 termination. Adsorption of PdO on each surface results in contraction of Pd-O bond lengths by approximately 0.1-0.2 Å from the Pd-O distance in bulk PdO. Adsorption of PdO_2 on each surface results in contraction of Pd-O bond lengths by approximately 0.05-0.19 Å from the Pd-O distance in bulk PdO_2. Contraction of Pd-O bond lengths upon adsorption of PdO and PdO_2 units to the CeO_2 surface is attributed to the lower coordination environment of Pd in both of these systems with respect to bulk PdO and PdO_2.

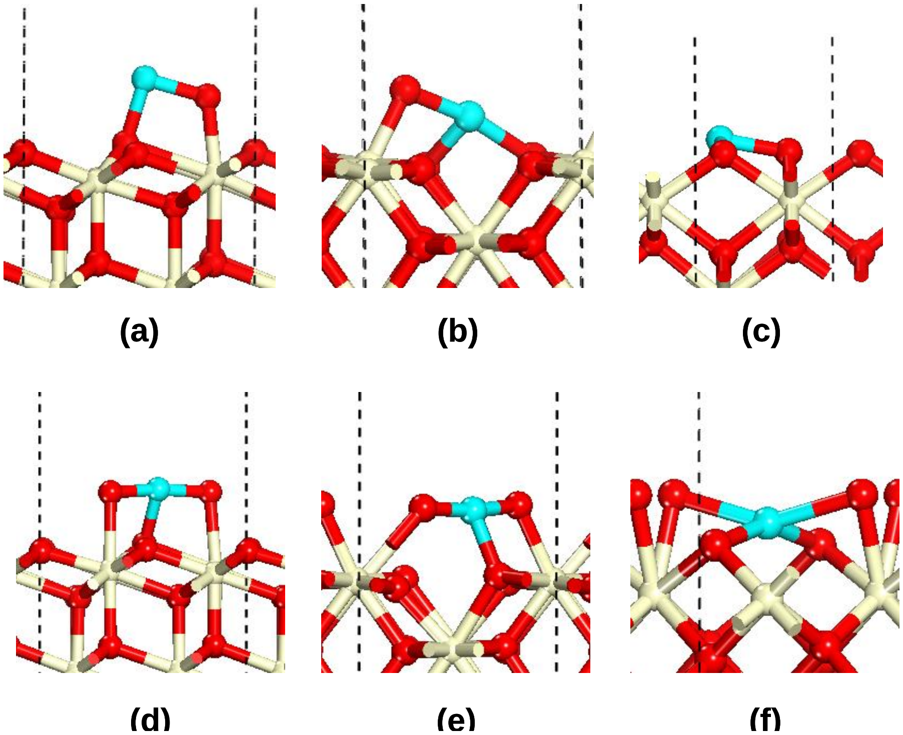

Figure 3-3. Optimal conformation of PdO* on the CeO_2(111) surface (a), (110) surface (b), (100) surface (c). PdO_2* on the CeO_2(111) surface (d), (110) surface (e), (100) surface (f). Ce atoms are tan (light), Pd atoms are blue (gray), and O atoms are red (dark).

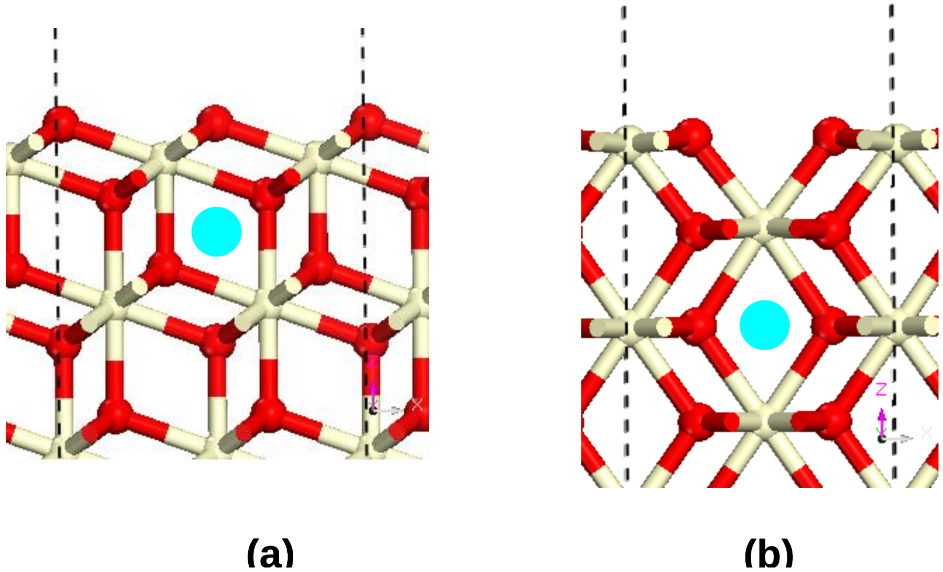

Figure 3-4. Insertion for Pd (blue, gray) in the CeO_2(111) surface (a), (110) surface (b).

3.3.2 Pd Insertion into CeO_2(111) and CeO_2(110)

Insertion of Pd atoms into void spaces beneath the CeO_2 surface was considered to evaluate the relative stability of interstitial Pd defects, similar to a previous study of Ni insertion into ceria.[42] The insertion energy of single Pd atoms into the void space beneath the first stoichiometric CeO_2 layer was calculated for the (111) and (110) surfaces. Insertion was not considered for the CeO_2 (100) surface as the specific geometry of the (100) termination results in insertion sites well below (~4 Å) the surface. Insertion is likely less probable due to this depth, but practically this depth requires thicker surface slabs than employed herein. Insertion energies for Pd into the CeO_2 (111) and (110) surfaces are tabulated in Table 3-1. Insertion into both the (111) and (110) surfaces is endothermic with reference to a single Pd atom in the gas phase, indicating that this state is substantially less thermodynamically favored over the adsorbed state. In considering relative energies via Eq. 3, palladium atoms inserted interstitially into the (110) surface is the highest energy state for this termination by more than 20 eV. For each surface, interstitial Pd atoms inserted beneath the surface CeO_2 layer is not favorable (high energy) mainly due to the close proximity between Pd and fully coordinated Ce and O atoms in the slab. The effective size of the interstitial space in CeO_2 is approximately 5 Å (estimated as the average between O-O and Ce-Ce nuclei distances across the space). The Van der Waals radii of Pd is approximately 1.94 Å,[57] and thus the effective diameter of Pd is near 4 Å which results in extremely close nearest neighbor distances when inserted.

3.3.3 Incorporation of Pd atoms into the CeO_2 surface

The incorporation of Pd atoms into Ce surface positions within the CeO_2 lattice was modeled by substituting a Pd atom into a Ce site in the Ce layer closest to the surface, on both sides of the mirrored slab, for each single crystal termination. Structures were optimized for Pd substituted into each surface at the MO_2 stoichiometry, and formation of one and two oxygen vacancies adjacent to the substituted Pd atom was considered. Our previous study indicated that oxygen vacancy formation energies are more exothermic for ceria surfaces with Pd incorporated,[25] and the structures used for Pd incorporation are identical to those in this previous study. Only one vacancy per unit cell was considered for the (100) surface, as the formation of 2 vacancies would result in a fully reduced Ce terminated slab. The intact and one vacancy structures for the Pd-substituted ceria surfaces used in this study are detailed and displayed in our previous study,[25] and 2 vacancy structures for the (111) and (110) surfaces are displayed in Figure 3-5.

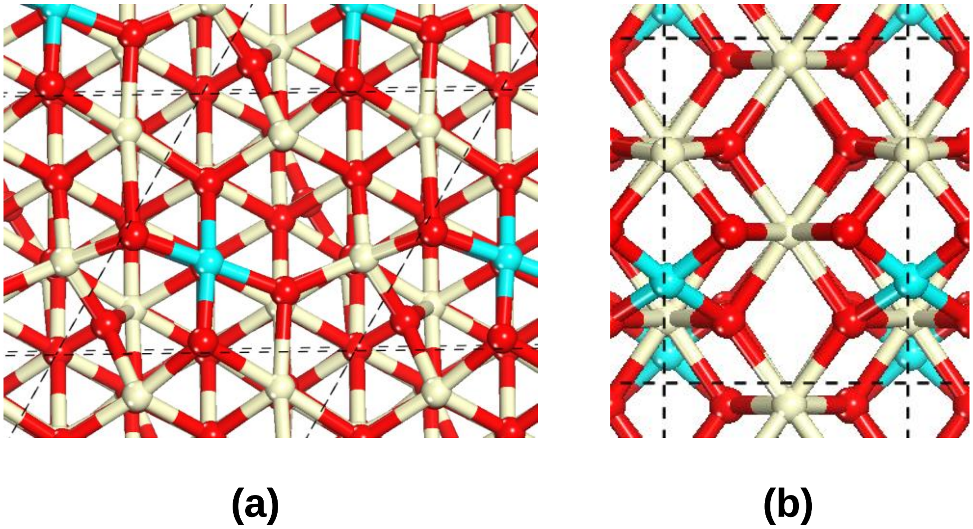
(a) (b)

Figure 3-5. The Pd/inc/2V_O surface for the CeO_2(111) termination(a), and (110) termination (b). Ce atoms are tan (light), Pd atoms are blue (gray), and O atoms are red (dark).

3.3.4 Relative Stability of Different States of Pd atoms on CeO_2 Surfaces

The relative stability of single Pd atoms incorporating into the CeO_2 surface versus remaining as single atom adsorbates, inserted atoms, single PdO_x unit adsorbates, bulk palladium metal or palladium oxides, has been evaluated using equation 3. Table 3-2 lists the DFT energy for each non-surface species and Table 3-3 lists the DFT energy for each surface slab used in our calculations. The chemical potential of oxygen, μ_O, as a function of temperature and pressure evaluated as per statistical mechanics is available as Supporting information and compared with experimental data.[57] From the data supplied in Tables 3-2 and 3-3, the Supporting information, and Equation 3, the relative stability of different structures can be calculated at any temperature, partial pressure of oxygen, and cell potential. The relative energy of each Pd state at 973 K is plotted in Figure 3-3, as a function of overall cell potential as described earlier, and also as a function of partial pressure of oxygen. The equilibrium cell potential of a solid oxide fuel cell can be expressed through the Nernst Equation as a function of the partial pressure of oxygen at the cathode and at the anode:

$$E = \left(\frac{RT}{2F}\right) \cdot \ln\left[\frac{\left(P^{O_2}_{cathode}\right)^{\frac{1}{2}}}{\left(P^{O_2}_{anode}\right)^{\frac{1}{2}}}\right] \qquad (19)$$

In Figures 3-6(a), 3-7(a), and 3-8(a), $\left(P^{O_2}_{cathode}\right)$ is set to atmospheric conditions (0.21 atm), in determining the U_{cell} axis value, for comparison with SOFC operating conditions.

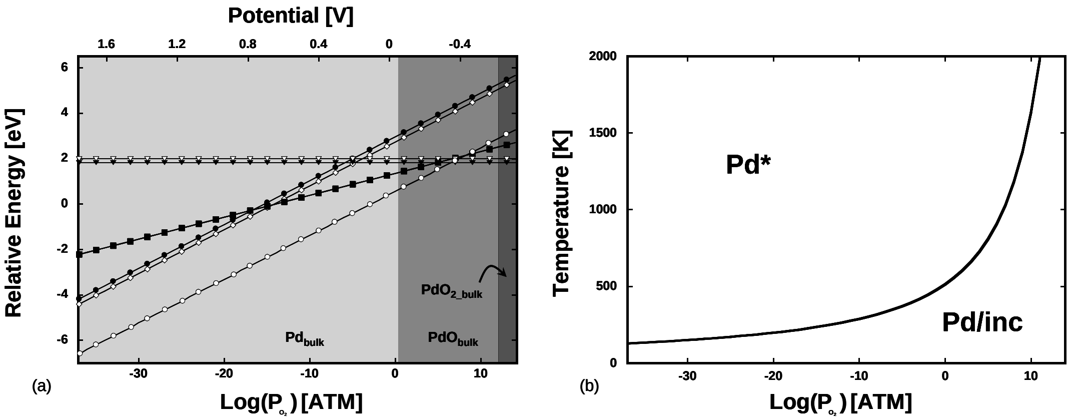

Figure 3-6. The relative stability of Pd-ceria(111) surface configurations (a) and phase diagram for most stable single Pd atom states on the (111) surface (b). Data in (a) is labeled as follows: (◊) Pd/ins, (▼) Pd/inc, (■) Pd/inc/V_O, (●) Pd/inc2V_O, (□) PdO*, (▽) PdO_2*, (○) Pd*.

The CeO_2(###)+Pd_{bulk} state, where the energies of Pd_{bulk} and each CeO_2 surface slab are calculated separately, can be considered as an approximation of extremely large Pd particles. The chemical potential of this state is unaffected by support interactions as well as the surface formation energy of facets on the particle. Similarly, the CeO_2(###)+PdO_{2_bulk} and CeO_2(###)+PdO_{bulk} states are an approximation of extremely large oxidized palladium particles. The bulk Pd-PdO-PdO_2 phase diagram is therefore independent of surface termination, and is displayed in Figure 3-3 as shaded regions of oxygen pressure and potential where either Pd, PdO

Table 3-2. DFT+U energy calculated for reference species used in calculating relative free energies (Eq. 3) and surface formation energies (Eq. 17).

Structure	DFT(+U) Energy (eV/formula unit)
$O_{2\_molecule}$	-9.82
Pd_{atom}	-1.49
$Pd_{particle}$	-3.17
Pd_{bulk}	-5.07
PdO_{bulk}	-11.11
PdO_{2_bulk}	-16.01
CeO_{2_bulk}	-24.58

and PdO_2 is the most stable species. At 973 K, bulk Pd metal is stable at all partial pressures of oxygen below 1 atm (galvanic cell potentials above -0.03 V). Between 1 atm and 10^{12} atm, bulk PdO is stable and PdO_2 becomes stable at oxygen pressures above 10^{12} atm. At lower temperatures, the transitions between Pd → PdO and PdO → PdO_2 occur at lower partial pressures of oxygen. The lowest free energy state for Pd on the CeO_2 surface at any cell potential or partial pressure of oxygen is that of a large particle of Pd, PdO or PdO_2 for any surface termination. The transition between bulk Pd and PdO as a function of temperature and partial pressure of oxygen was evaluated experimentally by Zhang et al.[58] using X-ray diffraction (XRD) and thermal gravimetric analysis (TGA). These authors determine that the PdO → Pd transition occurs at approximately 1050 K for 0.1 atm O_2, whereas we calculate the transition temperature as 877 K for 0.1 atm O_2. Our calculated values for the phase transition temperature at varying O_2 pressures match the experimental slope, indicating a constant error. Our values for transition temperature are approximately 180 K lower than the experimental values over this pressure range, which represents a 0.28 eV free energy difference per palladium atom in the bulk. This difference is due to the fact that we have only considered the internal energy of each bulk phase,

Table 3-3. DFT calculated energies for each surface system, used with data in Table 2, oxygen chemical potentials (tabulated in Supporting Information), and equations 3 and 17 to determine relative free energies and surface formation energies.

System	DFT(+U) Energy
$CeO_2(111)$	-388.85
$CeO_2(110)$	-338.35
$CeO_2(100)$	-191.22
$Pd^*/CeO_2(111)$	-395.41
$Pd^*/CeO_2(110)$	-344.91
$Pd^*/CeO_2(100)$	-200.77
$Pd_{ins}/CeO_2(111)$	-391.05
$Pd_{ins}/CeO_2(110)$	-291.67
$Pd_{inc}/CeO_2(111)$	-368.06
$Pd_{inc}/CeO_2(110)$	-317.57
$Pd_{inc}/CeO_2(100)$	-172.52
$CeO_{2-x}(111)$	-373.52
$CeO_{2-x}(110)$	-324.33
$CeO_{2-x}(100)$	-176.87
$Pd_{inc}/CeO_{2-x}(111)$	-356.82
$Pd_{inc}/CeO_{2-x}(110)$	-307.92
$Pd_{inc}/CeO_{2-x}(100)$	-162.80
PdO*/CeO2(111)	-406.00
PdO*/CeO2(110)	-358.9
PdO*/CeO2(100)	-212.09
PdO_2^*/CeO2(111)	-416.88
PdO_2^*/CeO2(110)	-367.83
PdO_2^*/CeO2(100)	-220.99

and neglected zero-point vibrational energy corrections. Configurational entropy terms are not considered in comparing the separated bulk phases and the single Pd atom structures.

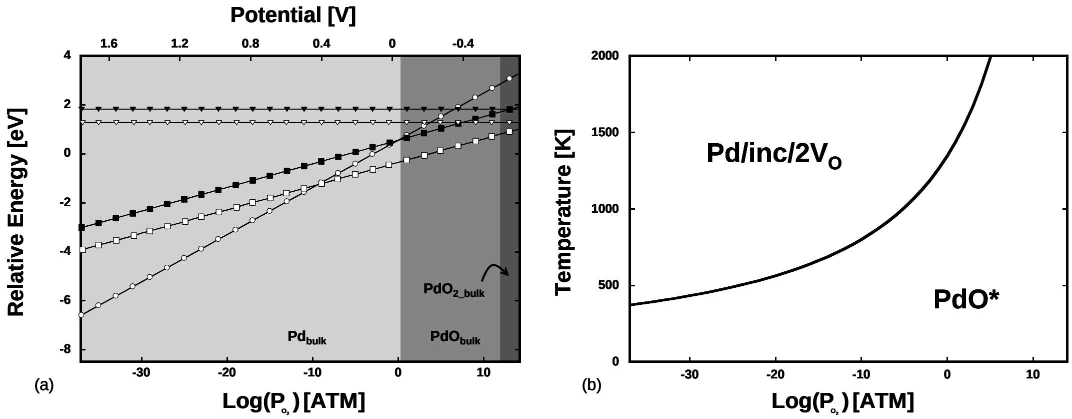

Figure 3-7. Relative stability of Pd-ceria (110) surface configurations (a) and phase diagram for most stable single Pd atom states on the (110) surface (b). Data in (a) is labeled as follows: (◊) Pd/ins, (▼) Pd/inc, (■) Pd/inc/V_O, (●) Pd/inc2V_O, (□) PdO*, (▽) PdO_2*, (○) Pd*).

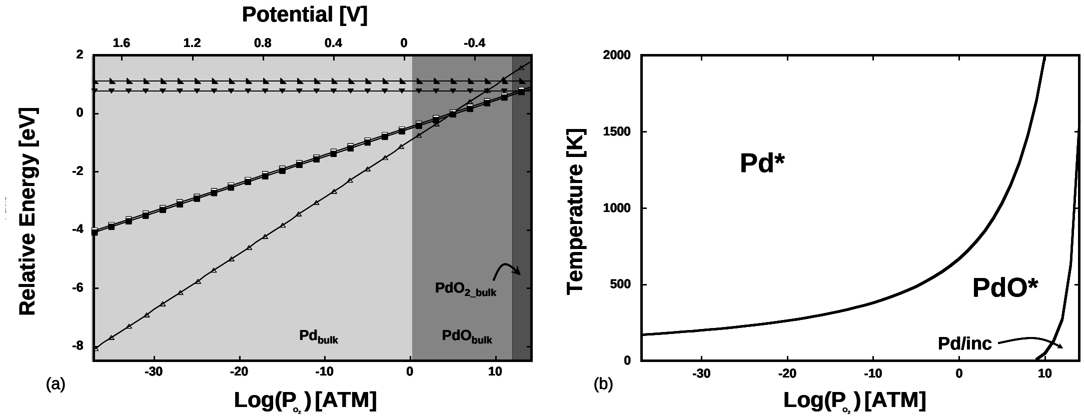

Figure 3-8. Relative stability of Pd-ceria (100) surface configurations (a) and phase diagram for most stable single Pd atom states on the (100) surface (b). Data in (a) is labeled as follows: (◊) Pd/ins, (▼) Pd/inc, (■) Pd/inc/V_O, (●) Pd/inc2V_O, (□) PdO*, (▽) PdO_2*, (○) Pd*).

Figures 3-6, 3-7, and 3-8 displays the relative energy for each ceria surface with single Pd atoms in different states. The relative energy is plotted in Figures 3-6(a), 3-7(a), and 3-8(a) as a function of partial pressure of oxygen and cell potential. At any given potential and pressure, the species with the lowest free energy is the most favorable (stable) state of Pd on the ceria surface. States which share the same formal oxidation state of palladium (either Pd^0, Pd^{2+}, or Pd^{4+}) have the same slope on each plot as they share the same number of oxygen. As the cell potential decreases or equivalently the partial pressure of oxygen increases, oxidized Pd species become more stable than reduced species for all systems. The data in Figures 3-6(a), 3-7(a) and 3-8(a) is for 973 K; as temperature decreases, oxidized species become relatively more stable (lower free energy) and thus temperature influences at what pressure and potential the transition between different stable states of Pd occurs. The relative energy between states with the same Pd oxidation state, as calculated herein, is not a function of T, P_{O_2} , or cell potential. Figures 3-6(b), 3-7(b), 3-8(b) display phase diagrams of the regions of T and P_{O_2} where each most stable single Pd atom state is favored for each ceria surface.

3.3.4.1 Stability of Single Pd States on the CeO_2(111) Surface

Figure 3-6(a) displays the relative energy of single Pd states on the ceria (111) surface. The Pd* state is the most stable Pd^0 state, Pd/incV_O and PdO* are nearly equal in energy as the favored Pd^{2+} states, and Pd/inc is the most stable Pd^{4+} state. At 973 K and below 10^7 atm O_2 (above -0.37 V), the lowest energy state of single Pd atoms on the CeO_2 (111) surface is as adsorbed adatoms. The strong interaction of Pd adatoms with oxygen of the ceria lattice stabilizes the reduced state over a greater range of conditions than for bulk Pd/large Pd particles, consistent with thermal gravimetric analysis (TGA) results which show that the reduction temperature for PdO → Pd is lowered when PdO is supported on CeO_2.[59] Above 10^7 atm O_2 (below -0.37 V; outside the galvanic cell range), single Pd atoms are lowest energy as incorporated into the CeO_2 lattice at Ce sites. This result suggests that for oxygen pressures above 10^7 atm the formation of a mixed palladium-ceria oxide at the (111) surface of CeO_2 is possible. Therefore, at 973 K an extreme pressure of O_2 is necessary to oxidize single adsorbed Pd atoms. At temperatures lower than 973 K, the formation of a mixed palladium-ceria oxide on the (111) termination is thermodynamically favorable at higher cell potentials and lower oxygen pressures. At 298 K and oxygen partial pressures above 10^{-10} atm (or cell potentials less than 0.14 V, the formation of this mixed surface oxide is thermodynamically favorable compared to other single Pd atom states. Figure 3-6(b) shows that below 500 K, oxygen pressures below atmospheric are sufficient to stabilize Pd/inc. Palladium is only favorable as single atoms in the Pd^0 (adsorbed) and Pd^{4+} (incorporated) oxidation states on the (111) CeO_2 termination.

Other conclusions can be drawn from the relative energy calculations for Pd on the CeO_2 (111) surface. The energy difference between PdO adsorbed and Pd incorporated into the CeO_2 lattice with an adjacent oxygen vacancy (0.01 eV) is negligible, though neither Pd^{2+} state has a stable range of temperature and pressure. The energy difference between PdO_2 adsorbed and Pd incorporated into CeO_2 at the MO_2 stoichiometry is 0.17 eV. At 973 K and 10^7 atm O_2 (0.37 V), the energies of Pd incorporated into the surface, adsorbed as a Pd adatom, incorporated with a vacancy, adsorbed as PdO, and adsorbed as PdO_2 are all within a range of 0.18 eV. Near this potential and oxygen pressure, an equilibrated distribution will contain populations of a variety of states. These results suggest that strong interactions between Pd atoms and the ceria support can result in the formation of oxidized Pd states on the ceria (111) surface including incorporation to form a mixed surface oxide. Figure 3-6(b) displays the range of temperatures and oxygen pressures for which this mixed oxide is the most stable single Pd atom state on CeO_2(111).

3.3.4.2 Stability of Single Pd States on the CeO_2(110) Surface

Figure 3-7(a) displays the relative energy of single Pd states on the ceria (110) surface. The lowest energy state of Pd^0 atoms for the CeO_2 (110) surface is Pd incorporated into the surface with two adjacent oxygen vacancies, whereas PdO* and PdO_2* are the most stable Pd^{2+} and Pd^{4+} oxidation states, respectively. This state is the most stable oxidation state at 973 K and oxygen pressures below 10^{-5} atm O_2 (above 0.21 V). Thus, at high cell potentials and low partial pressures of oxygen, a highly reduced (110) termination with Pd incorporated in the ceria surface is the most stable configuration. At pressures above 10^{-5} atm O_2 (below 0.21 V), adsorbed PdO is the lowest energy state, and at low cell potentials (>10^{15} atm O_2) adsorbed PdO_2 is the lowest energy. It is favorable for Pd atoms on the ceria (110) surface to incorporate and form a reduced (relative to the MO_2 stoichiometry) mixed oxide at low oxygen pressures, however as the partial pressure of oxygen increases, supported palladium oxide PdO_x species are more favorable than incorporated species. Palladium atoms supported on (110) termination of ceria are favorable in all three possible formal oxidation states, and as the partial pressure of oxygen increases the favored state transitions from Pd^0 (Pd/inc/2V_O) to Pd^{2+} (PdO*) to Pd^{4+} (PdO_2*).

The relative energy calculations for the (110) surface show that Pd incorporation into the CeO_2 (110) surface with MO_2 stoichiometry (formally as Pd^{4+}) is not favorable under any conditions. Incorporation into the reduced CeO_2 (110) surface is the lowest energy state at low partial pressures of oxygen (<10^{-5} atm), and is favorable with respect to single supported (adsorbed) Pd atoms by 0.36 eV. Figure 3-7(b) highlights at what temperatures and oxygen pressures Pd/inc/2V_O and PdO* are stable, with a narrow region at high pressures and low temperatures within which PdO_2* is stable. This result highlights the surface dependence of preferred states of deposited palladium on ceria, as a highly reduced mixed oxide is favored for the (110) termination, whereas under similar conditions single adsorbed Pd atoms are preferred on the (111) termination.

3.3.4.3 Stability of Single Pd States on the CeO_2(100) Surface

Figure 3-8(a) displays the relative energy of single Pd states on the ceria (100) surface. The Pd* state is the most stable Pd^0 state, PdO* and Pd/incV_O are very close in energy (~0.07 eV) as Pd^{2+} states, and Pd/inc is the most stable Pd^{4+} state. Single supported (adsorbed) Pd atoms are stable at potentials below 10^5 atm O_2 (above -0.27 V). Single supported Pd atoms are also only 0.30 eV higher in energy than a separated bulk Pd and CeO_2 (100) system, due to the strong adsorption of Pd to the (100) surface (1.5eV more exothermic than other terminations). This result suggests that, compared to the other ceria surface terminations studied, the (100) surface stabilizes dispersed Pd atoms. From 10^5 atm O_2 (-0.27 V) to 10^{13} atm O_2 (-0.66 V), PdO* is the most stable single Pd atom system, 0.07eV lower in energy than Pd/incV_O. Below -0.66V (above 10^{13} atm O_2), Pd incorporated into the ceria (100) surface with MO_2 stoichiometry is the lowest energy single Pd atom state.

Oxygen pressures of over 10^5 atm have to be reached to oxidize adsorbed Pd adatoms on the CeO_2 (100) surface. At temperatures less than 973 K, the point at which PdO species become favored will occur at lower oxygen partial pressures (10^{-25} atm O_2 at 298K). At low partial pressures of oxygen, Pd is favorable to occupy the Pd^0 formal oxidation state, and as the partial pressure of oxygen is increased Pd^{2+} is favorable as PdO^* and at even higher oxygen pressures Pd^{4+} as a mixed surface oxide, as shown in Figure 3-8(b).

3.3.5 Surface Formation Energies

The surface formation energies for each bare pure CeO_2 surface and for each surface containing single palladium atoms, in different formal oxidation states, are tabulated in Table 3-4. Whereas the results in the previous section provide for comparison between Pd states on a single ceria termination, surface energy comparison provide for stability comparison among Pd oxidation states across surface terminations. The surface energy calculated by equation 17 is listed for the (111) termination for pure CeO_2 at 973 K and 1 atm O_2, Pd*/CeO_2 (formally Pd^0), PdO*/CeO_2 (formally Pd^{2+}), and Pd/inc (formally Pd^{4+}). All other surface energies, listed in italics, are relative to the value within the same formal Pd oxidation state. For example, the energy for Pd/ins on CeO_2(110) in Table 4 is calculated as

$$\text{Relative Energy} = \Delta G_{\text{surf\_Pd/ins}(111)} - \Delta G_{\text{surf\_Pd*}(111)} \qquad (18)$$

Table 3-4 lists each surface energy calculated at 973 K and 1 atm O_2, however only the relative energies between Pd configurations of different oxidation states are a function of temperature and oxygen pressure.

The relative stability of the various surface terminations (111 vs. 110 vs. 100) is not altered, in most cases, due to interaction with Pd species. However, surface energy differences between terminations are reduced due to Pd interaction. For example, the bare (100) surface has a surface formation energy 0.78 J m^{-2} greater than the (111) surface, however this difference is only 0.37 J m^{-2} for Pd* due to the stronger bonding of Pd to the CeO_2 (100) surface. Exceptions include that the adsorption of PdO* on (110) becomes the most stable surface for the Pd^{2+} oxidation state, though the Pd^{2+} oxidation state is not the most favorable single atom state on the (111) surface in any temperature or oxygen pressure range. In all other cases of Pd interaction with the ceria surface, the trend of surface formation energies of $111 < 110 < 100$ is maintained.

Table 3-4. Surface formation energies for single Pd atom species on ceria, calculated at 973K and 1 atm. Italicized values are relative within each Pd oxidation state to species on the (111) surface. The non-italicized values are given in J m^{-2}.

Surface Formation Energies (J/m^2)			
	CeO_2		
	111	110	100
bare surface	0.7	*+0.4*	*+0.78*
	Pd^0/CeO_2		
Pd*	1.26	*+0.52*	*+0.37*
Pd/ins	*+0.68*	*+10.59*	*N/A*
Pdinc/2Vo	*+0.75*	*+0.38*	*N/A*
	Pd^{2+}/CeO_2		
PdO*	1.51	*-0.07*	*+0.36*
Pdinc/Vo	*0*	*+0.27*	*+0.39*
	Pd^{4+}/CeO_2		
Pd/inc	1.66	*+0.60*	*+0.91*
PdO2*	*+0.05*	*+0.39*	*+1.10*

3.3.6 Relative Energy of Pd_4 clusters

The adsorption of Pd_4 clusters on the ceria surface was considered to compare the relative stability of single atoms versus a larger palladium cluster. To compare the relative energy of this small supported palladium particle to single atoms, we calculate the energy for the following reaction:

$$4\mathrm{Pd}^* \rightarrow \mathrm{Pd}_4^* \quad (20)$$

where Pd* is a single adsorbed palladium atom on the ceria surface and Pd_4* is an adsorbed Pd cluster. To calculate this reaction energy, we construct a thermochemical cycle such that the reaction energy is the sum of the Pd atom desorption energy, gas-phase particle cohesive energy, and adsorption energy of the Pd_4 cluster. We calculate the gas-phase cohesive energy for the Pd_4 particle:

$$\Delta E_{coh} = \frac{\left(E_{Pd_4} - 4E_{Pd}\right)}{4} \qquad (21)$$

where E_{Pd_4} is the DFT energy of the Pd_4 cluster and E_{Pd} is the DFT energy of a single gas phase palladium atom. The cohesive energy of the Pd_4 tetrahedron is -1.68 eV, similar to the value of -1.63 eV found by Nava et al.[56] We also calculate the adsorption energy of Pd_4 per Pd atom in the cluster on each termination:

$$\Delta E_{ads} = \frac{E_{Pd_4*} - \left(E_{CeO_2(\#\#\#)} + 2E_{Pd_4}\right)}{8} \qquad (22)$$

where E_{Pd_4*} is the DFT energy of the ceria surface slab with Pd_4 adsorbed on each side. The reaction energy for equation 20 is calculated by

$$\Delta E_{4Pd* \to Pd_4*} = 4 \cdot \left[\Delta E_{ads}(Pd_4) - \Delta E_{ads}(Pd)\right] + 4 \cdot \Delta E_{coh} \qquad (23)$$

For the (111) surface, this reaction energy is exothermic (-2.45 eV), showing that small clusters of palladium atoms supported on the CeO_2 (111) surface are favorable to single supported atoms. This reaction energy is more exothermic for the (110) surface termination (-2.75 eV), due to more exothermic adsorption of Pd_4 to the surface. We did not consider oxidized Pd clusters on the ceria surface, nor do we include configurational entropy considerations, but these results do illustrate that the strong Pd-support interactions do not provide sufficient stability to anchor reduced Pd* single atoms on the (111) or (110) surface.

3.4 Conclusions

The DFT+U method and *ab initio* thermodynamics were used to evaluate the stability of Pd atoms, PdO_x species, and small Pd particles in varying configurations on ceria surfaces. Palladium incorporation to form a mixed surface oxide with MO_2 stoichiometry is thermodynamically favorable versus other single atom states of Pd on the ceria (111) surface at certain partial pressures of oxygen and temperatures. At room temperature (298 K), this palladium incorporation is favorable at oxygen pressures of greater than 10^{-10} atm. It is favorable for palladium atoms on CeO_2 (110) to incorporate into the surface in a reduced stoichiometry, $MO_{2-x,}$ at low partial pressures of oxygen ($<10^{-5}$ atm at 973 K), and to remain as supported palladium (II) oxide (PdO) species at higher oxygen pressures. Incorporation is favorable for palladium on the (100) termination of ceria at high partial pressures of oxygen ($>10^{13}$ atm at 973 K).

The relative stability of small Pd particles on the ceria surface was investigated by considering Pd_4 clusters. The method used herein can be used to evaluate the relative stability of supported catalysts of varying composition as a function of temperature and oxygen pressure. We show that temperature, oxygen pressure, and cell potential in an solid oxide fuel cell can influence the stable states of palladium supported on ceria surfaces, thus providing insight into structural stability during catalytic operation.

ACKNOWLEDGMENT: Acknowledgement is made to the Donors of the American Chemical Society Petroleum Research Fund #46724-G5 for support of this research.

3.5 References

(1) Trovarelli, A.; Leitenburg, C. d.; Boaro, M.; Dolvetti, G. *Catal. Today* **1999**, *50*, 353-367.

(2) Xiao, L.; Sun, K.; Xu, X.; Li, X. *Catalysis Communications* **2005**, *6*, 796-801.

(3) An, S.; Lu, C.; Worrell, W. L.; Gorte, R. J.; Vohs, J. M. *Solid State Ionics* **2004**, *175*, 135-138.

(4) Gorte, R. J.; Vohs, J. M.; McIntosh, S. *Solid State Ionics* **2004**, *175*, 1-6.

(5) McIntosh, S.; Gorte, R. J. *Chem. Rev.* **2004**, *104*, 4845-4865.

(6) McIntosh, S.; Vohs, J. M.; Gorte, R. J. *Electrochem. Solid-State Lett.* **2003**, *6*, A240-A243.

(7) Putna, E. S.; Stubenrauch, J.; Vohs, J. M.; Gorte, R. J. *Langmuir* **1995**, *11*, 4832-4837.

(8) Badri, A.; Binet, C.; Lavalley, J. C. *Journal of the Chemical Society, Faraday Transactions* **1996**, *92*, 1603-1608.

(9) Haack, G. *Catal. Lett.* **2000**, *67*, 99-105.

(10) Holles, J. H.; Davis, R. J.; Murray, T. M.; Howe, J. M. *J. Catal.* **2000**, *195*, 193-206.

(11) Jen, H. W.; Graham, G. W.; Chun, W.; McCabe, R. W.; Cuif, J. P.; Deutsch, S. E.; Touret, O. *Catal. Today* **1999**, *50*, 309-328.

(12) Matsumura, W. *Phys. Chem. Chem. Phys.* **2000**, *2*, 1519-1522.

(13) Shen, W.; Kobayashi, A.; Ichihashi, Y.; Matsumura, Y.; Haruta, M. *Catal. Lett.* **2001**, *73*, 161-165.

(14) Wang, X. G., R.J.; Wagner, J.P. *J. Catal.* **2002**, *212*, 225-230.

(15) Matsumura, Y.; Shen, W.; Ichihashi, Y.; Ando, H. *Catal. Lett.* **2000**, *68*, 181-183.

(16) Shen, W.-J.; Matsumura, Y. *Journal of Molecular Catalysis A: Chemical* **2000**, *153*, 165-168.

(17) Nagai, Y.; Hirabayashi, T.; Dohmae, K.; Takagi, N.; Minami, T.; Shinjoh, H.; Matsumoto, S. i. *J. Catal.* **2006**, *242*, 103-109.

(18) Fu, Q.; Saltsburg, H.; Flytzani-Stephanopoulos, M. *Science* **2003**, *301*, 935-938.

(19) Pierre, D.; Deng, W.; Flytzani-Stephanopoulos, M. *Topics in Catalysis* **2007**, *46*, 363-373.

(20) Luo, M.; Hou, Z.; Yuan, X.; Zheng, X. *Catal. Lett.* **1998**, *50*, 205-209.

(21) Li, J.; Singh, U. G.; Bennett, J. W.; Page, K.; Weaver, J. C.; Zhang, J. P.; Proffen, T.; Rappe, A. M.; Scott, S.; Seshadri, R. *Chem. Mater.* **2007**, *19*, 1418-1426.

(22) Abbet, S.; Heiz, U.; Maria Ferrari, A.; Giordano, L.; Di Valentin, C.; Pacchioni, G. *Thin Solid Films* **2001**, *400*, 37-42.

(23) Fu, Q.; Kudriavtseva, S.; Saltsburg, H.; Flytzani-Stephanopoulos, M. *Chemical Engineering Journal* **2003**, *93*, 41-53.

(24) Bozo, C.; Guilhaume, N.; Herrmann, J.-M. *J. Catal.* **2001**, *203*, 393-406.

(25) Mayernick, A. D.; Janik, M. J. *The Journal of Physical Chemistry C* **2008**, *112*, 14955-14964.

(26) Fabris, S.; Gironcoli, S. d.; Baroni, S.; Vicario, G.; Balducci, G. *Phys. Rev. B* **2005**, *71*, 041102.

(27) Fabris, S.; Gironcoli, S. d.; Baroni, S.; Vicario, G.; Balducci, G. *Phys. Rev. B* **2005**, *72*, 237102.

(28) Kresse, G.; Blaha, P.; Silva, J. L. F. D.; Ganduglia-Pirovano, M. V. *Phys. Rev. B* **2005**, *72*, 237101.

(29) Da Silva, J.; Ganduglia-Pirovano, M. V.; Sauer, J.; Bayer, V.; Kresse, G. *Physical Review B (Condensed Matter and Materials Physics)* **2007**, *75*, 045121-10.

(30) Herschend, B.; Baudin, M.; Hermansson, K. *Surf. Sci.* **2005**, *599*, 173-186.

(31) Nolan, M.; Grigoleit, S.; Sayle, D. C.; Parker, S. C.; Watson, G. W. *Surf. Sci.* **2005**, *576*, 217-229.

(32) Nolan, M.; Parker, S. C.; Watson, G. W. *Surf. Sci.* **2005**, *595*, 223-232.

(33) Yang, Z.; Lu, Z.; Luo, G.; Hermansson, K. *Physics Letters A* **2007**, *369*, 132-139.

(34) Yang, Z.; Luo, G.; Lu, Z.; Hermansson, K. *The Journal of Chemical Physics* **2007**, *127*, 074704-5.

(35) Herbst, J. F.; Watson, R. E.; Wilkins, J. W. *Phys. Rev. B* **1978**, *17*, 3089 LP - 3098.

(36) Anisimov, V. I.; Gunnarsson, O. *Phys. Rev. B* **1991**, *43*, 7570 LP - 7574.

(37) Shapovalov, V.; Metiu, H. *J. Catal.* **2007**, *245*, 205-214.

(38) Yang, Z.; Woo, T. K.; Hermansson, K. *The Journal of Chemical Physics* **2006**, *124*, 224704-7.

(39) Dutta, G.; Waghmare, U. V.; Baidya, T.; Hegde, M. S. *Chemistry of Materials* **2007**, *19*, 6430-6436.

(40) Yang, Z.; Luo, G.; Lu, Z.; Woo, T. K.; Hermansson, K. *Journal of Physics: Condensed Matter* **2008**, *20*, 035210.

(41) Yoshida, H.; Inagaki, T.; Miura, K.; Inaba, M.; Ogumi, Z. *Solid State Ionics* **2003**, *160*, 109-116.

(42) Chafi, Z.; Keghouche, N.; Minot, C. *Surf. Sci.* **2007**, *601*, 2323-2329.

(43) Kresse, G.; Furthmuller, J. *Comput. Mater. Sci.* **1996**, *6*, 15-50.

(44) Kresse, G.; Furthmuller, J. *Phys. Rev. B* **1996**, *54*, 11169-11186.

(45) Kresse, G.; Hafner, J. *Phys. Rev. B* **1993**, *47*, 558-561.

(46) Kresse, G.; Joubert, D. *Phys. Rev. B* **1999**, *59*, 1758 LP - 1775.

(47) Monkhorst, H. J.; Pack, J. D. *Phys. Rev. B* **1976**, *13*, 5188 LP - 5192.

(48) Perdew, J. P.; Chevary, J. A.; Vosko, S. H.; Jackson, K. A.; Pederson, M. R.; Singh, D. J.; Fiolhais, C. *Phys. Rev. B* **1992**, *46*, 6671.

(49) Nolan, M.; Parker, S. C.; Watson, G. W. *Phys. Chem. Chem. Phys.* **2006**, *8*, 216-218.

(50) Nolan, M.; Parker, S. C.; Watson, G. W. *J. Phys. Chem. B* **2006**, *110*, 2256-2262.

(51) Pacchioni, G. *The Journal of Chemical Physics* **2008**, *128*, 182505-10.

(52) Waser, J.; Levy, H. A.; Peterson, S. W. *Acta Crystallographica* **1953**, *6*, 661-663.

(53) Lazarev, I. *Russian Journal of Inorganic Chemistry* **1978**, *23*, 488.

(54) Reuter, K.; Scheffler, M. *Phys. Rev. B* **2001**, *65*, 035406.

(55) Mukherjee, J.; Linic, S. *Journal of The Electrochemical Society* **2007**, *154*, B919-B924.

(56) Nava, P.; Sierka, M.; Ahlrichs, R. *Phys. Chem. Chem. Phys.* **2003**, *5*, 3372-3381.

(57) *NIST Chemistry Webbook*; Mallard, P. J. L. W. G., Ed.; National Institute of Standards and Technology: United States of America, 2008.

(58) Zhang, H.; Gromek, J.; Fernando, G.; Marcus, H.; Boorse, S. *Journal of Phase Equilibria and Diffusion* **2002**, *23*, 246-248.

(59) Farrauto, R. J.; Lampert, J. K.; Hobson, M. C.; Waterman, E. M. *Applied Catalysis B: Environmental* **1995**, *6*, 263-270.

3.6 Supporting Information

COMPARISON OF CALCULATED AND EXPERIMENTAL[1] O_2 FREE ENERGY AT 1 ATM

log P_{O_2} [ATM]	T (K)									
	100	200	300	400	500	600	700	800	900	1000
	Experimental O_2 Free Energy (eV/molecule)									
0	-10.01	-10.23	-10.46	-10.71	-10.97	-11.23	-11.50	-11.78	-12.06	-12.34
	Calculated O_2 Free Energy (eV/molecule)									
0	-9.91	-10.13	-10.37	-10.61	-10.87	-11.14	-11.41	-11.68	-11.97	-12.25

---

[1] P. J. L. W. G. Mallard ed., *NIST Chemistry Webbook* (National Institute of Standards and Technology, United States of America, 2008).

CALCULATED FREE ENERGIES OF O_2

log P_{O_2} [ATM]	T (K)									
	100	200	300	400	500	600	700	800	900	1000
	DFT + Statistical Mechanics O_2 Free Energy (eV/molecule)									
-37	-10.64	-11.60	-12.57	-13.55	-14.54	-15.54	-16.55	-17.56	-18.57	-19.60
-36	-10.62	-11.56	-12.51	-13.47	-14.44	-15.42	-16.41	-17.40	-18.40	-19.40
-35	-10.60	-11.52	-12.45	-13.39	-14.34	-15.30	-16.27	-17.24	-18.22	-19.20
-34	-10.58	-11.48	-12.39	-13.31	-14.25	-15.18	-16.13	-17.08	-18.04	-19.00
-33	-10.56	-11.44	-12.33	-13.23	-14.15	-15.07	-15.99	-16.92	-17.86	-18.80

-32	-10.54	-11.40	-12.27	-13.15	-14.05	-14.95	-15.85	-16.76	-17.68	-18.60
-31	-10.52	-11.36	-12.21	-13.08	-13.95	-14.83	-15.71	-16.61	-17.50	-18.40
-30	-10.50	-11.32	-12.15	-13.00	-13.85	-14.71	-15.58	-16.45	-17.32	-18.21
-29	-10.48	-11.28	-12.09	-12.92	-13.75	-14.59	-15.44	-16.29	-17.15	-18.01
-28	-10.46	-11.24	-12.03	-12.84	-13.65	-14.47	-15.30	-16.13	-16.97	-17.81
-27	-10.44	-11.20	-11.97	-12.76	-13.55	-14.35	-15.16	-15.97	-16.79	-17.61
-26	-10.42	-11.16	-11.91	-12.68	-13.45	-14.23	-15.02	-15.81	-16.61	-17.41
-25	-10.40	-11.12	-11.85	-12.60	-13.35	-14.11	-14.88	-15.65	-16.43	-17.21
-24	-10.38	-11.08	-11.79	-12.52	-13.25	-13.99	-14.74	-15.49	-16.25	-17.02
-23	-10.36	-11.04	-11.74	-12.44	-13.15	-13.88	-14.60	-15.34	-16.07	-16.82
-22	-10.34	-11.00	-11.68	-12.36	-13.05	-13.76	-14.46	-15.18	-15.90	-16.62
-21	-10.32	-10.96	-11.62	-12.28	-12.96	-13.64	-14.32	-15.02	-15.72	-16.42
-20	-10.30	-10.92	-11.56	-12.20	-12.86	-13.52	-14.19	-14.86	-15.54	-16.22
-19	-10.28	-10.88	-11.50	-12.12	-12.76	-13.40	-14.05	-14.70	-15.36	-16.02
-18	-10.26	-10.84	-11.44	-12.04	-12.66	-13.28	-13.91	-14.54	-15.18	-15.83
-17	-10.24	-10.80	-11.38	-11.96	-12.56	-13.16	-13.77	-14.38	-15.00	-15.63
-16	-10.22	-10.76	-11.32	-11.88	-12.46	-13.04	-13.63	-14.22	-14.82	-15.43
-15	-10.20	-10.72	-11.26	-11.81	-12.36	-12.92	-13.49	-14.07	-14.65	-15.23
-14	-10.18	-10.68	-11.20	-11.73	-12.26	-12.80	-13.35	-13.91	-14.47	-15.03
-13	-10.16	-10.64	-11.14	-11.65	-12.16	-12.68	-13.21	-13.75	-14.29	-14.83
-12	-10.14	-10.60	-11.08	-11.57	-12.06	-12.57	-13.07	-13.59	-14.11	-14.63
-11	-10.12	-10.56	-11.02	-11.49	-11.96	-12.45	-12.94	-13.43	-13.93	-14.44
-10	-10.11	-10.53	-10.96	-11.41	-11.86	-12.33	-12.80	-13.27	-13.75	-14.24

-9	-10.09	-10.49	-10.90	-11.33	-11.76	-12.21	-12.66	-13.11	-13.57	-14.04
-8	-10.07	-10.45	-10.84	-11.25	-11.67	-12.09	-12.52	-12.95	-13.40	-13.84
-7	-10.05	-10.41	-10.78	-11.17	-11.57	-11.97	-12.38	-12.80	-13.22	-13.64
-6	-10.03	-10.37	-10.72	-11.09	-11.47	-11.85	-12.24	-12.64	-13.04	-13.44
-5	-10.01	-10.33	-10.66	-11.01	-11.37	-11.73	-12.10	-12.48	-12.86	-13.25
-4	-9.99	-10.29	-10.60	-10.93	-11.27	-11.61	-11.96	-12.32	-12.68	-13.05
-3	-9.97	-10.25	-10.54	-10.85	-11.17	-11.49	-11.82	-12.16	-12.50	-12.85
-2	-9.95	-10.21	-10.49	-10.77	-11.07	-11.37	-11.69	-12.00	-12.32	-12.65
-1	-9.93	-10.17	-10.43	-10.69	-10.97	-11.26	-11.55	-11.84	-12.15	-12.45
0	-9.91	-10.13	-10.37	-10.61	-10.87	-11.14	-11.41	-11.68	-11.97	-12.25
1	-9.89	-10.09	-10.31	-10.54	-10.77	-11.02	-11.27	-11.53	-11.79	-12.06
2	-9.87	-10.05	-10.25	-10.46	-10.67	-10.90	-11.13	-11.37	-11.61	-11.86
3	-9.85	-10.01	-10.19	-10.38	-10.57	-10.78	-10.99	-11.21	-11.43	-11.66
4	-9.83	-9.97	-10.13	-10.30	-10.48	-10.66	-10.85	-11.05	-11.25	-11.46
5	-9.81	-9.93	-10.07	-10.22	-10.38	-10.54	-10.71	-10.89	-11.07	-11.26
6	-9.79	-9.89	-10.01	-10.14	-10.28	-10.42	-10.57	-10.73	-10.90	-11.06
7	-9.77	-9.85	-9.95	-10.06	-10.18	-10.30	-10.44	-10.57	-10.72	-10.86
8	-9.75	-9.81	-9.89	-9.98	-10.08	-10.18	-10.30	-10.41	-10.54	-10.67
9	-9.73	-9.77	-9.83	-9.90	-9.98	-10.07	-10.16	-10.26	-10.36	-10.47
10	-9.71	-9.73	-9.77	-9.82	-9.88	-9.95	-10.02	-10.10	-10.18	-10.27

Chapter 4

Methane Oxidation on Pd-ceria: A DFT study of the mechanism over $Pd_xCe_{1-x}O_2$, Pd, and PdO

This chapter is published as: A. D. Mayernick, M. J. Janik. *Journal of Catalysis* 2011, 278, 16-25.

ABSTRACT: Palladium-ceria exhibits unique catalytic activity for hydrocarbon oxidation, however the chemical and structural properties of active sites on the palladium-ceria surface are difficult to characterize. Strong interactions between palladium and the ceria support stabilize oxidized $Pd^{\delta+}$ species, which may contribute to the significant activity of Pd-ceria for methane oxidation. We present a density functional theory (DFT+*U*) investigation of methane oxidation over Pd-ceria, and quantify the activity of the $Pd_xCe_{1-x}O_2$(111) mixed oxide surface in comparison to the PdO(100) and Pd(111) surfaces. Probing reaction energetic on each of these surface models provides insight into the oxidation activity of Pd-ceria mixed oxides, and of the facets of large supported Pd and PdO particles. The methane activation barrier is lowest over the $Pd_xCe_{1-x}O_2$(111) surface, even lower than over the Pd(111) surface or low coordinate stepped or kinked Pd sites. The low barrier over the $Pd_xCe_{1-x}O_2$(111) surface demonstrates that mixed ceria-noble metal oxides offer the potential for improved hydrocarbon oxidation performance with respect to dispersed noble metal particles on ceria.

4.1 Introduction

Ceria offers unique properties as a heterogeneous catalyst or catalyst support, of which the redox properties[1-4] and methane oxidation activity[5,6] can be altered by the addition of low levels of noble metals such as palladium. The oxidation state and morphology of Pd species on Pd-ceria are a function of preparation method[5,7-12] and catalytic operating conditions.[7,12-14] Palladium can be supported on ceria as metal particles[12,15] or PdO_x species,[8,11,16] and strong interactions between Pd and the ceria support may a surface mixed oxide phase ($Pd_xCe_{1-x}O_y$).[5,13,17] Each of the chemically distinct Pd species on Pd-ceria likely provides unique catalytic activity, however which sites contribute to the significant activity for methane oxidation are unclear. Computational methods have been used to probe the relative stability of Pd species on ceria[5,13] and to evaluate elementary reaction energies for methane oxidation over pure CeO_2,[18] however the catalytic activity of ceria-supported Pd species has not been investigated. We present a computational investigation, utilizing the density functional theory (DFT+*U*) method, of methane oxidation over the $CeO_2(111)$, $Pd_xCe_{1-x}O_2(111)$, PdO(100), and Pd(111) surfaces. The reaction barrier for methane oxidation is lowest over the $Pd_xCe_{1-x}O_2(111)$ surface, suggesting that this Pd-ceria surface mixed oxide provides unusually high catalytic activity. Our results detail the rate determining steps and stable intermediates for methane oxidation over each surface.

The morphology and oxidation state of Pd surface species on ceria are both strong functions of synthesis and pretreatment methods, as well as catalytic operating conditions. X-ray Photoelectron Spectroscopy (XPS) showed that Pd-ceria prepared by deposition-precipitation had a higher concentration of cationic $Pd^{\delta+}$ sites than Pd-ceria prepared by wet impregnation.[8] Preparation of Pd-ceria by solution-combustion synthesis methods can facilitate mixing of Pd atoms into the CeO_2 lattice framework. A combination of XPS, X-ray Diffraction (XRD) and Extended X-ray Absorption Fine Structure (EXAFS) results were used to determine that Pd/ceria prepared by solution-combustion synthesis contains Pd^{2+} cations incorporated into cubic fluorite CeO_2 as a solid solution whereas wet impregnation result in samples containing primarily metallic Pd.[17] Colussi et al. also recently reported that surface solid solutions of Pd^{2+}/CeO_x with distinct short and long range order can be prepared by solution-combustion synthesis. High-resolution Transmission Electron Microscopy (HRTEM) and DFT calculations confirm that their Pd^{2+}/CeO_x samples consist of a reconstructed $CeO_2(110)$ surface with Pd^{2+} ions substituted for Ce^{4+}. The oxidation state of palladium and the morphology of the palladium surface are also strongly correlated with catalytic operating conditions, even in the absence of strong interactions with ceria. The bulk transition for PdO decomposition to Pd occurs at approximately 1070K in 1 atm O_2,[19] however the temperature at which this transition occurs is a function of O_2 pressure and the barrier for surface oxidation particularly in the case of small Pd particles may facilitate oxidation at lower temperatures. Ribeiro et al. show that PdO decomposes to Pd at 907K in 1.5 torr O_2, and that this transition results in an order of magnitude drop in the methane combustion turnover rate.[20] Thus depending upon the temperature and oxygen pressure of operation in a catalytic combustor or solid oxide fuel cell (SOFC) Pd or PdO may be stable, with dramatic effects on catalytic activity. Strong interactions with ceria stabilize oxidized Pd and specifically Pd-O-Ce linkages, which may contribute to the unique activity of Pd-ceria for hydrocarbon oxidation.

Palladium is an active catalyst for methane oxidation,[8,21] and for Pd-ceria combinations ceria serves not only as a support to disperse Pd, as interactions between Pd and CeO_2 facilitate unique oxidation activity. The oxidation rate on Pd-ceria exceeds the rate over pure ceria, with particularly high catalytic activity displayed by Pd-ceria catalysts containing oxidized $Pd^{\delta+}$ species or Pd-O-Ce linkages. For the direct oxidation of methane in a SOFC, the addition of 1 wt% Pd to a pure ceria anode increased the maximum power density by a factor of 10. McIntosh et al. also showed that adding 1 wt% Pd to ceria increases the rate of *n*-butane oxidation in an

SOFC.[6] The rate of methane combustion on Pd^{2+}/CeO_x mixed surface oxides of 1 and 1.71 wt% Pd was nearly twice that of Pd/ceria samples of equivalent composition prepared by incipient wetness.[5] Despite numerous studies illustrating the catalytic activity of Pd-ceria for hydrocarbon combustion, characterization of active sites is challenged by the heterogeneity of the metal-metal oxide structure and structural changes which may occur during reaction. The computational chemistry methods utilized herein probe the catalytic activity of CeO_2, Pd, PdO, and $Pd_xCe_{1-x}O_2$ to isolate the contributions of each to the overall oxidation performance of Pd-ceria catalysts.

Computational chemistry methods can directly evaluate the relative energies of elementary reaction steps and activation barriers on heterogeneous supported catalysts, however, applying these methods to study catalytic reactions on ceria has been limited to the consideration of simple redox reaction mechanisms. Previous computational studies of hydrocarbon chemistry on ceria have focused on evaluating elementary reaction energies for CO oxidation[18,22,23] and H_2/H_2O cycling[24,25] on pure CeO_2, as well as CO oxidation on CeO_2 doped with single transition metal atoms such as Au, Ag, Cu,[26] and Zr.[27] The structural changes which result from doping as well as the effects of doping on reducibility have also been investigated using DFT methods for noble metal atoms such as Pd[28] and Pt.[29] Knapp et al. evaluated the reaction energy diagram for methane combustion to CO_2 over pure $CeO_2(111)$,[18] though the reaction energetics in the presence of added transition or noble metals was not considered. Herein, we report the reaction energetics for combustion of CH_4 to CO_2 over Pd-ceria to establish a complete hydrocarbon combustion cycle and quantify changes in catalytic activity upon formation of $Pd_xCe_{1-x}O_2$. We compare the reaction energetics over $CeO_2(111)$ and $Pd_xCe_{1-x}O_2(111)$ to those over PdO(100) and Pd(111) and to distinguish the catalytic activity of the Pd-ceria mixed oxide from that of other Pd species.

Our previous study used *ab initio* thermodynamics to evaluate the stability of different Pd species on $CeO_2(111)$, (110), and (100) surfaces. Under varying operating conditions, the Pd_xCe_{1-}

$_xO_2$(111) surface is stable with respect to other single atom states of Pd on the CeO_2(111) surface.[13] The oxygen vacancy formation energy on $Pd_xCe_{1-x}O_2$(111) is less endothermic than on CeO_2(111), and the methane activation barrier is lower over $Pd_xCe_{1-x}O_2$(111) than CeO_2(111). This work utilizes the DFT+*U* method to calculate the reaction free energies of elementary steps in methane oxidation over CeO_2(111), $Pd_xCe_{1-x}O_2$(111), PdO(100), and Pd(111). These models represent the surface facets of a pure ceria (CeO_2(111)), palladium-ceria mixed oxide ($Pd_xCe_{1-x}O_2$(111)), palladium (Pd(111)), or palladium oxide (PdO(100)) particle, respectively. Evaluation of the combustion mechanism over each of these surfaces facilitates comparison between the catalytic activity of Pd-ceria mixed oxides, Pd metal, and PdO. Regardless of the initial oxidation state, the oxidation state of Pd cycles about either Pd^0 and Pd^{2+} or Pd^{2+} and Pd^{4+} during the full reaction turnover of methane oxidation. Comparing the methane oxidation kinetics over Pd^{4+} thus allows for comprehensive evaluation of the activity of all possible Pd oxidation states. We report the activation barriers, rate determining steps, and stable intermediates for methane combustion over each surface, with discussion of adsorption sites and adsorbate geometries. We use *ab initio* thermodynamics to evaluate the dependence of rate determining steps and the overall reaction mechanism on catalytic operating conditions including temperature and partial pressure of reactants and products. We specifically consider operating regimes corresponding to catalytic combustion experiments and SOFC operation.

4.2 Methods

4.2.1 Electronic Structure Method

Calculations were carried out using the Vienna *ab initio* simulation program (VASP), an *ab initio* total-energy and molecular dynamics program developed at the Institute for Material

Physics at the University of Vienna.[30-32] The projector augmented wave method[33] was used to represent the core region, with valence electron wavefunctions expanded in a tractable plane wave basis set. The energy cutoffs of the plane wave basis sets used herein were 400 eV, 450 eV, and 500 eV for Pd metal, CeO_2, and PdO, respectively (chosen to ensure convergence of total energy with respect to energy cutoff). Valence configurations were $5s^2 5p^6 6s^2 4f^1 5d^1$ for cerium, $2s^2 2p^4$ for oxygen, $4d^{10}$ for Pd, $2s^2 2p^2$ for C, and $1s^1$ for H. Structural optimizations were performed by minimizing the forces on all atoms to below 0.05 eV $Å^{-1}$, and all calculations for CeO_2 and PdO were spin-polarized. The Perdew-Wang (PW91) version of the generalized gradient approximation (GGA) was used to incorporate exchange and correlation energies.[34] Due to well-established difficulties within DFT to accurately represent the nature of 4*f* states in ceria,[35-37] we implemented the DFT+*U* approach. The DFT+*U* method introduces the Hubbard *U* term as an on-site Coulombic interaction in the *f* states of ceria, which properly localizes electrons in these states for reduced ceria structures (CeO_{2-x}, or more generally $Ce_x^{3+}Ce_{1-x}^{4+}O_y$). We do not directly consider ceria surfaces reduced by oxygen vacancies herein, however our previous study illustrated that the adsorption of H atoms and CH_3 groups on pure CeO_2 reduces surface Ce^{4+} cations to Ce^{3+}.[38] We used a value of $U = 5$ eV, which is consistent with recommended values within the DFT+*U* method used in previous studies of ceria.[18,28,39-42] Chapter 2 includes evaluation of the dependence of methane activation and oxygen vacancy formation on the value of the Hubbard U term on CeO_2 and $Pd_xCe_{1-x}O_2$. For pure ceria, the vacancy formation energy and methane adsorption energy increase in exothermicity linearly with increasing U value (ΔE_{vac}, ΔE_{ads} α $0.4\Delta U$ (eV)).[38] Given the dependence of vacancy formation energy and adsorption energy on U for pure ceria, the quantitative values we calculate are inherently dependent on our specific choice of U value. For $Pd_xCe_{1-x}O_2$, the vacancy formation energy and methane adsorption energy linearly become less exothermic with increasing U value, however with much less dependence on U value than for pure ceria as Pd^{4+} is reduced rather than Ce^{4+} (ΔE_{vac}, ΔE_{ads} α

0.05ΔU (eV)).[38] We use a U value of 5 eV to accurately describe the electronic structure of reduced ceria, and the qualitative comparisons of reaction energies we report over $Pd_xCe_{1-x}O_2$ and Pd or PdO are not sensitive to the U value.

4.2.2 Surface Models

Figure 4-1 displays the slab models used for the CeO_2(111), $Pd_xCe_{1-x}O_2$ (111), PdO(100), and Pd(111) surfaces. The ceria surface is modeled as a 12-layer ($Ce_{16}O_{32}$) mirrored slab of the (111) termination of cubic fluorite CeO_2 separated by 15 Å of vacuum in the direction perpendicular to the surface. The surface energy of CeO_2(111) is lowest among single crystal terminations of ceria,[38-40] indicating that this surface termination will represent a large portion of a polycrystalline CeO_2 surface. The mirrored slab model of the ceria surface was used specifically to minimize slab to slab interactions which may result from a large net surface dipole moment upon the interaction of the surface with adsorbates and the reduction of surface metal ions. For example, the mirrored slab model includes symmetrical adsorbates on both sides of the slab. The optimized equilibrium lattice parameter of bulk ceria is 5.466 Å, which is within 1% of the reported experimental value of 5.411 Å.[43] The Brillouin zone was sampled using a (2×2×1) MP grid for the (111) surface, with the third vector perpendicular to the surface. We use a *p*(2×2) expansion of the surface unit cell, which results in a termination of four surface oxygen atoms on each side of the slab and four Ce atoms in the atomic layer below.

The Pd(111) and PdO(100) surfaces were modeled as slabs of face-centered cubic (fcc) Pd metal and tetragonal palladium (II) oxide (PdO), respectively, also separated by 15 Å of vacuum in the direction perpendicular to the surface. The lattice parameters of bulk fcc Pd metal and bulk PdO were optimized within 2% of their corresponding experimentally determined values.[44,45] We used a 4-layer non-mirrored slab to model the Pd(111) surface, with the bottom

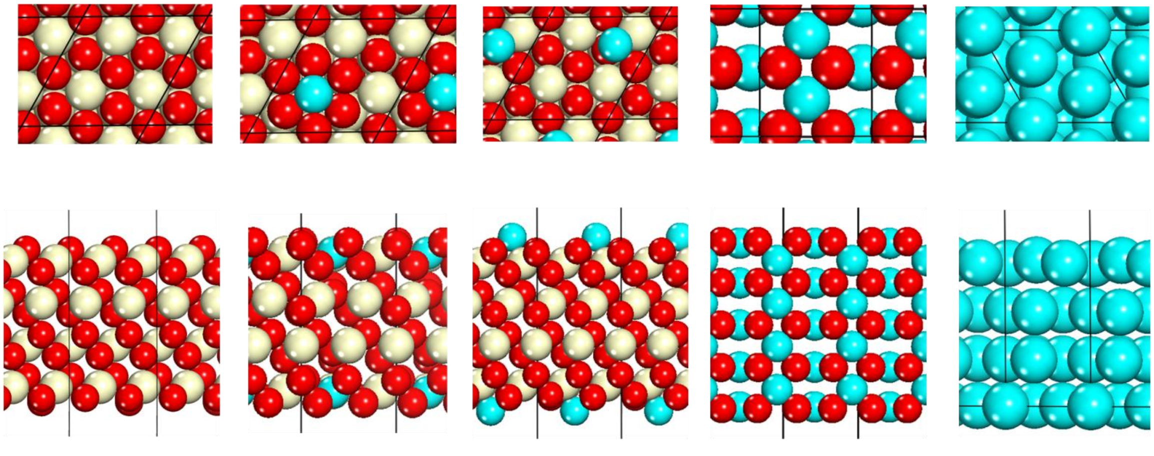

$CeO_2(111)$ $Pd_xCe_{1-x}O_2(111)$ $Pd^*/CeO_2(111)$ $PdO(100)$ $Pd(111)$

Figure 4-1. Top and side views of slab models for $CeO_2(111)$, $Pd_xCe_{1-x}O_2(111)$, $Pd^*/CeO_2(111)$, PdO(100), and Pd(111) surfaces. Ce is displayed as tan (light), Pd as light blue (gray), and O as red (dark).

two layers fixed at their bulk positions. The Pd(111) surface was represented in a $\left(\sqrt{3}\times\sqrt{3}\right)$ expansion, which results in a termination of 3 surface Pd atoms per unit cell. We used a 9-layer mirrored slab with a (2x1) expansion to model the PdO(100) surface, with all layers allowed to relax during structural optimizations. Scheffler et al. used DFT and *ab initio* thermodynamics to show that the surface formation energy of the (100) termination of PdO is less endergonic than all other single crystal terminations of PdO at O_2 pressures above 10^{-30} atm at 300K,[46] motivating its use in this study.

4.2.3 Reaction Free Energies

Reaction intermediates for methane oxidation over each surface were optimized by placing one adsorbate of the formula $C_1H_xO_y$ (with $0\leq x\leq 4$ and $0\leq y\leq 2$), or an isolated H atom adsorbate, in each surface unit cell. For each $C_1H_xO_y$ adsorbate, the O in $C_1H_xO_y$ corresponds to oxygen bound to the carbon atom which are not lattice oxygen of the stoichiometric surface.

Each adsorbate was placed at all high symmetry adsorption sites and configurations on each surface, and the lowest energy adsorption configuration for each adsorbate-surface pair was used to calculate the relative energies of elementary reaction steps. Using one adsorbate per unit cell results in relatively low coverage of reaction intermediates. For example, H* on $CeO_2(111)$ consists of an H atom adsorbed atop one of the 4 surface oxygen atoms in the unit cell, corresponding to an effective H coverage of 25%. Therefore reaction energies and analysis reported herein approximate the low coverage limit for methane oxidation. Harmonic vibrational modes were calculated to determine zero-point vibrational energy (ZPVE) corrections to the total energy of isolated molecules and adsorbed species. Optimizations of isolated gas-phase molecules were performed with one free molecule within a 15×15×15 Å unit cell. The free energies of gas-phase molecules were calculated as the sum of the electronic energy of the isolated molecule (E_{DFT}), ZPVE correction, entropy (ST), and a pressure volume term (PV) as follows:

$$G_{gas}= E_{DFT}+ZPVE-(S_{vib}+S_{trans}+S_{rot}+S_{elec})T+PV \qquad (1)$$

Constrained vibrational calculations were done for adsorbed species, where the Hessian matrix is populated solely with the second derivatives of energy with respect to position of the adsorbate atoms. This approximation is sufficient to capture large energy differences associated with the breaking of C-H bonds and the forming of O-H and O-C bonds. The free energies of adsorbed species were calculated as the sum of the electronic energy (E_{DFT}), ZPVE correction and vibrational entropy ($S_{\mathrm{vib}}T$):

$$G_{A*}= E_{DFT}+ZPVE-S_{vib}T \qquad (2)$$

Free energy differences for elementary reaction steps were calculated by subtracting the sum of free energies of the initial state from the sum of free energies of the product state, as follows for the example of CH_3 dissociation to adsorbed CH_2 and H fragments ($CH_3*+*\rightarrow CH_2*+H*$):

$$\Delta G_{rxn,\ CH_3*+*\rightarrow CH_2*+H*} = \frac{[G_{CH_2*}+G_{H*}]-[G_{CH_3*}+G_{bare}]}{2} \quad (3)$$

where G_{CH_2*}, G_{H*}, and G_{CH_3*} represent the free energies of adsorbed CH_2, H, and CH_3 species, respectively, and G_{bare} is the DFT energy of the bare surface. The bare surface energy G_{bare} is included to balance the stoichiometry of the elementary step as the energy of the surface is embedded in all G_{A*} terms. The denominator of two is included in equation 3 for energies calculated over the $CeO_2(111)$, PdO(100), Pd*/$CeO_2(111)$, and $Pd_xCe_{1-x}O_2(111)$ surfaces to account for the fact that mirrored slab models are used with one adsorbate on each side of the mirrored slab. Partial oxidation as well as total combustion pathways involving C-H breaking, O-H forming, and C-O forming steps were considered over the various surface modes.

To evaluate the minimum energy path for methane oxidation ($CH_4+2O_2\rightarrow CO_2+2H_2O$) over each surface, we also considered the formation energy of $CO_2(g)$ and $H_2O(g)$ from reaction intermediates. Water is formed by adsorption of H atoms on surface oxygen atoms followed by desorption of $H_2O(g)$ to leave a surface oxygen vacancy. The formation energy of $H_2O(g)$ from H* was calculated on the $CeO_2(111)$, PdO(100), Pd*/$CeO_2(111)$, $Pd_xCe_{1-x}O_2$ surfaces, as:

$$\Delta G_{H_2O\_formation} = \frac{[2\cdot G_{H_2O}+G_{vacant}+G_{bare}]-2\cdot G_{H*}}{2} \quad (4)$$

where G_{H*} is the free energy of adsorbed H (equation 2), G_{H_2O} is the free energy of $H_2O(g)$ (equation 1), and G_{vacant} is the DFT energy of the surface containing an oxygen vacancy on each side of the mirrored slab. The following equation was used to calculate the formation energy of $H_2O(g)$ on Pd(111):

$$\Delta G_{H_2O\_formation} = [G_{H_2O}+3\cdot G_{bare}]-[2\cdot G_{H*}+G_{O*}] \quad (5)$$

where G_{O*} is the free energy of adsorbed O, and water is formed by the formation of H_2O* from adsorbed H and O atoms, and then desorption of $H_2O(g)$. Water formation steps are included in the reaction energy diagrams reported herein as elementary steps immediately following C-H breaking steps which result in H* formation. For example, we consider the following three elementary steps for the dissociation of CH_3 to CH_2 $\left[CH_3{*}+\frac{1}{4}O_2(g)\rightarrow CH_2{*}+\frac{1}{2}H_2O(g)\right]$ on the $CeO_2(111)$, PdO(100), Pd*/$CeO_2(111)$, and $Pd_xCe_{1-x}O_2(111)$ surfaces:

$$A)\quad CH_3{*}+{*}\rightarrow CH_2{*}+H{*}$$

$$B)\quad H{*}\rightarrow \frac{1}{2}H_2O(g)+\frac{1}{2}V_O^{\cdot\cdot}+\frac{1}{2}{*}$$

$$C)\quad \frac{1}{2}V_O^{\cdot\cdot}+\frac{1}{4}O_2(g)\rightarrow \frac{1}{2}{*}$$

where $V_O^{\cdot\cdot}$ represents a surface oxygen vacancy. The following elementary steps were used for the dissociation of CH_3 to CH_2 on Pd(111):

$$A)\quad CH_3{*}+{*}\rightarrow CH_2{*}+H{*}$$

$$B)\quad H{*}+\frac{1}{2}O{*}\rightarrow \frac{1}{2}H_2O(g)+\frac{3}{2}{*}$$

$$C)\quad \frac{1}{4}O_2(g)+\frac{1}{2}{*}\rightarrow \frac{1}{2}O{*}$$

where the key difference between the reaction path over Pd(111) and each oxide surface is that adsorbed O* is consumed and replenished to complete the catalytic cycle on Pd(111) in contrast to lattice oxygen on each oxide surface.

The consideration of product formation and vacancy filling sequentially throughout the mechanism can be contrasted with the approach of Knapp et al.[18] Knapp et al. included all water formation energies at the final step and neglected vacancy filling in their analysis of the reaction energy diagram for methane oxidation over pure $CeO_2(111)$. The authors report that the final step in the catalytic cycle for $CH_4(g)+O_2(g)\rightarrow CO_2(g)+2H_2O(g)$ over $CeO_2(111)$ is $[CO_2(g)+2V_O^{\cdot\cdot}+4H{*}\rightarrow CO_2(g)+2H_2O(g)+2V_O^{\cdot\cdot}]$ with $\Delta E=+4.6$ eV.[18] Their analysis of methane oxidation does not consider the complete catalytic cycle by neglecting oxygen vacancy filling, and implies that the rate determining step for methane oxidation over ceria is water formation with an apparent barrier of nearly 450 kJ/mol (+4.6 eV). Our method of incorporating elementary steps for water formation into the reaction energy diagram for methane oxidation represents continuous water formation from H* during the overall reaction. This method also ensures that the reaction energy diagrams presented herein portray the minimum energy path without including numerous consecutive water formation steps as the rate determining process.

4.2.4 Reaction Free Energies

The majority of our analysis compares elementary reaction energies between surfaces. Activation barriers were computed for only C-H bond activation of methane. We do not calculate energy barriers for any reaction step following methane activation, as Knapp et al. show that the energy barrier for each C-H breaking step subsequent to methane activation is lower than the barrier for methane activation over the clean $CeO_2(111)$ surface.[18] We use a 3x3 unit cell to calculate the methane activation barrier on Pd(111) to accommodate both CH_3 and H within the unit cell. The climbing image nudged elastic band method (CI-NEB)[47-49] was used to isolate transition states and calculate reaction energy barriers for methane activation ($CH_4(g) \rightarrow CH_3{*}+H{*}$). Within the CI-NEB method, a sequence of images along the reaction path are optimized with the highest energy image required to climb up in energy along the elastic band to estimate the saddle point along the minimum energy path.[48] Four equally spaced images between reactant and product states were used in each search (six images total), and transition states were identified as the maximum energy image with an absolute tangential force of less than $0.04\ \mathrm{eV \cdot \AA^{-1}}$.

4.3 Results and Discussion

4.3.1 Reaction Free Energy Diagrams for Methane Oxidation

The reaction free energy of each elementary step in methane oxidation over each surface is calculated at 0K as well as at catalytic combustion conditions. Each reaction free energy diagram presented herein is calculated at T=298K and P_{CH_4}= 0.01 atm, P_{O_2}= 0.04 atm, P_{H_2O}= P_{CO_2}= 10^{-6} atm, to represent typical experimental catalytic combustion conditions at 0% conversion.[8,50] Reaction free energies are calculated at T=298K as this temperature corresponds to the low conversion (low T) region of the methane oxidation light-off curve over CeO_2.[21,50] The methane activation barriers displayed in each reaction free energy diagram are calculated as the Gibbs free energy of activation ($\Delta^{\ddagger}G$) at these catalytic combustion conditions, relative to the free energy of CH_4(g):

$$\Delta^{\ddagger}G = G_{TS}-\left(G_{CH_4(g)}+G_{*}\right) \quad (6)$$

In each reaction energy diagram presented herein, intermediate energies are referenced to the free energy of CH_4(g)+$2O_2$(g). Table 4-1 displays the barriers at 0K (E_{act}) and the standard Gibbs free energy of activation $\Delta^{\ddagger}G^0$ (at 273K and P_{CH_4}= 1.0 atm) for methane activation on each surface. Table 4-2 displays the reaction free energies for each step in methane oxidation at 0K. Adsorption geometries for all adsorbates on each surface are provided in the Supporting Information. The reaction free energy diagram for methane oxidation on Pd*/CeO_2(111) is also included in the Supporting Information.

Table 4-1. Activation barriers at 0K, free energies of activation at catalytic combustion conditions, relative combustion rate (normalized to the rate over $CeO_2(111)$) and stable intermediates for methane oxidation over $CeO_2(111)$, $Pd_xCe_{1-x}O_2(111)$, PdO(100), Pd(111), and Pd*/$CeO_2(111)$. [a]-calculated at 273K, P_{CH_4}= 1 atm; [b]-$\Delta^{\ddagger}S^0$ approximated at 0.33 eV

Surface	0K E_{act} (eV)	$\Delta^{\ddagger}G^0$ (eV)[a]	Relative Combustion Rate	Most Stable Intermediate
$CeO_2(111)$	+1.65	+1.88	1 (normalized)	HCO* ($HCOO^-$)
$Pd_xCe_{1-x}O_2(111)$	+0.18	+0.53	$6.97 \cdot 10^{22}$	H* (-OH)
PdO(100)	+1.08	+1.41	$8.97 \cdot 10^{7}$	HCO* ($HCOO^-$)
PdO(101)[55]	+0.65	+0.98[b]	$1.69 \cdot 10^{15}$	--
Pd*/$CeO_2(111)$	+1.30	+1.70	$1.11 \cdot 10^{3}$	CO*
Pd(111)	+0.89	+1.32	$2.99 \cdot 10^{9}$	CH_3* (-OCH_3)
Pd step[56]	+0.38	+0.71[b]	$6.28 \cdot 10^{19}$	--
Pd kink[56]	+0.41	+0.74[b]	$1.95 \cdot 10^{19}$	--

4.3.1.1 Methane Oxidation on $CeO_2(111)$

Figure 4-2 displays the reaction free energy diagram for methane oxidation on $CeO_2(111)$ at catalytic combustion conditions.

Methane adsorption on $CeO_2(111)$ proceeds through H abstraction by a surface oxygen atom to form a methyl radical ($\cdot CH_3$), followed by adsorption of $\cdot CH_3$.[38] Figure 4-3(a) displays the transition state for methane activation on $CeO_2(111)$. The methane activation barrier over $CeO_2(111)$ is +1.65 eV ($\Delta^{\ddagger}G$ = +2.05 eV at 298K), with the ($\cdot CH_3$+*H) state 0.2 eV lower in energy (+1.40 eV at 0K,[38] +1.85 eV at 298K) than the transition state. Our previous study reported the energy of $\cdot CH_3$+H* as the highest energy state between CH_4(g) and CH_3*+H*,[38] however subsequent finer searches along the reaction coordinate identified this higher energy

Table 4-2. Reaction energies at 0K for each elementary step in methane oxidation over CeO_2(111), $Pd_xCe_{1-x}O_2$(111), PdO(100), Pd*/CeO_2(111), and Pd(111).

CeO_2(111)	0K ΔE (eV)	Pd*/CeO_2(111)	0K ΔE (eV)
$CH_4(g) \rightarrow CH_3^* + H^*$	-0.81	$CH_4(g) \rightarrow CH_3^* + H^*$	-0.71
$CH_3^* \rightarrow CH_2^* + H^*$	+0.51	$CH_3^* \rightarrow CH_2^* + H^*$	-0.72
$CH_2^* \rightarrow CH^* + H^*$	+0.19	$CH_2^* \rightarrow CH^* + H^*$	-0.12
$CH^* \rightarrow HCO^*$	-1.82	$CH^* \rightarrow HCO^*$	-0.60
$HCO^* \rightarrow CO^* + H^*$	+0.78	$HCO^* \rightarrow CO^* + H^*$	-0.83
$CO^* \rightarrow CO_2(g)$	-0.18	$CO^* \rightarrow CO_2(g)$	+1.65
$Pd_xCe_{1-x}O_2$(111)		PdO(100)	
$CH_4(g) \rightarrow CH_3^* + H^*$	-2.29	$CH_4(g) \rightarrow CH_3^* + H^*$	-1.05
$CH_3^* \rightarrow CH_2^* + H^*$	-2.05	$CH_3^* \rightarrow CH_2^* + H^*$	-0.67
$CH_2^* \rightarrow CH^* + H^*$	-0.96	$CH_2^* \rightarrow CH^* + H^*$	-0.06
$^*CH \rightarrow {}^*HCO$	-1.58	$^*CH \rightarrow {}^*HCO$	-0.75
$HCO^* \rightarrow CO^* + H^*$	-1.94	$HCO^* \rightarrow CO^* + H^*$	+0.29
$CO^* \rightarrow CO_2(g)$	+0.60	$CO^* \rightarrow CO_2(g)$	-1.01
Pd(111)			
$CH_4(g) \rightarrow CH_3^* + H^*$	-1.96		
$CH_3^* \rightarrow CH_2^* + H^*$	+0.20		
$CH_2^* \rightarrow CH^* + H^*$	-0.40		
$^*CH \rightarrow {}^*HCO$	-0.42		
$HCO^* \rightarrow CO^* + H^*$	-1.61		
$CO^* \rightarrow CO_2(g)$	+0.23		

transition state. This transition state for methane activation over $CeO_2(111)$ has a single imaginary vibrational frequency along the reaction coordinate (in contrast to the absence of a imaginary frequency in the transition state reported previously[38]), an absolute tangential force of less than 0.04 $eV\cdot Å^{-1}$, and forces on all atoms below 0.05 eV $Å^{-1}$. The reaction free energy for ($CH_4(g) \rightarrow CH_3* + H*$) is slightly exergonic at -0.14 eV, however each subsequent C-H breaking step over pure ceria is endergonic (with the most endergonic step $HCO* \rightarrow CO* + H*$ at +0.71 eV). Each water formation step $\left(*H \rightarrow \frac{1}{2}H_2O(g) + \frac{1}{2}V_O^{\cdot\cdot} + \frac{1}{2}*\right)$ over ceria is endergonic by +0.45eV, and each oxygen vacancy filling step $\left(\frac{1}{4}O_2 + \frac{1}{2}V_O^{\cdot\cdot} \rightarrow \frac{1}{2}*\right)$ is exergonic by -2.44 eV (-4.88 eV per $V_O^{\cdot\cdot}$). Methane activation over the hydroxylated surface was not considered as the barrier would be expected to increase. We instead presume that water desorption and vacancy refilling by oxygen must precede C-H activation in the catalytic cycle.

Each CH_x species ($1 \leq x \leq 3$) adsorbs atop a surface oxygen atom on $CeO_2(111)$, with elongation of each adjacent Ce-O bond. The lowest energy path of methane oxidation proceeds over $CeO_2(111)$ by breaking the first three C-H bonds to form CH*, oxidizing to HCO*, breaking the final C-H bond to form CO*, which desorbs as $CO_2(g)$ leaving an oxygen vacancy. Carbon monoxide binds weakly atop a Ce atom and is easily oxidized on $CeO_2(111)$, as evidenced by the favorable free energy of -1.04 eV at 298K for $CO* \rightarrow CO_2(g) + 2H_2O(g) + V_O^{\cdot\cdot}$. This result is similar to the findings of previous DFT+U studies of CO adsorption on ceria.[51,52] Carbon dioxide adsorption to $CeO_2(111)$ is equivalent to CO_3^{2-} formation on an oxygen vacancy. However, carbonate formation is not preferable as it is more exergonic for CO* to desorb as $CO_2(g)$ (-1.04 eV at 298K) than to form CO_2* (-0.61 eV at 298K). Intermediates including CH_3O*, CH_3OH*, H_2CO*, H_2COH*, HCOH*, C*, and HCOO* were also considered. The formation of each of these was endergonic with respect to other intermediates along the lowest energy path.

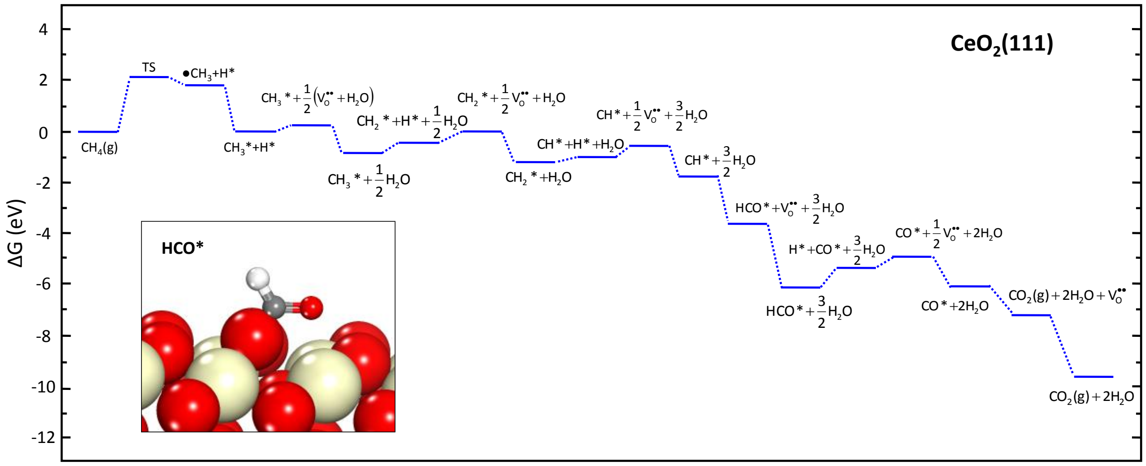

Figure 4-2. Reaction free energy diagram for $CH_4(g) + 2O_2(g) \rightarrow CO_2(g) + 2H_2O(g)$ over $CeO_2(111)$. Inset: HCO* ($HCOO^-$), the most stable intermediate in methane oxidation over $CeO_2(111)$. Ce is displayed as tan (light), O as red (dark), C as gray, and H as white. Oxygen (O_2) is not explicitly included in the oxidation mechanism, as addition of O_2 to the surface occurs in oxygen vacancy filling steps.

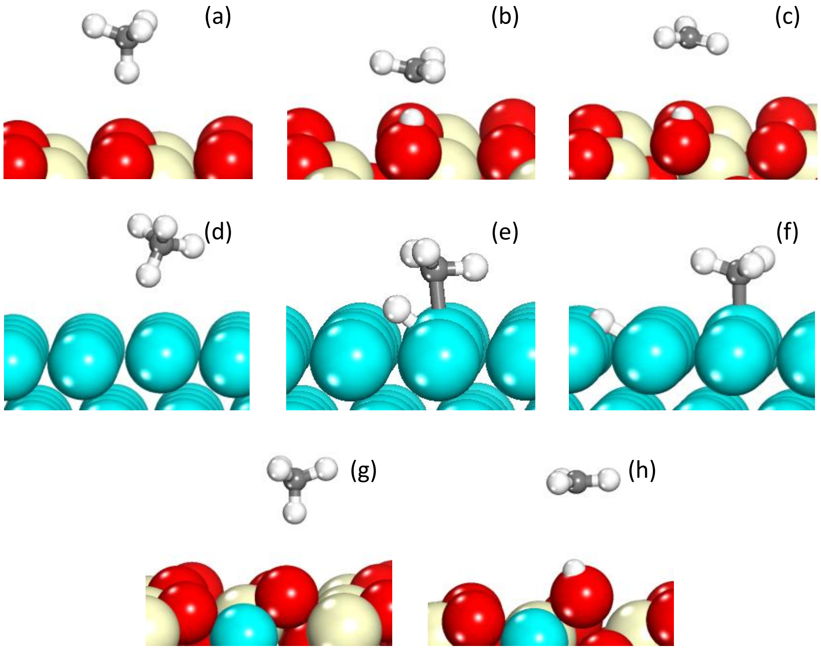

Figure 4-3. Initial (a, d, g), transition (b, e), and final (c, f, h) states for methane activation on $CeO_2(111)$ (a, b, c), Pd(111) (d, e, f) and $Pd_xCe_{1-x}O_2(111)$ (g, h). Ce is displayed as tan (light), Pd as light blue (gray), O as red (dark), C as grey, and H as white.

Stable intermediates along the lowest energy path were identified as those for which the subsequent reaction step is uphill (endergonic) in free energy. The “most stable intermediate” is identified as the intermediate from which the subsequent reaction step in the most endergonic. The most stable intermediate over $CeO_2(111)$ is HCO*, which adsorbs with the carbon atom atop a surface oxygen, and is equivalent to formate ($HCOO^-$) adsorbed atop an oxygen vacancy. Diffuse Reflection Infrared Fourier Transform Spectroscopy (DRIFTS) analysis confirmed the presence and stability of surface formates on ceria during low-temperature water-gas shift reaction conditions.[53,54] These DRIFTS studies determine the stretching bands for formate on ceria to be 2950 cm^{-1} for C-H stretch and 1580 cm^{-1} for O-C-O asymmetric stretching;[53,54] we calculate 2970 cm^{-1} for C-H stretch and 1599 cm^{-1} for O-C-O asymmetric stretching. Stable intermediates other than HCO* on $CeO_2(111)$ include CH_3*, CH_2*, and H*. The stability of CH_3* and CH_2* is further evidence of C-H breaking activity as the limiting factor in hydrocarbon oxidation activity. The stability of H* suggests that hydroxyl groups will be present on the ceria surface during reaction. The formation energies of partial oxidation products such as methanol (CH_3OH), formaldehyde (H_2CO), and formic acid (H_2COOH) were thermodynamically unfavorable at both 0K and at catalytic combustion conditions compared to further steps towards total oxidation (CO_2), and thus are not included in the minimum energy path over $CeO_2(111)$.

4.3.1.2 *Methane Oxidation on $Pd_xCe_{1-x}O_2(111)$*

Figure 4-4 displays the reaction free energy diagram for methane oxidation on $Pd_xCe_{1-x}O_2(111)$ at catalytic combustion conditions. Methane adsorption on $Pd_xCe_{1-x}O_2$ proceeds through H abstraction by a surface oxygen atom to form $\cdot CH_3$, followed by adsorption of CH_3.[38] Subsequent finer searches along the reaction coordinate over $Pd_xCe_{1-x}O_2(111)$ (equivalent to our approach over $CeO_2(111)$), indicated a monotonic increase in energy between $CH_4(g)$ and

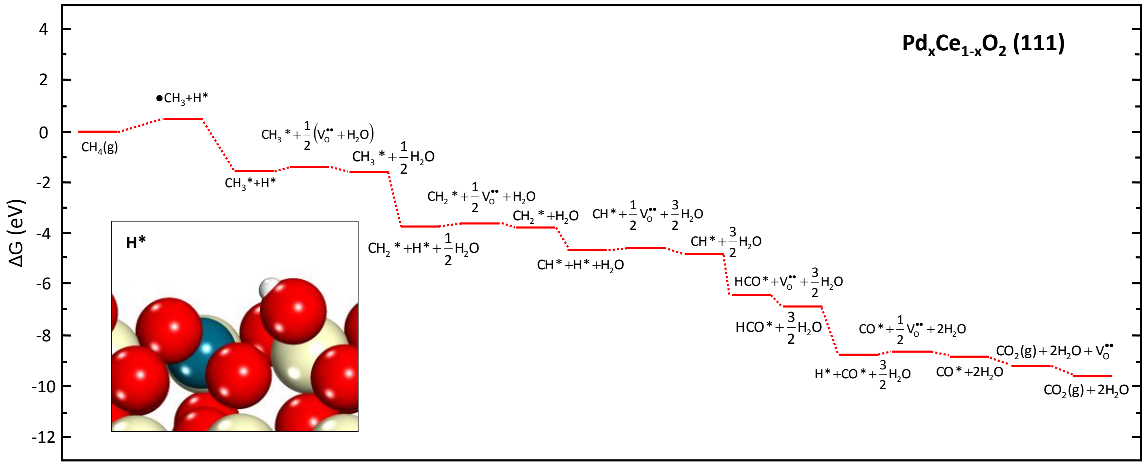

Figure 4-4. Reaction free energy diagram for $CH_4(g)$ + $2O_2(g)$ → $CO_2(g)$ + $2H_2O(g)$ over $Pd_xCe_{1-x}O_2(111)$. Inset: H* (-OH), the most stable intermediate in methane oxidation over $Pd_xCe_{1-x}O_2$ (111). Ce is displayed as tan (light), O as red (dark), Pd as light blue (gray), and H as white.

($\cdot CH_3$+H*), in contrast to the higher energy transition state between these two states found on pure ceria. The free energy ($\Delta^{\ddagger}G$) of the ($\cdot CH_3$+H*) state over $Pd_xCe_{1-x}O_2(111)$ is +0.70 eV (E_{act}=+0.22 eV at 0K[38]) with respect to $CH_4(g)$, substantially lower than that over pure ceria ($\Delta^{\ddagger}G$ =+1.85 eV, E_{act}=+1.40 eV at 0K).

Each C-H breaking step over $Pd_xCe_{1-x}O_2(111)$ is more exergonic than the corresponding step over $CeO_2(111)$. The minimum energy path on $Pd_xCe_{1-x}O_2(111)$ follows the same intermediates as for methane oxidation on $CeO_2(111)$ (i.e. C-H breaking to CH*, C-O forming to HCO*, C-H breaking to CO*, then desorption as CO_2 + $V_O^{\cdot\cdot}$). Carbon dioxide adsorbs equivalent to CO_3^{2-} on an oxygen vacancy on $Pd_xCe_{1-x}O_2(111)$, however it is exergonic for CO* to desorb as $CO_2(g)$ (-0.34 eV at 298K), whereas the formation of CO_2* is endergonic (+0.13 eV at 298K). Each CH_x species ($1 \leq x \leq 3$) adsorbs atop a surface oxygen atom on $Pd_xCe_{1-x}O_2(111)$, with elongation of adjacent Pd-O and Ce-O bonds. Our previous study of Pd substituted ceria surfaces highlighted that Pd substitution increases surface reducibility with respect to pure ceria and thereby provides more active surface oxygen for oxidation reactions. Adsorption of CH_x and H on the $Pd_xCe_{1-x}O_2(111)$ surface results in reduction of the incorporated Pd^{4+} species, which is more exothermic than reduction of Ce^{4+}.[38] In the bare $Pd_xCe_{1-x}O_2(111)$ surface, Pd^{4+} is approximately octahedrally coordinated by O atoms, as expected based on crystal field theory arguments for the d^6 metal center. Upon adsorption of H or CH_x fragments Pd-O bonds lengthen, and specifically elongation of a Pd-O subsurface bond provides for a nearly square planar O environment about the d^8 Pd^{2+} atom. The Pd atom therefore provides the reduction center and incorporation into the CeO_2 lattice provides for structural flexibility to stabilize both the Pd^{4+} and Pd^{2+} states.

The most stable intermediate over $Pd_xCe_{1-x}O_2(111)$ is H*, as the only endergonic reaction steps following methane activation are water formation steps. The formation energies of partial oxidation products such as methanol (CH_3OH), formaldehyde (H_2CO), and formic acid (H_2COOH) were more endergonic than further steps towards total oxidation (CO_2), and thus are not included in the minimum energy path over $Pd_xCe_{1-x}O_2(111)$.

4.3.1.3 Methane Oxidation on PdO(100)

Though the low methane activation barrier over $Pd_xCe_{1-x}O_2(111)$ suggests that incorporated Pd^{4+} ions in ceria provide high activity for methane oxidation, it is possible that the active cationic Pd species identified experimentally correspond to PdO_x clusters. We use the PdO(100) surface to approximate the surface of a PdO particle because the surface formation energy of the (100) termination of PdO is less endergonic than all other single crystal terminations of PdO at O_2 pressures above 10^{-30} atm at 300K.[46] Figure 4-5 displays the reaction energy diagram for methane oxidation on PdO(100) at catalytic combustion conditions. Methane adsorption on PdO(100) occurs dissociatively with CH_3 and H fragments adsorbing atop surface

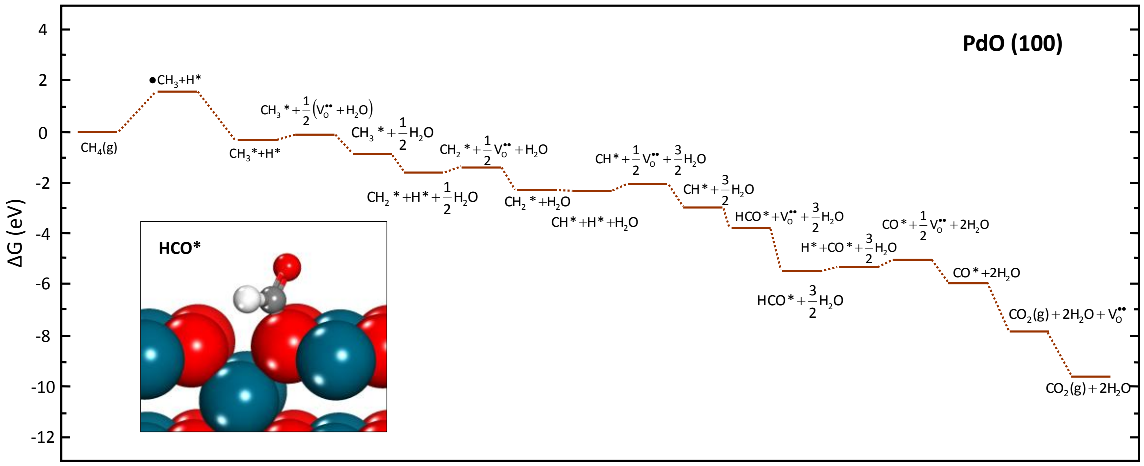

Figure 4-5. Reaction free energy diagram for CH_4(g) + $2O_2$(g) → CO_2(g) + $2H_2O$(g) over PdO(100). Inset: HCO* ($HCOO^-$), the most stable intermediate in methane oxidation over PdO(100). Pd is displayed as light blue (grey), O as red (dark), C as grey and H as white.

oxygen atoms, similar to methane dissociative adsorption on pure ceria.[38] Searches along the reaction coordinate over PdO(100) indicated a monotonic increase in energy between CH_4(g) and ($\cdot CH_3$+H*), and we approximate the energy barrier for methane activation on PdO(100) as the energy of $CH_4 \rightarrow \cdot CH_3$+H* (H abstraction and methyl radical formation). Product or transition states that involved interaction of H and CH_3 fragments with surface Pd^{2+} were higher in energy than H* and CH_3* atop surface oxygen atoms. The free energy of the $\cdot CH_3$+H* state ($\Delta^{\ddagger}G$) is +1.58 eV (+1.08 eV at 0K), lower than over pure ceria and Pd*/CeO_2(111), but higher than that over $Pd_xCe_{1-x}O_2$(111).

Methane activation on PdO may also occur over coordinatively unsaturated Pd atoms, either present near oxygen vacancies or on surfaces terminated by Pd with less than six-fold oxygen coordination. Weaver et al. reported a DFT calculated methane activation barrier of 0.65 eV on PdO(101) at 0K via metal insertion of a coordinatively unsaturated surface Pd atom.[55] Methane dissociation over an oxygen vacancy on Pd(100) is endergonic at +0.03 eV at 298K, 0.4

eV more endergonic than over the stoichiometric surface (-0.37 eV at 298K). The more endergonic methane dissociation energy over PdO(100)/$V_O^{\cdot\cdot}$ suggests that methane activation over oxygen vacancies on PdO(100) is not favorable relative to activation by H abstraction over the stoichiometric surface. Methane activation transition state searches over PdO(100)/$V_O^{\cdot\cdot}$ indicate that activation via metal insertion does not stabilize a transition state lower in energy than activation via H abstraction over the intact PdO(100) surface. The activation barrier and transition state over PdO(101) illustrate, however, that methane activation can be facile over PdO surface terminations which expose unsaturated Pd atoms of specific coordination and geometry, and that the methane activation barrier on PdO via either metal insertion is lower than via H abstraction on PdO(100).

Each C-H breaking step over PdO(100) is exergonic, with the exception of HCO*→CO*. Every C-H breaking step subsequent to $CH_4 \rightarrow CH_3^* + H^*$ is more exergonic than over CeO_2(111), but less exergonic than over Pd*/CeO_2(111) or $Pd_xCe_{1-x}O_2$(111). The minimum energy path on PdO(100) follows the same intermediates as on each ceria surface, and each adsorbate sits atop one surface O atom or bridged between two surface O atoms. The most stable intermediate is CO*, which binds strongly at a site bridging between two surface oxygen and is equivalent to a carbonate ion, CO_3^{2-}, adsorbed on two adjacent oxygen vacancies. This adsorption mode for CO* is also equivalent to CO_2 adsorbed on a single oxygen vacancy; no stable adsorption site was found for CO_2 on the intact PdO(100) surface. The vacancy formation energy on PdO(100) (+2.16 eV at 0K) is less than that on CeO_2(111) (+2.76 eV at 0K) or Pd*/CeO_2(111) (+2.64 eV at 0K), and thus water formation is more exergonic and oxygen vacancy filling is more endergonic on PdO than over CeO_2(111) or Pd*/CeO_2(111). The formation of partial oxidation products was prohibitively endergonic as found for ceria-based surfaces.

4.3.1.4 Methane Oxidation on Pd(111)

We use the Pd(111) surface to approximate the surface of a large reduced palladium (Pd^0) particle, and evaluate methane oxidation energetics over Pd(111) for comparison with other surface models. Figure 4-6 displays the reaction energy diagram for methane oxidation on Pd(111) at catalytic combustion conditions. Methane oxidation on Pd(111) occurs via the reaction of adsorbed CH_x* species and adsorbed oxygen atoms O*, in contrast to this reaction on each oxide surface in which CH_x* species react with lattice oxygen. Figure 4-3(b) displays the transition state for methane activation on Pd(111), which occurs via cleavage of a C-H bond of methane and the formation of CH_3* and H*. The free energy of activation ($\Delta^{\ddagger}G$) over Pd(111) is +1.49 eV (+0.89 eV at 0K), which is higher only than the barrier over $Pd_xCe_{1-x}O_2(111)$. The 0K methane activation barrier over stepped or kinked Pd surfaces is 0.38 and 0.41 eV (at 0K),[56] respectively, of which both values are higher than over $Pd_xCe_{1-x}O_2(111)$. Methane oxidation follows the same intermediates over Pd(111) as over each ceria surface and PdO, with the only endergonic step being $CH_3^* \rightarrow CH_2^* + H^*$. Every other elementary step is exergonic over Pd(111), including both water formation and oxygen dissociation $\left(\frac{1}{2}O_2 \rightarrow O^*\right)$.

Adsorbed oxygen (O*) will be present on the Pd surface during reaction, and methane activation may also occur over O* species. Preliminary calculations indicate that the methane activation reaction energy and barrier are higher over oxygen covered Pd(111) than over Pd(111) or Pd steps or kinks, emphasizing the role of metallic sites in dictating the activity of Pd for methane combustion.

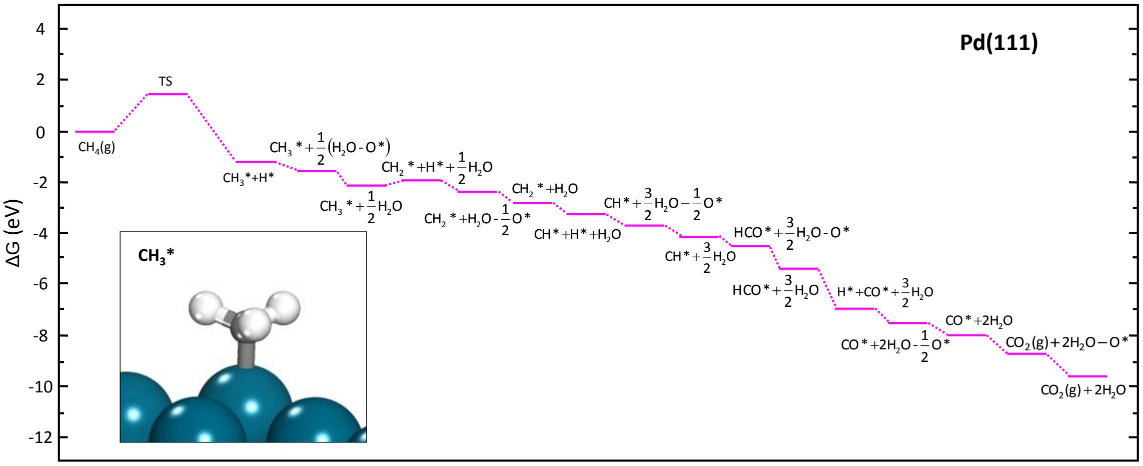

Figure 4-6. Reaction free energy diagram for $CH_4(g) + 2O_2(g) \rightarrow CO_2(g) + 2H_2O(g)$ over Pd(111). Inset: CO*, the most stable intermediate in methane oxidation over Pd(111). Pd is displayed as light blue (gray), O as red (dark), and C as gray.

4.3.2 Dependence of Rate Determining Steps on Operating Conditions

We compare operating regimes for the catalytic combustion of methane and methane electro-oxidation in a SOFC within which distinct elementary steps over each surface are rate determining (provide the largest energy barrier). The free energy of methane activation ($\Delta^{\ddagger}G$), as well as the free energies of product desorption steps are a function of temperature and the partial pressures of reactants and products, and thus the rate determining step is also of function of temperature and partial pressures. For example, at very high pressures of $H_2O(g)$ product, the desorption of H_2O may be more endergonic than any other elementary reaction energy or barrier. At low O_2 pressures, oxygen vacancy filling will become rate limiting. The $\Delta^{\ddagger}G$ for methane activation is also dependent on the methane pressure, with higher pressures reducing $\Delta^{\ddagger}G$. We implement Murdoch's procedure[57] to identify the rate determining step of methane oxidation within each operating regime. Murdoch's procedure involves dividing the reaction free energy diagram into sections of steadily decreasing free energy, and identifying the reaction sequence which passes through the largest ΔG barrier of any given section as the rate determining step.[57]

The partial pressures of reactants and products used to represent catalytic combustion reactor conditions at conversions greater than 0% were fixed by the stoichiometry of the overall reaction. SOFC conditions were set as 973K, 1 atm CH_4 at the anode (pure methane anode feed), and 0.21 atm O_2 at the cathode (air cathode feed), equivalent to experimental conditions in previous studies of direct oxidation of hydrocarbons in SOFCs.[58-60] The partial pressure of O_2 at the anode was fixed by the cell potential by the Nernst relationship:

$$E= \left[\frac{RT}{2F}\right] \ln \left[\frac{\left(P_{O_2}^{cathode}\right)^{\frac{1}{2}}}{\left(P_{O_2}^{anode}\right)^{\frac{1}{2}}}\right] \qquad (7)$$

where the cell potential E is set at the equilibrium potential of 1.05 V (@973K) for 0% conversion.[59] The partial pressures of H_2O and CO_2 at the anode are also fixed by the Nernst relationship, which can be rewritten for methane oxidation as:

$$E= E^0+ \left[\frac{RT}{8F}\right] \ln \left[\frac{\left(P_{CH_4}^{anode}\right)\cdot\left(P_{O_2}^{cathode}\right)^2}{\left(P_{H_2O}^{anode}\right)^2\cdot\left(P_{CO_2}^{anode}\right)}\right] \qquad (8)$$

where $P_{H_2O}^{anode}$, $P_{CO_2}^{anode}$, $P_{CH_4}^{anode}$, and $P_{O_2}^{cathode}$ values at conversions greater than 0% are fixed by the stoichiometry of the overall reaction.

Figure 4-7 depicts regions of O_2 and H_2O partial pressures within which either of the following segments of the method oxidation path over $CeO_2(111)$ are rate determining:

$$\text{A)}\ CH_4(g)\rightarrow\cdot CH_3+H^*\rightarrow\cdot CH_3{}^*+H^*$$

$$\text{B)}\ HCO^*+{}^*\rightarrow H^*+CO^*\rightarrow CO^*+\frac{1}{2}H_2O(g)+\frac{1}{2}V_O^{\cdot\cdot}+\frac{1}{2}\,{}^*$$

$$\text{C)}\ HCO^*+{}^*\rightarrow H^*+CO^*\rightarrow CO^*+\frac{1}{2}H_2O(g)+\frac{1}{2}V_O^{\cdot\cdot}+\frac{1}{2}\,{}^*\rightarrow CO^*+\frac{1}{2}H_2O(g)+{}^*$$

Segments B and C represent H_2O formation and vacancy filling, respectively, each referenced to HCO* since it is the most stable intermediate over $CeO_2(111)$. At catalytic combustion conditions (Figure 4-7(a)), methane oxidation on $CeO_2(111)$ is rate limited by CH_4 activation at all conversions. The regions of O_2 and H_2O pressures within which water formation or vacancy filling are endergonic to the extent that the rate determining step is altered are characterized by extremely low O_2 pressures ($<10^{-80}$ atm) and extremely high H_2O pressures ($>10^{20}$ atm). At SOFC conditions, methane oxidation over ceria is also rate limited by CH_4 activation, however the region within which vacancy filling contributes to the rate determining step is much larger at the higher SOFC temperature; the free energy of O_2(g) is lower and thus vacancy filling is more endergonic at higher temperatures.

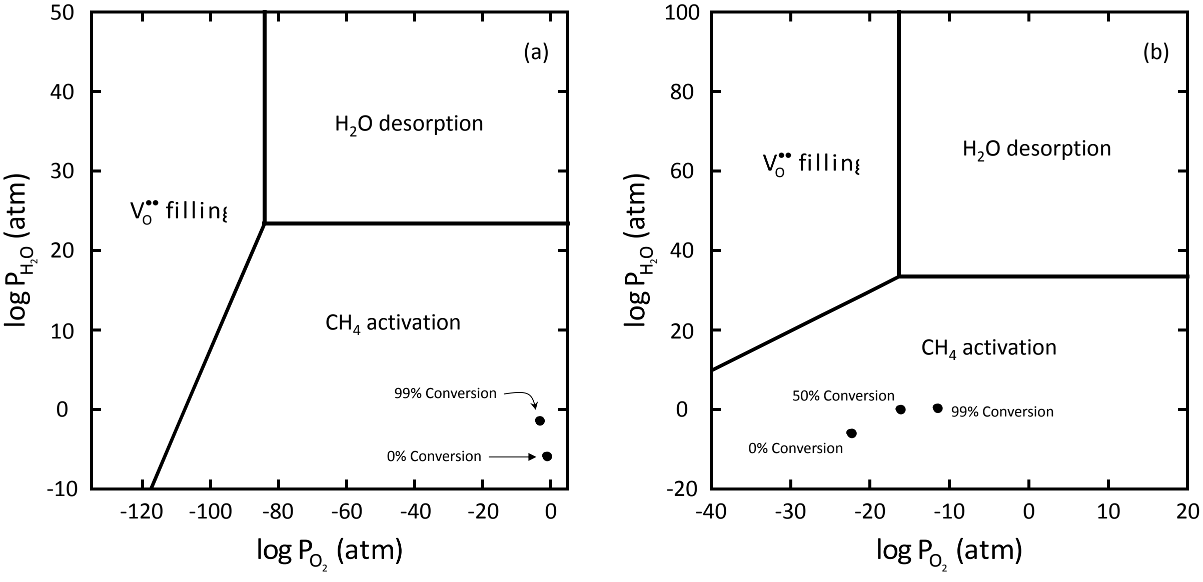

Figure 4-7. Phase regions of rate determining steps of methane oxidation over $CeO_2(111)$ at 298K/catalytic combustion operating conditions (a) and 973K/SOFC conditions (b). Filled circles (•) represent conditions at the labeled conversions for (a) 298K/catalytic combustion and (b) 973K/SOFC.

Over $Pd_xCe_{1-x}O_2(111)$, the methane activation barrier is lower than over $CeO_2(111)$ and therefore the conditions over which H_2O desorption or vacancy filling are limiting may be expected to vary. Figure 4-8 depicts regions of O_2 and H_2O partial pressures within which methane activation, water formation, or vacancy filling over $Pd_xCe_{1-x}O_2(111)$ are rate determining. Methane activation is more exergonic over $Pd_xCe_{1-x}O_2(111)$ than $CeO_2(111)$, which contracts the region within which methane activation is rate determining. Although this region is contracted, methane oxidation remains rate limited by CH_4 activation at all conditions of interest over $Pd_xCe_{1-x}O_2$(111). The regions of H_2O and O_2 pressures within which water formation and/or vacancy filling are rate determining over $Pd_xCe_{1-x}O_2$(111) are characterized by lower H_2O pressures and higher O_2 pressures than over CeO_2(111), because the $Pd_xCe_{1-x}O_2$(111) surface is more reducible.

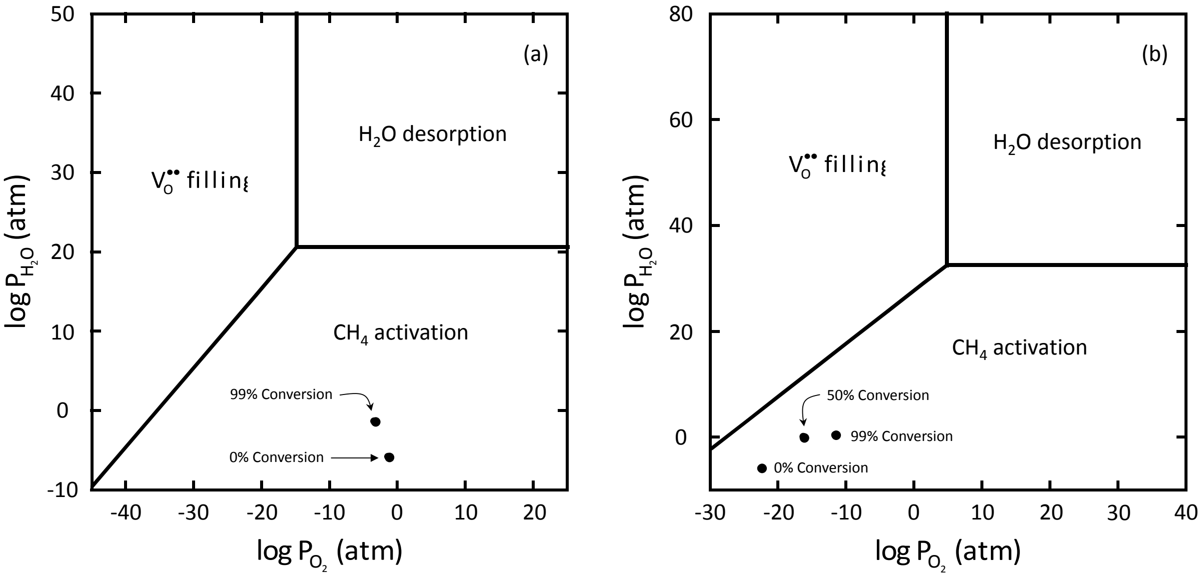

Figure 4-8. Phase regions of rate determining steps of methane oxidation over $Pd_xCe_{1-x}O_2$(111) at 298K/catalytic combustion operating conditions (a) and 973K/SOFC conditions (b). Filled circles (•) represent conditions at the labeled conversions for (a) 298K/catalytic combustion and (b) 973K/SOFC.

The comparison of rate determining regions on $Pd_xCe_{1-x}O_2$(111) versus CeO_2(111) illustrate the trade-off in the development of ceria-based mixed oxide catalysts between surface reducibility and C-H bond activity as established in our previous study.[38] The incorporation of Pd^{4+} ions into the CeO_2 lattice increases the reducibility of the ceria surface, and thereby the catalytic activity for methane oxidation. Though the tradeoff is that increased reducibility will make vacancy filling more difficult, vacancy filling is rate determining only at very low O_2 ($<10^{-30}$ atm) pressures at both 298K and 973K, suggesting that the catalysis of hydrocarbon oxidation by ceria-based oxides is only dependent on the energetics of C-H activation.

Plots depicting the dependence of rate determining steps on operating pressures at 298K and 973K for methane oxidation over PdO(100), Pd(111), and Pd*/CeO_2(111), are included in the Supporting Information. At both 298K and 973K, methane oxidation is limited by C-H activation over Pd*/CeO_2(111), PdO(100), and Pd(111) at all conversions.

4.4 Conclusions

The DFT+*U* method was used to calculate the free energies of elementary methane oxidation reaction steps over pure CeO_2(111), $Pd_xCe_{1-x}O_2$(111), PdO(100), and Pd(111). Methane oxidation over Pd-ceria is limited by C-H activation, the barrier of which is affected by the oxidation state, morphology and chemical composition of the surface. At low coverage, methane oxidation occurs over each surface via C-H breaking steps to CH*, C-O forming to form HCO* (equivalent to $HCOO^-$ atop an oxygen defect for each oxide surface), subsequent C-H breaking to CO*, and finally C-O formation and desorption as CO_2(g). The formation of C* is not favored over any surface, suggesting that, under the reaction conditions considered, deactivation due to the formation of carbon deposits is not likely. The formation of partial oxidation products is also not thermodynamically favorable, in agreement with the selectivity of ceria, palladium, and palladium-ceria for the complete oxidation of CH_4 to CO_2.

Table 4-1 lists the activation barrier, relative combustion rate, and most stable intermediate over each surface considered. Rate constants were calculated as:

$$k=\frac{k_B T}{h} e^{\frac{-\Delta^{\ddagger} G^0}{RT}}$$

where k_B is boltzmann's constant, T is temperature, h is planck's constant, R is the universal gas constant, and $\Delta^{\ddagger}G^0$ is the standard free energy of activation. The relative combustion rates listed in Table 4-1 are the ratios of the rate constant over each surface to the rate constant over CeO_2(111). Methane activation is rate determining over each surface, at both catalytic combustion and SOFC operating conditions. The methane activation barrier is lowest over $Pd_xCe_{1-x}O_2$(111), lower than that over Pd(111), stepped Pd(211),[56] kinked Pd(211),[56] PdO(100), Pd*/CeO_2(111), and CeO_2(111). The relative rate of methane oxidation over $Pd_xCe_{1-x}O_2$(111) is three orders of magnitude larger than that over stepped Pd(111), and much larger (> 13 orders of magnitude) than over Pd(111), CeO_2(111), and PdO(100).

These results indicate that incorporated Pd^{4+} ions in ceria provide higher catalytic activity for methane oxidation than large Pd particles (Pd(111)) or large palladium oxide particles (PdO(100)). An actual Pd-ceria catalyst will contain a heterogeneous distribution of surface sites, particle sizes, and Pd oxidation states. The relative rate of methane oxidation over $Pd_xCe_{1-x}O_2$(111) shows that, even if the concentration of incorporated Pd^{4+} atoms is 1000 times smaller than that of stepped or kinked sites on metallic particles, the rate of methane oxidation over incorporated Pd^{4+} will provide the majority of the overall reaction rate. Stable intermediates differ over incorporated Pd^{4+} versus Pd^0, Pd^{2+}, or CeO_2, and thus intermediates identified experimentally may correspond to those present on less active sites than incorporated Pd^{4+}.

Our models represent the limits of ideally dispersed Pd^{4+} and infinitely large Pd or PdO particles. Experimental studies establish the importance of Pd-O-Ce linkages and more generally oxidized Pd species in dictating the catalytic activity of Pd-ceria, however these sites could exist on the edge of metal or PdO clusters. Consideration of all possible particle sizes and morphologies is computationally prohibitive and it is possible that highly active sites at the boundary between PdO_x particles and the CeO_2 support could provide activity similar to incorporated $Pd_xCe_{1-x}O_2$(111). This study illustrates that mixed noble metal-ceria oxides can provide enhanced activity for hydrocarbon oxidation by tuning the reducibility of the mixed nobel metal-ceria surface, and thereby the methane activation kinetics. These results provide insight into the catalytic activity and surface functionality of Pd-ceria for hydrocarbon oxidation, and motivate future efforts in the development of noble metal-ceria mixed oxide catalysts.

4.5 References

(1) Zhou, G.; Shah, P. R.; Montini, T.; Fornasiero, P.; Gorte, R. J. *Surface Science* **2007**, *601*, 2512-2519.

(2) Aneggi, E.; Boaro, M.; Leitenburg, C. d.; Dolcetti, G.; Trovarelli, A. *Journal of Alloys and Compounds* **2006**, *408-412*, 1096-1102.

(3) Bensalem, A.; Bozon-Verduraz, F.; Perrichon, V. *Journal of the Chemical Society, Faraday Transactions* **1995**, *91*, 2185-2189.

(4) Wang, B.; Weng, D.; Wu, X.; Fan, J. *Catalysis Today* **2010**, *153*, 111-117.

(5) Colussi, S.; Gayen, A.; Camellone, M. F.; Boaro, M.; Llorca, J.; Fabris, S.; Trovarelli, A. *Angewandte Chemie International* **2009**, *48*, 8481-8484.

(6) McIntosh, S.; Vohs, J. M.; Gorte, R. J. *Electrochemical and Solid-State Letters* **2003**, *6*, A240-A243.

(7) Oh, S. H.; Hoflund, G. B. *Journal of Physical Chemistry A* **2006**, *110*, 7609-7613.

(8) Xiao, L.; Sun, K.; Xu, X.; Li, X. *Catalysis Communications* **2005**, *6*, 796-801.

(9) Badri, A.; Binet, C.; Lavalley, J. C. *Journal of the Chemical Society, Faraday Transactions* **1996**, *92*, 1603-1608.

(10) Graham, G. W.; Jen, H. W.; McCabe, R. W.; Straccia, A. M.; Haack, L. P. *Catalysis letters* **2000**, *67*, 99-105.

(11) Jen, H. W.; Graham, G. W.; Chun, W.; McCabe, R. W.; Cuif, J. P.; Deutsch, S. E.; Touret, O. *Catalysis Today* **1999**, *50*, 309-328.

(12) Wang, X. G., R.J.; Wagner, J.P. *Journal of Catalysis* **2002**, *212*, 225-230.

(13) Mayernick, A. D.; Janik, M. J. *Journal of Chemical Physics* **2009**, *131*.

(14) Holles, J. H.; Davis, R. J.; Murray, T. M.; Howe, J. M. *Journal of Catalysis* **2000**, *195*, 193-206.

(15) Matsumura, Y.; Shen, W.-J.; Ichihashi, Y.; Ando, H. *Catalysis Letters* **2000**, *68*, 181-183.

(16) Matsumura, W. *Physical Chemistry Chemical Physics* **2000**, *2,* 1519-1522.

(17) Priolkar, K. R.; Parthasarathi, B.; Sarode, P. R.; Hegde, M. S.; Emura, S.; Kumashiro, R.; Lalla, N. P. *Chemistry of Materials* **2002**, *14*, 2120-2128.

(18) Knapp, D.; Ziegler, T. *The Journal of Physical Chemistry C* **2008**, *112*, 17311-17318.

(19) Zhang, H.; Gromek, J.; Fernando, G.; Marcus, H.; Boorse, S. *Journal of Phase Equilibria and Diffusion* **2002**, *23*, 246-248.

(20) Guanghui Zhu, J. H., Dmitri Yu. Zemlyanov, Fabio H. Ribeiro *Journal of Physical Chemistry B* **2005**, *109*, 2331-2337.

(21) Bozo, C.; Guilhaume, N.; Herrmann, J.-M. *Journal of Catalysis* **2001**, *203*, 393-406.

(22) Mei, D.; Aaron Deskins, N.; Dupuis, M. *Surface Science* **2007**, *601*, 4993-5001.

(23) Muller, C.; Freysoldt, C.; Baudin, M.; Hermansson, K. *Chemical Physics* **2005**, *318*, 180-190.

(24) Watkins, M. B.; Foster, A. S.; Shluger, A. L. *J. Phys. Chem. C* **2007**, *111*, 15337-15341.

(25) Kumar, S.; Schelling, P. *Journal of Chemical Physics* **2006**, *125*.

(26) Shapovalov, V.; Metiu, H. *Journal of Catalysis* **2007**, *245*, 205-214.

(27) Yang, Z.; Fu, Z.; Wei, Y.; Lu, Z. *The Journal of Physical Chemistry C* **2008**, *112*, 15341-15347.

(28) Yang, Z.; Luo, G.; Lu, Z.; Hermansson, K. *The Journal of Chemical Physics* **2007**, *127*, 074704-5.

(29) Yang, Z.; Luo, G.; Lu, Z.; Woo, T. K.; Hermansson, K. *Journal of Physics: Condensed Matter* **2008**, *20*, 035210.

(30) Kresse, G.; Furthmuller, J. *Computational Materials Science* **1996**, *6*, 15-50.

(31) Kresse, G.; Furthmuller, J. *Physical Review B* **1996**, *54*, 11169-11186.

(32) Kresse, G.; Hafner, J. *Physical Review B* **1993**, *47*, 558-561.

(33) Kresse, G.; Joubert, D. *Physical Review B* **1999**, *59*, 1758 LP - 1775.

(34) Perdew, J. P.; Chevary, J. A.; Vosko, S. H.; Jackson, K. A.; Pederson, M. R.; Singh, D. J.; Fiolhais, C. *Physical Review B* **1992**, *46*, 6671.

(35) Fabris, S.; Gironcoli, S. d.; Baroni, S.; Vicario, G.; Balducci, G. *Physical Review B* **2005**, *71*, 041102.

(36) Fabris, S.; Gironcoli, S. d.; Baroni, S.; Vicario, G.; Balducci, G. *Physical Review B* **2005**, *72*, 237102.

(37) Kresse, G.; Blaha, P.; Silva, J.; Ganduglia-Pirovano, M. V. *Physical Review B* **2005**, *72*, 237101.

(38) Mayernick, A. D.; Janik, M. J. *The Journal of Physical Chemistry C* **2008**, *112*, 14955-14964.

(39) Nolan, M.; Grigoleit, S.; Sayle, D. C.; Parker, S. C.; Watson, G. W. *Surface Science* **2005**, *576*, 217-229.

(40) Nolan, M.; Parker, S. C.; Watson, G. W. *Surface Science* **2005**, *595*, 223-232.

(41) Herschend, B.; Baudin, M.; Hermansson, K. *Surface Science* **2005**, *599*, 173-186.

(42) Yang, Z.; Lu, Z.; Luo, G.; Hermansson, K. *Physics Letters A* **2007**, *369*, 132-139.

(43) Kummerle, E. A.; Heger, G. *Journal of Solid State Chemistry* **1999**, *147*, 485-500.

(44) Waser, J.; Levy, H. A.; Peterson, S. W. *Acta Crystallographica* **1953**, *6*, 661-663.

(45) Lazarev, I. *Russian Journal of Inorganic Chemistry* **1978**, *23*, 488.

(46) Rogal, J.; Reuter, K.; Scheffler, M. *Physical Review B* **2004**, *69*.

(47) Henkelman, G.; Jonsson, H. *Journal of Chemical Physics* **2000**, *113,* 9978-9985.

(48) Henkelman, G.; Uberuaga, B. P.; Jonsson, H. *Journal of Chemical Physics* **2000**, *113,* 9901-9904.

(49) Mills, G.; Jonsson, H.; Schenter, G. K. *Surface Science* **1995**, *324,* 305-337.

(50) Bozo, C.; Guilhaume, N.; Garbowski, E.; Primet, M. *Catalysis Today* **2000**, *59*, 33-45.

(51) Huang, M.; Fabris, S. *Journal of Physical Chemistry C* **2008**, *112*, 8643-8648.

(52) Nolan, M.; Parker, S. C.; Watson, G. W. *Surface Science* **2006**, *600*, 175-178.

(53) Jacobs, G.; Patterson, P. M.; Williams, L.; Chenu, E.; Sparks, D.; Thomas, G.; Davis, B. H. *Applied Catalysis A: General* **2004**, *262*, 177-187.

(54) Jacobs, G.; Ricote, S.; Graham, U. M.; Patterson, P. M.; Davis, B. H. *Catalysis Today* **2005**, *106*, 259-264.

(55) Jason F. Weaver, J. A. H. J., Can Hakanoglu, Abbin Antony, Jeffery M. Hawkins, Aravind Asthagiri. *Catalysis Today* **2010**, *(in press)*.

(56) Liu, Z.; Hu, P. *Journal of the American Chemical Society* **2003**, *125*, 1958-1967.

(57) Murdoch, J. R. *Journal of Chemical Education* **1981**, *58,* 32.

(58) An, S.; Lu, C.; Worrell, W. L.; Gorte, R. J.; Vohs, J. M. *Solid State Ionics* **2004**, *175*, 135-138.

(59) McIntosh, S.; Gorte, R. J. *Chemical Reviews* **2004**, *104*, 4845-4865.

(60) Putna, E. S.; Stubenrauch, J.; Vohs, J. M.; Gorte, R. J. *Langmuir* **1995**, *11*, 4832-4837.

4.6 Supporting Information

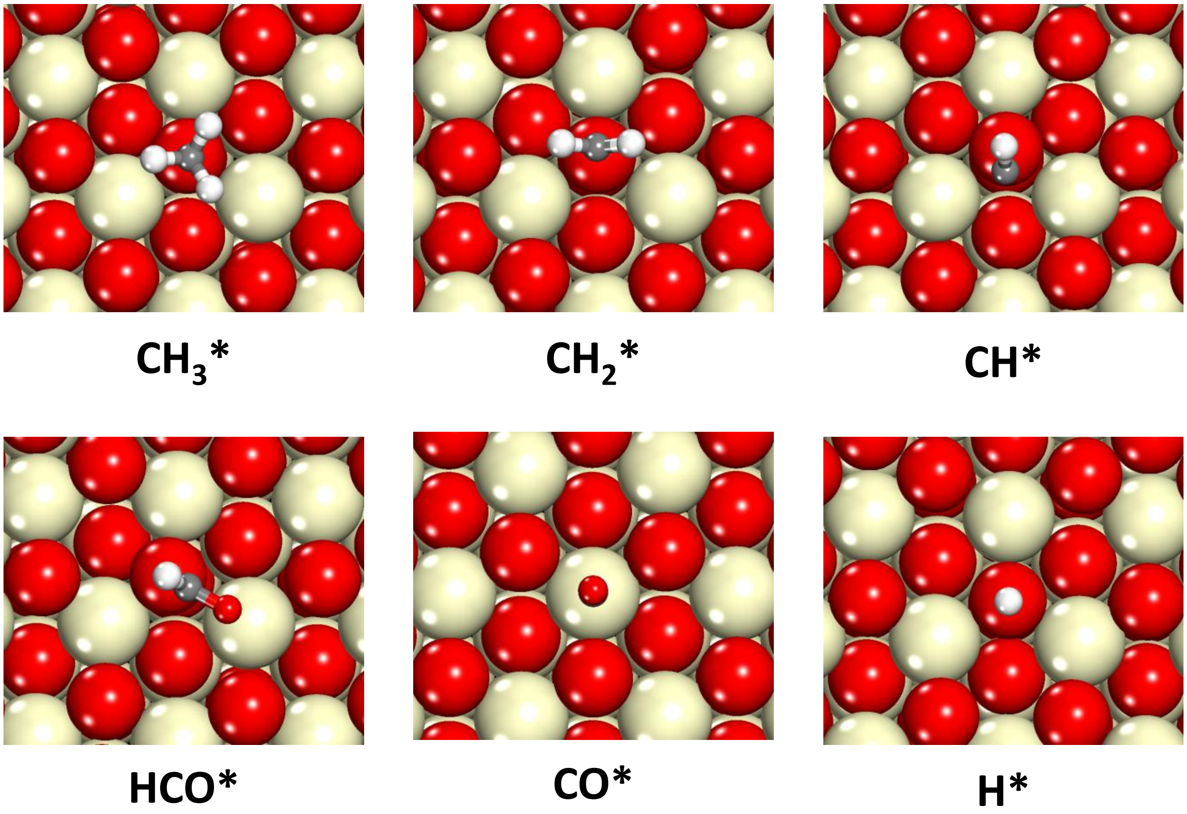

CH_3*

CH_2*

CH*

HCO*

CO*

H*

Supporting Information Figure S1. Adsorption geometries for methane oxidation intermediates on CeO_2(111).

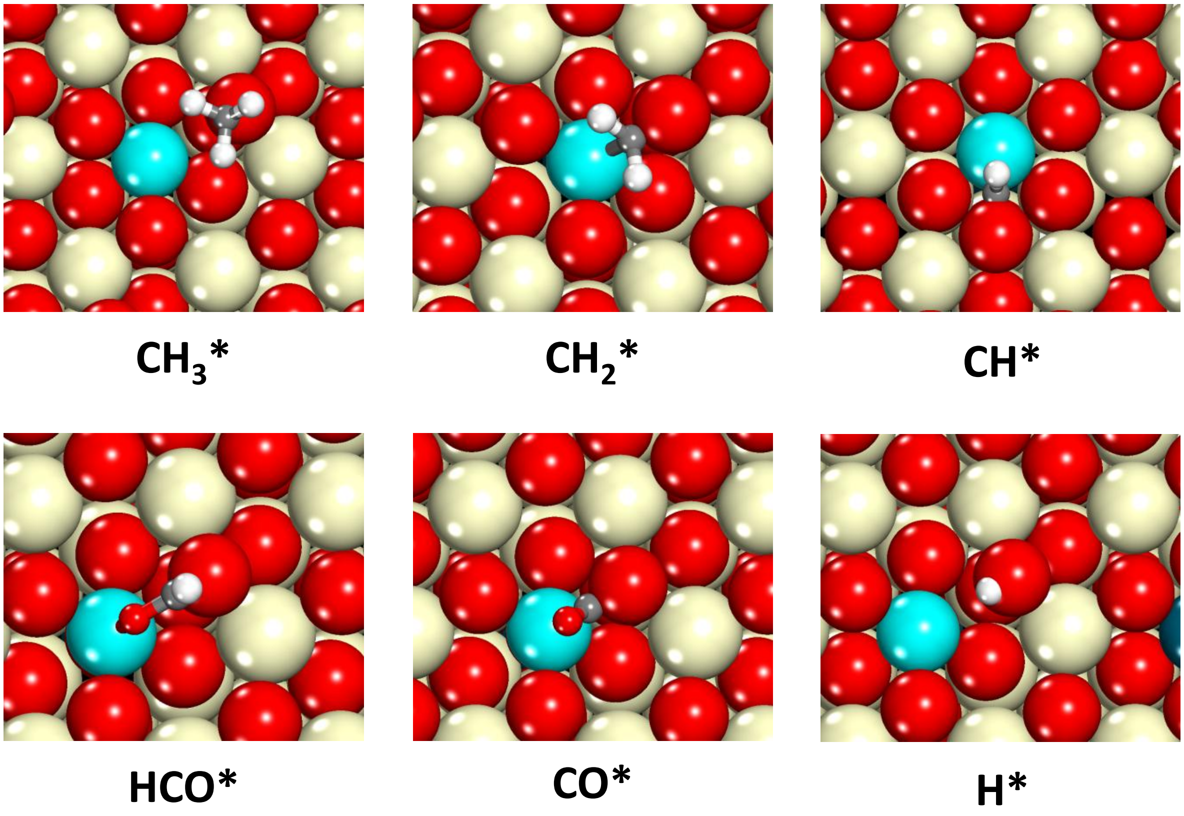
CH_3*
CH_2*
CH*
HCO*
CO*
H*

Supporting Information Figure S2. Adsorption geometries for methane oxidation intermediates on $Pd_xCe_{1-x}O_2$(111).

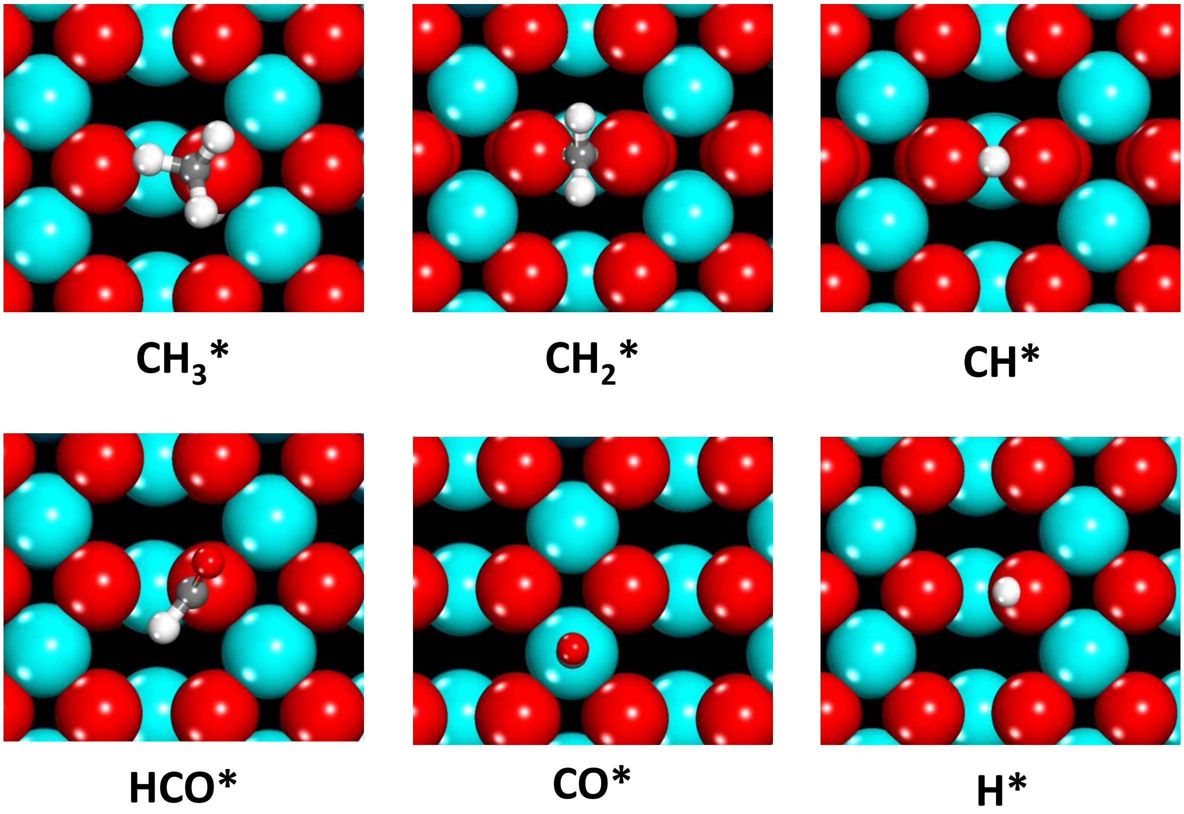

CH_3*

CH_2*

CH*

HCO*

CO*

H*

Supporting Information Figure S3. Adsorption geometries for methane oxidation intermediates on PdO(100).

Supporting Information Section 1.1 Methane Oxidation on Pd*/CeO_2(111)

The Pd*/CeO_2(111) surface was modeled by placing a single Pd atom on each side of the mirrored CeO_2(111) slab at the O_h adsorption site, at which the adsorption of a single Pd atom is more exothermic than all other sites on the CeO_2(111) surface.[1] The Pd*/CeO_2(111) surface model presented herein corresponds to the most stable single atom state of Pd on CeO_2(111) at high temperatures and low oxygen partial pressures, as discussed in our previous study.[1]

Figure S5 displays the reaction free energy diagram for methane oxidation on Pd*/CeO_2(111) at catalytic combustion conditions. Methane activation on Pd*/CeO_2(111) is characterized by minimal interaction of H or CH_3 fragments with the Pd adatom. We were unable to locate an adsorption mode for both CH_3 and H on the single Pd adatom, and adsorption of either CH_3 or H to the Pd*/CeO_2(111) surface is more stable atop a surface oxygen atom than on the Pd atom. The dissociative adsorption energy of methane for H atop the Pd adatom and CH_3 atop a surface oxygen atom (CH_4(g) + Pd* → (H-Pd)* + CH_3*) at 298K is +1.35 eV and for CH_4(g) + Pd* → (CH_3-Pd)* + H* is +0.55 eV, in contrast with a free energy of -0.03 eV for adsorption of both CH_3 and H atop surface oxygen atoms (CH_4(g) → H* + CH_3*). Because it is unfavorable for the single supported Pd atom to participate in CH_4 activation, we approximate the methane activation barrier over the Pd*/CeO_2(111) surface as the energy of $CH_4(g)\rightarrow\cdot CH_3+H^*$ (H abstraction and methyl radical formation). The free energy of ($\cdot CH_3+H^*$) over Pd*/CeO_2(111) is +1.87 eV (+1.30 eV at 0K), similar to that over pure ceria (+1.83 eV, +1.29 eV at 0K).

The lack of activity of single supported Pd^0 atoms on ceria for the activation of C-H bonds can be explained based on the electronic interaction between Pd d electrons and the σ orbitals of C-H bonds during activation. The d electrons of a single Pd atom occupy a discrete energy level with an energy gap between the filled d orbitals (d^{10}) and the next highest energy level. As the number of Pd atoms in a supported cluster increases, this energy gap decreases and unfilled Pd states lie directly above the filled d states.[2] Activation of a methane C-H bond over a metallic Pd cluster is dependent on donation of e^- from the σ bonding orbital to Pd, and back donation to the σ* orbital of the C-H bond. This process of C-H activation is unfavorable if the energy gap between the filled and unfilled states on the metal cluster is too large, suggesting that the activity of Pd clusters supported on ceria depends on a balance between large enough clusters to allow for electronic delocalization of the band structure and small enough clusters to provide a high fraction of exposed Pd atoms and under-coordinated surface sites. The H abstraction mechanism which occurs over CeO_2 and $Pd_xCe_{1-x}O_2$ also will not occur over single Pd atoms as reduction of Pd^0 is unfavorable.

Each C-H breaking step over $Pd^*/CeO_2(111)$ is exergonic, with each step after CH_3 more exergonic than the corresponding step on pure ceria due to strong interactions between adsorbates and the Pd adatom. Each CH_x species ($1 \leq x \leq 3$) adsorbs atop a surface oxygen atom on $Pd^*/CeO_2(111)$, shifted off-center towards the Pd adatom. Water formation is more exergonic and oxygen vacancy filling more endothermic by 0.24 eV on $Pd^*/CeO_2(111)$ than pure ceria. The most stable intermediate over $Pd^*/CeO_2(111)$ is *CO, which binds strongly to the Pd adatom on $CeO_2(111)$. The formation of partial oxidation products as well as CO_2^* is prohibitively endergonic over $Pd^*/CeO_2(111)$.

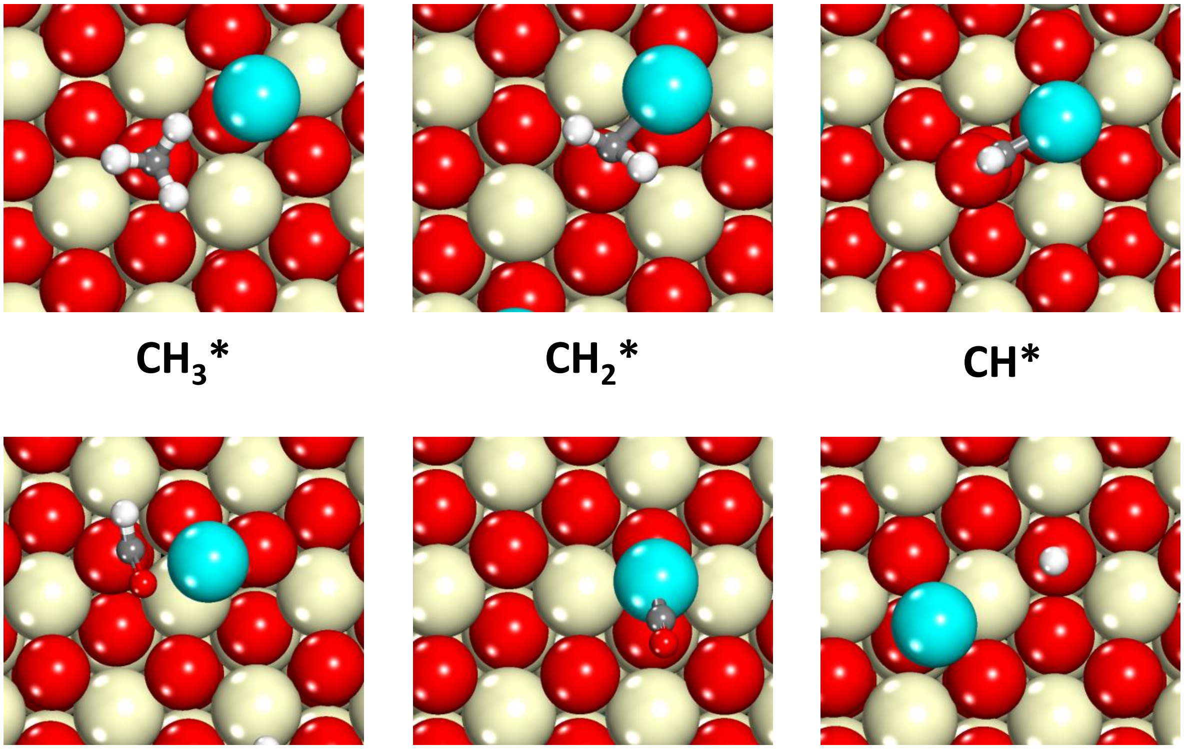

CH_3* CH_2* $CH*$

$HCO*$ $CO*$ $H*$

Supporting Information Figure S4. Adsorption geometries for methane oxidation intermediates on Pd*/CeO_2(111).

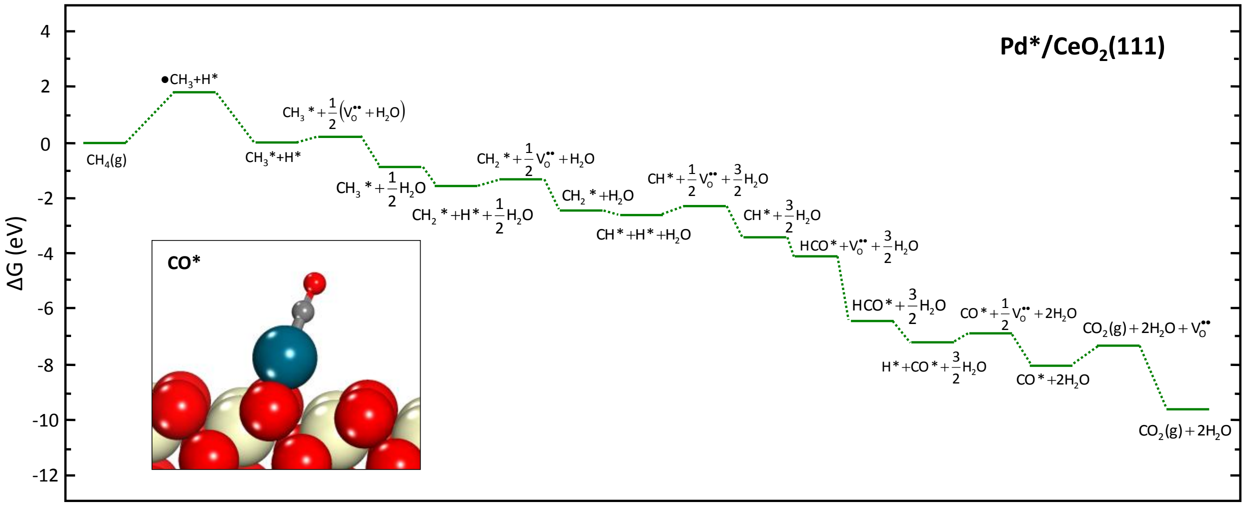

Supporting Information Figure S4. Reaction free energy diagram for $CH_4(g) + 2O_2(g) \rightarrow CO_2(g) + 2H_2O(g)$ over Pd*/CeO$_2$(111) at T=298K and P_{CH_4}= 0.01 atm, P_{O_2}= 0.04 atm, P_{H_2O}= P_{CO_2}= 10^{-6} atm. Inset: CO*, the most stable intermediate in methane oxidation over Pd*/CeO$_2$(111). Ce is displayed as tan (light), O as red (dark), C as grey, and H as white. Oxygen (O_2) is not explicitly included in the oxidation mechanism, as addition of O_2 to the surface occurs in oxygen vacancy filling steps.

Pd*/CeO$_2$(111)	0K ΔE (eV)
$CH_4(g) \rightarrow CH_3^* + H^*$	-0.71
$CH_3^* \rightarrow CH_2^* + H^*$	-0.72
$CH_2^* \rightarrow CH^* + H^*$	-0.12
$CH^* \rightarrow HCO^*$	-0.60
$HCO^* \rightarrow CO^* + H^*$	-0.83
$CO^* \rightarrow CO_2(g)$	+1.65

Table S1. Reaction energies at 0K for each elementary step in methane oxidation over Pd*/CeO$_2$(111).

Supporting Information Section 1.2 Methane Oxidation on Pd(111)

We used a 4-layer non-mirrored slab to model the Pd(111) surface, with the bottom two layers fixed at their bulk positions. The Pd(111) surface was represented in a $(\sqrt{3}\times\sqrt{3})$ expansion, which results in a termination of 3 surface Pd atoms per unit cell. The following equation was used to calculate the formation energy of $H_2O(g)$ on Pd(111):

$$\Delta G_{H_2O\_formation} = [G_{H_2O} + 3\cdot G_{bare}] - [2\cdot G_{H*} + G_{O*}] \qquad (1)$$

where G_{O*} is the free energy of adsorbed O, and water is formed by the formation of H_2O* from adsorbed H and O atoms, and then desorption of $H_2O(g)$.

We use the Pd(111) surface to approximate the surface of a large reduced palladium (Pd^0) particle, and evaluate methane oxidation energetics over Pd(111) for comparison with other surface models. Figure S6 displays the reaction energy diagram for methane oxidation on Pd(111) at catalytic combustion conditions. Methane oxidation on Pd(111) occurs via the reaction of adsorbed CH_x* species and adsorbed oxygen atoms O*, in contrast to this reaction on each oxide surface in which CH_x* species react with lattice oxygen. Figure 4-3(b) displays the transition state for methane activation on Pd(111), which occurs via cleavage of a C-H bond of methane and the formation of CH_3* and H*. The free energy of activation ($\Delta^{\ddagger}G$) over Pd(111) is +1.49 eV (+0.89 eV at 0K), which is higher only than the barrier over $Pd_xCe_{1-x}O_2(111)$. The 0K methane activation barrier over stepped or kinked Pd surfaces is 0.38 and 0.41 eV (at 0K),[3] respectively, of which both values are higher than over $Pd_xCe_{1-x}O_2(111)$. Methane oxidation follows the same intermediates over Pd(111) as over each ceria surface and PdO, with the only endergonic step being $CH_3^* \rightarrow CH_2^* + H^*$. Every other elementary step is exergonic over Pd(111), including both water formation and oxygen dissociation $\left(\frac{1}{2}O_2 \rightarrow O^*\right)$.

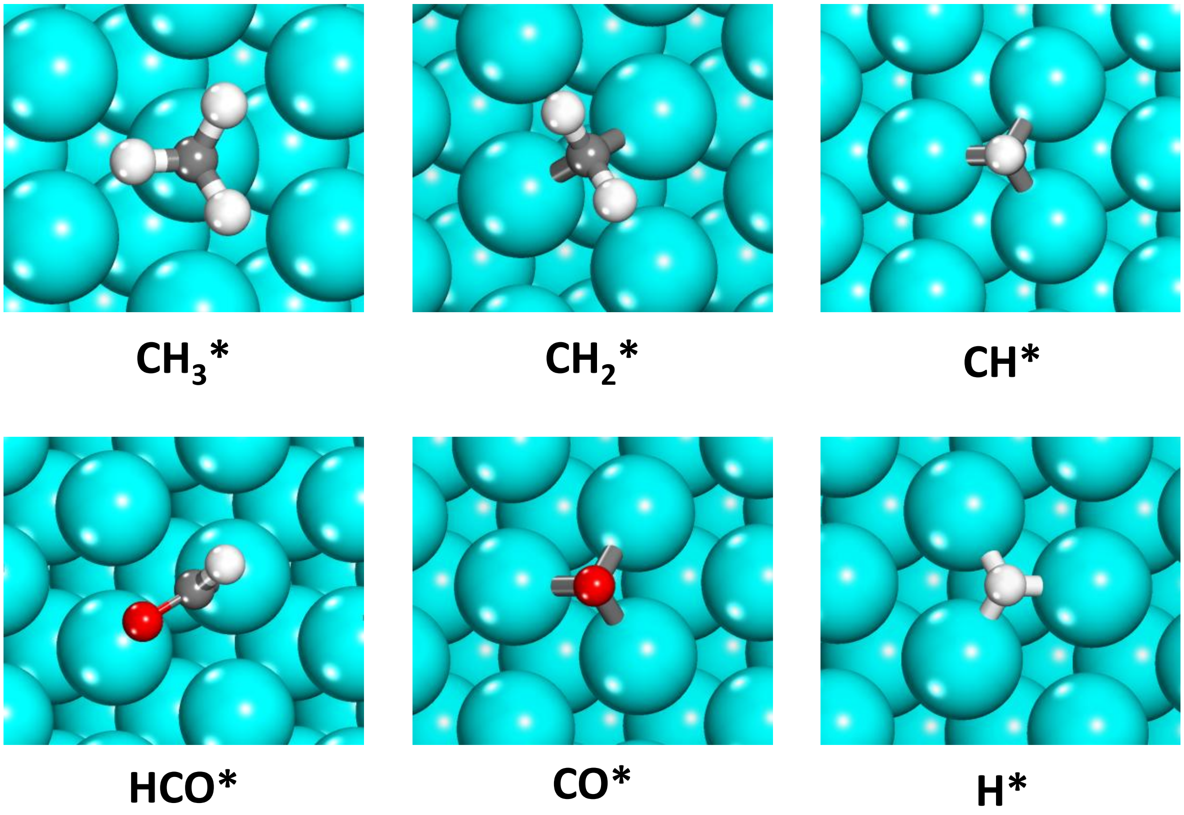

CH_3^* CH_2^* CH^*

HCO^* CO^* H^*

Supporting Information Figure S5. Adsorption geometries for methane oxidation intermediates on Pd(111).

Pd(111)	0K ΔE (eV)
$CH_4(g) \rightarrow CH_3^* + H^*$	-1.96
$CH_3^* \rightarrow CH_2^* + H^*$	+0.20
$CH_2^* \rightarrow CH^* + H^*$	-0.40
$^*CH \rightarrow {}^*HCO$	-0.42
$HCO^* \rightarrow CO^* + H^*$	-1.61
$CO^* \rightarrow CO_2(g)$	+0.23

Table S2. Reaction energies at 0K for each elementary step in methane oxidation over Pd(111).

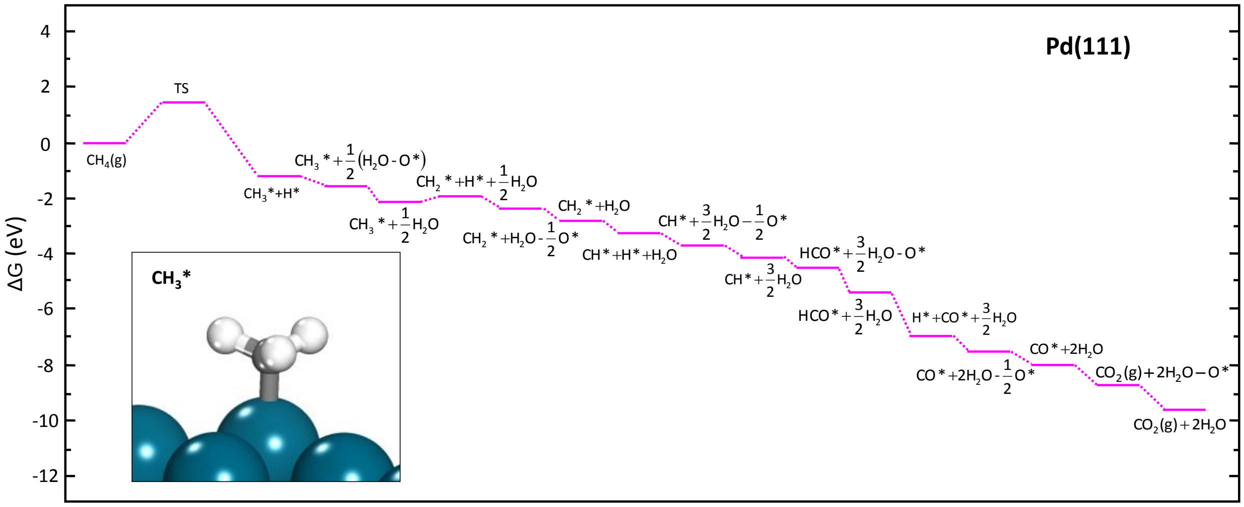

Figure S6. Reaction free energy diagram for $CH_4(g) + 2O_2(g) \rightarrow CO_2(g) + 2H_2O(g)$ over Pd(111) at T=298K and $P_{CH_4}= 0.01$ atm, $P_{O_2}= 0.04$ atm, $P_{H_2O}= P_{CO_2}= 10^{-6}$ atm.. Inset: CO*, the most stable intermediate in methane oxidation over Pd(111). Pd is displayed as light blue (grey), O as red (dark), and C as grey.

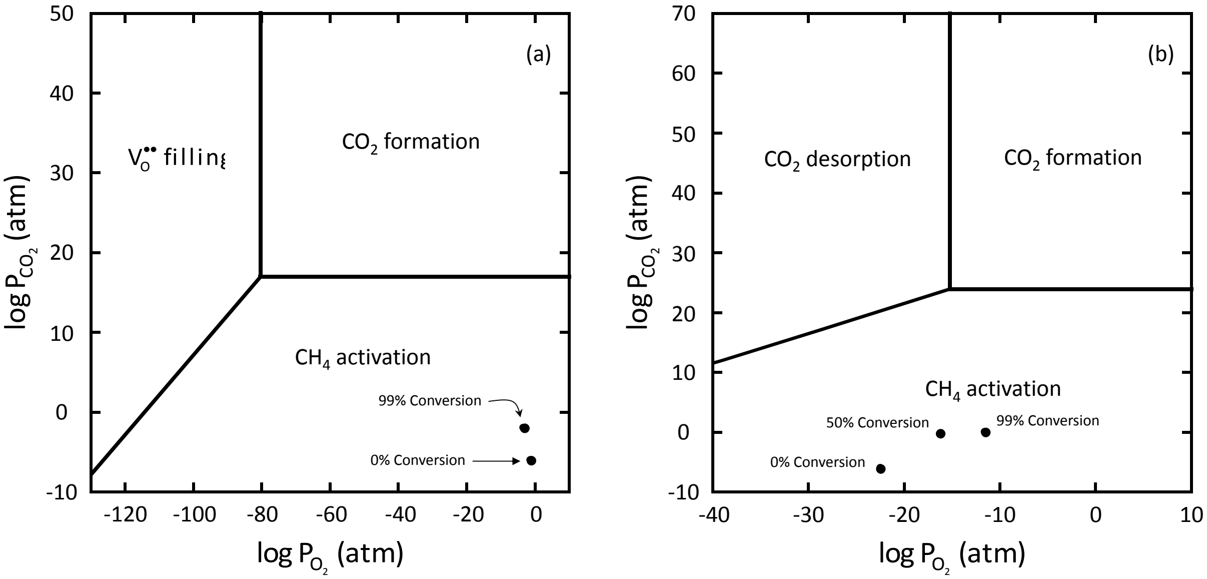

Supporting Information Figure S7. Phase regions of rate determining steps of methane oxidation over Pd*/CeO$_2$(111) at 298K/catalytic combustion operating conditions (a) and 973K/SOFC conditions (b). Filled circles (•) represent conditions at the labeled conversions for (a) 298K/catalytic combustion and (b) 973K/SOFC.

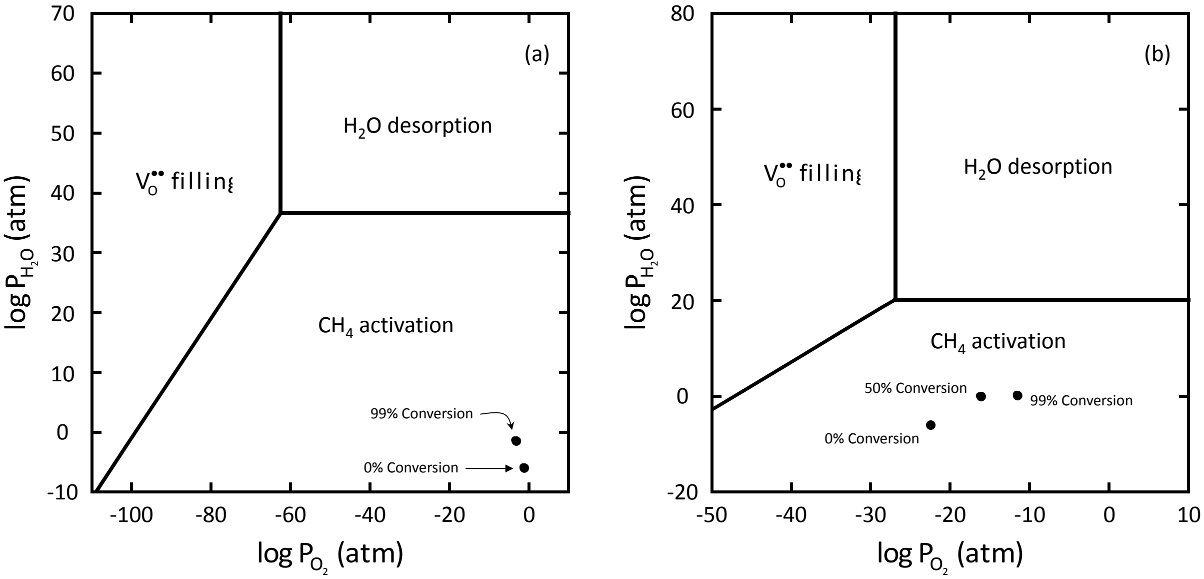

Supporting Information Figure S8. Phase regions of rate determining steps of methane oxidation over PdO(100) at 298K/catalytic combustion operating conditions (a) and 973K/SOFC conditions (b). Filled circles (•) represent conditions at the labeled conversions for (a) 298K/catalytic combustion and (b) 973K/SOFC.

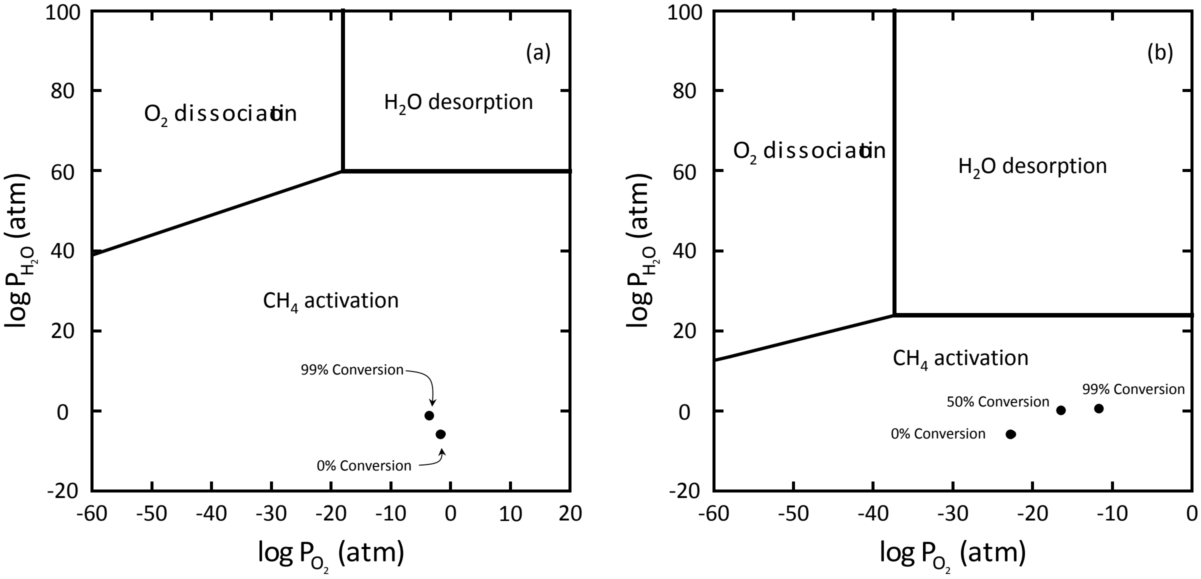

Supporting Information Figure S9. Phase regions of rate determining steps of methane oxidation over Pd(111) at 298K/catalytic combustion operating conditions (a) and 973K/SOFC conditions (b). Filled circles (•) represent conditions at the labeled conversions for (a) 298K/catalytic combustion and (b) 973K/SOFC.

SUPPORTING INFORMATION REFERENCES

(1) Mayernick, A. D.; Janik, M. J. *Journal of Chemical Physics* **2009**, *131*.

(2) Saillard, J. Y.; Hoffmann, R. *Journal of the American Chemical Society* **1984**, *106*, 2006-2026.

(3) Liu, Z.-P.; Hu, P. *Journal of the American Chemical Society* **2003**, *125*, 1958-1967.

Chapter 5

Correlating C-H bond Activity and Oxide Reducibility: Electronic Structure Analysis of the Catalytic Activity of Dopant Metals in Ceria

ABSTRACT: The hydrocarbon oxidation activity and thermodynamic stability of the mixed palladium-ceria surface ($Pd_xCe_{1-x}O_2$(111)) is established in Chapters 2 through 4. The stability of Pd^{4+} in the ceria lattice is due to the geometry and flexibility of oxygen atoms in the coordination shell of Pd, which allow for approximately octahedral and square planar coordination for the Pd^{4+} and Pd^{2+} oxidation states, respectively. The low methane activation barrier over $Pd_xCe_{1-x}O_2$(111) is due to exergonic reduction of Pd^{4+} to Pd^{2+}, which is more exergonic than reduction of Ce^{4+} to Ce^{3+}. This chapter extends the correlation between surface reducibility and C-H bond activity established in Chapter 2 for CeO_2, $Pd_xCe_{1-x}O_2$, and $Zr_xCe_{1-x}O_2$, across *d*-block transition metal dopants in CeO_2(111). Transition metals including Ni and Cu increase the reducibility of the ceria surface (lower the oxygen vacancy formation energy, methane adsorption energy) further than Pd, and the oxygen vacancy formation energy correlates with dissociative methane adsorption energy.

5.1 Introduction

Doping of ceria with transition metals alters the catalytic activity for breaking C-H bonds. For example, doping Pd in ceria results in a lower methane activation barrier than that over the pure ceria or Pd surface (Chapters 2, 4).[1,2] Palladium is widely used in catalytic combustors due to the catalytic activity of the pure metal for hydrocarbon oxidation,[3] however the low barrier over the $Pd_xCe_{1-x}O_2$ surface illustrates that the C-H bond activity of ceria-based mixed oxides may be greater than that of the pure metal constituents. Methane activation over the ceria surface occurs via dissociative adsorption of CH_3* and H* and a 2 e^- reduction of surface metal atoms (Chapter 2);[1] dopant transition metals substituted into the ceria surface may serve as more reducible metal centers than Ce^{4+} or may perturb the ceria surface structure and thereby increase the reducibility of Ce^{4+}. The dissociative adsorption energy of methane correlates with the oxygen vacancy formation energy of the ceria surface (Chapter 2),[1] suggesting that optimization of ceria-based oxidation catalysts may be achieved by tailoring composition to maximize surface reducibility. This chapter addresses the correlation between surface reducibility and methane activation energetics across a series of transition metals, and probes the surface and electronic structure of the oxidized and reduced $Pd_xCe_{1-x}O_2(111)$ surface.

The incorporation of metals such as Zr or Pd into the ceria lattice at the surface decreases the energy of oxygen vacancy formation, as well as the reaction energy and barrier for methane adsorption (Chapter 2).[1] Oxygen vacancy formation energy and methane activation energy correlate over the (111), (110), (100) CeO_2 surface terminations for pure CeO_2 and for Pd and Zr-substituted CeO_2 (Chapter 2).[1] The dissociative methane adsorption energy is more exothermic over $Pd_xCe_{1-x}O_2$ than over $Zr_xCe_{1-x}O_2$ and pure CeO_2. Adsorption of CH_3* and H* to $Pd_xCe_{1-x}O_2$ results in reduction of Pd^{4+} to Pd^{2+}.[1] The methane activation barrier is lower over Pd_xCe_{1-}

${}_xO_2$(111) than over Pd or PdO (Chapter 4).[2] Methane activation is the rate limiting step in methane oxidation to CO_2 and H_2O over CeO_2(111), $Pd_xCe_{1-x}O_2$(111), PdO, and Pd, confirming that methane oxidation proceeds at a faster rate over $Pd_xCe_{1-x}O_2$(111) than over Pd or PdO. The $Pd_xCe_{1-x}O_2$(111) surface is thermodynamically favorable with respect to supported Pd atoms on CeO_2(111) at low temperatures and high oxygen partial pressures (below 500K in air at 1 atm, Chapter 3).[4] The lower methane activation barriers over Zr and Pd-substituted ceria surfaces and the fact that methane activation is rate limiting over CeO_2(111) and $Pd_xCe_{1-x}O_2$(111) suggests that the hydrocarbon oxidation activity of ceria-based oxides may be further optimized by identifying dopant metals which decrease the oxygen vacancy formation energy (reducibility) below that of the $Pd_xCe_{1-x}O_2$ surface.

This chapter investigates the correlation between surface reducibility and C-H bond breaking energetics for a series of transition metals dopants. Our goal is to identify dopant metals which may offer increased C-H breaking activity with respect to palladium. The electronic structure of the $Pd_xCe_{1-x}O_2$(111) surface is probed using a projected density of states (PDOS) analysis, to resolve the thermodynamic stability and C-H dissociation activity of Pd^{4+} ions in $Pd_xCe_{1-x}O_2$(111). Specific Pd d states are imaged on the $Pd_xCe_{1-x}O_2$(111) lattice and the electronic structure about the doped Pd^{4+} or Pd^{2+} ion is interpreted using crystal field splitting principles.

5.2 Methods

5.2.1 Electronic Structure Method

Calculations were performed using the Vienna *ab initio* simulation program (VASP), an *ab initio* total-energy and molecular dynamics program developed at the Institute for Material Physics at the University of Vienna.[5-7] The projector augmented wave method[8] was used to represent the core region, with valence electron wavefunctions expanded in a tractable plane wave basis set. The energy cutoff of the plane wave basis set used herein was 450 eV (chosen to ensure convergence of total energy with respect to energy cutoff). Valence configurations were $5s^2 5p^6 6s^2 4f^1 5d^1$ for cerium, $2s^2 2p^4$ for oxygen, $4d^{10}$ for Pd, $2s^2 2p^2$ for C and $1s^1$ for H. Valence configurations used for each transition metal other than Ce or Pd utilized herein are listed in the Supporting Information. Structural optimizations were performed by minimizing the forces on all atoms to below 0.05 eV $Å^{-1}$, and all calculations were spin-polarized. The Perdew-Wang (PW91) version of the generalized gradient approximation (GGA) was used to incorporate exchange and correlation energies.[9] Due to well-established difficulties within DFT to accurately represent the nature of 4*f* states in ceria,[10-12] we implemented the DFT+*U* approach. We used a value of $U = 5$ eV, which is consistent with recommended values within the DFT+*U* method used in previous studies of ceria[13-18] and ensures proper localization of 4*f* electrons. The dependence of absolute values for adsorption and oxygen vacancy formation energies on U value is discussed in Chapter 1.[1]

5.2.2 Surface Models

Figure 5-1 displays the $Pd_xCe_{1-x}O_2(111)$ surface, as an example of the surface model used for the transition metal doped ceria surface. Each surface model consists of a mirrored slab on which methane adsorption and oxygen vacancy formation are considered on both sides of the slab. The mirrored slab model of the ceria surface was used specifically to minimize slab to slab interactions which may result from a large net surface dipole moment upon the interaction of the surface with adsorbates and the reduction of surface metal ions. The ceria surface is modeled as a 12-layer ($Ce_{16}O_{32}$) mirrored slab of the (111) termination of cubic fluorite CeO_2 separated by 15 Å of vacuum in the direction perpendicular to the surface. The surface energy of CeO_2(111) is lowest among single crystal terminations of ceria,[1,13,14] indicating that this surface termination will represent a large portion of a polycrystalline CeO_2 surface. The Brillouin zone was sampled using a (2×2×1) MP grid for the (111) surface, with the third vector perpendicular to the surface. We use a *p*(2×2) expansion of the surface unit cell, which results in a termination of four surface oxygen atoms on each side of the slab and four Ce atoms in the atomic layer below. For doped ceria surfaces, two transition metal atoms are substituted for two surface Ce atoms, one on each surface of the mirrored slab.

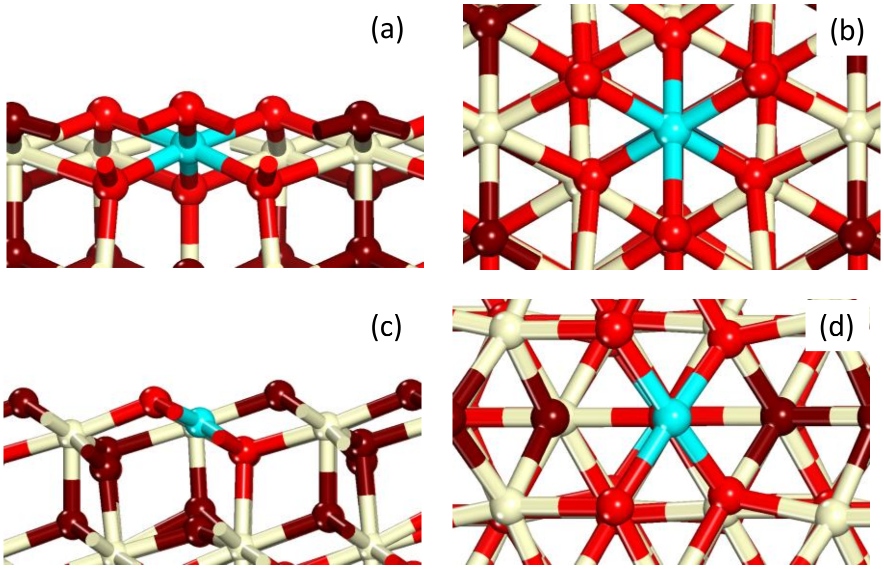

Figure 5-1. Side (a),(c) and top (b), (d) views of the $Pd_xCe_{1-x}O_2$(111) (a), (b) and the oxygen vacant $Pd_xCe_{1-x}O_y$(111) (c), (d) surfaces. Ce atoms are colored tan, Pd are colored blue, and oxygen are colored red. Oxygen atoms not coordinated to the Pd atom in (b) and (d) are colored brown.

5.2.3 Adsorption, Oxygen Vacancy Formation, and Work Function

Oxygen vacancy formation energy is calculated by removing a surface oxygen atom adjacent to the transition metal dopant in the $CeO_2(111)$ surface:

$$\Delta E_{vac}= \frac{E_{M_xCe_{1\text{-}x}O_{2\text{-}\delta}}+E_{O_2}\text{-}E_{M_xCe_{1\text{-}x}O_2}}{2} \qquad (1)$$

where $E_{M_xCe_{1\text{-}x}O_{2\text{-}\delta}}$ is the energy of the oxygen vacant surface, E_{O_2} is the energy of the isolated oxygen molecule, and $E_{M_xCe_{1\text{-}x}O_2}$ is the energy of the intact surface. The denominator of 2 is included as vacancy formation occurs in both the top and bottom of the mirrored slab. The optimal oxygen vacancy position may be in the subsurface oxygen layer,[19] however our goal is to correlate oxygen vacancy formation and surface C-H bond dissocation energetics. The dissociative methane adsorption energy is calculated for adsorption of CH_3* and H* to surface oxygen atoms adjacent to the transition metal dopant:

$$\Delta E_{ads}= \frac{E_{CH_3*+H*}\text{-}\left(E_{M_xCe_{1\text{-}x}O_2}+2\cdot E_{CH_4}\right)}{2} \qquad (2)$$

where E_{CH_3*+H*} is the energy of the surface with CH_3* and H* adsorbates and E_{CH_4} is the energy of the isolated CH_4 molecule. Optimizations of isolated gas-phase molecules were performed with one free molecule within a 15×15×15 Å unit cell. The work function of the surface slab is calculated by referencing the DFT calculated Fermi level to the potential at the center of the vacuum layer:

$$\phi= E_{Fermi}\text{-}\Phi_{vacuum} \qquad (4)$$

where E_{fermi} is the DFT calculated fermi energy and Φ_{vacuum} is the potential of the vacuum layer.

5.3 Results and Discussion

5.3.1 Electronic Structure of the $Pd_xCe_{1-x}O_2(111)$ Surface

Figure 5-2 displays the crystal field splitting diagram for the d orbitals of a free ion, an atom in an octahedral field and an atom in a square planar field. The position of oxygen ligands in the ceria surface directly impacts the stability of each possible oxidation state for metal atoms in ceria. Figure 5-1(a),(b) displays the $Pd_xCe_{1-x}O_2(111)$ surface in which a single Pd atom is substituted for a single Ce atom in the ceria lattice. Palladium is in the 4+ oxidation state in the $Pd_xCe_{1-x}O_2(111)$ surface, and the thermodynamic stability of this substituted ion in the ceria surface demonstrated in Chapter 3[4] is due to the flexibility of the ceria surface to accommodate nearly an octahedral coordination of oxygen ions with the Pd^{4+} ion. Ce atoms in bulk CeO_2 are 8 coordinate with oxygen atoms; a single oxygen coordination is lost for surface Ce atoms upon cleaving the (111) surface. Substitution of Pd^{4+} for Ce^{4+} into the $CeO_2(111)$ surface results in displacement of a subsurface oxygen atom in the coordination shell of Pd^{4+} which permits an approximately octahedral coordination shell. The Pd^{4+} ion has 6 valence d electrons, which in an octahedral field (in the presence of octahedral ligand coordination) results in three degenerate occupied d orbitals (d_{xy}, d_{yz}, d_{xz}) and 2 degenerate unoccupied orbitals ($d_{x^2-y^2}$, d_{z^2}). The inset images in Figure 5-3 display the band decomposed density for the specific occupied Pd d states and unoccupied Pd d states. The projected d electron density of states (PDOS) for the $Pd_xCe_{1-x}O_2(111)$ surface and the oxygen vacant $Pd_xCe_{1-x}O_y(111)$ surface. In Figure 5-3(a) the peak labeled * corresponds to the three occupied d orbitals in $Pd_xCe_{1-x}O_2(111)$, which the inset image labeled * displays as the combination of d_{xy}, d_{yz}, and d_{xz} orbitals surrounding Pd^{4+}. The inset image labeled • in Figure 5-3(a) displays the electron density associated with the unoccupied orbitals $d_{x^2-y^2}$ and d_{z^2} surrounding Pd^{4+}. The flexibility and position of oxygen atoms in the ceria surface thus stabilizes the 4+ oxidation state of Pd, by permitting three filled Pd d orbitals to occupy space in a minimum energy configuration with respect to repulsive electrostatic interactions with oxygen ligands.

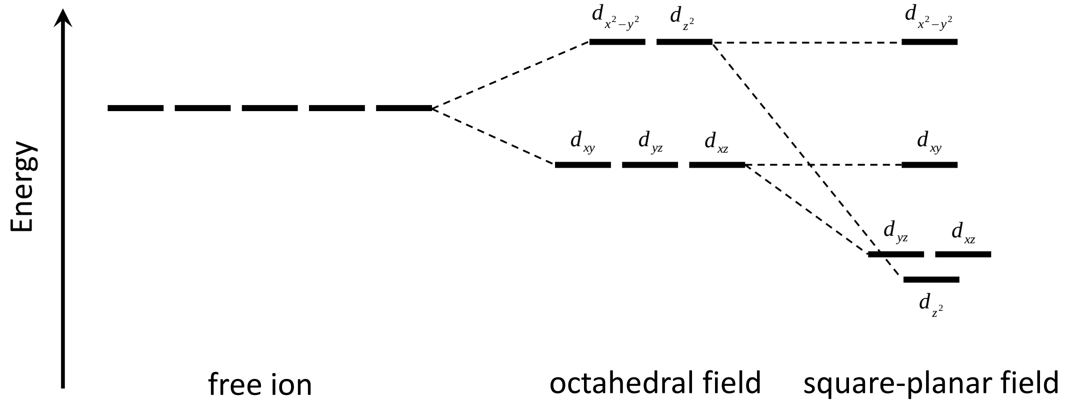

Figure 5-2. Crystal field splitting diagram for d orbitals in octahedral and square-planar fields.

Removal of an oxygen atom from the $Pd_xCe_{1-x}O_2(111)$ surface results in 5 nearest neighbor oxygen atoms, and an oxygen atom in the subsurface layer is displaced farther from the Pd ion to facilitate square planar coordination. The Pd^{2+} ion has 8 valence d electrons, which in a square planar field results in four occupied d orbitals (d_{xy}, d_{yz}, d_{xz}, and d_{z^2}) and one unoccupied orbital ($d_{x^2-y^2}$). The PDOS for the oxygen vacant $Pd_xCe_{1-x}O_y(111)$ surface is shown in Figure 5-3(b), with the occupied d_{z^2} orbital visualized as the inset image. Occupied d orbitals for both Pd^{4+} and Pd^{2+} align orthogonal to oxygen ligands, which is emphasized in the image of the d_{z^2} orbital in which the lobes align perpendicular to the plane of the square planar configuration. The stability of both Pd^{4+} and Pd^{2+} in the $CeO_2(111)$ surface is advantageous for oxidation catalysis, where the catalytic cycle for oxidation of reactant species involves cycling between oxidation states on the catalyst surface. Palladium metal or palladium oxide (PdO) catalysts permit cycling between Pd^{2+} and Pd^0 oxidation states, however in the absence of ceria Pd^{4+} is relatively unstable

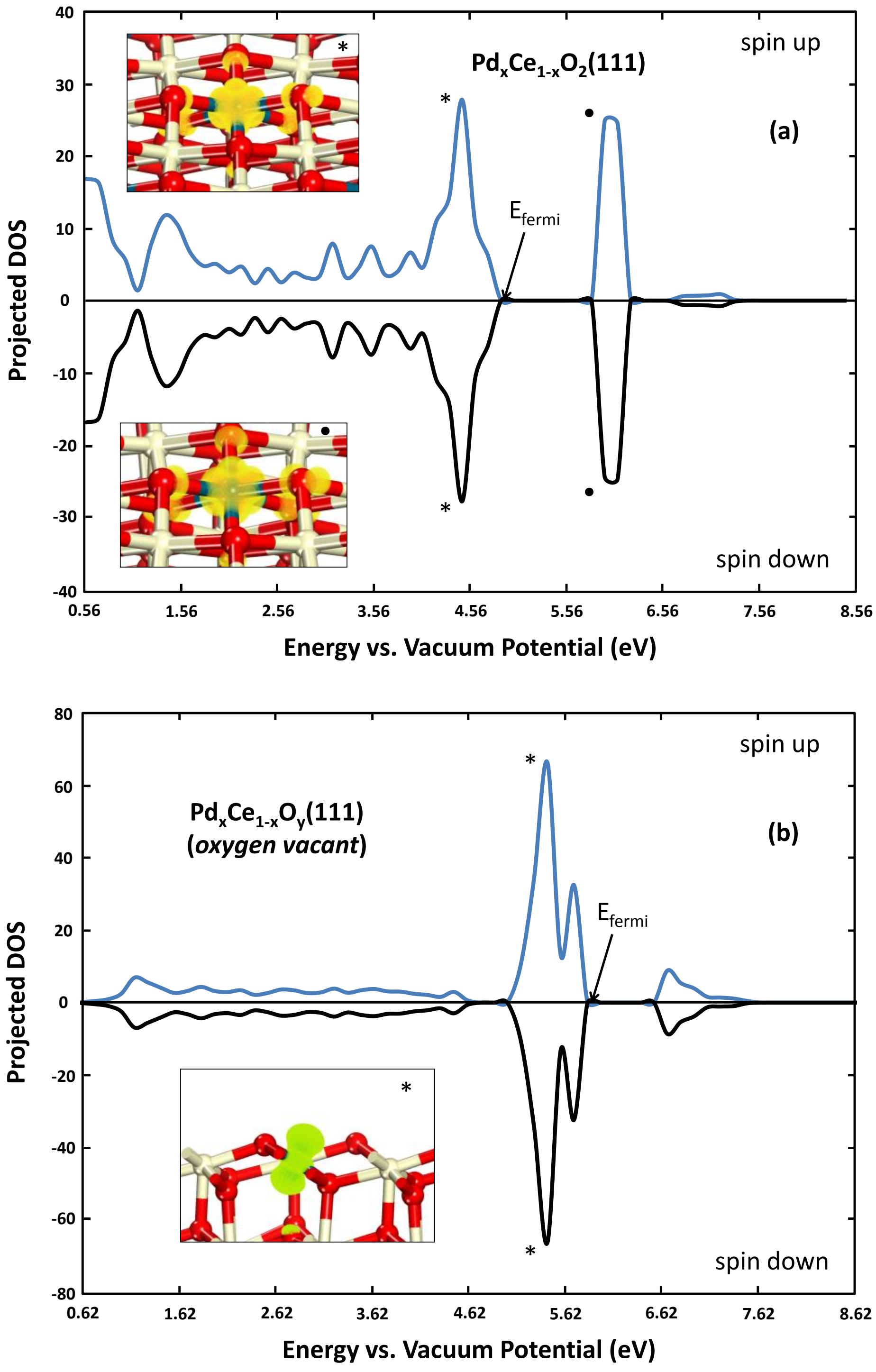

Figure 5-3. Side (a),(c) and top (b), (d) views of the Pd$_x$Ce$_{1-x}$O$_2$(111) (a), (b) and the oxygen vacant Pd$_x$Ce$_{1-x}$O$_y$(111) (c), (d) surfaces. Ce atoms are colored tan, Pd are colored blue, and oxygen are colored red. Oxygen atoms not coordinated to the Pd atom in (b) and (d) are colored brown.

(bulk PdO_2 stable at an O_2 pressure of $>10^{12}$ atm at 973K).[4] By stabilizing Pd^{4+} and Pd^{2+}, ceria allows the more exergonic Pd^{4+} to Pd^{2+} oxidation cycle over which the barrier for activating C-H bonds is lower than for Pd^{2+} to Pd^{0}.[2]

5.3.2 Correlations between C-H Bond Activity and Surface Reducibility

Figure 5-4 displays the dissociative methane adsorption energy, oxygen vacancy formation energy, and work function of the CeO_2(111) surface with a series of transition metal dopants. Figure 5-4(a) plots ΔE_{ads} vs. ΔE_{vac}, which shows a correlation between C-H activity (ΔE_{ads}) and surface reducibility (ΔE_{vac}). The correlation between C-H bond breaking activity and surface reducibility is established between ΔE_{ads} and ΔE_{vac} for the CeO_2(111), (110), and (100) surfaces for Zr and Pd dopants in Chapter 2.[1] The data in Figure 5-4(a) indicate that this correlation exists for numerous transition metal dopants in ceria. The following metals decrease the oxygen vacancy formation energy (increase the reducibility) and decrease the methane adsorption energy (increase the C-H bond breaking activity) below that of Pd: Co, Sc, Ni, Ag, Hg, Cd, Cu, and Zn. Nickel-ceria exhibits catalytic activity for steam reforming[20] and Cu-ceria has shown promise as an active material for anodes in direct hydrocarbon solid oxide fuel cells.[21] Both steam reforming and direct oxidation require facile C-H bond breaking.

Data points in Figure 5-4(a) are labeled corresponding to the most common oxidation states for each transition metal in complexes or compounds as identified in Mendeleev's table of oxidation states.[22] Metals with 4+ listed as a common oxidation state in Mendeleev's table are labeled with filled circles (●), metals without 4+ as a common oxidation state are labeled with open circles (○), and metals with both 4+ and 2+ as common oxidation states with stars (★).

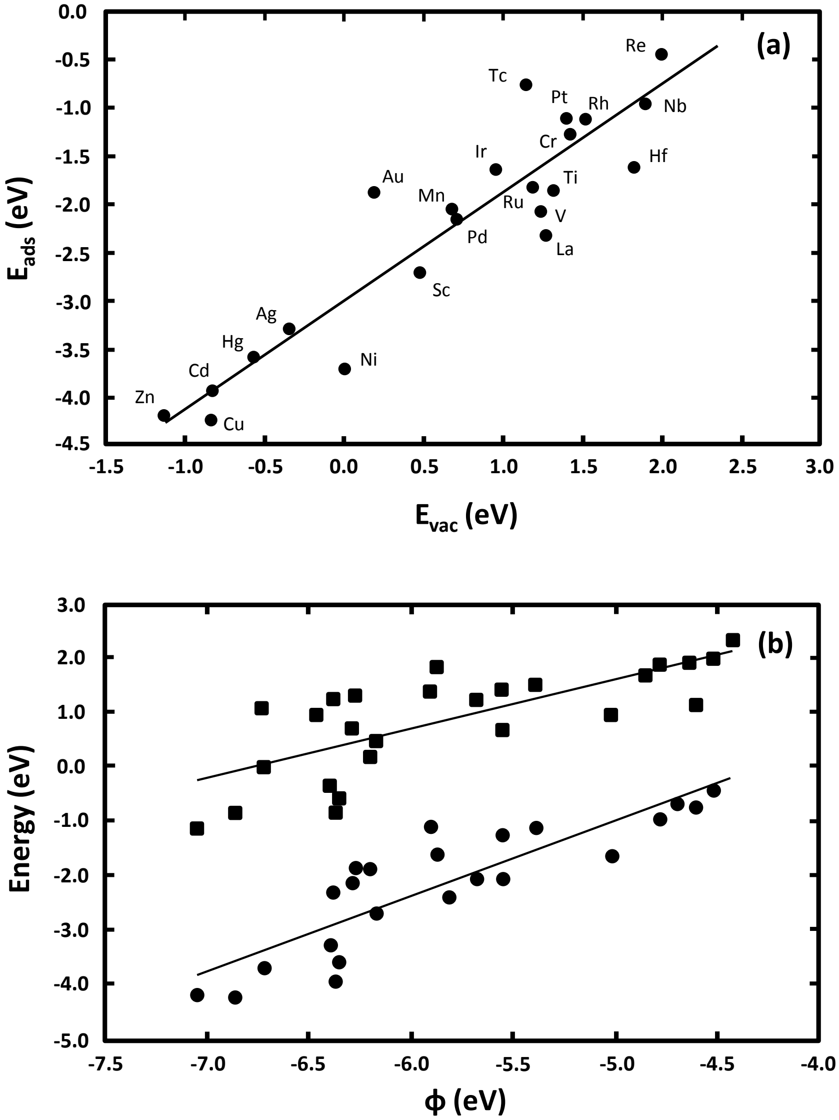

Figure 5-4. (a) Methane dissociative adsorption energy (E_{ads}) vs. oxygen vacancy formation energy (E_{vac}) and (b) E_{ads} (•), E_{vac}(■) vs. work function (φ) for single metal atoms substituted for Ce atoms into the $CeO_2(111)$ surface.

Transition metals with both 4+ and 2+ as common oxidation states are Pt, Pd, and Mn. Oxygen vacancy formation over each transition metal dopant with 4+ as a common oxidation state is endothermic, whereas every transition metal for which oxygen vacancy formation is exothermic are known not to be stable in the 4+ oxidation state. Metals without stable 4+ oxidation states thus may not form $M_xCe_{1-x}O_2$ mixed oxides, and our calculations simply reflect this instability with oxygen vacancy formation or methane dissociation easily reducing these M^{4+} ions to more stable lower valency oxidation states. Metals with stable 4+ oxidation states but unstable 2+ or 3+ oxidation states facilitate altered oxygen vacancy formation and methane dissociation energetics by perturbing the structure of the ceria lattice and altering the reduction energetics of Ce^{4+} to Ce^{3+}.

Neglecting stability considerations, these calculations would suggest any dopants appearing to the left of Pd in Figure 5-4(a) could impart greater methane dissociation activity than $Pd_xCe_{1-x}O_2$. Methane oxidation activity, however, also requires refilling of the oxygen vacancy created by desorption of H_2O(g) or CO_2(g). Transition metals which appear to the left dashed line in Figure 4(a) correspond to those that lower the oxygen vacancy formation energy to the extent that refilling of the vacancy from O_2(g) ($E_{vac} = -E_{refill}$) at 0K is greater than the 0K methane activation barrier over $Pd_xCe_{1-x}O_2(111)$ (+0.18 eV). This 0K analysis provides a rough estimate of this transition; a more accurate analysis of $\Delta G^{\ddagger}$ vs. ΔG_{refill} could be done as in Chapter 4. Methane oxidation over transition metal dopants in $CeO_2(111)$ with $\Delta E_{vac} < -0.18$ eV thus may be rate limited by oxygen vacancy refilling in contrast to methane activation. Stability considerations and re-oxidation requirements therefore eliminate all dopants to the left of Pd as providing potential for improved methane combustion activity. Manganese and nickel merit further consideration as appear to the right of the re-oxidation limit and left of Pd.

Figure 5-4(b) plots ΔE_{ads} and ΔE_{vac} vs. the work function (the energy to remove the highest energy electron from the surface, or equivalently the energy of the highest energy electronic state referenced to the potential of vacuum) of the doped ceria surface. The oxygen vacancy formation energy of the doped ceria surface increases as the work function increases. The work function is a measure of surface reducibility as the energy to add an additional electron to the surface (to reduce the surface) depends on the energy of the highest occupied electronic state. The dissociative methane adsorption energy also increases as work function increases, further illustrating the correlation between surface reducibility and C-H bond breaking activity. The work function is the energy to move an electron from the fermi level to vacuum, however, not a measure of the energy to add electrons to (reduce) the surface. The correlation between work function, E_{vac} and E_{ads}, while consistent with the correlation between surface reducibility and both E_{vac} and E_{ads}, is empirical and merits further study.

5.4 Conclusions

This chapter addresses the electronic structure of the doped ceria surface, and establishes the correlation between surface reducibility and C-H bond activity across a series of dopants in the $CeO_2(111)$ surface. The $Pd_xCe_{1-x}O_2(111)$ surface provides unique activity for C-H bond breaking,[1,2] and the stability of the Pd^{4+} ion is due to the structure and flexibility of oxygen ligands in the coordination shell of Pd in the CeO_2 surface. Imaging of Pd d orbitals confirms that occupied Pd d states align orthogonal to the position of oxygen ligands in the $CeO_2(111)$ surface. Surface reducibility, evaluated by both oxygen vacancy formation energy and work function, correlates with the dissociative adsorption energy of methane (C-H bond break activity). Certain transition metals including Ni and Cu in ceria may provide increased surface reducibility and thereby increase C-H bond breaking kinetics with respect to the active $Pd_xCe_{1-x}O_2(111)$ surface.

The results presented herein illustrate the efficacy of tailoring the composition of ceria-based mixed oxides to optimize catalytic activity. The preparation of mixed oxides of a given composition is only possible, however, if the mixed phase is stable with respect to the isolated metals or metal oxide components, or if there are large kinetic barriers to the reordering of substituted dopant atoms into separate phases. Thus the optimization of ceria-based mixed metal oxide catalysts involves novel efforts in synthesis techniques, as well as multi-scale modeling efforts to probe the ceria-transition metal surface at varying length scales and surface dynamics at varying time scales. Chapter 7 addresses coupling DFT methods with reactive force field methods to build larger (>200 atoms) models of metal oxide catalyst surfaces, and probe dynamics of surface reorganization in catalytic environments.

5.5 References

(1) Mayernick, A. D.; Janik, M. J. *The Journal of Physical Chemistry C* **2008**, *112*, 14955-14964.

(2) Mayernick, A. D.; Janik, M. J. *Journal of Catalysis*, *In Press*, *Corrected Proof*.

(3) Guanghui Zhu, J. H., Dmitri Yu. Zemlyanov, Fabio H. Ribeiro *Journal of Physical Chemistry B* **2005**, *109*, 2331-2337.

(4) Mayernick, A. D.; Janik, M. J. *Journal of Chemical Physics* **2009**, *131*.

(5) Kresse, G.; Furthmuller, J. *Computational Materials Science* **1996**, *6*, 15-50.

(6) Kresse, G.; Furthmuller, J. *Physical Review B* **1996**, *54*, 11169-11186.

(7) Kresse, G.; Hafner, J. *Physical Review B* **1993**, *47*, 558-561.

(8) Kresse, G.; Joubert, D. *Physical Review B* **1999**, *59*, 1758 LP - 1775.

(9) Perdew, J. P.; Chevary, J. A.; Vosko, S. H.; Jackson, K. A.; Pederson, M. R.; Singh, D. J.; Fiolhais, C. *Physical Review B* **1992**, *46*, 6671.

(10) Fabris, S.; Gironcoli, S. d.; Baroni, S.; Vicario, G.; Balducci, G. *Physical Review B* **2005**, *71*, 041102.

(11) Fabris, S.; Gironcoli, S. d.; Baroni, S.; Vicario, G.; Balducci, G. *Physical Review B* **2005**, *72*, 237102.

(12) Kresse, G.; Blaha, P.; Silva, J. L. F. D.; Ganduglia-Pirovano, M. V. *Physical Review B* **2005**, *72*, 237101.

(13) Nolan, M.; Grigoleit, S.; Sayle, D. C.; Parker, S. C.; Watson, G. W. *Surface Science* **2005**, *576*, 217-229.

(14) Nolan, M.; Parker, S. C.; Watson, G. W. *Surface Science* **2005**, *595*, 223-232.

(15) Herschend, B.; Baudin, M.; Hermansson, K. *Surface Science* **2005**, *599*, 173-186.

(16) Yang, Z.; Lu, Z.; Luo, G.; Hermansson, K. *Physics Letters A* **2007**, *369*, 132-139.

(17) Yang, Z.; Luo, G.; Lu, Z.; Hermansson, K. *The Journal of Chemical Physics* **2007**, *127*, 074704-5.

(18) Knapp, D.; Ziegler, T. *The Journal of Physical Chemistry C* **2008**, *112*, 17311-17318.

(19) Ganduglia-Pirovano, M. V.; oacute; nica; Da Silva, J. L. F.; Sauer, J. *Physical Review Letters* **2009**, *102*, 026101.

(20) Zhuang, Q.; Qin*, Y.; Chang, L. *Applied Catalysis* **1991**, *70*, 1-8.

(21) McIntosh, S.; Gorte, R. J. *Chemical Reviews* **2004**, *104*, 4845-4865.

(22) Greenwood, N.; Earnshaw, A. *Chemistry of the Elements*; Oxford: Butterworth-Heinemann, 1997.

5.6 Supporting Information

The following valence configurations were used for the transition metal dopants utilized in this Chapter:

Zn – $3d^{10}4s^{2}$
Cu - $3d^{10}4s^{2}$
Cd - $4d^{10}5s^{2}$
Hg - $5d^{10}6s^{2}$
Ag - $4d^{10}5s^{1}$
Ni – $3d^{8}4s^{2}$
Sc – $3d^{1}4s^{2}$
Au - $5d^{10}6s^{1}$
Mn – $3d^{5}4s^{2}$
Pd - $4d^{10}$
Ir - $5d^{7}6s^{2}$
Ru - $4d^{7}5s^{1}$
V – $3d^{3}4s^{2}$
Ti – $3d^{2}4s^{2}$
La – $5s^{2}5p^{6}5d^{1}6s^{2}$
Cr – $3d^{5}4s^{1}$
Pt – $5d^{9}6s^{1}$
Tc – $4d^{6}5s^{1}$
Rh – $4d^{8}5s^{1}$
Hf – $5d^{2}6s^{2}$
Nb – $4p^{6}4d^{4}5s^{1}$
Re – $5d^{5}6s^{2}$

	ΔE_{ads} (eV)	ΔE_{vac} (eV)
Ag	-3.29	-0.35
Au	-1.88	0.19
Cd	-3.94	-0.82
Co	-2.39	0.42
Cr	-1.27	1.43
Cu	-4.24	-0.83
Fe	-1.88	1.09
Hf	-1.63	1.82
Hg	-3.59	-0.56
Ir	-1.64	0.95
La	-2.32	1.27
Mn	-2.07	0.68
Mo	-0.71	2.34
Nb	-0.96	1.89
Ni	-3.70	0.01
Os	-0.69	1.48
Pd	-2.15	0.71
Pt	-1.11	1.40
Re	-0.44	1.99
Rh	-1.12	1.52
Ru	-1.82	1.19
Sc	-2.71	0.48
Ta	-1.31	1.68

Tc	-0.75	1.15
Ti	-1.86	1.31
V	-2.07	1.23
W	-0.82	1.93
Y	-2.60	0.97
Zn	-4.19	-1.13
Zr	-1.39	1.63

Table S1. Methane dissociative adsorption energies (ΔE_{ads}) and oxygen vacancy formation energies (ΔE_{vac}) over transition metal dopants in $CeO_2(111)$.

Chapter 6

Energetics and Mechanism for H_2S Adsorption by Ceria-Lanthanide Mixed Oxides: Implications for the Desulfurization of Biomass Gasifier Effluents.

ABSTRACT: Density functional theory (DFT+*U*) and *ab initio* thermodynamics are used to calculate the free energies of H_2S adsorption and dissociation on $CeO_2(111)$ as well as La-doped and Tb-doped $CeO_2(111)$. Rate limiting steps in H_2S dissociation over each surface are identified, and the free energies of substituting sulfur atoms for surface oxygen atoms are calculated. Sulfur adsorption capacity is limited by the surface kinetics of H_2S adsorption and dissociation to SH*, which occurs over surface oxygen vacancies. The apparent barrier for H_2S adsorption and dissociation is lowest over the ceria-lanthana surface, followed by ceria-terbia, and largest over the pure ceria surface. Experimental measurements show that the sulfur adsorption capacity of ceria-lanthana mixtures is larger than that of ceria-terbia mixtures, which we attribute to faster kinetics of H_2S adsorption and dissociation on the mixed oxide surface.

6.1 Introduction

Gasification of biomass to syngas facilitates energy production from a renewable feedstock when coupled with downstream catalytic processing to liquid fuels or direct utilization in a fuel cell. Syngas produced from biomass contains up to as much as 1% H_2S,[1] which must be removed prior to further processing or utilization steps to avoid poisoning of downstream catalysts and SO_x production. It is advantageous to perform syngas desulfurization at the high temperatures of gasification (>850K) to permit efficient integration of desulfurization in between gasification and further processes.[2] Ceria is stable at gasification temperatures, and the sulfur adsorption capacity of ceria may be altered by mixing ceria with other rare earth oxides such as lanthana[3] and terbia. Mixing ceria with lanthana or terbia may alter the kinetics or thermodynamics of H_2S adsorption and dissociation, however the mechanism and energetics on ceria-based rare earth oxides are not well characterized. The optimization of ceria-based high temperature desulfurization sorbents is thus dependent on characterizing the H_2S sorption process at the atomic scale and identifying kinetic or thermodynamic limits for H_2S removal.

Numerous properties are necessary for efficient and long-term high temperature desulfurization operation including rapid initial H_2S adsorption kinetics, favorable sulfidation thermodynamics, and high temperature stability including both bulk phase stability and surface area stability. Biomass gasification temperatures range from approximately 673K-1473K,[4] motivating the use of materials with high temperature stability such as ceria. Mixed rare earth oxides of ceria maintain the lattice structure of cubic CeO_2 upon mixing with lanthana or terbia, up to x = 0.6 for $Ce_{1-x}La_xO_y$[5] and x = 0.5 for $Ce_{1-x}Tb_xO_y$.[6] Flytzani-Stephanopoulos et al. showed that ceria-lanthana ($Ce_{0.7}La_{0.3}O_y$) has a higher sulfur adsorption capacity (mg $S/g_{sorbent}$), at 1073K and a H_2S pressure of 0.001 atm than either pure CeO_2 or pure La_2O_3.[3] The increased capacity of ceria-lanthana with respect to pure ceria evidences the potential for the design and optimization of mixed oxide ceria-based sulfur sorbents. It is unclear, however, which properties of the mixed metal oxide lead to the increased sulfur capacity realized experimentally.

The increased sulfur adsorption capacity of ceria-based mixed oxides with respect to pure ceria may be due to a number of factors including increased surface area stability, increased reducibility of the oxide mixture, stronger adsorption and faster kinetics on the mixed oxide surface, or a thermodynamically favorable bulk transition from the oxide to an oxysulfide ($M_xO_yS_z$) with a higher sulfur stoichiometry. The addition of low valency metals such as La(3+)[7] and Tb(3+)[6] to CeO_2 results in the presence of stoichiometric oxygen vacancies and also lowers the energy of forming subsequent oxygen vacancies (reduction of Ce^{4+} to Ce^{3+}). Oxygen vacancies may serve as active sites for surface adsorption and dissociation of H_2S, and may also increase bulk diffusion rates of sulfur atoms within the ceria lattice to facilitate bulk sulfidation. Kay et al. proposed that the increased sulfur adsorption capacity of ceria-lanthana is due to more exergonic free energies of formation of lanthanum oxysulfides and sulfides than those of cerium.[8] Breakthrough curves for H_2S adsorption over ceria and ceria-lanthana display gradual increases in outlet H_2S concentration, however, which the authors attribute to kinetic limitations.[8] The H_2S adsorption capacity of pure ceria is proportional to surface area,[9] evidencing that surface kinetics of H_2S adsorption and dissociation influence adsorption capacity. The sulfur capacity per surface area of ceria-lanthana also exceeds that of pure ceria, suggesting that the chemical functionality of the surface influences sulfur adsorption capacity.[3] The relevance of surface functionality and kinetics are thus established experimentally, however the reaction mechanism and energetics of H_2S adsorption and dissociation have not been characterized.

Experimental characterization of ceria-based sulfur sorbents *in situ* is complicated by structural and chemical transformations which occur during the desulfurization process, and previous computational studies of H_2S chemistry on the ceria surface have been limited to consideration of pure ceria as well as energetics only over the intact (fully oxidized) surface. Lin et al. report density functional theory (DFT+*U*) calculated reaction energies and activation barriers for H_2S dissociation on $CeO_2(111)$, however their study does not consider adsorption and dissociation energetics over oxygen vacancies on the reduced ceria surface.[10] The partial pressure of oxygen may be very low ($< 10^{-20}$ atm, see Section 2.4 for calculation of equilibrium oxygen pressure) in gasifier streams. At these low oxygen pressures and temperatures exceeding 850K, oxygen vacancies will be present on the ceria surface. The formation of oxysulfides or sulfides involves the substitution of sulfur atoms for oxygen atoms within the ceria lattice, which may occur via adsorption and dissociation of H_2S over oxygen vacancies. Lin et al.'s study also only includes DFT calculated internal energy differences, which are not accurate estimates of free energy differences for H_2S adsorption at high temperatures and low H_2S pressures ($< 10^{-2}$ atm[1]). To the best of our knowledge, no previous computational study considered the free energies of H_2S adsorption and dissociation over reduced ceria or ceria-based rare-earth oxide mixtures such as ceria-lanthana and ceria-terbia.

This chapter utilizes density functional theory and *ab initio* thermodynamics to calculate the free energies of H_2S adsorption and dissociation on $CeO_2(111)$ as well as La-doped and Tb-doped $CeO_2(111)$. The free energies of H_2S adsorption, dissociation, and oxygen vacancy formation are evaluated at 1100K and partial pressures of $H_2S(g)$ and $O_2(g)$ corresponding to operating conditions for the high temperature desulfurization of biomass gasifier effluents. Surface adsorption and subsurface incorporation of sulfur are considered, and the equilibrium sulfur content of the surface is calculated over a range of possible pressures of $H_2S(g)$ and $O_2(g)$. Experimental measurements of sulfur adsorption capacities on ceria-lanthana and ceria-terbia are reported for comparison of observed trends in sulfur adsorption capacity with computational results. Previous studies have evaluated the relative trends in sulfur adsorption capacity between pure ceria and ceria-lanthana, however sulfur adsorption capacities for ceria-terbia mixtures have not been reported. These results provide insight into limiting factors in the desulfurization reaction over ceria, ceria-lanthana, and ceria-terbia. We identify kinetic and thermodynamic limitations to H_2S adsorption and dissociation from the gas phase, and discuss each in the context of the optimization of ceria-based high temperature desulfurization sorbents.

6.2 Methods

6.2.1 Synthesis of Ceria-Lanthana and Ceria-Terbia

Ceria-lanthana and ceria-terbia samples were synthesized as high surface area mesoporous materials at >2.0 nm average pore diameter by adapting a surfactant-templated method.[11,12] Measured amounts of ceric (IV) ammonium nitrate $(NH_4)_2Ce(NO_3)_6$ (Aldrich 99.9%; FW = 548.25) and either lanthanum precursor $La(NO_3)_3 \bullet 6\ H_2O$ (Alfa Aesar 99.9%; FW = 433.1) or terbium chloride hexahydrate (Aldrich, 99.9%) were added to measured amounts of water and 1% tetramethylammonimum hydroxide (Acros, 25% in methanol) surfactant with stirring. The salts dissolved immediately to a clear solution, to which was slowly added $NH_4(OH)$ (Alfa Aesar, 28-30% NH_3), until precipitation occurred (pH ~10.3-10.5). The temperature was raised to 363 K and the gel stirred for 4 days, adjusting the pH as necessary. The centrifuged precipitate was washed with acetone and deionized water, dried at 373 K, then calcined in flowing air at 773 K with a ramp of 2 K/min and a final hold of 6 h.

6.2.2 Sulfur Adsorption Capacity Measurements

Sulfur adsorption capacity measurements were performed for H_2S on ceria-lanthana and ceria-terbia from a simulated gasifier effluent, followed by temperature programmed desorption and then final regeneration. The adsorption tests were at 900 K and after saturation the gas was switched to helium and temperature-programmed from 900 to 1073 K. The simulated effluent gas contained 0.1% H_2S, 22% H_2, 31% CO_2, 8% H_2O, 38.9% N_2. The surface adsorption capacities reported herein are short-bed, non-equilibrium data with a 1 g bed at gas hourly space velocity (GHSV) of 15500 (vol%), and a pre-breakthrough concentration of roughly 10 ppmv. Final regeneration was performed at 873 K in air for 30 min.

6.2.3 Electronic Structure Method

Calculations were performed using the Vienna *ab initio* simulation program (VASP), an *ab initio* total-energy and molecular dynamics program developed at the Institute for Material Physics at the University of Vienna.[13-15] The projector augmented wave method[16] was used to represent the core region, with valence electron wavefunctions expanded in a tractable plane wave basis set. The energy cutoff of the plane wave basis set used herein was 450 eV (chosen to ensure convergence of total energy with respect to energy cutoff). Valence configurations were $5s^25p^66s^24f^15d^1$ for cerium, $2s^22p^4$ for oxygen, $5s^25p^65d^16s^2$ for La, $4f^9$ for Tb, $3s^23p^4$ for S, and $1s^1$ for H. Structural optimizations were performed by minimizing the forces on all atoms to below 0.05 eV Å^{-1}, and all calculations were spin-polarized. The Perdew-Wang (PW91) version of the generalized gradient approximation (GGA) was used to incorporate exchange and correlation energies.[17] Due to well-established difficulties within DFT to accurately represent the nature of 4*f* states in ceria,[18-20] we implemented the DFT+*U* approach. The DFT+*U* method introduces the Hubbard *U* term as an on-site Coulombic interaction in the *f* states of ceria, which localizes 4*f* electrons on Ce^{3+} in reduced ceria. We used a value of $U = 5$ eV, which is consistent with recommended values within the DFT+*U* method used in previous studies of ceria[21-26] and ensures proper localization of 4*f* electrons. Absolute reduction energies are a function of *U* value, though relative trends in reduction energetics are preserved with varying *U*.[27] The absolute free energies presented herein thus may not directly compare to experimental values and as such we focus on relative trends in energetics between ceria, ceria-lanthana, and ceria-terbia.

6.2.4 Surface Models

Figure 6-1 displays the slab models used for the ceria, ceria-lanthana and ceria-terbia surfaces. Each surface model consists of a mirrored slab on which adsorption and oxygen vacancy formation are considered on both sides of the slab. The mirrored slab model of the ceria surface was used specifically to minimize slab to slab interactions which may result from a large net surface dipole moment upon the interaction of the surface with adsorbates and the reduction of surface metal ions. The ceria surface is modeled as a 12-layer ($Ce_{16}O_{32}$) mirrored slab of the (111) termination of cubic fluorite CeO_2 separated by 15 Å of vacuum in the direction perpendicular to the surface. The surface energy of CeO_2(111) is lowest among single crystal terminations of ceria,[21,22,27] indicating that this surface termination will represent a large portion of a polycrystalline CeO_2 surface. The Brillouin zone was sampled using a (2×2×1) MP grid for the (111) surface, with the third vector perpendicular to the surface. We use a *p*(2×2) expansion of the surface unit cell, which results in a termination of four surface oxygen atoms on each side of the slab and four Ce atoms in the atomic layer below. Two lanthanum or terbium atoms are substituted into the ceria slab for two Ce atoms in the ceria-lanthana and ceria-terbia models, respectively, with a single oxygen atom removed to maintain the 3+ oxidation state of La and Tb. The La and Tb pairs are substituted into the ceria slab with one atom in the surface metal layer and one atom in the subsurface metal layer. We limit our study to this single configuration of La or Tb atoms in the ceria surface to identify trends in H_2S adsorption and dissociation energetics over ceria and rare earth doped ceria, however, ceria-lanthana and ceria-terbia surfaces may contain a heterogeneous distribution of metal atoms, oxygen atoms and oxygen vacancies. The

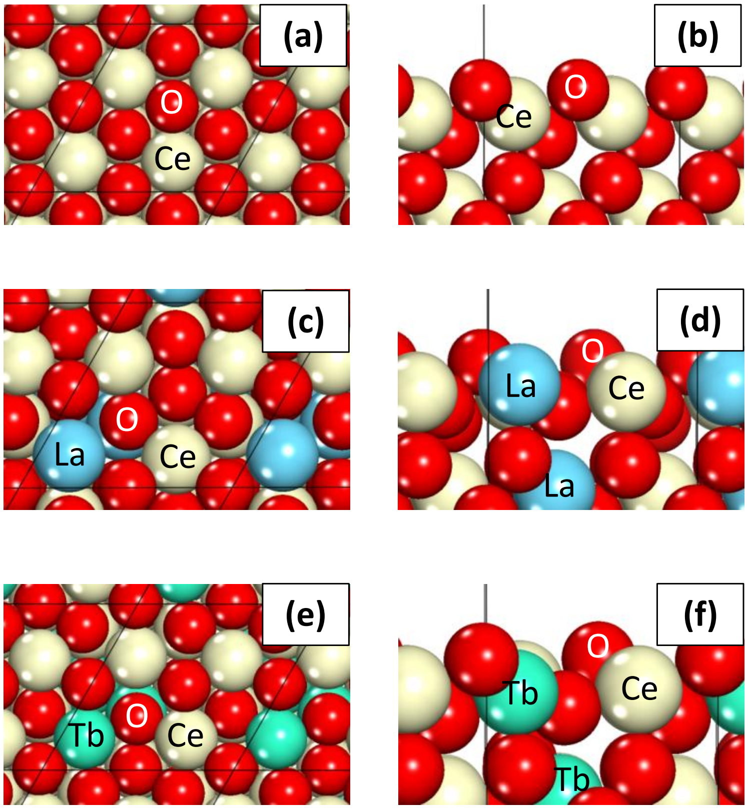

Figure 6-1. Top (a), (c), (e), and side (b), (d), (f) views of surface unit cell for (a), (b), $CeO_2(111)$, (c), (d) $La_2O_3/CeO_2(111)$, and (e), (f) $Tb_2O_3/CeO_2(111)$. Ce atoms are colored tan (light), O atoms red (dark), La atoms blue (gray), and Tb atoms teal (dark gray).

formation energy for the stoichiometric oxygen vacancy in our ceria-terbia surface model is lowest (most exothermic) at a surface oxygen coordinated to Tb. For ceria-lanthana, the oxygen vacancy formation energy is lowest at the next nearest neighbor position to La.

6.2.5 Free Energies of H_2S Adsorption and Dissociation

Reaction intermediates for H_2S dissociation over each surface were optimized by placing H_2S, SH, S, and H adsorbates in each surface unit cell. Each adsorbate was placed at all high symmetry adsorption sites and configurations on each surface, and the lowest energy adsorption configuration for each adsorbate-surface pair was used to calculate the relative energies of elementary reaction steps. Harmonic vibrational modes were calculated to determine zero-point vibrational energy (ZPVE) corrections to the total energy of isolated molecules and adsorbed species. Optimizations of isolated gas-phase molecules were performed with one free molecule within a 15×15×15 Å unit cell. The free energies of gas-phase molecules and surface adsorbates were calculated as the sum of the electronic energy (E_{DFT}), ZPVE correction, entropy (ST), and a pressure volume term (PV) as follows:

$$G_{gas} = E_{DFT} + ZPVE - (S_{vib} + S_{trans} + S_{rot})T + PV \tag{1}$$

For surface adsorbates, translational and rotational entropy terms are zero. Constrained vibrational calculations were done for adsorbed species, where the Hessian matrix is populated solely with the second derivatives of energy with respect to position of the adsorbate atoms. Free energy differences for elementary reaction steps were calculated by subtracting the sum of free energies of the initial state from the sum of free energies of the product state, as follows for the example of H_2S dissociation to adsorbed SH and H ($H_2S^* + {}^* \rightarrow SH^* + H^*$):

$$\Delta G_{rxn,\ H_2S^*+{}^*\rightarrow SH^*+H^*} = \frac{[G_{SH^*} + G_{H^*}] - \left[G_{H_2S^*} + G_{bare}\right]}{2} \tag{2}$$

where G_{SH^*}, G_{H^*}, and $G_{H_2S^*}$ represent the free energies of adsorbed SH, H, and H_2S species, respectively, and G_{bare} is the DFT energy of the bare surface. The denominator of two is included in equation 2 to account for the fact that mirrored slab models are used with one adsorbate on each side of the mirrored slab.

Adsorption and dissociation of H_2S was considered over the intact (fully oxidized) and oxygen reduced ceria, ceria-lanthana, and ceria-terbia surfaces. Oxygen vacancy formation free energies were incorporated into the free energy diagrams for H_2S adsorption and dissociation, calculated as follows:

$$\Delta G_{vac} = \frac{G_{reduced} + G_{O_2} - G_{intact}}{2} \tag{3}$$

where $G_{reduced}$ and G_{intact} are the free energies of the surface containing an oxygen vacancy and the intact surface, respectively, and G_{O_2} the free energy of O_2(g). Free energies of gas phase species are calculated at 1100K, and P_{H_2} = 0.35 atm, P_{H_2S} = 10^{-2} atm, and P_{H_2O} = 0.03 atm to approximate high temperature desulfurization conditions.[8] Due to DFT errors associated with the overestimation of the O_2 binding energy,[28] we estimate the free energy of O_2 by assuming equilibrium between H_2O(g), H_2(g), and O_2(g):

$$G_{O_2} = (G_{H_2O} - G_{H_2})\cdot 2 \qquad (4)$$

where G_{O_2} is the free energy of O_2(g), G_{H_2O} is the free energy of H_2O(g), and G_{H_2} is the free energy of H_2(g).

6.3 Results and Discussion

6.3.1 Experimental Sulfur Adsorption Capacities

Figure 6-2 displays the sulfur adsorption capacities for ceria-lanthana and ceria-terbia mixtures of $Ce_{0.86}M_{0.14}O_x$ and $Ce_{0.75}M_{0.25}O_x$ (M=La or Tb) compositions. Table 6-1 lists the surface areas after calcinations for each ceria-lanthana and ceria-terbia composition. The surface areas for all of the ceria-lanthana or ceria-terbia mixtures are in the range of 200-240 m^2 g^{-1}. The sulfur adsorption capacity of ceria-lanthana is larger than that of ceria-terbia at both compositions studied ($Ce_{0.86}M_{0.14}O_x$ and $Ce_{0.75}M_{0.25}O_x$). The larger sulfur adsorption capacity of ceria-lanthana with respect to ceria-terbia for samples of similar surface area may indicate that the H_2S adsorption and dissociation kinetics are faster over the ceria-lanthana than over ceria-terbia. The experimental data reported herein are thus a useful metric for evaluating the performance of ceria-based desulfurization sorbents, however do not inform novel sorbent design approaches. We utilize computational chemistry approaches to corroborate experimental trends in sulfur adsorption capacity across ceria-based mixed oxides of varying composition, and identify limiting factors in the desulfurization reaction.

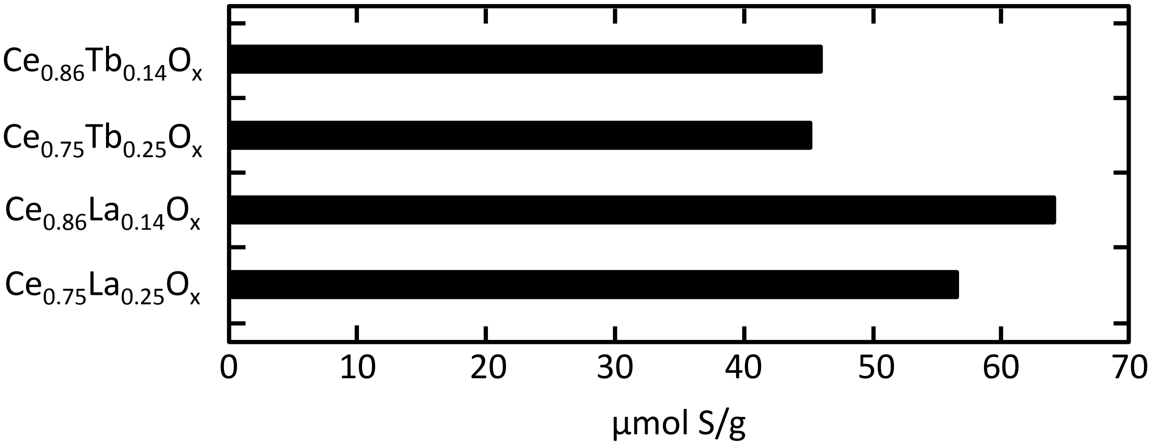

Figure 6-2. Top (a), (c), (e), and side (b), (d), (f) views of surface unit cell for (a), (b), $CeO_2(111)$, (c), (d) $La_2O_3/CeO_2(111)$, and (e), (f) $Tb_2O_3/CeO_2(111)$. Ce atoms are colored tan (light), O atoms red (dark), La atoms blue (gray), and Tb atoms teal (dark gray).

Table 6-1. Surface areas for ceria-lanthana and ceria-terbia mixtures after calcination in flowing air at 773K.

Composition	Calcined Surface Area (m^2/g)
$Ce_{0.86}Tb_{0.14}O_x$	200
$Ce_{0.75}Tb_{0.25}O_x$	210
$Ce_{0.86}La_{0.14}O_x$	200
$Ce_{0.75}La_{0.25}O_x$	240

6.3.2 H_2S Adsorption and Dissociation

Figure 6-3 displays the lowest energy adsorption configurations for H_2S, SH, and S on an oxygen vacancy on the $CeO_2(111)$ surface. Adsorption of H_2S, SH, and S was also considered over the intact $CeO_2(111)$ surface, however adsorption is more exergonic over an oxygen vacancy. The adsorption configurations and orientation of adsorbates with respect to surface atoms are similar for H_2S, SH, and S adsorption on ceria, ceria-lanthana, and ceria-terbia, with small differences in surface atom-adsorbate distances. Adsorption configurations and inter-atom distances are included in detail in the Supporting Information.

Figures 6-4(a), 6-5(a), and 6-6(a) display the free energy diagrams for H_2S adsorption and dissociation over the reduced ceria, ceria-lanthana, and ceria-terbia surfaces, respectively, at 1100K, and P_{H_2} = 0.35 atm, P_{H_2S} = 10^{-2} atm, and P_{H_2O} = 0.03 atm. Free energies for H_2S adsorption and dissociation are plotted over each fully oxidized surface as well as reduced surfaces for which the free energy of forming an oxygen vacancy is exergonic. Vacancy formation energies for each reduced surface are included on the free energy diagrams prior to adsorption and dissociation steps, and the most favorable product state is labeled in bold.

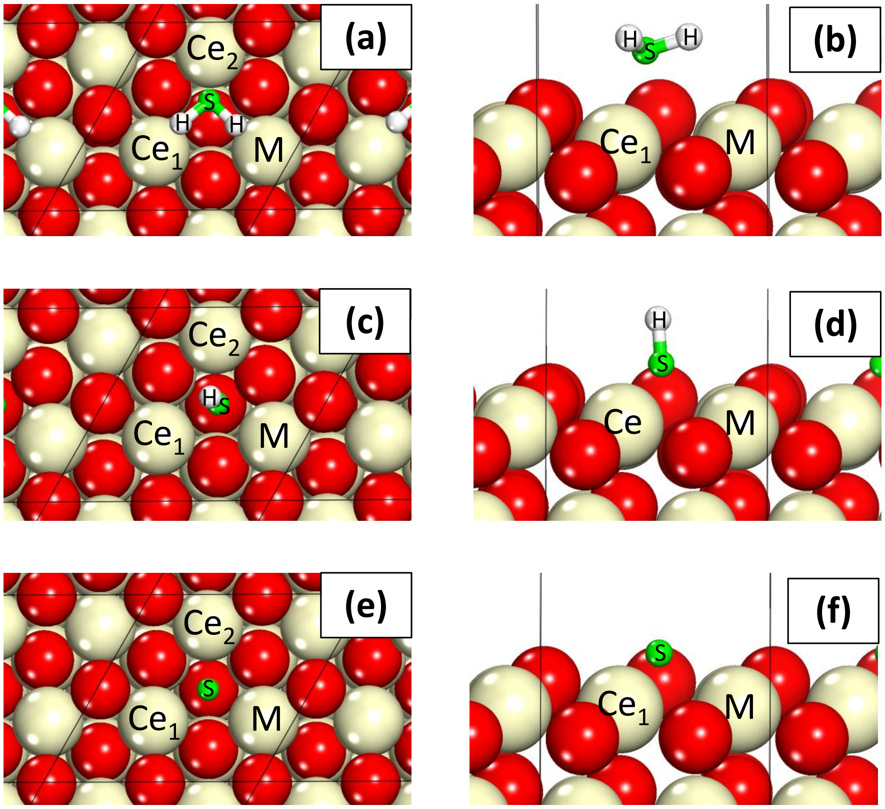

Figure 6-3. Top (a), (c), (e), and side (b), (d), (f) views of surface unit cell for H_2S* (a), (b), SH* (c), (d) and S* (e), (f) on $CeO_2(111)$. Ce atoms are colored tan (light), O atoms red (dark), S atoms green (gray), and H atoms white. Surface metal atoms are denoted Ce_1, Ce_2, and M as referenced in The Supporting Information for bond lengths between surface atoms and adsorbed sulfur species.

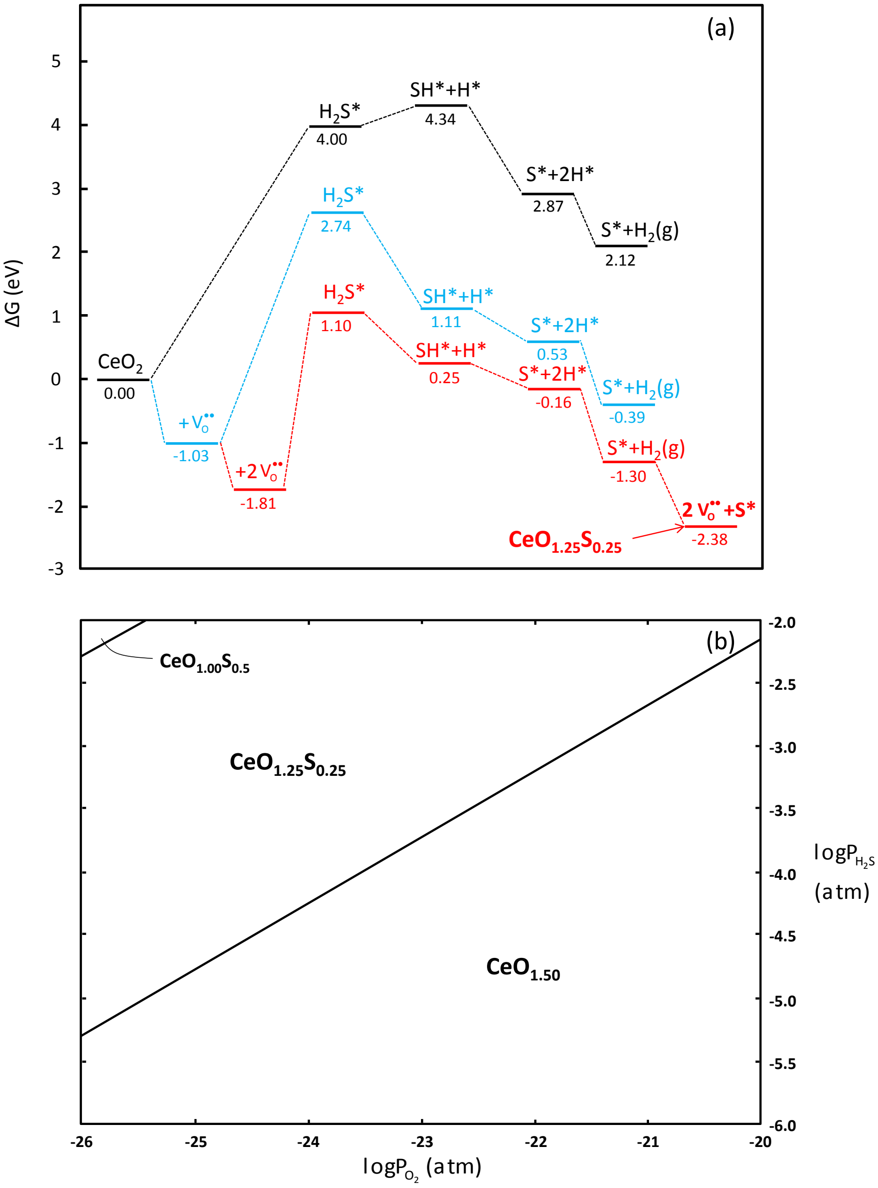

Figure 6-4. (a) Free energy diagram for H_2S adsorption dissociation over $CeO_2(111)$ at 1100K, and $P_{H_2} = 0.35$ atm, $P_{H_2S} = 10^{-2}$ atm, and $P_{H_2O} = 0.03$ atm and (b) phase diagram for $CeO_2(111)$ surface at 1100K as a function of $H_2S(g)$ and $O_2(g)$ pressure. Oxygen vacancies are denoted $V_{O}^{\cdot\cdot}$.

6.3.2.1 H_2S Adsorption and Dissociation on $CeO_2(111)$

Molecular adsorption of H_2S on the intact $CeO_2(111)$ surface is highly endergonic (+4.00 eV) at 1100K and $P_{H_2S} = 10^{-2}$ atm due to large translational entropy contributions to the free energy of $H_2S(g)$ at this high temperature and low partial pressure, and weak interaction between the H_2S molecule and the ceria surface. The DFT energy (ΔE_{ads}) of molecular H_2S adsorption is -0.22 eV (in contrast to the free energy of +4.00 eV), illustrating the magnitude of entropic contributions to adsorption energies and the inaccuracy of DFT energies in describing adsorption energies at high temperatures. Dissociation of H_2S to SH* is also endergonic (+0.34 eV), with dissociation of SH* to S* and subsequent desorption of 2H* to $H_2(g)$ exergonic. Adsorption of H_2S, SH, and S on the intact $CeO_2(111)$ surface occurs atop a surface Ce atom, atop a surface oxygen atom, and bridged between a surface Ce and surface O, respectively, in equivalent configurations to those presented by Lin et al.[10] Hydrogen atoms adsorb atop surface oxygen atoms, equivalent to surface hydroxyls (-OH). The overall process of S* formation on the stoichiometric $CeO_2(111)$ surface is highly endergonic (+2.12 eV) indicating this adsorption, studied by Lin et al.,[10] will not occur. This result highlights the need to consider ΔG(T) versus 0K ΔE values when evaluating H_2S adsorption processes.

We do not include energy barriers for H_2S dissociation herein over any surface, as climbing image nudged elastic band (CI-NEB) searches were unable to locate a transition state for $H_2S^* \rightarrow SH^* + H^*$. Attempts to locate a transition state along an H abstraction pathway ($H_2S(g) \rightarrow SH(g) + H^* \rightarrow SH^* + H^*$) indicated a monotonic increase in energy from $H_2S(g) \rightarrow SH(g) + H^*$. Lin et al. report activation barriers of 0.08 eV for $H_2S^* \rightarrow SH^* + H^*$ and 0.36 eV for $SH^* + H^* \rightarrow SH^* + 2H^*$ over $CeO_2(111)$.[10] The barrier of 0.36 eV for $SH^* + H^* \rightarrow SH^* + 2H^*$ suggests based on our free energy diagram that the transition state for this reaction step will be the highest energy state and dictate the apparent barrier (+4.70 eV) over $CeO_2(111)$, however the highly endergonic thermodynamics of H_2S adsorption contributes the majority of this energy barrier.

Formation of two oxygen vacancies in our unit cell (50% of surface oxygen) is exergonic on $CeO_2(111)$ at 1100K, $P_{H_2} = 0.35$ atm, and $P_{H_2O} = 0.03$ atm. Free energies for H_2S adsorption and dissociation over the $CeO_2(111)$ with one (25% vacant) and two (50% vacant) vacancies per surface unit cell are displayed in Figure 6-4(a). Molecular adsorption of H_2S is highly endergonic over the reduced $CeO_2(111)$ surface, at +3.77 eV with one vacancy and +2.91 eV with two vacancies, however less endergonic than over intact $CeO_2(111)$. Molecular adsorption of H_2S occurs via weak interaction between the sulfur atom of H_2S and Ce atoms nearest neighbor to an oxygen vacancy ($V_O^{\cdot\cdot}$) on reduced $CeO_2(111)$. Dissociation of H_2S to SH* and S* is exergonic over each reduced ceria surface, and SH* and S* adsorb on the oxygen vacancy site. With S* replacing a surface oxygen, it is exergonic to form an additional $V_O^{\cdot\cdot}$, leaving a surface with $2V_O^{\cdot\cdot}$ and S* adsorbed to a third oxygen vacancy. The lowest energy path for H_2S adsorption and dissociation (labeled in red on Figure 6-4(a)) results in a final product with stoichiometry in the surface layer (top Ce layer, top 2 oxygen layers) of $CeO_{1.25}S_{0.25}$. The reaction free energy diagram for H_2S adsorption and dissociation over $CeO_2(111)$ at 1100K, and $P_{H_2} = 0.35$ atm, $P_{H_2S} = 10^{-2}$ atm, and $P_{H_2O} = 0.03$ atm thus illustrates that it is thermodynamically favorable for sulfur atoms from $H_2S(g)$ to substitute into the ceria surface for oxygen atoms. The overall process of adding an S* from H_2S to the doubly vacant surface is exergonic by 0.57 eV. Further sulfidation involving addition of S* to oxygen vacancy sites or further replacement of surface oxygen atoms with sulfur atoms is not favorable, as will be discussed in Section 3.3. The sulfur adsorption process occurs via H_2S adsorption and dissociation over oxygen vacancies, and is rate limited by strongly endergonic molecular adsorption of H_2S.

6.3.2.2 H_2S Adsorption and Dissociation on $La_2O_3/CeO_2(111)$

Molecular adsorption of H_2S is also highly endergonic (+3.88 eV, Figure 6-5(a)) on the $La_2O_3/CeO_2(111)$ surface, adsorbing atop the stoichiometric oxygen vacancy. Subsequent dissociation steps to SH* and S* are endergonic, as is the overall sulfidation reaction to form S*

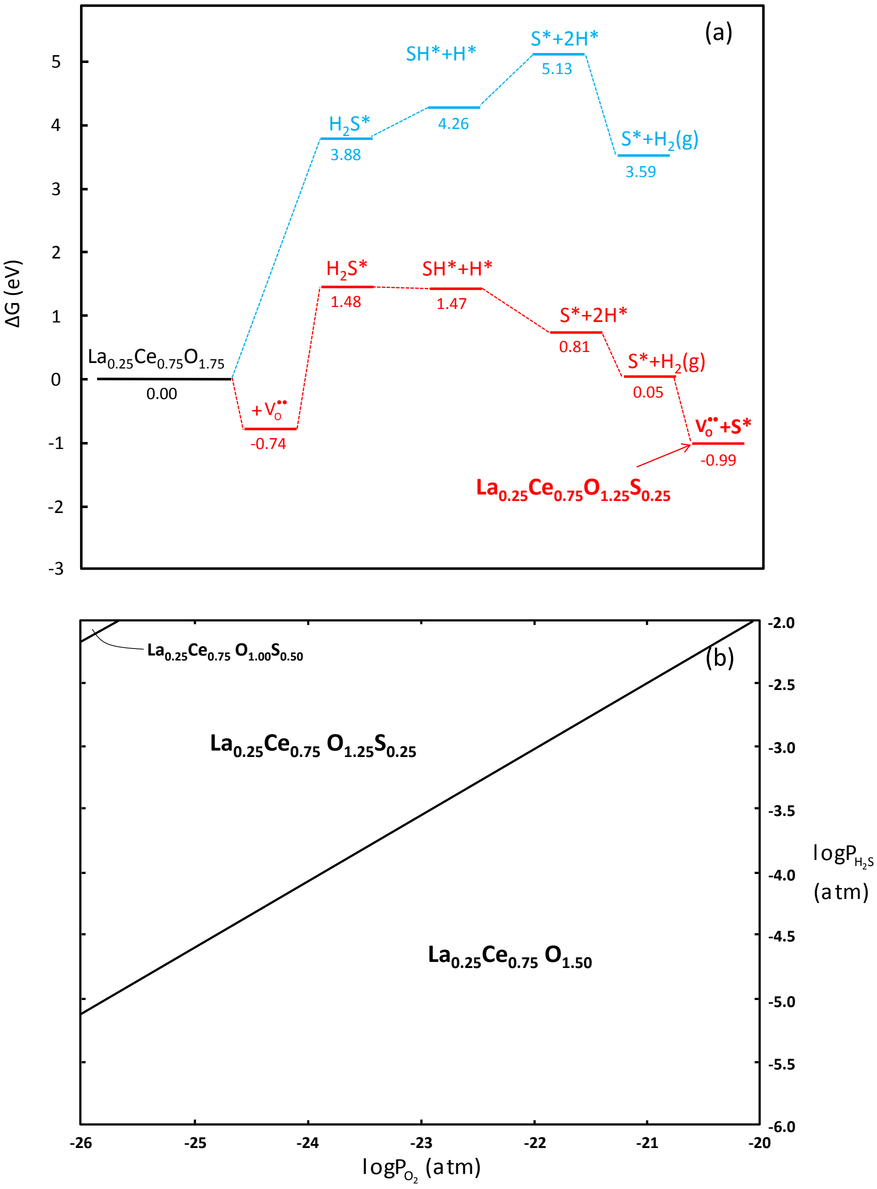

Figure 6-5. (a) Free energy diagram for H_2S adsorption dissociation over $La_2O_3/CeO_2(111)$ at 1100K, and P_{H_2} = 0.35 atm, $P_{H_2S} = 10^{-2}$ atm, and P_{H_2O} = 0.03 atm and (b) phase diagram for

$La_2O_3/CeO_2(111)$ surface at 1100K as a function of $H_2S(g)$ and $O_2(g)$ pressure. Oxygen vacancies are denoted $V_O^{\cdot\cdot}$.

and desorb $H_2(g)$. It is not favorable for sulfur atoms from $H_2S(g)$ to incorporate into the stoichiometric oxygen vacancy on $La_2O_3/CeO_2(111)$ because La and Ce atoms in the surface are in their highest stable oxidation states (La^{3+} and Ce^{4+}). In the presence of a second oxygen vacancy (-0.74 eV $V_O^{\cdot\cdot}$ formation free energy), which results in the reduction of $2Ce^{4+}$ to $2Ce^{3+}$, molecular H_2S adsorption is less endergonic (+2.23 eV) and H_2S dissociation more exergonic than on the intact $La_2O_3/CeO_2(111)$ surface. Adsorption and dissociation of H_2S over the reduced $La_2O_3/CeO_2(111)$ surface occurs via adsorption of H_2S*, SH* and S* species at an oxygen vacancy site nearest neighbor to the 3 surface Ce atoms in the unit cell. Formation of an additional oxygen vacancy is exergonic with S* present, and the surface stoichiometry of the final product state over $La_2O_3/CeO_2(111)$ is $La_{0.25}Ce_{0.75}O_{1.25}S_{0.25}$, equivalent to the oxygen and sulfur stoichiometry of the final product over $CeO_2(111)$. The overall free energy of formation of this final product from the doubly vacant surface is -0.25 eV, in comparison to –0.57 eV over pure ceria, which illustrates that the thermodynamics of sulfur incorporation over the pure ceria surface are more favorable than over the ceria-lanthana surface. The apparent energy barrier for H_2S adsorption and dissociation over $La_2O_3/CeO_2(111)$ is at a minimum +2.23 eV (the molecular adsorption energy of H_2S, assuming no S-H breaking activation barrier), much lower than over $CeO_2(111)$ (at a minimum +2.91 eV). Thus the kinetics of H_2S adsorption and dissociation over $La_2O_3/CeO_2(111)$ are much faster than over $CeO_2(111)$, which would dictate sulfur adsorption capacity under kinetically limited operating regimes.

6.3.2.3 H_2S Adsorption and Dissociation on $Tb_2O_3/CeO_2(111)$

Molecular adsorption of H_2S on $Tb_2O_3/CeO_2(111)$ is slightly stronger (+3.86 eV) than on $CeO_2(111)$ or $La_2O_3/CeO_2(111)$, however adsorption is still highly unfavorable over the stoichiometric oxygen vacancy. Adsorption and dissociation are more exergonic over the reduced $Tb_2O_3/CeO_2(111)$ surface, which occurs by adsorption of H_2S*, SH* and H* over an oxygen vacancy nearest neighbor to 2 surface Ce atoms and one surface Tb atom. Adsorption of H_2S is slightly more endergonic (+2.30 eV) over the reduced $Tb_2O_3/CeO_2(111)$ surface than over the reduced $La_2O_3/CeO_2(111)$ surface (+2.23 eV). Dissociation steps subsequent to H_2S adsorption are exergonic, and the final product of the lowest energy path is $Tb_{0.25}Ce_{0.75}O_{1.25}S_{0.25}$, equivalent to that formed on $CeO_2(111)$ and $La_2O_3/CeO_2(111)$.

6.3.3 Thermodynamic Limit for Sulfidation of Oxide Surfaces

The free energy diagrams presented herein are evaluated at specific conditions (1100K, and $P_{H_2} = 0.35$ atm, $P_{H_2S} = 10^{-2}$ atm, and $P_{H_2O} = 0.03$ atm), however we also calculate the equilibrium composition of the ceria, ceria-lanthana, and ceria-terbia surfaces over a range of possible H_2S(g) and O_2(g) pressures. Pressure ranges for H_2S(g) are estimated from compositional analysis of syngas produced from the gasification of ten different biomass sources.[1] Effective O_2(g) pressure ranges are estimated by assuming equilibrium between H_2(g) and H_2O(g), or CO(g) and CO_2(g) in the syngas streams, and setting range limits as the largest and smallest values for O_2(g) pressure calculated from either H_2(g) and H_2O(g) equilibrium or CO(g) and CO_2(g) equilibrium in the ten compositions studied by Vermeulen et al.[1] We estimate the pressure ranges in syngas produced from biomass gasification as 10^{-6}-10^{-2} atm H_2S(g) and 10^{-26}-10^{-20} atm O_2(g).

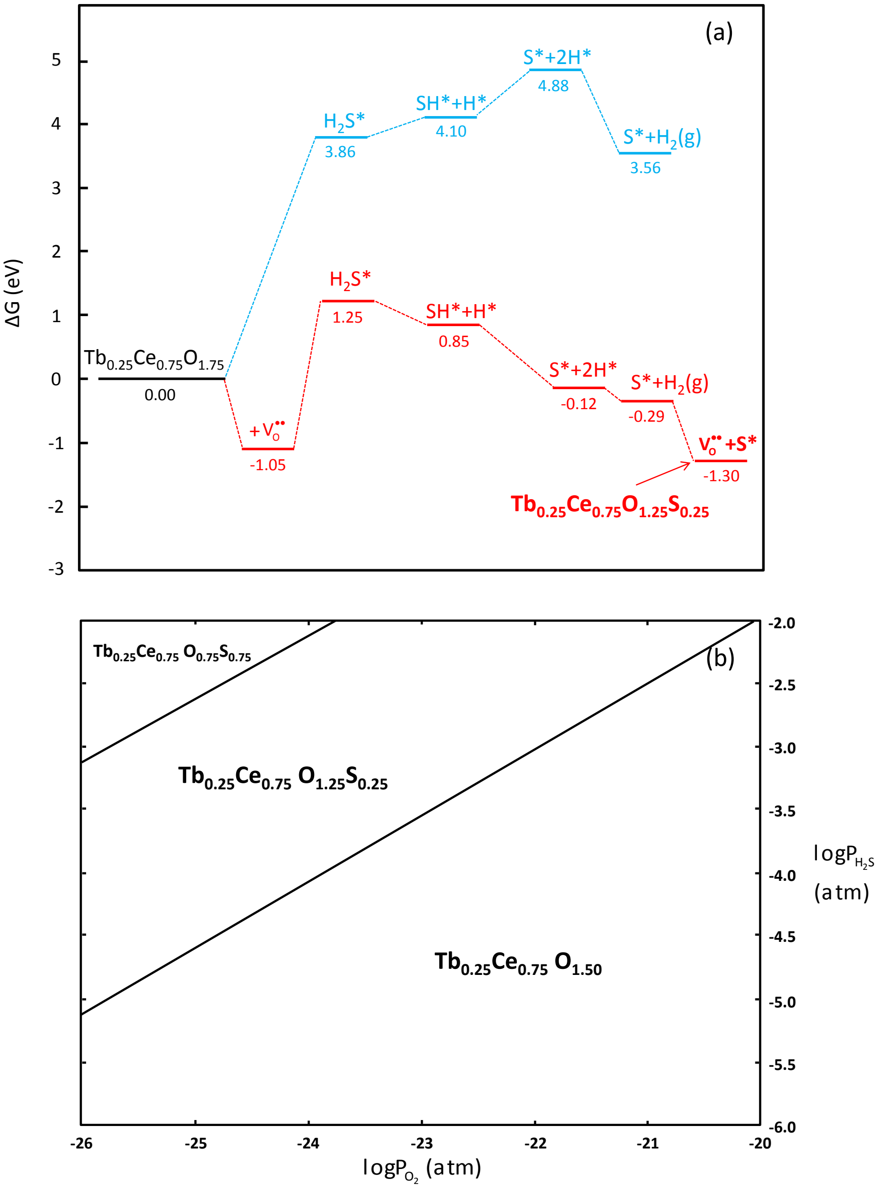

Figure 6-6. (a) Free energy diagram for H_2S adsorption dissociation over $Tb_2O_3/CeO_2(111)$ at 1100K, and P_{H_2} = 0.35 atm, P_{H_2S} = 10^{-2} atm, and P_{H_2O} = 0.03 atm and (b) phase diagram for $Tb_2O_3/CeO_2(111)$ surface at 1100K as a function of $H_2S(g)$ and $O_2(g)$ pressure. Oxygen vacancies are denoted $V_O^{\cdot\cdot}$.

Phase diagrams for the sulfur content of the ceria, ceria-lanthana, or ceria-terbia surface are constructed by calculating the free energy of the following reaction as a function of H_2S and O_2 pressure:

$$zH_2S+MO_xS_y \rightarrow MO_{x-z}S_{y+z}+zH_2+\frac{z}{2}O_2 \quad (5)$$

where sulfur atoms from H_2S substitute into the ceria lattice for oxygen atoms. Formation of either O_2(g) and H_2(g) or H_2O(g) as reaction products is equivalent by assuming equilibrium between H_2O(g), H_2(g), and O_2(g) as stated in equation (4). Substitution of oxygen atoms for sulfur atoms is considered for the surface and subsurface layers of oxygen atoms in the ceria, ceria-lanthana, and ceria-terbia surfaces. Stoichiometries considered for the surface metal layer include configurations of sulfur and oxygen from fully oxidized to fully reduced:

$$1.5<\frac{n_{oxygen}+n_{sulfur}}{n_{metal}}<2 \qquad (6)$$

where n_{oxygen}, n_{sulfur}, and n_{metal} are the number of oxygen atoms, sulfur atoms, and metal atoms, respectively in the surface CeO_2 layer (surface metal layer and surface and subsurface oxygen atom layers). In equation (6), $n_{metal} = 4$ for all stoichiometries as the p(2x2) surface unit cell contains 4 metal atoms in the surface metal layer, and $n_{oxygen} + n_{sulfur} = 6, 7, \text{or } 8$ corresponding to the total number of oxygen and sulfur atoms in the surface and subsurface layers. To locate the lowest energy structure for each stoichiometry, structural optimizations were performed with oxygen and sulfur atoms in all possible configurations with respect to surface metal atoms and oxygen vacancies. The optimized structures reported for each stoichiometry of oxygen and sulfur are constrained by the size of the surface unit cell, which only permits surface reordering on the length scales of the p(2x2) expansion. The phase diagrams we report are useful, however, in identifying trends between ceria, ceria-lanthana, and ceria-terbia for the thermodynamic limit of surface sulfur incorporation while the underlying cubic fluorite bulk lattice is maintained.

6.3.3.1 Phase Diagram for Sulfidation of CeO_2(111)

Figure 6-4(b) displays the phase diagram for the sulfidation of the CeO_2 (111) surface as a function of H_2S(g) and O_2(g) pressure at 1100K. At low H_2S and the highest relevant O_2 pressure, the reduced ceria surface (surface stoichiometry of $CeO_{1.75}$) is stable with respect to other surface compositions. At lower O_2 pressure and increasing H_2S pressures, the $CeO_{1.25}S_{0.25}$ surface stoichiometry is favorable, and at the edge of the range of biomass gasifier partial pressures (high H_2S and low O_2 pressure), $CeO_{1.00}S_{0.5}$ is favorable. The $CeO_{1.25}S_{0.25}$ surface is stable over a wide range of H_2S and O_2 pressures, including the conditions used to evaluate H_2S adsorption free energies in Section 6.3.2. The wide range over which the $CeO_{1.25}S_{0.25}$ surface is thermodynamically favorable indicates that further sulfidation relative to this stoichiometry is not favorable. The surface stoichiometry of $CeO_{1.00}S_{0.5}$ is comprised of 2 surface sulfur atoms, 1 surface oxygen and 3 subsurface oxygen (1 oxygen vacancy formed subsurface). Kay et al. report that over the same H_2S (10^{-6}-10^{-2} atm) and O_2 (10^{-26}-10^{-20} atm) pressure ranges considered herein, Ce_2O_2S, CeO_x ($1.73 < x < 1.83$), and Ce_2O_3 are thermodynamically favorable bulk phases.[8] Over the majority of these H_2S and O_2 pressures, the authors report that Ce_2O_2S is thermodynamically favorable,[8] which is equivalent to a surface stoichiometry of $CeO_{1.00}S_{0.5}$ in the p(2x2) unit cell.

Both the H_2S adsorption and free energy diagram and the phase diagram for the CeO_2(111) surface show that substitution of sulfur atoms into oxygen lattice positions is only favorable when multiple adjacent oxygen vacancies are present. Sulfur-metal distances are longer than oxygen-metal distances in the ceria surface, and the ionic radius of sulfur is approximately 1 Å compared to approximately 0.6 Å for oxygen.[29] Sulfur incorporation into the ceria surface is thus only favorable if multiple adjacent oxygen vacancies are present to provide the structural flexibility necessary to accommodate the larger coordination shell of sulfur atoms than oxygen atoms in the ceria lattice.

6.3.3.2 Phase Diagram for Sulfidation of $La_2O_3/CeO_2(111)$

Figure 6-5(b) displays the phase diagram for the sulfidation of the $La_2O_3/CeO_2(111)$ surface as a function of H_2S (g) and O_2 (g) pressure at 1100K. The phase diagram for La_2-$O_3/CeO_2(111)$ is comprised of regions of identical surface sulfur and oxygen stoichiometry to those of $CeO_2(111)$, however the transition from $La_{0.25}Ce_{0.75}O_{1.75}$ to $La_{0.25}Ce_{0.75}O_{1.25}S_{0.25}$ occurs at much lower O_2 and higher H_2S pressure than the transition from $CeO_{1.75}$ to $CeO_{1.25}S_{0.25}$. Sulfur incorporation is also only favorable with the formation of multiple oxygen vacancies within the surface unit cell over the $La_2O_3/CeO_2(111)$ surface. The phase diagram over La_2O_3/CeO_2 is consistent with the free energies of H_2S adsorption over La_2O_3/CeO_2 and pure ceria. The thermodynamics of H_2S dissociation are more exergonic over pure ceria, and thus transition to a a sulfided surface stoichiometry occurs at lower H_2S(g) and higher O_2(g) pressures on ceria than on ceria-lanthana. The positions of lanthanum dopants in the ceria surface are arbitrary and fixed, however these results illustrate that the ceria-lanthana mixtures may not stabilize higher surface sulfur concentrations with respect to pure ceria.

6.3.3.3 Phase Diagram for Sulfidation of $Tb_2O_3/CeO_2(111)$

Figure 6-6(b) displays the phase diagram for the sulfidation of the $Tb_2O_3/CeO_2(111)$ surface as a function of H_2S(g) and O_2(g) pressure at 1100K. The transition from $Tb_{0.25}Ce_{0.75}O_{1.75}$ to $Tb_{0.25}Ce_{0.75}O_{1.25}S_{0.25}$ occurs a slightly lower O_2 and slightly higher H_2S pressure than the transition from $CeO_{1.75}$ to $CeO_{1.25}S_{0.25}$. The phase diagram over ceria-terbia, however, does show that formation of a more highly sulfided surface than on ceria or ceria-lanthana ($Tb_{0.25}Ce_{0.75}O_{0.75}S_{0.75}$) is thermodynamically favorable at high H_2S and low O_2 pressure. The $Tb_{0.25}Ce_{0.75}O_{0.75}S_{0.75}$ surface is terminated by 3 surface sulfur atoms with 3 oxygen atoms in the subsurface layer. This transition to larger sulfur content of the ceria-terbia surface suggests that the equilibrium sulfur capacity of the ceria-terbia surface may be larger than that of ceria or ceria-lanthana for certain syngas compositions (high P_{H_2S}, low P_{O_2}).

The phase diagrams for sulfidation of the ceria, ceria-lanthana, and ceria-terbia surfaces illustrate the importance of oxygen vacancies as active sites for high temperature H_2S adsorption and dissociation. The thermodynamic driving force for the H_2S adsorption process is dictated by the relative energy of substituting sulfur atoms from H_2S for oxygen atoms in the metal oxide lattice. The equilibrium sulfur capacity of the metal oxide surface is thus a function of the partial pressure of H_2S and the effective O_2 partial pressure (dictated by the partial pressures of H_2, H_2O, CO, and CO_2) in the gas phase. The free energy to form a surface stoichiometry of $MO_{1.25}S_{0.25}$ is most exergonic on the pure ceria surface, and the ceria-terbia surface may have the largest equilibrium sulfur capacity under high P_{H_2S} and low P_{O_2}. Considering the H_2S pressures at which formation of the $MO_{1.25}S_{.25}$ stoichiometry forms, our thermodynamic calculations indicate that sulfur adsorption is most favorable on pure ceria, with adsorption on ceria-terbia more favorable than on lanthana-ceria. The experimental sulfur adsorption capacities reported herein and previous comparison of the sulfur adsorption capacities of pure ceria ceria-lanthana,[3] however indicate that ceria-lanthana has a larger sulfur adsorption capacity than both pure ceria and ceria-terbia. The fact that sulfur adsorption capacity does not correlate with the overall thermodynamics of sulfur substitution into the oxide surface indicates that sulfur adsorption capacities may be dictated by the kinetics of H_2S dissociation.

6.3.4 Thermodynamic Cycle for H_2S adsorption by Ceria-Based Mixed Oxides

Figure 6-7 displays the thermodynamic cycle for H_2S adsorption and dissociation over the reduced ceria surface. The surface in Figure 6-7 is denoted $MO_{1.75}$, to signify a surface stoichiometry of either $CeO_{1.75}$, $La_{0.25}Ce_{0.75}O_{1.75}$, or $Tb_{0.25}Ce_{0.75}O_{1.75}$. The free energies for each step (vacancy formation, H_2S adsorption, and H_2S dissociation) over $CeO_{1.75}$, $La_{0.25}Ce_{0.75}O_{1.75}$, and $Tb_{0.25}Ce_{0.75}O_{1.75}$ at 1100K, and P_{H_2} = 0.35 atm, $P_{H_2S} = 10^{-2}$ atm, and P_{H_2O} = 0.03 atm are listed in Table 6-2. The overall free energy to form $MO_{1.25}S_{0.25}$ is most exergonic over CeO_2, mainly due to strongly exergonic H_2S dissociation energetics. The ceria-terbia surface is more reducible than the ceria or ceria-lanthana surfaces, with an oxygen vacancy formation energy of -1.05 eV. Molecular H_2S adsorption is strongest over ceria-lanthana at +2.23 eV, compared to +2.30 eV over ceria-terbia and +2.91 eV over ceria. The thermodynamics of the overall H_2S adsorption process do not correlate with oxygen vacancy formation energy, implying that the optimization of ceria-based sulfur sorbents cannot be achieved by tailoring composition to maximize the reducibility of the oxide mixture. The rate limiting step for H_2S adsorption and dissociation involves reaching the transition state for dissociation of the first S-H bond to form

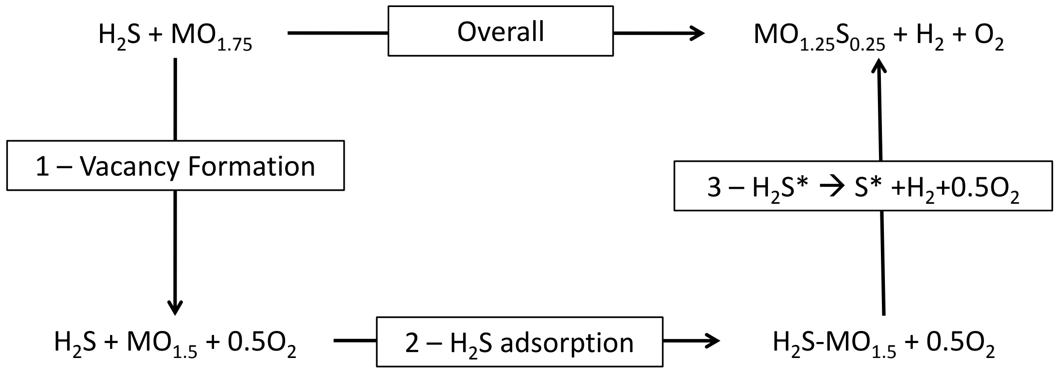
$H_2S + MO_{1.75}$
Overall
$MO_{1.25}S_{0.25} + H_2 + O_2$
1 – Vacancy Formation
3 – $H_2S^* \rightarrow S^* + H_2 + 0.5O_2$
$H_2S + MO_{1.5} + 0.5O_2$
2 – H_2S adsorption
$H_2S\text{-}MO_{1.5} + 0.5O_2$

Figure 6-7. Thermodynamic cycle for H_2S adsorption and dissociation on ceria-based mixed metal oxide.

SH*+H* (>2.23 eV over each surface), and the rate is highest over ceria-lanthana (rate over ceria-lanthana > ceria-terbia > ceria). This trend in H_2S adsorption and dissociation rates agrees with our experimental trend of sulfur adsorption capacities as well as those presented previously,[3] reinforcing that sulfur adsorption capacity is limited by surface kinetics.

Table 6-2. Energies for thermodynamic cycle (Figure 6-7) over CeO_2, $LaCeO_x$, and $TbCeO_x$.

	Energy (eV)		
	CeO_2	La_2O_3/CeO_2	Tb_2O_3/CeO_2
Overall	-1.35	-0.98	-1.30
1	-0.78	-0.74	-1.05
2	+2.91	+2.23	+2.30
3	-3.48	-2.47	-2.55

6.4 Conclusions

The DFT+*U* method and *ab initio* thermodynamics were used to evaluate the free energies of H_2S adsorption and dissociation over ceria, ceria-lanthana, and ceria-terbia. Surface models consisted of the (111) single crystal termination of CeO_2, as well as the CeO_2(111) surface with lanthanum and terbium atoms substituted for Ce atoms. We evaluate the free energies of H_2S adsorption and dissociation in contrast to purely DFT energies, which illustrate the role of entropic contributions to the driving force for adsorption of gas phase species at high temperature and low partial pressure. Molecular adsorption of H_2S is endergonic over the fully oxidized and intact ceria, ceria-lanthana, and ceria-terbia surfaces at high temperature desulfurization conditions. Adsorption of H_2S involves $V_O^{\cdot\cdot}$ formation, filling of $V_O^{\cdot\cdot}$ with S*, and subsequent $V_O^{\cdot\cdot}$ formation; H_2S adsorption requires multiple adjacent oxygen vacancies to provide structural flexibility to accomodate large S^{2-} ions. The energy barriers of H_2S adsorption and dissociation over ceria are much larger than those over ceria-lanthana and ceria-terbia, suggesting that the larger sulfur adsorption capacity observed experimentally is due to faster surface kinetics over the mixed oxide surfaces. The reducibility of the oxide mixture does not correlate with sulfur adsorption and dissociation energetics, and the optimization of ceria-based mixed oxide sulfur sorbents may lie in the design of mixed oxides with increased H_2S dissociation kinetics.

6.5 References

(1) van der Drift, A.; van Doorn, J.; Vermeulen, J. W. *Biomass and Bioenergy* **2001**, *20*, 45-56.

(2) Meng, X. M.; De Jong, W.; Verkooijen, A. H. M. *Environmental Progress & Sustainable Energy* **2009**, *28*, 360-371.

(3) Flytzani-Stephanopoulos, M.; Sakbodin, M.; Wang, Z. *Science* **2006**, *312*, 1508-1510.

(4) Kuramochi, H.; Wu, W.; Kawamoto, K. *Fuel* **2005**, *84*, 377-387.

(5) Wilkes, M. F.; Hayden, P.; Bhattacharya, A. K. *Journal of Catalysis* **2003**, *219*, 305-309.

(6) Zhou, G.; Gorte, R. J. *The Journal of Physical Chemistry B* **2008**, *112*, 9869-9875.

(7) Bernal, S.; Blanco, G.; Cifredo, G.; Pérez-Omil, J. A.; Pintado, J. M.; RodrIguez-Izquierdo, J. M. *Journal of Alloys and Compounds* **1997**, *250*, 449-454.

(8) Kay, A. R.; Wilson, W. G.; Jalan, V. *Journal of Alloys and Compounds* **1993**, *192*, 11-16.

(9) Kempegowda, R.; Laosiripojana, N.; Assabumrungrat, S. *Korean Journal of Chemical Engineering* **2008**, *25*, 223-230.

(10) Chen, H.-T.; Choi, Y.; Liu, M.; Lin, M. C. *The Journal of Physical Chemistry C* **2007**, *111*, 11117-11122.

(11) Terribile, D.; Trovarelli, A.; Llorca, J.; de Leitenburg, C.; Dolcetti, G. *J. Catal.* **1998**, *178*, 299-308.

(12) Randery, S. D.; Warren, J. S.; Dooley, K. M. *Appl. Catal. A* **2002**, *226*, 265-280.

(13) Kresse, G.; Furthmuller, J. *Computational Materials Science* **1996**, *6*, 15-50.

(14) Kresse, G.; Furthmuller, J. *Physical Review B* **1996**, *54*, 11169-11186.

(15) Kresse, G.; Hafner, J. *Physical Review B* **1993**, *47*, 558-561.

(16) Kresse, G.; Joubert, D. *Physical Review B* **1999**, *59*, 1758 LP - 1775.

(17) Perdew, J. P.; Chevary, J. A.; Vosko, S. H.; Jackson, K. A.; Pederson, M. R.; Singh, D. J.; Fiolhais, C. *Physical Review B* **1992**, *46*, 6671.

(18) Fabris, S.; Gironcoli, S. d.; Baroni, S.; Vicario, G.; Balducci, G. *Physical Review B* **2005**, *71*, 041102.

(19) Fabris, S.; Gironcoli, S. d.; Baroni, S.; Vicario, G.; Balducci, G. *Physical Review B* **2005**, *72*, 237102.

(20) Kresse, G.; Blaha, P.; Silva, J.; Ganduglia-Pirovano, M. V. *Physical Review B* **2005**, *72*, 237101.

(21) Nolan, M.; Grigoleit, S.; Sayle, D. C.; Parker, S. C.; Watson, G. W. *Surface Science* **2005**, *576*, 217-229.

(22) Nolan, M.; Parker, S. C.; Watson, G. W. *Surface Science* **2005**, *595*, 223-232.

(23) Herschend, B.; Baudin, M.; Hermansson, K. *Surface Science* **2005**, *599*, 173-186.

(24) Yang, Z.; Lu, Z.; Luo, G.; Hermansson, K. *Physics Letters A* **2007**, *369*, 132-139.

(25) Yang, Z.; Luo, G.; Lu, Z.; Hermansson, K. *The Journal of Chemical Physics* **2007**, *127*, 074704-5.

(26) Knapp, D.; Ziegler, T. *The Journal of Physical Chemistry C* **2008**, *112*, 17311-17318.

(27) Mayernick, A. D.; Janik, M. J. *The Journal of Physical Chemistry C* **2008**, *112*, 14955-14964.

(28) Wang, L.; Maxisch, T.; Ceder, G. *Physical Review B* **2006**, *73*, 195107.

(29) Slater, J. C. *Journal of Chemical Physics* **1964**, *41*, 3199.

6.6 Supporting Information

Adsorbed Species	Surface Composition	M	Ce_1 - S bond length (Å)	Ce_2 - S bond length (Å)	M - S bond length (Å)
H_2S	$CeO_{1.75}$	Ce	3.87	3.35	3.91
	$CeO_{1.5}$	Ce	4.09	3.66	4.14
	$La_{0.25}Ce_{0.75}O_{1.75}$	Ce	3.97	3.58	3.97
	$La_{0.25}Ce_{0.75}O_{1.5}$	Ce	4.06	3.58	3.88
	$Tb_{0.25}Ce_{0.75}O_{1.75}$	Tb	3.90	3.48	4.19
	$Tb_{0.25}Ce_{0.75}O_{1.5}$	Tb	3.96	3.52	4.11
SH	$CeO_{1.75}$	Ce	3.02	2.96	2.96
	$CeO_{1.5}$	Ce	3.03	3.00	3.00
	$La_{0.25}Ce_{0.75}O_{1.75}$	Ce	3.00	3.03	3.00
	$La_{0.25}Ce_{0.75}O_{1.5}$	Ce	2.97	3.18	3.06
	$Tb_{0.25}Ce_{0.75}O_{1.75}$	Tb	3.04	2.98	3.03
	$Tb_{0.25}Ce_{0.75}O_{1.5}$	Tb	2.94	3.00	2.98
S	$CeO_{1.75}$	Ce	2.79	2.80	2.80
	$CeO_{1.5}$	Ce	2.77	2.83	2.80
	$La_{0.25}Ce_{0.75}O_{1.75}$	Ce	2.91	2.92	2.97
	$La_{0.25}Ce_{0.75}O_{1.5}$	Ce	2.80	2.85	2.80
	$Tb_{0.25}Ce_{0.75}O_{1.75}$	Tb	2.78	2.76	2.82
	$Tb_{0.25}Ce_{0.75}O_{1.5}$	Tb	2.75	2.78	2.83

Table S1. Bond lengths for H_2S*, SH*, and S* on reduced $CeO_2(111)$, $La_2O_3/CeO_2(111)$, and $Tb_2O_3/CeO_2(111)$.

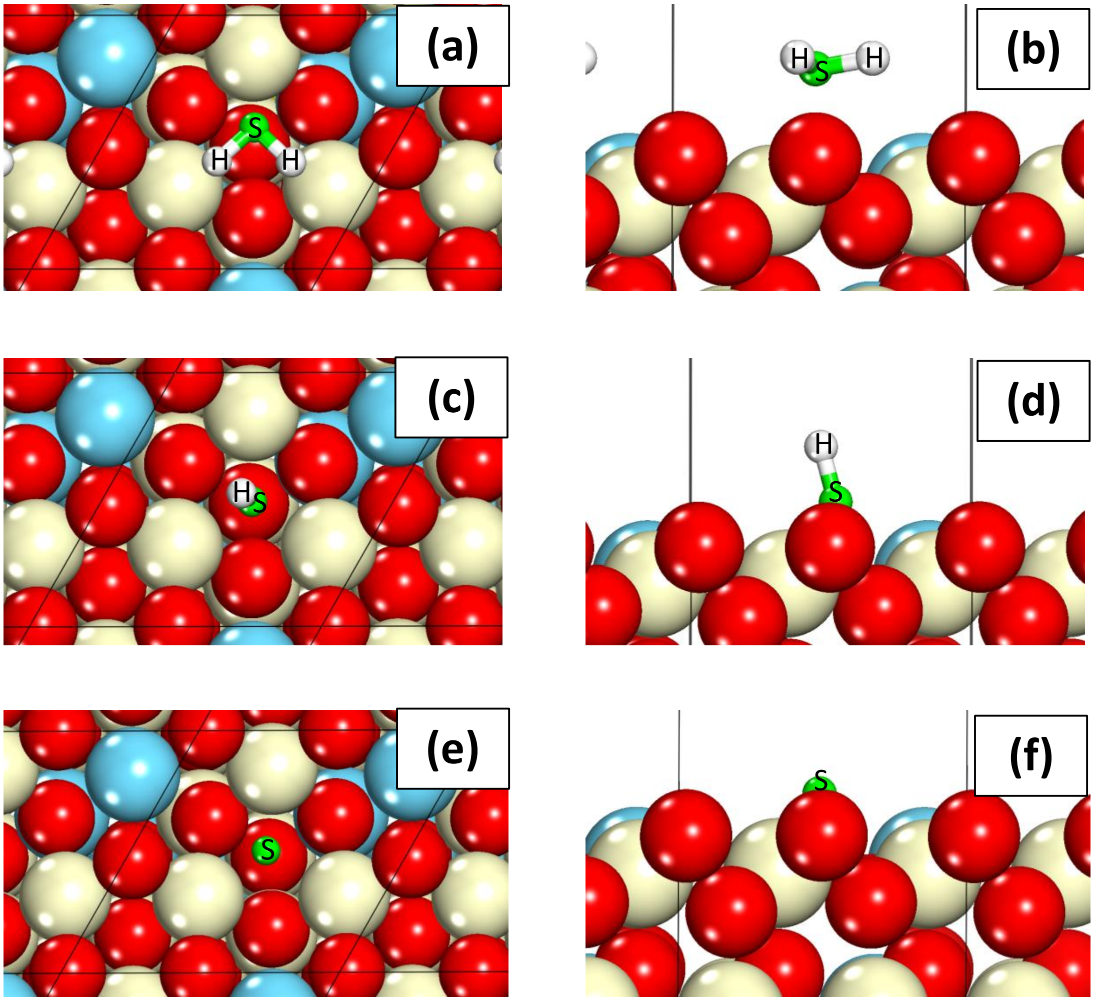

Figure S1. Top (a), (c), (e), and side (b), (d), (f) views of surface unit cell for H2S* (a), (b), SH* (c), (d), and S* (e), (f) on $La_2O_3/CeO_2(111)$. Ce atoms are colored tan (light), La atoms blue (gray), O atoms red (dark), S atoms green (gray), and H atoms white.

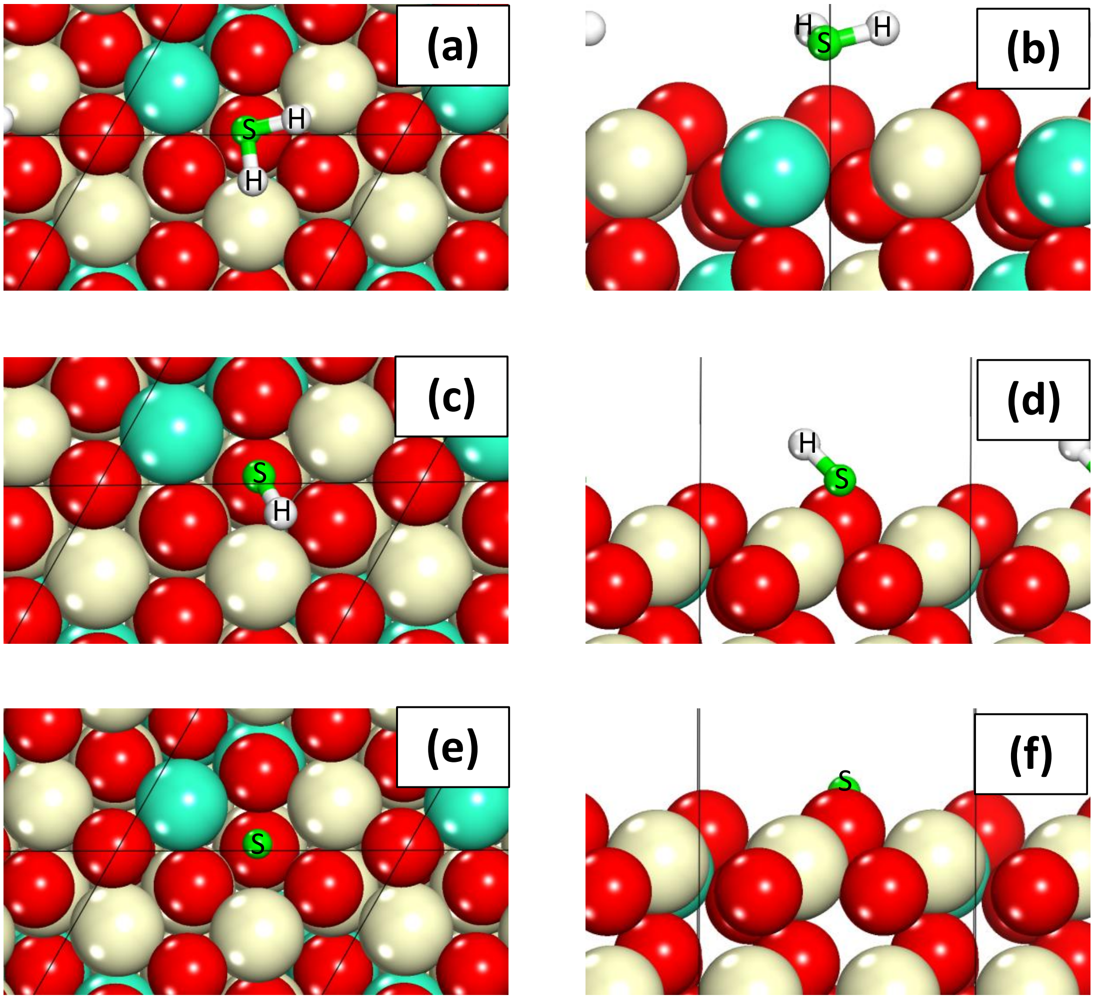

Figure S2. Top (a), (c), (e), and side (b), (d), (f) views of surface unit cell for H2S* (a), (b), SH* (c), (d), and S* (e), (f) on $Tb_2O_3/CeO_2(111)$. Ce atoms are colored tan (light), La atoms blue (gray), O atoms red (dark), S atoms green (gray), and H atoms white.

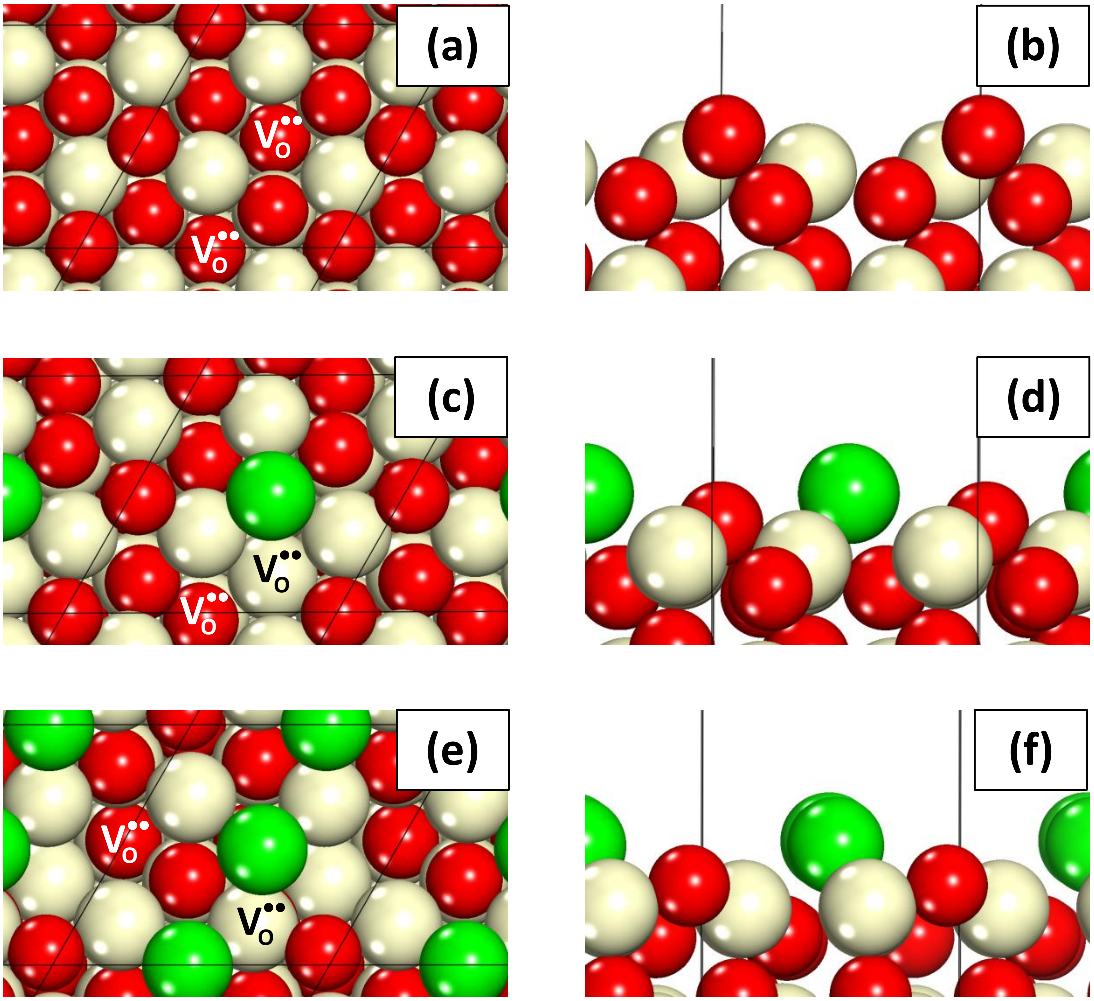
(a)
$V_O^{\bullet\bullet}$
$V_O^{\bullet\bullet}$
(b)
(c)
$V_O^{\bullet\bullet}$
$V_O^{\bullet\bullet}$
(d)
(e)
$V_O^{\bullet\bullet}$
$V_O^{\bullet\bullet}$
(f)

Figure S3. Top (a), (c), (e), and side (b), (d), (f) views of surface unit cell for $CeO_{1.5}$ (a), (b), $CeO_{1.25}S_{0.25}$ (c), (d), and $Ce_{1.00}S_{0.5}$ (e), (f). Ce atoms are colored tan (light), O atoms red (dark), and S atoms green (gray). Surface oxygen vacancies ($V_O^{\cdot\cdot}$, white colored font) and subsurface oxygen vacancies ($V_O^{\cdot\cdot}$, black colored font) are labeled.

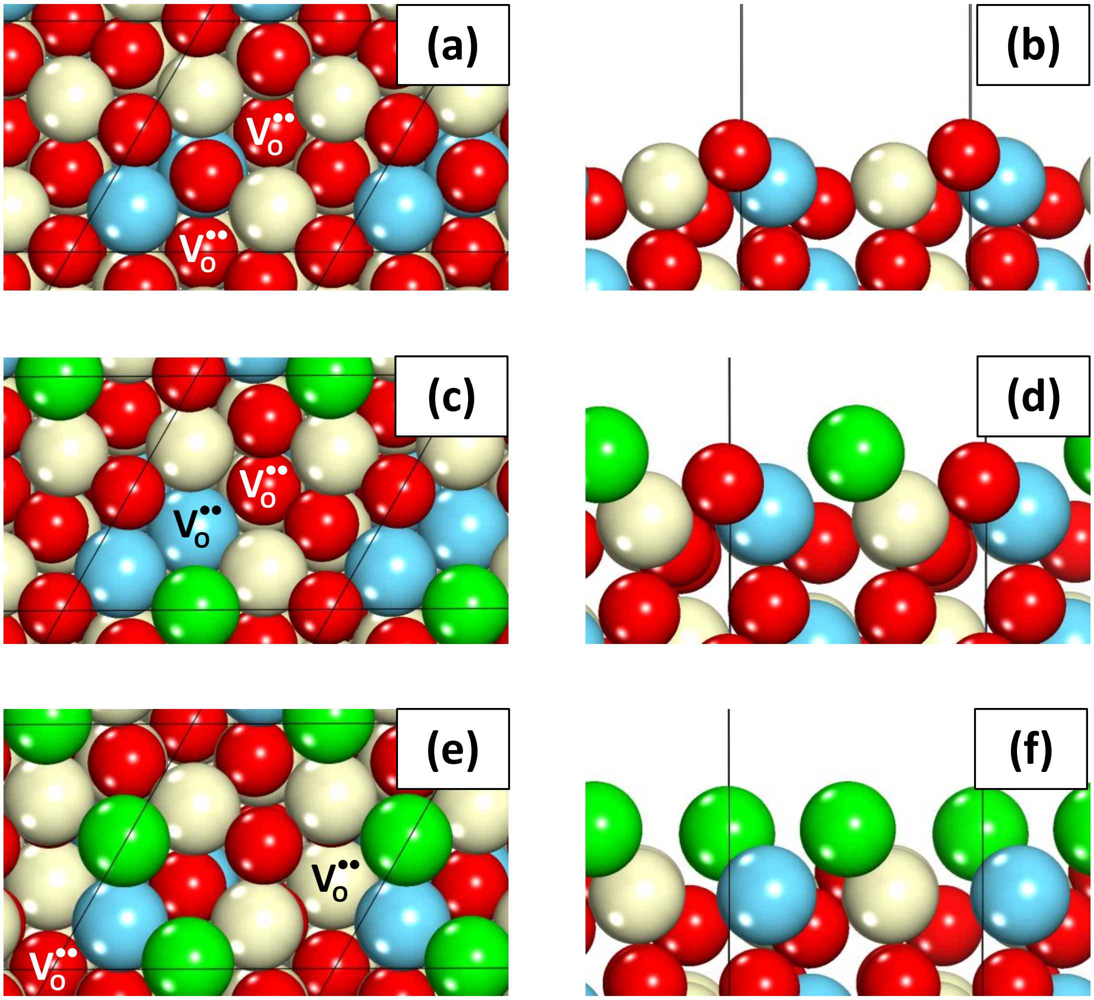
(a)
$V_O^{\bullet\bullet}$
$V_O^{\bullet\bullet}$
(b)
(c)
$V_O^{\bullet\bullet}$
$V_O^{\bullet\bullet}$
(d)
(e)
$V_O^{\bullet\bullet}$
$V_O^{\bullet\bullet}$
(f)

Figure S4. Top (a), (c), (e), and side (b), (d), (f) views of surface unit cell for $La_{0.25}Ce_{0.75}O_{1.5}$ (a), (b), $La_{0.25}Ce_{0.75}O_{1.25}S_{0.25}$ (c), (d), and $La_{0.25}Ce_{0.75}O_{1.00}S_{0.50}$ (e), (f). Ce atoms are colored tan (light), La atoms blue (gray), O atoms red (dark), and S atoms green (gray). Surface oxygen vacancies ($V_O^{\cdot\cdot}$, white colored font) and subsurface oxygen vacancies ($V_O^{\cdot\cdot}$, black colored font) are labeled.

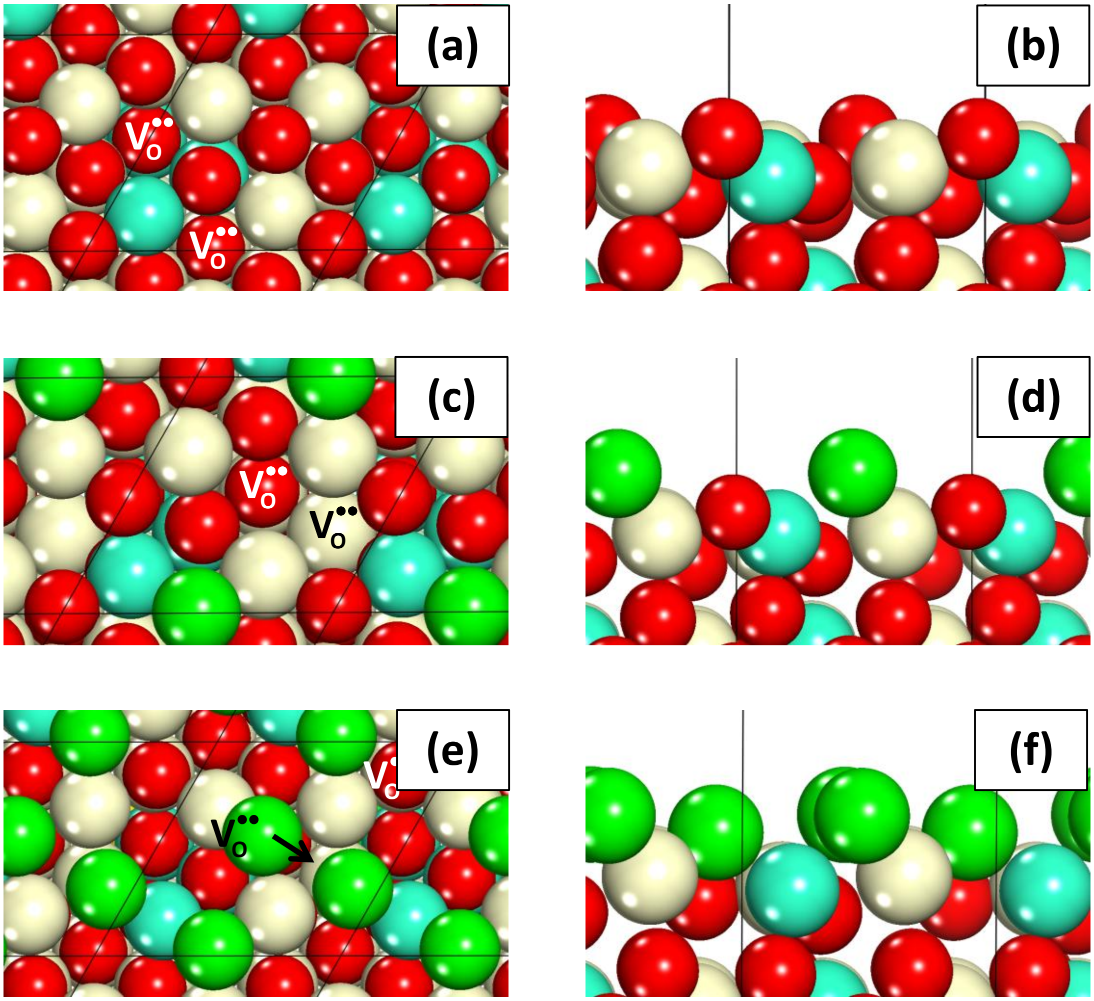
(a)
$V_O^{\bullet\bullet}$
$V_O^{\bullet\bullet}$
(b)
(c)
$V_O^{\bullet\bullet}$
$V_O^{\bullet\bullet}$
(d)
(e)
$V_O^{\bullet\bullet}$
$V_O^{\bullet\bullet}$
(f)

Figure S5. Top (a), (c), (e), and side (b), (d), (f) views of surface unit cell for $Tb_{0.25}Ce_{0.75}O_{1.5}$ (a), (b), $Tb_{0.25}Ce_{0.75}O_{1.25}S_{0.25}$ (c), (d), and $Tb_{0.25}Ce_{0.75}O_{0.75}S_{0.75}$ (e), (f). Ce atoms are colored tan (light), Tb atoms teal (dark gray), O atoms red (dark), and S atoms green (gray). Surface oxygen vacancies ($V_O^{\cdot\cdot}$, white colored font) and subsurface oxygen vacancies ($V_O^{\cdot\cdot}$, black colored font) are labeled. The arrow in (e) indicates that the subsurface oxygen vacancy in $Tb_{0.25}Ce_{0.75}O_{0.75}S_{0.75}$ is beneath a surface sulfur atom.

Chapter 7

A ReaxFF Reactive Monte Carlo Study of Surface Enrichment and Step Structure on Yttria-Stabilized Zirconia

This chapter is published as: A. D. Mayernick, M. Batzill, A. van Duin, M. J. Janik. *Surface Science* 2010, 604, 1438-1444.

ABSTRACT: To investigate surface segregation in yttria-stabilized zirconia (YSZ), DFT energies describing surface energy as a function of yttrium lattice position were used to parameterize a reactive-force field (ReaxFF). We used ReaxFF to perform Monte Carlo (MC) simulated annealing to sample structural configurations of flat YSZ (111) and vicinal YSZ (111) stepped surfaces. We evaluated yttrium surface segregation, oxygen vacancy position, and surface step composition for flat and stepped YSZ surfaces. It is thermodynamically favorable for yttrium atoms to segregate to the surface of YSZ, and specifically to step edge sites. Surface saturation of yttrium occurs at approximately 40% (40:60 Y:Zr ratio) while yttrium concentration at the step edge does not approach a saturation value, suggesting that steps on the YSZ surface are mainly yttria-terminated. We found that it is thermodynamically favorable for oxygen vacancies to occupy positions in the subsurface layer of YSZ, and a higher fraction of vacancies occupy positions NN to Y than NN to Zr. Yttrium segregation to step edges on the YSZ surface does not lower the surface formation energy of the stepped surface below that of the flat (111) termination, suggesting that the stability of YSZ surface steps observed experimentally is due to kinetic barriers for surface re-ordering.

7.1 Introduction

Yttria-stabilized zirconia (YSZ) is a mixed metal oxide which exhibits ionic conductivity at high temperatures, motivating the use of YSZ in oxygen sensors,[1] supported catalysis,[2,3] and as an electrolyte in solid-oxide fuel cells (SOFC).[4,5] The addition of approximately 4-7 mol% yttria (Y_2O_3) to zirconia (ZrO_2) stabilizes the cubic phase of zirconia and results in the presence of oxygen vacancies.[6] These oxygen defects increase oxygen mobility with respect to ZrO_2, evidenced by the ionic conductivity of YSZ at high temperatures. The specific morphology and composition of the YSZ surface impacts functionality in each of the applications listed above. Characterization of YSZ surfaces by x-ray photoelectron spectroscopy (XPS)[7-9] and secondary ion mass spectrometry (SIMS)[10] methods indicates surface segregation of yttrium, suggesting that perturbations of the ZrO_2 surface structure may occur even at low bulk yttria content.

To investigate the surface behavior of YSZ-materials, we have to first consider the YSZ bulk structure. The cubic fluorite phase of pure zirconia is stable only at high temperatures (>2500K) relative to monoclinic or tetragonal phases, however the addition of low valency dopants such as yttrium stabilizes the fluorite phase at temperatures as low as room temperature.[8] The addition of Y_2O_3 to ZrO_2 results in an oxygen-deficient cubic fluorite phase in which oxygen vacancies facilitate oxygen ion mobility sufficiently to provide ionic conductivity at high temperatures (>625K).[11-13] This oxygen deficient phase contains a distribution of yttrium, zirconium, and oxygen atoms for which the lowest energy configuration is difficult to characterize experimentally. The complex structure of this mixed metal oxide has resulted in conflicting data addressing the position of oxygen vacancies within the YSZ lattice. X-ray absorption studies of bulk YSZ have indicated that vacancies may be nearest neighbor (NN) to Zr^{4+},[14,15] while other such studies have indicated that vacancies may be nearest neighbor to Y^{3+}.[16,17] The configuration of yttrium, zirconium, oxygen atoms and oxygen defects is thus not conclusively characterized for bulk YSZ. The distribution of Y dopants and oxygen vacancies in bulk YSZ has previously been examined using reactive force field (ReaxFF) methods. This study showed that the oxygen coordination numbers (c.n.) of Zr and Y atoms in bulk YSZ-14 (1:3 Y:Zr ratio) are 6.9 and 7.9, respectively, implying that oxygen vacancies in bulk YSZ are NN to Zr^{4+}.[18]

The structural details of YSZ surfaces are also difficult to elucidate experimentally, where the composition may differ significantly from the bulk. Characterization of YSZ surfaces has indicated that the yttrium composition is increased with respect to bulk concentration,[7,8,10] and that corrugated surfaces containing a high density of steps may be stable relative to flat YSZ surfaces or kinetically inhibited from annealing.[9,19,20] X-ray photoelectron spectroscopy (XPS) studies on YSZ surfaces have indicated that yttrium segregates to the YSZ surface and that the surface Y content may be increased more than two-fold with respect to the bulk Y concentration.[7-9] Lahiri et al. used angle-dependent XPS analysis to conclude that the YSZ (111) surface of 10% Y bulk YSZ (Y:Zr = 10:90) is comprised of either a yttrium-enriched top layer at 45% yttrium (Y:Zr = 45:55) or an enriched top two layers at 30% yttrium (Y:Zr = 30:70).[9] Auger electron spectroscopy, low-energy electron diffraction (LEED), and SIMS experiments have also indicated yttrium enrichment of the YSZ (100) and (110) terminations.[10] Despite numerous methods for characterizing the composition of YSZ surfaces, direct imaging with electron microscopy techniques is challenged by the electron insulating properties of YSZ. Atomic force microscopy (AFM) studies have indicated that the stable morphology of the YSZ (100) termination is composed of a series of parallel steps,[19] however AFM images cannot achieve atomic level resolution. The first scanning tunneling microscopy (STM) images of the YSZ (111) surface indicate the presence of monatomic steps before and after annealing at 1000K and ion sputtering.[9,20] These results suggest that a highly stepped YSZ termination may be stable relative to a flat surface, however step composition and the surface thermodynamics of step formation are poorly understood.

Computational chemistry approaches to modeling oxide surfaces can investigate structural details which can be difficult to characterize experimentally, and provide insight into the electronic structure at the surface. Density functional theory (DFT) methods provide the means to directly calculate surface formation energies and evaluate the thermodynamic stability of surfaces with different geometry and composition. Previous DFT studies of the surfaces of YSZ have focused on evaluating the thermodynamic stability[21,22] and catalytic activity[3] of YSZ surfaces. Wang et al.[22] used DFT methods to show that it is thermodynamically favorable for yttrium atoms to segregate to the subsurface layer of YSZ (111). The computational intensity of DFT calculations challenges the evaluation of the multitude of configurations of yttrium atoms and oxygen vacancies possible on a YSZ surface. Catlow et al.[23] used interatomic potential-based methods to calculate segregation energies of yttrium for flat YSZ surfaces and showed that yttrium segregation to the YSZ (111) surface is exothermic. No previous computational study has addressed corrugated YSZ surfaces and evaluated the thermodynamic stability or composition of stepped surface morphologies. To evaluate the structure and composition of vicinal YSZ (111) surfaces with monatomic steps, it is necessary to implement a computational methodology which samples surface configurations of oxygen, metal atoms, and defects within an energy minimization scheme. This methodology must also permit the use of large surface models (>1000 atoms) relative to DFT calculations (~100-200 atoms) to accurately represent the heterogeneity of stepped surface structures.

Herein, we describe the results of a combined DFT and reactive force field (ReaxFF) based Monte Carlo study, aiming to calculate the surface formation energy of flat and stepped ZrO_2 and YSZ (111) surfaces. We use DFT energies to extend an existing YSZ-ReaxFF reactive force field[18] and perform Monte Carlo (MC) simulated annealing to sample structural configurations of flat YSZ (111) and vicinal YSZ (111) stepped surfaces. The use of ReaxFF allows for the consideration of larger stepped surface models, and the MC simulations we report facilitate greater sampling of possible surface configurations and compositions than is computationally tractable with DFT methods. Our ReaxFF-MC approach allows yttrium and zirconium atoms as well as oxygen atoms and oxygen vacancies to swap lattice positions while continuously performing local structure energy minimization. Using this methodology we lower the temperature until we have reached a minimum energy configuration for each surface model, and determine the optimum surface composition. We evaluate yttrium surface segregation, oxygen vacancy position, and surface step composition for flat and stepped YSZ surfaces. We show that it is thermodynamically favorable for yttrium atoms to segregate to the surface of YSZ, and specifically to step edge sites. It is thermodynamically favorable for oxygen vacancies to occupy positions in the subsurface layer of YSZ, and a higher fraction of vacancies occupy positions NN to Y than NN to Zr.

Table 7-1. Energy differences for yttrium and oxygen vacancy location at the YSZ(111) surface calculated by ReaxFF and DFT.

YSZ(111)	(eV)		
Energy Difference	Ffield E	DFT E	E Difference
(Y_{surf}) - ($Y_{subsurf}$)	-1.31	-1.27	+0.04
(Vac NN to Zr_{surf}) - (Vac NN to Y_{surf})	-1.95	-2.11	-0.16
(Vac NN to Zr_{surf}) - (Vac NN to $Zr_{subsurf}$)	-1.50	-1.00	+0.51
(Vac NN to Zr_{surf}) - (Vac NN to $Y_{subsurf}$)	-2.54	-2.57	-0.03

7.2 Methods

7.2.1 Electronic Structure Method

Quantum-chemical calculations were carried out using the Vienna Ab-initio Simulation Program (VASP), an ab-initio total-energy and molecular dynamics program developed at the Institute for Material Physics at the University of Vienna.[24,25,26] The projector augmented wave (PAW) method[27] was used to represent the core region, with valence electron wavefunctions expanded in a tractable plane wave basis set (with an energy cutoff of 450 eV, all calculations spin-polarized). Valence configurations were $4s^2 4p^6 4d^2 5s^2$ for zirconia, for oxygen $2s^2 2p^4$, and for Y $4s^2 4p^6 4d^2 5s^1$. The Brillouin zone was sampled using a (2x2x2) Monkhorst Pack (MP) grid[28] for bulk zirconia, and a (2x2x1) MP grid for surfaces, with the third vector perpendicular to the surface. Structural optimizations were performed by minimizing the forces on all atoms to below 0.05 $\mathrm{eV \cdot Å^{-1}}$. The Perdew-Wang (PW91) version of the generalized gradient approximation (GGA) is used to incorporate exchange and correlation energies.[29]

7.2.2 Model Construction

Figure 7-1 displays the top (a) and side (b) views of the flat ZrO_2 surface cell, with the cell length and cell width defined. The optimized equilibrium lattice parameter of cubic zirconia is 5.127 Å, which is within 1% of the reported experimental value of 5.090 Å.[30] The ZrO_2/YSZ (111) surface is modeled as a slab of cubic fluorite ZrO_2 separated by 15 Å of vacuum in the direction perpendicular to the surface. Figure 7-1 displays the slabs used to model the flat and stepped ZrO_2 surfaces, for each expansion of the surface unit cell. Slabs of different cell width and length are used to model the ZrO_2 flat and stepped surfaces to consider different surface yttrium and oxygen vacancy concentrations, as well as different concentrations of step edges. For

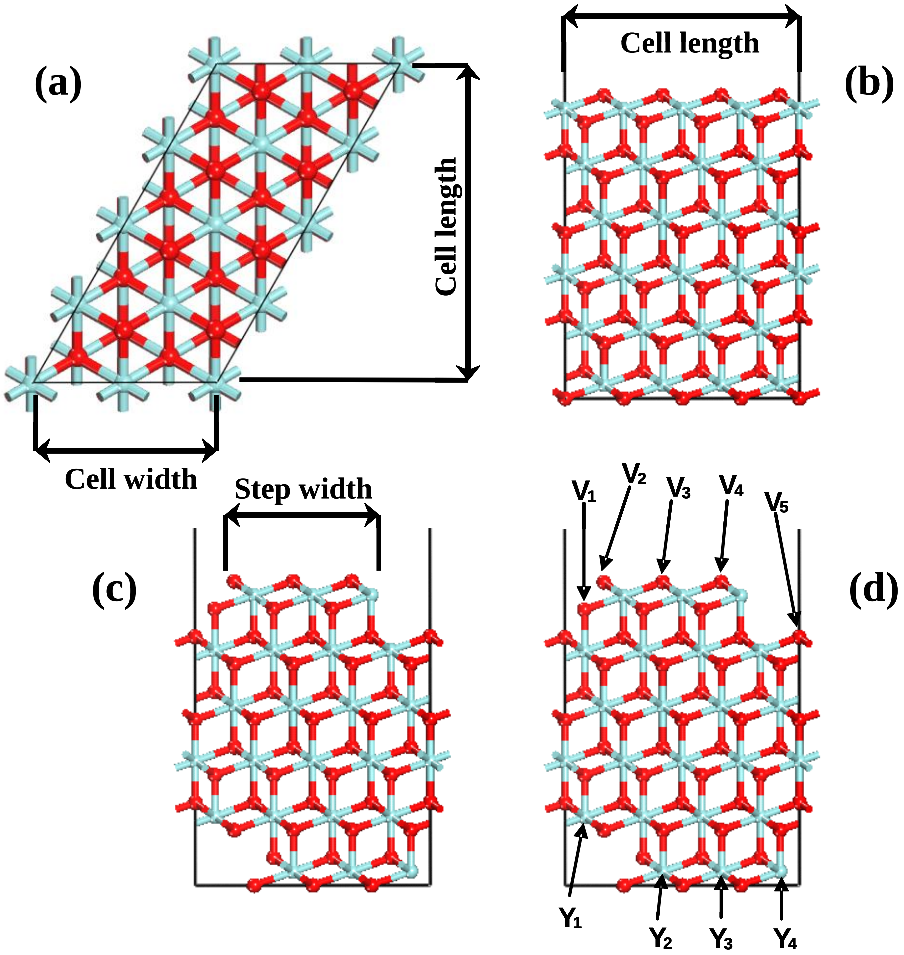

Figure 7-1. DFT slab models of (a) ZrO_2 (111) surface (top view), (b) ZrO_2 (111) surface (side view), and (c), (d) stepped ZrO_2 (111) surface. Cell length and cell width are defined in (a) and (b), step width in (c), and oxygen vacancy sites (V_x) and yttrium doping sites (Y_x) in (d).

each stepped surface slab, the step is constructed from the flat surface by removing ZrO_2 surface rows to form a single ZrO_2 unit plateau on the (111) surface. Similar models of (111) plateaus were used in DFT models to represent steps on cubic fluorite CaF_2.[31] The step width for each stepped surface slab is set at 3 ZrO_2 units to allow yttrium placement at either side or in the middle of the non-symmetric plateau. Structural optimizations were performed allowing the top ZrO_2 layer (which includes only atoms in the plateau for stepped surfaces) to relax, and also allowing the top two layers to relax (which includes both atoms in the plateau and the ZrO_2 layer beneath the plateau for stepped surfaces). Structural optimizations were performed with yttrium atoms substituted into the surface layer as well as subsurface layer of ZrO_2, and oxygen vacancies in varying lattice positions with respect to the surface and with respect to yttrium atoms. For each DFT calculation, yttrium atoms were substituted for Zr atoms as pairs with one oxygen vacancy per Y_2 pair to obtain the stoichiometry of ZrO_2/Y_2O_3. Yttrium atoms were substituted into and oxygen atoms were removed from the zirconia lattice at the surface sites detailed in Figure 7-1(d) for each stepped surface model. Each slab model was mirrored to avoid spurious dipole interactions between slabs that may occur for slabs containing oxygen vacancies within the periodic model. The largest DFT unit cell considered in this study included 144 atoms, and required 102 hours of run time on 16 3.0 GHz Intel Xeon E5472 (Woodcrest) Quad-Core Processors to perform structural optimization.

7.2.3 Calculation of Surface Formation Free Energies

To compare relative energies between flat and stepped surfaces of different sizes and configuration, we calculate the surface formation energy:

$$\Delta G_{surf} = \frac{E_x - (n_{ZrO_2} \cdot \mu_{ZrO_2} + n_{Y_2O_3} \cdot \mu_{Y_2O_3})}{2 \cdot A_{slab}} \qquad (1)$$

where A_{slab} is the surface area of the mirrored surface slab, μ_{ZrO_2} and $\mu_{Y_2O_3}$ are the bulk chemical potentials of zirconia and yttria, respectively, E_x is the DFT energy of the surface slab, and n_{ZrO_2} and $n_{Y_2O_3}$ are the number of formula units of zirconia and yttria in the slab, respectively. Bulk solid chemical potentials are taken from optimized DFT structures, and therefore neglect entropic and enthalpic (T) corrections, consistent with the treatment of surface structures.[32,33]

7.2.4 ReaxFF Methodology

7.2.4.1 ReaxFF Force Field Development

ReaxFF is a bond-order based force field, allowing for the formation and dissociation of chemical bonds during a simulation.[34] ReaxFF combines a continuous bond order with a polarizable charge calculation, which enables application of ReaxFF to covalent, metallic and ionic materials. The ReaxFF force field was earlier parameterized to describe the structure and interactions in bulk YSZ-materials.[18] This earlier YSZ-ReaxFF description matched the equation of state for bulk YSZ as well as for metallic Y and Zr phases, monoclinic, tetragonal, and cubic ZrO_2 and cubic Y_2O_3.[18] The DFT optimizations described in the previous section were used to re-parameterize this force field to accurately model the YSZ (111) surface. The force field was parameterized to specifically match the DFT calculated energy differences for yttrium surface segregation and oxygen vacancy position. Table 7-1 displays the energy differences which were most highly weighted in the parameterization of the ReaxFF force field. The full training set of DFT values which were used to parameterize the ReaxFF force field for accurate description of YSZ surfaces can be found in the Supporting Information. The ReaxFF force field file used herein is included in the Supporting Information, and is compatible with the open-source LAMMPS code as well as the stand-alone ReaxFF code (available upon request from corresponding author van Duin[γ]). The values displayed in Table 7-1 are for the flat YSZ (111) surface, and confirm the preference for yttrium to occupy surface sites and oxygen vacancies to prefer surface sites nearest neighbor (NN) to Zr atoms.

7.2.4.2 Monte Carlo Simulated Annealing with ReaxFF

The ReaxFF Monte Carlo Reactive Dynamics Method was developed to resolve partial or mixed occupation of crystallographic sites of mixed metal oxides and previously applied to the system of MO_3VO_x.[35] Monte Carlo (MC) simulations were performed to sample possible surface configurations for yttrium and oxygen vacancy concentration and locate minimum energy geometries. Interchange of the lattice positions of Y and Zr atoms or oxygen atoms and oxygen vacancies was performed, followed by re-optimization of the system energy. A Metropolis criteria was used to determine whether the interchange (and thus the new structure) was allowed. Oxygen vacancies were represented as weakly interacting atoms which were allowed to occupy oxygen lattice positions, for which our method includes a weak Van der Waals (VDW) interaction with the surrounding lattice and weak repulsion between vacancies. This method of describing oxygen vacancies permits swapping of oxygen and oxygen vacancies to determine optimum vacancy position while the weak VDW interaction between vacancies and other atoms prevents dissociation of vacancies from the YSZ surface.

Mirrored slabs of pure and Y-doped ZrO_2 were constructed to model the vicinal YSZ (111) surface, separated by 15Å in the z-direction. Figure 7-2 displays a stepped slab model used in our ReaxFF Monte Carlo simulations. The stepped YSZ (111) surface was modeled by vicinal surface slabs of termination (10 10 8), with one step on each side of the slab. The (10 10 12) termination was also considered, however its surface formation energy is greater than that of (10 10 8) due to lower coordination numbers for edge atoms at the step edge. Surface and step edge sites are labeled in Figure 7-2 as they are referred to in this study. The total yttrium concentration in our slab model was varied to evaluate the trend in surface and step composition with respect to bulk yttrium content. To investigate the dependence of yttrium surface segregation on the YSZ bulk:surface ratio (which represents the relative size of the bulk “yttrium reservoir”), simulations were performed using different slab thicknesses.

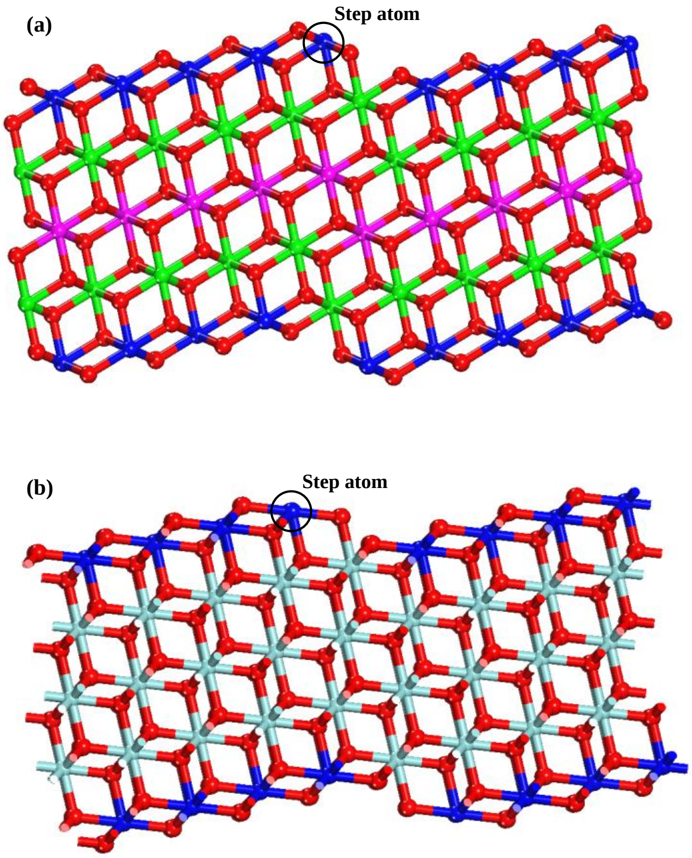

Figure 7-2. (a) Thinnest ReaxFF slab model of the (10 10 8) YSZ surface with blue atoms corresponding to surface metal atoms, green atoms as 2nd layer metal atoms, purple atoms as third layer metal atoms and red atoms as oxygen. (b) ReaxFF slab model of the (10 10 12) YSZ surface with blue atoms corresponding to surface metal atoms.

Simulated annealing Monte Carlo simulations were performed by cooling from 1750K to 250K in 250K intervals with 10,000 MC steps at each temperature to ensure convergence with respect to total system energy. This simulated annealing cycle was performed *n* times for each initial composition studied herein, each time beginning with the same initial structure. The values reported for surface site composition in Section 3.2 are the mean values over all *n* repetitions for each model. Error for each surface site composition is estimated by the 95% confidence interval of the mean:

$$95\% \ \mathbf{C.I.} = 1.96 \cdot \frac{\sigma}{\sqrt{n}} \qquad (2)$$

where σ is the standard deviation of the compositions calculated for all repetitions, and *n* is the number of MC repetitions. The number of MC repetitions *n*=49 for our thinnest slab as shown in Figure 7-2, and *n*=25 for all other slab thicknesses considered. The number of MC repetitions *n* used for each model was chosen to ensure convergence of the mean and standard deviation of the mean of each surface site composition with respect to *n*, and to achieve error bars small enough to make qualitative comparisons between data sets. The largest ReaxFF unit cell considered in this study included approximately 2200 atoms, and required 62 hours of run time on one 3.0 GHz Intel Xeon E5472 (Woodcrest) Quad-Core Processor to complete one MC annealing cycle.

7.3 Results and Discussion

7.3.1 DFT Surface Energies of YSZ(111)

Surface formation energies indicate that the stepped YSZ (111) surface has a higher surface energy than the flat (111) surface. Table 7-2 displays the DFT surface formation energies for the largest DFT models considered of flat and stepped ZrO_2 and YSZ (111) surfaces. The complete set of DFT structures and their surface formation energies are available as Supporting Information. The surface energy for the flat YSZ surface listed in Table 7-2 is that of the lowest energy surface configuration, for which the one oxygen vacancy included in the unit cell is located nearest neighbor (NN) to surface zirconium atoms. This data shows that the formation energy of the flat YSZ (111) surface is less than that of the pure zirconia (111) surface. The surface formation energy of the stepped YSZ (111) surface is larger than that of pure zirconia, and is dependent on the relative positions of yttrium and oxygen vacancies. The size limitations required for a tractable DFT calculation necessitate the use of an asymmetric slab model, and the stability of the two different step configurations can not be independently evaluated. Furthermore, the small 3 MO_2 unit width of the step allows for minimal sampling of possible yttrium and oxygen vacancy configurations and limits the conclusiveness of the DFT results.

Table 7-2. Surface Formation Energies for the cubic fluorite ZrO_2 and YSZ (111) surfaces calculated by DFT. Yttrium and oxygen vacancy positions within the step model are noted as labeled in Figure 7-1(d).

System	Surface Energy (eV/Å^2)
ZrO_2_flat	0.05
YSZ_flat	0.04
ZrO_2	0.08
YSZ_Y_1_V_5	0.10
YSZ_Y_2_V_2	0.09
YSZ_Y_3_V_3	0.08
YSZ_Y_4_V_4	0.09

7.3.2 DFT Surface Energies of YSZ(111)

7.3.2.1 Step Edge and Surface Composition as a Function of Bulk Yttrium Concentration

The surface and step edge yttrium content was evaluated by calculating the percentage of surface and step edge metal sites occupied by yttrium atoms,

$$\text{site}\,Y\% = \left(\frac{\#\ of\ "x"\ sites\ occupied\ by\ Yttrium}{total\ \#\ of\ "x"\ sites} \right) \cdot 100 \quad (3)$$

where “x” refers to either “step edge,” “surface,” “2nd layer” (1st subsurface layer), or “3rd layer” (2nd subsurface layer) sites. The bulk yttrium content (bulk Y%) in our models is similarly defined as the ratio of yttrium atoms to total metal atoms. Figure 7-3 displays the the site Y% for the vicinal (10 10 8) YSZ surface calculated from our MC simulations for our thinnest slab model (Figure 7-2(a)), for 8, 10, and 12% bulk Y%. The larger error bars for the step Y% reflect the lesser number of step sites in the slab model as compared to the number of surface sites (1:9 step:surface site ratio).

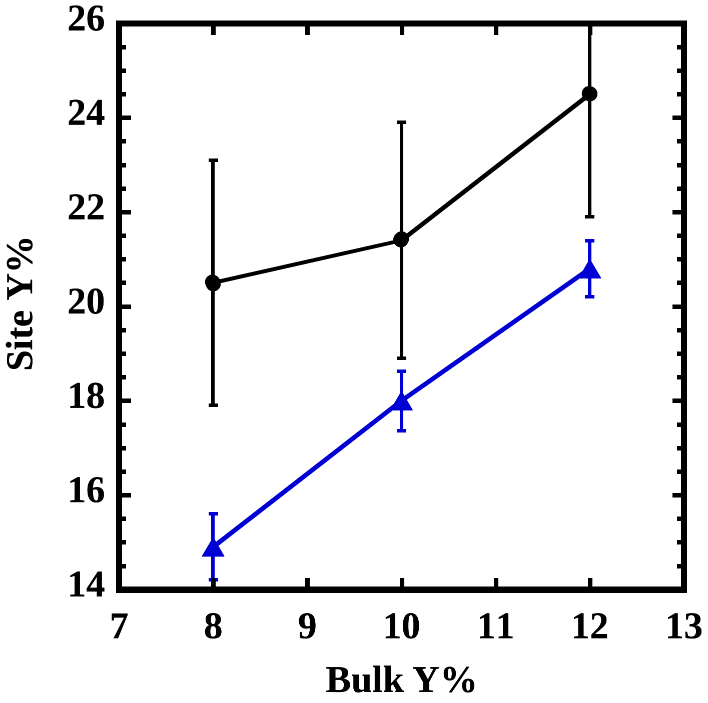

Figure 7-3. Y% at the step edge (●) and surface (▲) on the YSZ surface as a function of bulk yttrium concentration.

It is thermodynamically favorable for yttrium atoms to segregate to the surface of YSZ, and specifically to step edge sites. Yttrium surface content increases as bulk content increases, and in all compositions from 8% bulk%Y to 12% bulk%Y the surface content exceeds that of the bulk. The step edge site%Y exceeds both the bulk%Y as well as the surface site%Y. This data shows that yttrium atoms specifically segregate to step edge sites on the YSZ surface, and that the concentration of yttrium at step edge and surface sites increases as bulk yttrium concentration increases.

7.3.2.2 Yttrium Step Edge and Surface Saturation

To evaluate the dependence of yttrium segregation on the size of the bulk "yttrium reservoir," we performed MC annealing runs on thicker (10 10 8) slabs with 10% bulk Y%. Figure 7-4 displays the percentage of metal sites occupied by yttrium at the step edge, surface, and subsurface layers of YSZ versus slab thickness. The slab thickness is normalized to the thinnest slab considered (Figure 7-2(a)). In most experimental systems, the macroscopic depth of YSZ provides for a substantial reservoir of bulk yttria that may segregate to the surface. Therefore, the computational results should be extrapolated to infinite thickness for comparison with the experimental system. The concentration of yttrium at the step edge exceeds that of the bulk as well as the surface for each slab thickness considered. The concentration of yttrium at the surface also exceeds that of the bulk as well as the second and third subsurface layers. Yttrium enrichment of the surface begins to approach a saturation point at which the change in surface Y% with respect to slab thickness reaches zero. This result shows that if the bulk:surface ratio of YSZ is large enough, yttrium enrichment of the surface will saturate at a concentration less than that at the step edge. Lahiri et al. report angle-dependent XPS results which suggest that the surface saturation point occurs at 45% yttrium if only the surface layer is yttrium enriched.[9] Our simulations show that yttrium enrichment only occurs in the surface layer of YSZ and we estimate this saturation point at ~40% yttrium (using a $A-\frac{B}{\sqrt{\tau}}$ data fit for the surface Y%, where τ is the normalized slab thickness). The concentration of yttrium at the step edge does not approach a saturation level, however, suggesting that steps on the YSZ surface are mainly yttria-terminated. The result that YSZ step edges are mainly yttria-terminated is in agreement with the fact that the selectivity for formic acid decomposition of the YSZ surface is similar to that of pure Y_2O_3.[9]

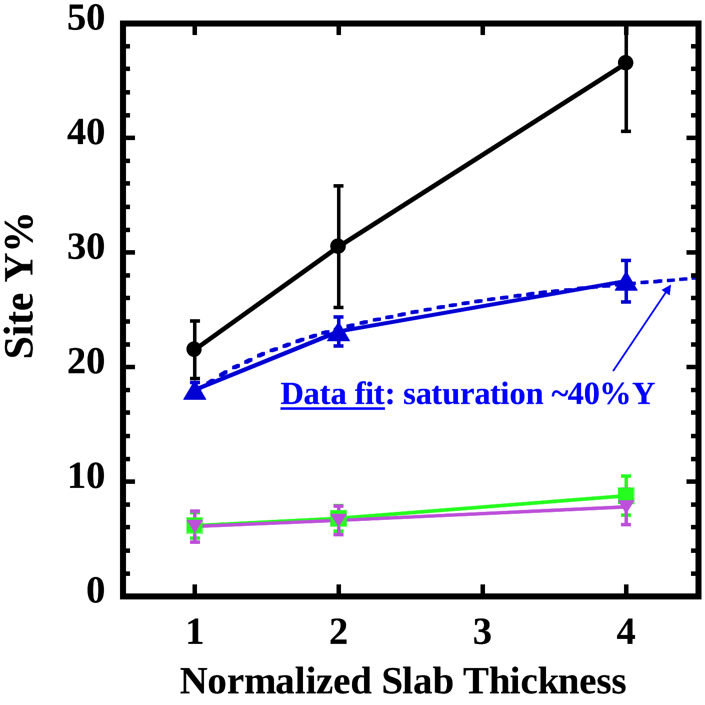

Figure 7-4. Y% at the step edge (●), surface (▲), 2nd surface layer (■), and 3rd surface layer (▼) on the YSZ surface as a function of slab thickness.

We also calculate surface and step Y% for the (10 10 12) YSZ termination (shown in Figure 7-2(b)) to evaluate the dependence of yttrium segregation on step structure. We calculate the step Y% and surface Y% as 10.9%±5.04 and 17.6%±1.54, respectively for the (10 10 12)

YSZ termination for a slab of the thickness displayed in Figure 7-2(b) (the same thickness as the thinnest slab considered for the (10 10 8) termination). These values for step and surface Y% on the (10 10 12) termination indicate the opposite trend in yttrium segregation to step and surface sites as compared to the (10 10 8) termination. This result illustrates that yttrium segregation to the step edge is dependent on the structure and coordination environment of the step edge sites. The majority of our calculations have utilized the (10 10 8) termination as this surface has a lower surface formation energy than the (10 10 12) termination, and thus YSZ step edges are more likely to be terminated as shown in our (10 10 8) slab model.

7.3.2.3 Distribution of Yttrium, Zirconium, Oxygen and Oxygen Vacancies

To evaluate the distribution of yttrium, zirconium, oxygen and oxygen vacancies, we calculate the atomic radial pair distribution function *g(r)*:

$$g(r) = \frac{n(r)}{\rho \cdot 4\pi r^2 \cdot \Delta r} \qquad (5)$$

where *n(r)* is the number of atoms within Δr at distance r with respect to a central atom, and ρ is the bulk density. The values of *g(r)* that we calculate are the averages for the x output structures of MC simulated annealing for each surface model. We use g(r) to calculate the coordination number *(c.n.)*:

$$(c.n.) = \int_0^{r_1} \left[\rho \cdot 4\pi r^2 \cdot g(r)\right] dr \qquad (6)$$

where r_1 is the radial distance from each atom at the first minimum of g(r), and *(c.n.)* represents the number of atoms in the first coordination shell of the central atom. Both *g(r)* and *(c.n.)* are calculated for the atom pairs of Zr-O, Y-O, Zr-$\mathrm{V_O^{\bullet\bullet}}$, and Y-$\mathrm{V_O^{\bullet\bullet}}$ for each surface model. The g(r) plots are included as Supporting Information, and the coordination numbers calculated from these are given in Table 7-3.

Table 7-3 displays the overall *(c.n.)* calculated for each pair for the thickest slab model with 10% yttrium, as well as the *(c.n.)* for Y and Zr atoms in the surface layer only. Zirconium atoms in bulk cubic fluorite ZrO_2 are eight-fold oxygen coordinate, whereas we calculated an average oxygen *(c.n.)* of 6.99 because our model includes zirconium atoms at under-coordinated surface sites as well as oxygen vacancies. The average coordination number for Y atoms is 6.38, less than that of Zr atoms. The lower coordination of yttrium relative to zirconium is due to two factors: (1) a higher percentage of the yttrium atoms relative to zirconium atoms in each unit cell occupy surface sites versus bulk lattice positions and (2) the $V_O^{\bullet\bullet}$ *(c.n.)* for Y is greater than the $V_O^{\bullet\bullet}$ *(c.n.)* for Zr over the entire slab as well as in the surface layer. The overall $V_O^{\bullet\bullet}$ *(c.n.)* for Zr and Y are 0.15 and 0.39, respectively, showing that a higher percentage of oxygen vacancies are located NN to Y than Zr. This distribution of oxygen vacancies differs from the previous ReaxFF study of bulk YSZ,[18] indicating a difference in vacancy position in layers near the YSZ surface versus the bulk. The $V_O^{\bullet\bullet}$ *(c.n.)* for Zr and Y in the surface layer are 0.21 and 0.32, respectively, indicating that there is shift in the distribution of oxygen vacancies at the YSZ surface towards a higher fraction of vacancies occupying sites NN to Zr.

To differentiate between oxygen vacancies at the YSZ surface, in the subsurface layer (both of which contribute to the *(c.n.)* for Y and Zr atoms in the surface metal layer), and coordinated to step edge atoms, we calculate the oxygen vacancy concentration at topmost (surface), the 2nd (subsurface) oxygen layers, and in the first coordination shell of step edge atoms. Table 7-4 displays the concentration of oxygen vacancies in the surface and subsurface layers and at the step edge. The concentration of oxygen vacancies at the YSZ surface and step edge is similar to that of the entire slab, however the concentration of oxygen vacancies in the

Table 7-3. Coordination numbers of oxygen and oxygen vacancies ($V_O^{\bullet\bullet}$) for Zr and Y atoms in the overall YSZ slab and for Zr and Y atoms in the surface layer.

Pair	Overall (c.n.)	surface (c.n.)
Zr-O	6.99	5.92
Zr- $V_O^{\bullet\bullet}$	0.15	0.21
Y-O	6.38	5.74
Y- $V_O^{\bullet\bullet}$	0.39	0.32

Table 7-4. Oxygen vacancy concentration in different regions of the YSZ surface slab.

Region	Vacancy concentration
step edge	2.85% ± 1.61
surface layer	2.64% ± 0.68
subsurface layer	7.27% ± 1.35
entire slab	2.50% ± 0.00

subsurface layer is nearly three times greater than the overall composition. This result shows that it is thermodynamically favorable for oxygen vacancies to segregate to the subsurface layer in YSZ. The high concentration of subsurface oxygen vacancies also illustrates that the trends we observe in $V_O^{\bullet\bullet}$ *(c.n.)* for Y and Zr in the surface layer are dominated by subsurface oxygen vacancies.

7.3.2.4 Relative Energy of Flat and Stepped YSZ Surfaces

To evaluate the relative stability of steps on YSZ surfaces, we calculate the energy difference between the flat (111) surface and our vicinal stepped surface model for ZrO_2 and 10% bulk Y%. Figure 7-5 displays the relative surface formation energies for flat and stepped pure zirconia and YSZ. The surface energy difference in Figure 7-5 for ZrO_2 is calculated from the energies of flat and stepped zirconia surface models which have been structurally optimized using the conjugate-gradient method. The surface energy difference in Figure 7-5 for YSZ is calculated as the average of energies of flat and stepped YSZ output structures from MC annealing cycles, which have also been structurally optimized using the conjugate-gradient method. The energy differences between the ReaxFF flat surface and stepped surface models for both ZrO_2 and YSZ are much lower than the energy differences calculated in our DFT models, due to much lower step density in our ReaxFF models. The energies in Figure 7-5 show that the vicinal stepped ZrO_2 surface has a higher surface formation energy than the flat ZrO_2 (111) surface, and that the energy difference between flat and stepped is less than that for YSZ. This result suggests that yttrium doping of zirconia does not stabilize step formation on the cubic zirconia surface and that the formation of surface steps is not thermodynamically favorable on pure zirconia or YSZ. The relative energy difference between a flat and stepped termination is low for both pure zirconia and YSZ, however, suggesting that in an experimental system steps may be present in varying concentration depending on sample preparation method.

7.4 Conclusions

We performed Monte Carlo (MC) simulated annealing, using a ReaxFF reactive force field based on DFT data describing YSZ surface energies, to sample structural configurations of flat YSZ (111) and vicinal YSZ (111) stepped surfaces. Yttrium surface segregation, oxygen vacancy position, and surface step composition for flat and stepped YSZ surfaces was evaluated. We observed that the specific termination of step edges influences yttrium segregation behavior, however yttrium atoms segregate to the surface and specifically to step edge sites for the low energy YSZ (111) vicinal stepped (10 10 8) surface. We found that surface saturation of yttrium occurs at approximately 40% (40:60 Y:Zr ratio), which is in agreement with XPS results which suggest that this saturation point occurs at 40% yttrium.[9] Our radial distribution function analysis indicates that it is thermodynamically favorable for oxygen vacancies to occupy positions in the subsurface layer of YSZ, and a higher fraction of vacancies occupy positions NN to Y than NN to Zr. Yttrium segregation to step edges on the YSZ surface does not lower the surface formation energy of the stepped surface below that of the flat (111) termination, and the formation of surface steps of the specific geometry considered herein is not thermodynamically favorable on pure zirconia or YSZ.

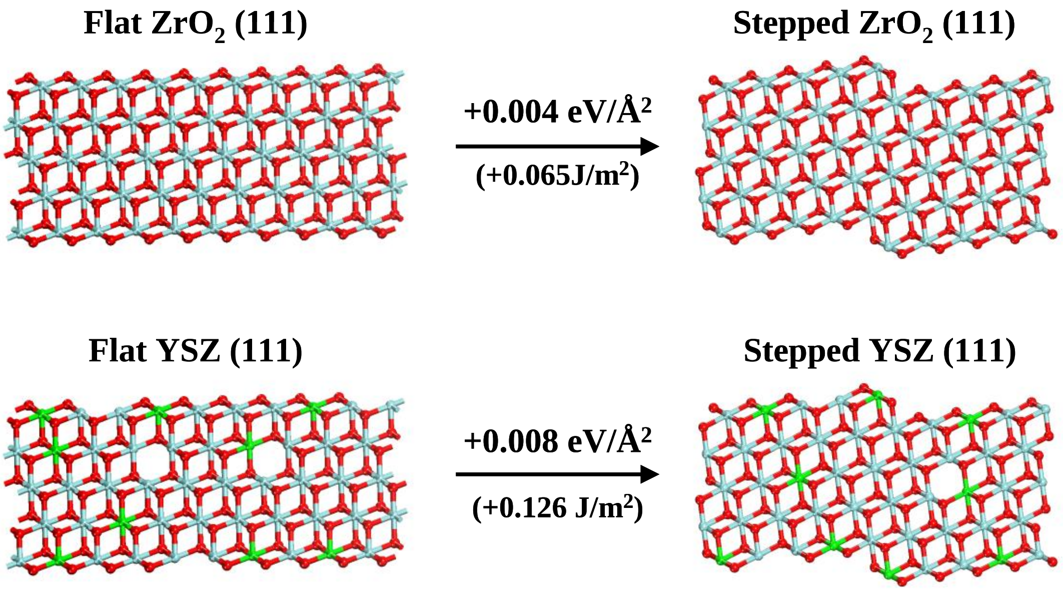

Figure 7-5. Relative surface formation energies for flat and stepped pure zirconia (ZrO_2) and YSZ surfaces.

This study shows that the specific structure and morphology of the YSZ surface influences the surface segregation of yttrium. Stepped YSZ surfaces afford altered chemical functionality with respect to flat surfaces, as active step edge sites are mainly occupied by yttrium atoms. We demonstrate that our ReaxFF-MC methodology is a useful computational tool for evaluating the structure and composition of complex mixed metal oxide surfaces, for which direct consideration of lattice defects is necessary.

7.5 References

(1) Park, J. S.; Park, C. O.; Kim, H. J.; Miura, N. *Solid State Ionics* **2005**, *176*, 1371-1375.

(2) Itome, M.; Nelson, A. E. *Catalysis Letters* **2006**, *106*, 21-27.

(3) Shishkin, M.; Ziegler, T. *The Journal of Physical Chemistry C* **2008**, *112*, 19662-19669.

(4) Vogler, M.; Bierberle-Hutter, A.; Gauckler, L.; Warnatz, J.; Bessler, W. *Journal of The Electrochemical Society* **2009**, *156*, B663-B672.

(5) Martinez-Amesti, A.; Larranaga, A.; Rodriguez-Martinez, L. M.; No, M. L.; Pizarro, J. L.; Laresgoiti, A.; Arriortua, M. I. *Journal of The Electrochemical Society* **2009**, *156*, B856-B861.

(6) Etsell, T. H.; Flengas, S. N. *Chemical Reviews* **1970**, *70*, 339.

(7) Majumdar, D.; Chatterjee, D. *Thin Solid Films* **1991**, Medium: X; Size: Pages: 349-354.

(8) Majumdar, D.; Chatterjee, D. *Journal of Applied Physics* **1991**, *70*, 988-992.

(9) Lahiri, J.; Mayernick, A. D.; Morrow, S. L.; Koel, B. E.; van Duin, A. C. T.; Janik, M. J.; Batzill, M. *Journal of Physical Chemistry C* **2009**.

(10) Herman, G. S.; Henderson, M. A.; Starkweather, K. A.; McDaniel, E. P. *Journal of Vacuum Science & Technology A: Vacuum, Surfaces, and Films* **1999**, *17*, 939-944.

(11) Nowotny, J. *Solid State Ionics* **1991**, *49*, 119-128.

(12) Steele, B. C. H. *Journal of Power Sources* **1994**, *49*, 1-14.

(13) Steele, B. C. H.; Dell, R. M. *Philosophical Transactions: Mathematical, Physical, and Engineering Sciences* **1996**, *354*, 1695-1710.

(14) Catlow, C. R. A.; Chadwick, A. V.; Greaves, G. N.; Moroney, L. M. *Journal of the American Ceramic Society* **1986**, *69*, 272.

(15) Li, P.; Chen, I.W.; Penner-Hahn, J. *Journal of the American Ceramic Society* **1994**, *77*, 118.

(16) Tuilier, M. H.; Dexpert-Ghys, J.; Dexpert, H.; Lagarde, P. *Journal of Solid State Chemistry* **1987**, *69*, 153.

(17) Roth, W. L.; Wong, R.; Goldman, A. I.; Canova, E.; Kao, Y. H.; Dunn, B. *Solid State Ionics* **1986**, *18*, 1115.

(18) Duin, A. C. T. v.; Merinov, B. V.; Jang, S. S.; III, W. A. G. *Journal of Physical Chemistry A* **2008**, *112*, 3133-3140.

(19) Thome, T.; Van, L. P.; Cousty, J. *Journal of the European Ceramic Society* **2004**, *24*, 841-846.

(20) Morrow, S. L.; Luttrell, T.; Carter, A.; Batzill, M. *Surface Science* **2009**, *603*, L78-L81.

(21) Ballabio, G.; Bernasconi, M.; Pietrucci, F.; Serra, S. *Physical Review B* **2004**, *70*, 075417.

(22) Wang, X.-G. *Surface Science Letters* **2008**, *602*, L5-L9.

(23) Xia, X.; Oldman, R.; Catlow, C. R. A. *Chemistry of Materials* **2009**, *21*, 3576-3585.

(24) Kresse, G.; Furthmuller, J. *Computational Materials Science* **1996**, *6*, 15-50.

(25) Kresse, G.; Furthmuller, J. *Physical Review B* **1996**, *54*, 11169-11186.

(26) Kresse, G.; Hafner, J. *Physical Review B* **1993**, *47*, 558-561.

(27) Kresse, G.; Joubert, D. *Physical Review B* **1999**, *59*, 1758 LP - 1775.

(28) Monkhorst, H. J.; Pack, J. D. *Physical Review B* **1976**, *13*, 5188 LP - 5192.

(29) Perdew, J. P.; Chevary, J. A.; Vosko, S. H.; Jackson, K. A.; Pederson, M. R.; Singh, D. J.; Fiolhais, C. *Physical Review B* **1992**, *46*, 6671.

(30) Ruff, O.; Ebert, F. *Journal of Inorganic and General Chemistry* **1929**, *180*, 252.

(31) Cooper, T. G.; Leeuw, N. H. d. *Journal of Materials Chemistry* **2002**, *13,* 93-101.

(32) Reuter, K.; Scheffler, M. *Physical Review B* **2001**, *65*, 035406.

(33) Mayernick, A. D.; Janik, M. J. *Journal of Chemical Physics* **2009**, *131*.

(34) van Duin, A. C. T.; Dasgupta, S.; Lorant, F.; Goddard III, W. A. *The Journal of Physical Chemistry A* **2001**, *105,* 9396-9409.

(35) Chenoweth, K.; van Duin, A. C. T.; Goddard III, W. A. *Angewandte Chemie International* **2009**, *48*, 7630-7634.

7.6 Supporting Information

Model	Configuration	Top Layer relaxed		Top 2 Layers relaxed	
		DFT Energy (eV)	Surface Energy (eV/Å^2)	DFT Energy (eV)	Surface Energy (eV/Å^2)
Flat 4x3	ZrO_2	-1690.44	0.05	-1691.62	0.05
	YSZ_Vac_NN_Y	-1667.07	0.06	-1668.81	0.05
	YSZ_Vac_NN_Zr	-1667.72	0.05	-1670.92	0.04
	YSZ_Vac_NN_Y$_{subsurf}$	--	--	-1668.35	0.05
	YSZ_Vac_NN_Zr$_{subsurf}$	--	--	-1669.92	0.05
Stepped 4x3	ZrO_2	-1491.73	0.16	-1508.64	0.10
	$Y_1\_V_5$	--	--	-1486.54	0.09
	$Y_2\_V_2$	-1467.51	0.17	-1484.97	0.10
	$Y_3\_V_3$	-1467.69	0.17	-1485.84	0.10
	$Y_4\_V_4$	-1464.97	0.18	-1484.15	0.10
Stepped 4x2	$Y_1\_V_5$	--	--	--	--
	$Y_2\_V_2$	-969.75	0.17	-980.95	0.07
	$Y_3\_V_3$	-969.70	0.17	-982.79	0.07
	$Y_4\_V_4$	-967.09	0.19	-985.34	0.06
Stepped 6x2	$Y_1\_V_5$	--	--	-1315.56	0.10
	$Y_2\_V_2$	-1304.58	0.14	-1316.72	0.09
	$Y_3\_V_3$	-1303.57	0.14	-1318.81	0.08
	$Y_4\_V_4$	-1301.54	0.15	-1317.28	0.09

Table S1. DFT surface formation energies for each flat and stepped ZrO_2 and YSZ surface model.

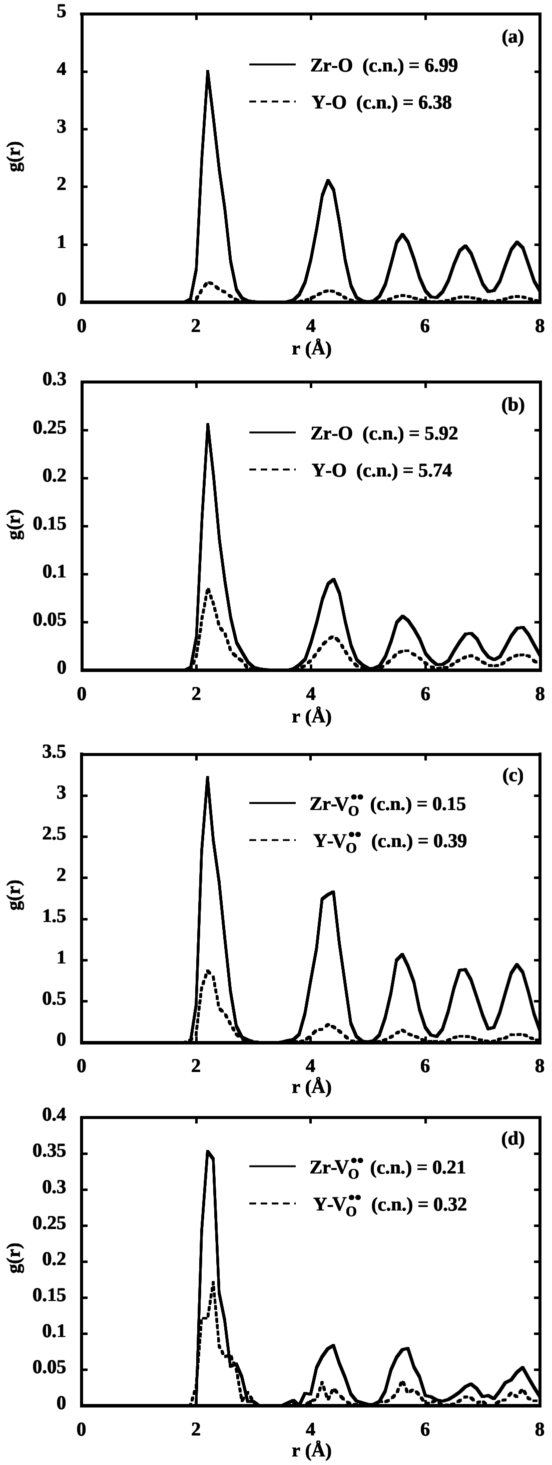

Figure S1. Radial distribution function for Zr-O and Y-O for entire surface slab (a) and only surface metal atoms (b). Radial distribution function for Zr- $V_O^{\bullet\bullet}$ and Y- $V_O^{\bullet\bullet}$ for entire surface slab (c) and only surface metal atoms (d).

Chapter 8

Summary, Conclusions, and Recommendations for Future Study

8.1 Hydrocarbon Oxidation on Ceria-Based Mixed Oxides

Density functional theory (DFT+*U*) was utilized to probe the electronic structure and quantify the catalytic activity of ceria-transition mixed metal oxides. Chapters 2-4 focus on evaluating the thermodynamic stability and catalytic activity of $Pd_xCe_{1-x}O_2$ for methane oxidation with respect to separate components (Pd, PdO, and CeO_2). Palladium substitution into the CeO_2 lattice introduces Pd^{4+} as a more reducible metal center than Ce^{4+}, increasing the reducibility of the surface (decreasing the oxygen vacancy formation energy) and thereby decreasing the energy barrier for methane activation. The lowest energy path for methane oxidation over $Pd_xCe_{1-x}O_2$, PdO, Pd, and CeO_2 proceeds via identical intermediates, with the lowest apparent barrier over $Pd_xCe_{1-x}O_2$. Chapter 5 details the correlation between C-H bond activation energetics and surface reducibility, illustrating that certain transition metal-ceria mixed oxides may offer greater combustion activity than palladium-ceria.

Chapter 2 establishes that methane activation over the mixed $M_xCe_{1-x}O_2$ surface (for both M = Zr and Pd) occurs via H abstraction to form $CH_3\bullet+H^*$ and results in a $1e^-$ reduction of the surface. The energy of the methyl radical transition state and methane dissociative adsorption ($CH_4 \rightarrow CH_3^*+H^*$) correlate with the oxygen vacancy formation energy of the mixed oxide surface, as methane activation and oxygen vacancy formation are both surface reduction processes. Methane activation does not occur over exposed metal coordination sites on oxygen vacancies; dissociative adsorption of methane occurs over surface oxygen atoms to form CH_3* (-OCH_3) and H* (-OH). The absolute energies of methane adsorption and oxygen vacancy formation on pure ceria are dependent on choice of U value within the DFT+*U* method, however a U value of 5 eV results in proper localization of Ce 4f electrons and preserves trends in relative energies. For $Pd_xCe_{1-x}O_2$, oxygen vacancy formation and methane adsorption result in reduction of Pd^{4+}, and thus the energies of both processes are nearly independent of U value (ΔE_{vac} and ΔE_{ads} are proportional to -0.05ΔU(eV)). The results presented in Chapter 2 thus establish that the DFT+U method is a reliable modeling approach for evaluating relative energy trends between ceria surfaces of varying composition.

The low methane activation barrier (+0.22 eV) over $Pd_xCe_{1-x}O_2(111)$ presented in Chapter 2 motivates consideration of the thermodynamic stability of $Pd_xCe_{1-x}O_2$ surfaces, which is examined in Chapter 3. The ceria surface stabilizes oxidized palladium species, thereby shifting the transitions for supported palladium species between oxidation states ($Pd^{4+}\leftrightarrow Pd^{2+}\leftrightarrow Pd^0$) to higher temperatures and lower oxygen partial pressures with respect to bulk palladium. The $Pd_xCe_{1-x}O_2(111)$ surface is thermodynamically favorable with respect to other single atom states of Pd on ceria at low temperatures and high oxygen partial pressures ($<10^{-10}$ atm O_2 at 298K). Large palladium particles are thermodynamically favorable to $Pd_xCe_{1-x}O_2$ mixed oxide surfaces, however, illustrating that the presence of incorporated Pd^{4+} in ceria is only possible if appropriate synthesis conditions are applied to form the mixed oxide and Pd^{4+} ions are isolated in the ceria lattice such that there are large kinetic barriers to reordering and particle formation.

Chapter 4 details the free energies of elementary steps in CH_4 oxidation to H_2O and CO_2 over $Pd_xCe_{1-x}O_2(111)$, PdO, Pd, and $CeO_2(111)$. Chapter 2 establishes that the methane activation barrier over the $Pd_xCe_{1-x}O_2(111)$ surface is low (+0.22 eV), and the methane oxidation energetics presented in Chapter 4 confirm that methane activation is the rate limiting step in methane oxidation over $Pd_xCe_{1-x}O_2(111)$. The barrier over $Pd_xCe_{1-x}O_2(111)$ is lower than that over several single crystal surface terminations of PdO and Pd, as well as over Pd surface defects (surface step and kink sites) which may represent surface sites on the edge of Pd particles. Methane oxidation proceeds via identical intermediates over $Pd_xCe_{1-x}O_2(111)$, PdO, Pd, and $CeO_2(111)$, however stable intermediates differ over each surface. An actual palladium-ceria catalyst will contain a heterogeneous distribution of surface sites, and thus surface intermediates identified *in situ* may correspond to those present on less active sites than Pd^{4+} in CeO_2. The relative rate of methane oxidation over the $Pd_xCe_{1-x}O_2(111)$ surface is nearly 1000 times greater than that over stepped or kinked Pd metal sites, suggesting that substituted Pd^{4+} may provide the majority of the reaction rate on Pd-ceria catalysts even if the Pd^{4+} concentration is very small.

Chapters 2-4 illustrate that Pd^{4+} is thermodynamically stable in the $Pd_xCe_{1-x}O_2(111)$ surface and that this mixed oxide surface offers unique hydrocarbon oxidation activity. Chapter 5 details the correlation between C-H bond activation energetics and surface reducibility, and indicates that certain transition metals such as Cu and Ni may form mixed oxides with ceria that exhibit faster hydrocarbon oxidation kinetics than $Pd_xCe_{1-x}O_2(111)$. The correlation between the surface reducibility and hydrocarbon oxidation activity of ceria-based mixed oxides indicates that catalytic activity may be optimized by maximizing the reducibility of the oxide mixture. The free energy of oxygen vacancy formation, however, is a function of the partial pressure of oxidants such as O_2 and H_2O and thus the mixed oxide surface may contain a large concentration of oxygen vacancies under reducing operating conditions. Though the hydrocarbon oxidation activity of ceria-based mixed oxides is correlated with surface reducibility, these mixed oxides will not maintain oxidation activity if the free energy to replenish surface oxygen (fill oxygen vacancies) is prohibitively endergonic. The free energies of filling oxygen vacancies over the $Pd_xCe_{1-x}O_2(111)$ surface under both catalytic combustion and solid oxide fuel cell (SOFC) operating conditions are discussed in Chapter 4. The energy barrier for methane activation is larger than the free energy to fill oxygen vacancies at both catalytic combustion and SOFC operating conditions on $Pd_xCe_{1-x}O_2(111)$. This result that methane activation is rate limiting over $Pd_xCe_{1-x}O_2(111)$ under highly reducing atmospheres (for SOFC, as low as 10^{-23} atm O_2) and at high temperature (for SOFC, 973K) suggests that deactivation of ceria-based mixed oxides due to formation of large concentrations of surface oxygen vacancies will not occur. The low methane activation barrier over the $Pd_xCe_{1-x}O_2(111)$ surface and correlation between reducibility and activity across transition metal-ceria mixtures thus motivates the design of novel mixed oxide catalysts for catalytic applications involving C-H bond activation.

8.2 Ceria-Based Mixed Oxides for Syngas Cleanup

Chapters 2-4 establish the activity of $Pd_xCe_{1-x}O_2$ surfaces for C-H dissociation and Chapter 5 addresses the impact on C-H activity of numerous transition metal dopants in ceria. The results and discussion in Chapters 2-5 focus on probing hydrocarbon oxidation activity, whereas Chapter 6 considers the desulfurization activity of ceria-based mixed oxides. Ceria-lanthanide mixtures display altered sulfur adsorption capacities than pure ceria,[1-3] and desulfurization activity coupled with C-H bond breaking activity may permit application of ceria-based mixed oxides as simultaneous reforming catalysts and H_2S sorbents for biomass syngas cleanup. Chapter 6 details the free energies of H_2S adsorption and dissociation on ceria, ceria-lanthana, and ceria-terbia. Molecular adsorption is highly endergonic over ceria, ceria-lanthana, and ceria-terbia at the high temperatures (>900K) and low H_2S pressures ($>10^{-2}$ atm) of biomass gasifier effluents. Adsorption of H_2S occurs over surface oxygen vacancies, with the thermodynamic driving force for adsorption involving the relative energy of substituting S atoms from H_2S for surface oxygen atoms. The energy barrier for H_2S adsorption over ceria is much larger (>0.68 eV) over ceria-lanthana and ceria-terbia, suggesting that the larger sulfur adsorption capacity observed experimentally is due to faster kinetics over the mixed oxide surfaces. The reducibility of the oxide mixture does not correlate with sulfur adsorption and dissociation energetics, and the optimization of ceria-based mixed oxide sulfur sorbents may lie in the design of mixed oxides with increased H_2S dissociation kinetics.

8.3 Perspective and Suggestions for Future Study

Consideration of entropy corrections to DFT energies is necessary to accurately establish thermodynamic driving forces (free energies) for chemical reactions. For example, the DFT energies of elementary steps in methane oxidation (Chapter 4) show that the most endothermic step at 0K over $Pd_xCe_{1-x}O_2(111)$ is $CO^* \rightarrow CO_2(g)$ at +0.60 eV; at 298K and $P_{CO_2} = 10^{-6}$ atm, the ΔG of $CO^* \rightarrow CO_2(g)$ is -1.04 eV. Methane activation is +0.18 eV (DFT energy) at 0K over $Pd_xCe_{1-x}O_2(111)$, whereas the free energy of activation $\Delta^{\ddagger}G$ at 298K, $P_{CH_4} = 0.01$ atm is +2.05 eV. In the absence of entropy corrections, DFT energies thus show that CO_2 desorption is rate limiting step over $Pd_xCe_{1-x}O_2(111)$, whereas free energies for elementary steps in methane oxidation show that methane activation is rate limiting at both SOFC and catalytic combustion operating conditions (Chapter 4). The differences in conclusions that are drawn concerning the energetics and mechanism of methane oxidation over $Pd_xCe_{1-x}O_2(111)$ underscore the importance of calculating free energies at catalytic operating conditions. Energies of bond breaking steps for surface species are well represented by DFT energies, however energetics of reaction steps involving gas phase species require consideration of entropy and specifically translation entropy corrections. The translational entropy correction ($S_{translational}T$) for $CH_4(g)$ at 298K and $P_{CH_4} = 0.01$ atm is 0.55 eV, greater than the 0K methane activation barrier over $Pd_xCe_{1-x}O_2(111)$ and of similar magnitude to the energies of elementary steps in methane oxidation over $CeO_2(111)$, $Pd_xCe_{1-x}O_2(111)$, PdO(100), and Pd(111) (Chapter 4). The highly endergonic molecular adsorption of $H_2S(g)$ on ceria (+2.91 eV) at 1100K and $P_{H2S} = 10^{-2}$ atm (Chapter 6) also illustrates the inaccuracy inherent in comparing adsorption energies of gas phase species and surface reaction energetics using 0K energetics. The free energy ($\Delta G(T)$) of H_2S adsorption over CeO_2 (111) is +4.00 eV (1100K, $P_{H2S} = 10^{-2}$ atm), whereas the DFT energy (ΔE_{ads}) is -0.22 eV, indicating the magnitude of entropic contributions to adsorption energies at high temperature and low pressure. Utilization of DFT and *ab initio* thermodynamics to calculate free energies of elementary reaction steps is thus necessary to accurately characterize the energetics of catalytic processes.

The use of density functional theory to accurately describe driving forces in catalytic systems therefore necessitates the utilization of ZPVE and TS corrections with DFT calculated energetics. Despite model size and complexity limitations within DFT, advances in the application of electronic structure methodologies to catalyst development are prevailingly muddled by consideration of thermodynamically unfavorable surface sites and reaction paths. Free energy estimations utilizing *ab initio* thermodynamics and DFT calculated internal energies are useful, however, in evaluating relative trends in elementary reaction energies over varying surfaces as well as the free energies of formation of differing surface structures and oxidation states.

Chapters 2-6 utilized DFT and *ab initio* thermodynamics methods to investigate hydrocarbon oxidation and H_2S adsorption on ceria-based mixed metal oxides, however modeling efforts were constricted to the consideration of small unit cells and a finite number of surface configurations. Chapter 7 details the combined use of DFT and ReaxFF methods to probe the composition and thermodynamic stability of surface steps on the YSZ(111) surface. DFT energies were used to parameterize a reactive force field to accurately describe interactions on the YSZ surface, and ReaxFF Monte Carlo simulations were used to evaluate minimum energy configurations of yttrium atoms, zirconium atoms, oxygen atoms, and oxygen vacancies. It is thermodynamically favorable for yttrium atoms to segregate to the YSZ surface in greater concentration than the bulk, and specifically to segregate to surface step edge sites. Yttrium segregation to step edge sites is in agreement with the selectivity of YSZ(111) steps to the dehydration of HCOOH, similar to that over Y_2O_3.[4]

The use of DFT and ReaxFF to accurately represent the length scales of surface steps on YSZ(111) and evaluate a large number of configurational possibilities of metal and oxygen atoms and oxygen vacancies exemplifies the utilization of such techniques to study complex heterogeneous catalyst surfaces. Multi-scale simulation efforts using both DFT and force field methods provide both electronic structure level insight into catalytic reactions as well as facilitate consideration of large surface models and structural dynamics. Consideration of larger surface models than are accessible within DFT is particularly important in the case of ceria. Scanning tunneling microscopy (STM) images of the CeO_2(111) surface display oxygen vacancies in linear and triangular clusters,[5] indicating that consideration of isolated oxygen vacancies may not be sufficient to accurately describe the reduced ceria surface. Segregation of dopant metals in ceria to form enriched surfaces or bulk microphases, such as ceria pyrochlores ($Ce_2M_2O_7$) which have been observed for ceria-zirconia,[6] may also occur in ceria-based mixed oxides. The implementation of multi-scale simulation methods in close tandem with detailed synthesis and characterization experiments therefore may facilitate design of new ceria-based catalysts.

The results in this dissertation are encouraging for the study of ceria-based catalysts, and provide insight into the structural and electronic nature of active sites on the doped ceria surface. Further studies will investigate surface dynamics and morphologies using both DFT and ReaxFF, for palladium-ceria oxidation catalysts and ceria-lanthanide syngas cleanup catalysts. The design of novel ceria-based catalysts will be spurred by advances in synthesis techniques to yield well-defined surfaces, but also will hinge on the capacity of characterization techniques to isolate active species on the heterogeneous metal oxide surface.

8.4 References

(1) Flytzani-Stephanopoulos, M.; Sakbodin, M.; Wang, Z. *Science* **2006**, *312*, 1508-1510.

(2) Wang, Z.; Flytzani-Stephanopoulos, M. *Energy & Fuels* **2005**, *19*, 2089-2097.

(3) Zeng, Y.; Kaytakoglu, S.; Harrison, D. P. *Chemical Engineering Science* **2000**, *55*, 4893-4900.

(4) Lahiri, J.; Mayernick, A. D.; Morrow, S. L.; Koel, B. E.; van Duin, A. C. T.; Janik, M. J.; Batzill, M. *Journal of Physical Chemistry C* **2009**.

(5) Nörenberg, H.; Briggs, G. A. D. *Physical Review Letters* **1997**, *79*, 4222 LP - 4225.

(6) T. Masui, T. O., G. Adachi, Z. Kang, L. Eyring *Chemistry Letters* **2000**, *29*.

Appendix A

Standard INCAR file for CeO_2

Standard INCAR file for CeO_2

```
# Must be standard in runs that will be compared
  LREAL  =     T    real-space projection
  PREC   =  NORMAL
  VOSKOWN = 1
  EDIFF  =  1E-04   stopping-criterion for ELM



# May be changed to tune speed/convergence and still compare calculations of different parameters
  IALGO  =     38   algorithm
  NELM   =     400
  ISYM   =     0
  ISMEAR =   2;   SIGMA  =   0.05 broadening in eV -4-tet -1-fermi 0-gaus
```

Davidson, algorithm, more reliable convergence than “FAST” or VERY_FAST”

Optimized and taken from literature

```
# System/calculation specific and extremely important to confirm
  ISPIN  =     2   spin polarized calculation?
  ENCUT   = 450
  EDIFFG =  -.5E-01   stopping-criterion for IOM
  LDAU = .TRUE.
  LDAUTYPE = 2
  LDAUL = 3 -1
  LDAUU = 5 0
  LDAUJ = 0 0
  AMIX = 0.2
  BMIX = 0.0001
  AMIX_MAG = 0.8
  BMIX_MAG = 0.0001
  LMAXMIX = 6
  ADDGRID = .TRUE.
```

All Ce systems run spin polarized

Switches on on-site Coulomb interaction for DFT+U

Default DFT+U algorithm

l-quantum number for each atom type (-1 = no on-site correction, 3=f)

On-site Coulombic interaction parameter (U) value (eV) for each atom type

On-site Exchange interaction parameter (J) value (eV) for each atom type

Mixing flags to address SCF convergence issues – see cms.mpi.univie.ac.at/vasp/vasp/Mixing_tags_IMIX_INIMIX_MAXMIX_AMIX_BMIX_AMIX_MAG_BMIX_MAG_AMIN_MIXPRE_WC.html for further details (VASP Guide)

```
# Parameters that specify the type of calculation, write flags, additional output/features (RWIGS, LVTOT, etc)
  NSW    =    200    number of steps for IOM
  IBRION =     2   ionic relax: 0-MD 1-quasi-New 2-CG
  ISIF   =     2
  POTIM  = 0.5
  LCHARG = .FALSE.
  LWAVE  = .FALSE.




# Miscellaneous
  LCORR  =     T    Harris-correction to forces
  LDIAG  =     T    sub-space diagonalisation
```

VITA

Adam D. Mayernick

Education

B.S. Chemical Engineering **–** University of Rochester **2006**
Ph.D. Chemical Engineering – The Pennsylvania State University **2011**

Awards and Honors

Catalysis Society of Metropolitan New York Poster Award – Third Place (2010)
Penn State Chemical Engineering Research Symposium Best Presentation Award (2009)
59th Meeting of Nobel Laureates in Chemistry - Travel Award and Invitation (2009)
Pittsburgh-Cleveland Catalysis Society Oral Presentation Award – Second Place (2008)
University of Rochester Rush Rhees Scholarship
University of Rochester Bausch and Lomb Science Award Scholarship

Publications

1. **A. D. Mayernick,** M. J. Janik. "Methane Activation and Oxygen Vacancy Formation over CeO_2 and Zr, Pd substituted CeO_2 surfaces." *Journal of Physical Chemistry C* 2008, 112(38), 14955-14964.
2. **A. D. Mayernick**, M. J. Janik. "Ab initio thermodynamic evaluation of Pd atom interaction with CeO_2 surfaces." *Journal of Chemical Physics* 2009, 131(8), 084701.
3. J. Lahiri, **A. D. Mayernick**, S. Morrow, B. Koel, A. van Duin, M. J. Janik, M. Batzill. "Modification of Active Sites on YSZ(111) by Yttria Segregation." *Journal of Physical Chemistry C* 2010, 114, 5990-5996.
4. **A. D. Mayernick**, M. Batzill, A. van Duin, M. J. Janik. "A ReaxFF Reactive Monte Carlo Study of Surface Enrichment and Step Structure on Yttria-Stabilized Zirconia." *Surface Science* 2010, 604, 1438-1444.
5. **A. D. Mayernick**, M. J. Janik. "Methane Oxidation on Pd-ceria: A DFT Study of the Combustion Mechanism over Supported Pd Atoms, Palladium Oxide and Palladium Metal Surfaces." *Journal of Catalysis* 2011, 278, 16-25.